The University Of Sheffield.

Design of a Novel Synchronous Reluctance Traction Machine with a Multipart Composite Rotor.

Edward John William Stone

A thesis submitted in partial fulfilment of the requirements for the degree of Doctor of Philosophy

The University of Sheffield
Faculty of Engineering
Department of Electronic and Electrical Engineering

Submission Date: July 2021

Abstract

This thesis reports on a programme of research undertaken on part with an industrial sponsored project concerned with a new concept for a synchronous reluctance machine with a novel multipart composite material rotor for use as a traction machine in combination with a high-speed gearbox for all-electric and hybrid-electric vehicles.

The market technical requirements for electric vehicles are reviewed alongside an assessment of the competing machine technologies with a particular focus on synchronous reluctance machines.

The thesis reports on a series of structured and systematic design studies spanning different rotor and stator structures for high-speed synchronous reluctance machines. These studies encompass both electromagnetic and mechanical behaviour with a wide range of rotor and stator combinations. The investigations explore issues including rotor geometry and machine pole number, including considerations of losses, torque density and ripple torque. A central question which is addressed via these studies is the maximum operating speed capability of the proposed rotor concept and the merits of different mechanical design features, including a detailed assessment in the role of adhesive bonds in retaining flux guides within composite rotors. These design studies are underpinned by an extensive use of advanced modelling and simulation tools spanning electromagnetic, structural, rotor-dynamic and system simulations. These include an extensive use of finite element analysis. The thesis concludes by choosing a design of 12 pole rotor that was extensively tested both mechanically and electromagnetically as well as a report on progress towards a hardware build for testing.

Declaration

I, the author, confirm that the Thesis is my own work. I am aware of the University's Guidance on the Use of Unfair Means. This work has not been previously presented for an award at this, or any other, University.

Edward Stone

16/07/2021

Acknowledgements

I would like to pay my gratitude to my supervisor Prof. Geraint Jewell, for his academic support and guidance throughout my time studying for this Ph.D. I have gained valuable knowledge of this subject field and the wider study into research under his guidance. I would also like to thank my second supervisor Prof. Martin Foster for his support and guidance where needed.

I would like to acknowledge and thank Ricardo for giving me the opportunity to study this thesis, specifically; Andrew Atkins, Eddie Wearing, Raymond Coles and Chris Whitby for their help and support during the early stage of the project.

I would also like to thank my parents and friends for their help and moral support during the final stages of this project and through the entirety of the COVID19 pandemic. Specifically, Cooper McCallum whose evening walks were a much needed distraction from the monotony of writing during a pandemic.

Finally, I would like to thank my friends and colleagues in my office for interesting and informative conversations on different topics surrounding our subject.

Contents

1. Introduction

1.1. Societal Context

There is an increasing focus on reducing global greenhouse gas emissions to combat global warming across almost all aspects of industry and wider society. The response of the UK government to climate change was to set a 'net zero' emissions target for the UK by 2050 [1]. One of the biggest contributors to UK emissions is the transport sector, with passenger vehicles, defined as cars and taxis making up 55% of transport sector emissions [2]. Furthermore, these emissions and associated pollutants are often localised in urban areas which raises health and well-being issues. These concerns fed into the air quality plan introduced in 2017, which proposed ending the sales of new conventional diesel and petrol engine cars and vans by 2040 [3] a date that has since been brought forward to 2030 [4]. This was announced as a measure to both tackle nitrogen dioxide pollutions at the roadside, and tackle air pollution in general.

Driven by the interest in reducing vehicle emissions, over the last few years there has been a significant increase in the purchase and adoption of electric vehicle (EV) drivetrains [5] [6]. Electric powertrains are significantly less polluting than internal combustion engine (ICE) systems, and therefore exhibit a smaller carbon footprint when compared to their ICE counterparts [7]. All vehicle original equipment manufacturers (OEM's) are now concentrating their design efforts on EV and hybrid-EV based systems to allow them to meet ICE vehicle production bans when they come into effect.

Currently, EV drivetrains are focussed on the use of batteries for the primary energy storage in the vehicle, with the stored energy then being used in an electric motor / drive system to provide the torque to the vehicles wheels. The choice of motor topology, for use within a vehicle design, is wide and is discussed in detail in chapter 2.

In addition to the development and research being carried out by vehicle OEMs, their tier 1 suppliers are also carrying out work on possible drivetrain solutions to achieve a marketable product for the OEMs of future vehicle designs / production. In addition to OEMs and Tier 1 suppliers, there is also significant interest amongst drive train consultancies, with a need to keep ahead of the curve with developing technologies, and hence migrate their expertise into the area of EV drivetrains. One such consultancy is Ricardo PLC, who conceived this project and supported it for the first two years or so.

1.2. Project Scope and History

The genesis of this project was a long-standing interest of Ricardo in the use of synchronous reluctance (SYNCREL) machines for electric vehicle traction drives [8] since they have been promoted as one

candidate technology to eliminate the reliance of the EV market on rare-earth magnet materials. The underlying premise of their approach was to overcome the recognised torque density limitations of this type of machine by operating at very high rotational speed, i.e. of the order of 30,000rpm which is 2-3 times higher than is currently considered to be mainstream in PM traction machines for automotive applications. This in turn would require a lightweight high-speed gearbox to produce a useful traction output speed while maintaining a cost and weight competitive package. The gearbox was outside the scope of the research programme reported in this thesis but is nevertheless an important enabler, and formed the substance of an associated PhD project at The University of Sheffield.

The project was conceived to understand the performance capability and limitation of this as a concept rather than the design of a specific machine to a particular performance specification. This said, for reasons of integration with a realistic gearbox and other drive-trains components, some ballpark dimensions were specified by Ricardo, viz. a rotor diameter of ~170mm, an overall stator diameter of ~300mm and an active stack length up to 100mm. Indications from sizing studies based on a conventional 4 pole rotor, and which are discussed in detail in chapter 3, suggest a torque in the range 80-100Nm for an operating rms current density of 10A/mm^2 (a realistic value for a water jacket cooled machine). This in turn would translate into a power level of between 83kW – 105kW per 10,000rpm of achievable maximum speed. The initial discussion centered around the use of an 800V converter, commensurate with the trend towards increasing voltage in EV's, aimed at keeping I^2R loss low throughout the electrical system.

The topology concept proposed by Ricardo involved a composite rotor. A hub manufactured from E-glass fibre reinforced composite would provide the main rotor structure, into which would be incorporated soft magnetic inserts to achieve the rotor saliency required for torque production. The light-weight nature of this rotor was identified as not only offering overall drive-train mass advantages but also rotor dynamic benefits, due to the high stiffness and low mass. This would move the critical speeds upwards, and provide a cost effective manufacturing route for volume applications via an over-moulding process using bulk moulding compound (BMC). This torque requirement of 85Nm was taken as a starting specification, with the speed rating, and hence power rating, ultimately being determined by subsequent design studies. In this regard, this unusual starting specification does not include a power rating as such. Indeed, the achievable speed and hence power of this machine concept is a key outcome of the research. It is important to note that the maximum speed is not solely a mechanical consideration since, as will be shown later in this thesis, steps to improve mechanical performance can have a very adverse effect on the electromagnetic performance.

The key aim of this thesis is therefore to explore the electromagnetic and mechanical behaviour of a high-speed SYNCREL concept based on a novel composite fibre-glass and silicon iron rotor. It is worth noting that little or no preliminary analysis of this concept had been undertaken before the start of this project, beyond some drive-train level studies of the benefits of high-speed operation of the electrical machine.

1.3. Thesis Structure

This thesis starts to research around, and potentially answer the question of, whether it is possible to design a high speed synchronous reluctance motor that uses a novel concept rotor to understand the complexities in the electromagnetic, mechanical and manufacturing of the design, to enable it to perform at high speed. The thesis is structured into 8 chapters as follows:

Chapter 1 provides the wider societal context for the research, introduces the project scope and lays out the structure for the remainder of the thesis.

Chapter 2 presents a literature review spanning general trends in electrical machines for electric and hybrid-electric vehicles, the commercial environment which is driving much of the research into eliminating permanent magnets from next-generation machines, and provide a technical review of competing machine types. The performance and features of synchronous reluctance machines are a particular focus of the technical review of machines as this is the machine type at the centre of this programme of research.

Chapter 3 presents a series of electromagnetic design studies on different 4 pole rotor topologies including cruciform salient pole rotors and various configurations of flux barrier and flux guide rotors, spanning from single-piece lamination cross-sections to an array of separate pole pieces in a nonmagnetic hub.

Chapter 4 is a systematic study of the influence of pole number on electromagnetic performance with detailed finite element based predictions of several aspects of the design. This includes further parametric investigation of the down-selected 12 pole machine, and a consideration of the impact of pole number on iron loss.

Chapter 5 reports on a detailed investigation into the mechanical behaviour of a large number of rotor variants within the context of establishing a well-founded and rigorous basis for selecting the preferred rotor topology and establishing the maximum speed capability of the machine. The investigation encompasses both structural considerations of stress and deformation, and rotor dynamic behaviour. With the extensive use of three-dimensional structural finite element analysis,

the chapter includes consideration of the role of adhesive bonding, captive flux guides, overwrap sleeves and single piece arrangements of flux guides. Although primarily focussed on the mechanical behaviour, further electromagnetic simulations are performed for mechanical features that are likely to have electromagnetic consequences.

Chapter 6 describes the development of a SIMULINK based dynamic model of the down-selected 12 pole machine and its deployment to investigate the design of a winding. The SIMULINK model including a comprehensive characterisation of the non-linear electromagnetic behaviour of the machine. The SIMULINK model is compared against analytical equations in order to explore the role of harmonics and non-linearity's in winding design.

Chapter 7 summarises the progress made towards building a prototype machine to provide experimental validation of the modelling and design performed in the preceding chapters.

Chapter 8 draws the key conclusions from the research findings and proposes several areas for future work.

2. Literature Review.

2.1. Electrical Machine Requirements for All-Electric and Hybrid-Electric Vehicles

All-electric and hybrid-electric vehicles are becoming an increasingly important segment in the automotive market, with growing demands on performance and cost reduction to meet customer expectations. An important element in all EVs and HEVs is the electrical machine, or in some cases multiple machines, which provide the means of propulsion for the vehicle. The primary performance measures for electrical machines for EVs and HEVs are torque density, power density (both gravimetric and volumetric), efficiency and cost.

The future requirements for electrical machines in terms of these performance indicators are laid out in published technology roadmaps which gather input from industry on market requirements and, in some cases, anticipated technology development. One of the most recent and authoritative technology roadmaps is the 2020 revision of the UK Automotive Council and Advanced Propulsion Centre roadmap for electrical machines [9]. An extract from this road-map which deals specifically with mass-market, high volume traction machines in the 100kW range is shown in figure 2.1. WLTP Average Efficiency, which stands for 'World harmonised Light-duty vehicles Test Procedure', is the standard test drive cycle for an electric machine. As shown there are expectations of both an almost halving of the cost per kW, at the same time as a more than doubling of the gravimetric power density. It is worth noting that these targets in terms of power density are more modest than those being proposed for aerospace, where values up to 20kW/kg are anticipated by 2035 [10]. The key difference between these two sectors is the relentless driving down of costs in the automotive sector which inevitably precludes the opportunity to use best-in-class materials such as Cobalt-Iron laminated cores or very advanced thermal management methods.

		2020	2025	2035
Electric Machine Indicators	Cost ($/kW)	6	4.8	3.3
	Volumetric Power Density (kW/l)	8	25	30
	Gravimetric Power Density (kW/kg)	4	8	10
	WLTP Average Efficiency	93%	95%	97%

Figure 2.1 UK Automotive Council and APC Technology indicators for cost effective, high volume applications (Source [9]**)**

The per unit mass and volume targets outlined in figure 2.1 are associated with specific performance expectations for mass-market EV machines, with some of the improvement coming from increasing power ratings and changing supply specifications, as illustrated in another extract from the roadmap which is shown in figure 2.2.

Electric Machine Indicators Spec	2020	2025	2035
Peak Power	100kW	100kW	100kW
Continuous Power	50kW	50kW	70kW
Input voltage (nominal)	400V	400V	800V
Output current (max)	450A rms	450A rms	225A rms
Coolant inlet temperature	65°C	65°C	65°C
Production volume	>100k	>100k	>200k

Figure 2.2 UK Automotive Council and APC Technology indicator representative specifications for cost effective, high volume applications (Source: [9]**)**

In setting out these targets, it recognised that power density and efficiency are very often conflicting objectives in electrical machine design. In general terms, power density is enhanced by increasing the current density in the coils and the flux density in the core, both of which dramatically increase loss density at a rate which outweighs the reduction in mass and volume, and hence results in reduced overall efficiency. Hence, some trade-off is required in order to simultaneously address both of these targets.

The headline efficiencies of many commercially produced EV machines in 2020 are already in the 90%+ range over much of their operating range. However, as demonstrated in figure 2.3, which shows a typical efficiency map for an interior permanent magnet machine from a Nissan Leaf [11] , there is some variation in efficiency over the operating envelope of the machine, and hence over a common driving cycle. There is a fairly large sweet-spot with efficiencies of up to 95%. However, the actual impact on the energy consumption and hence the range depends on the driving cycle requirements as detailed in [12].

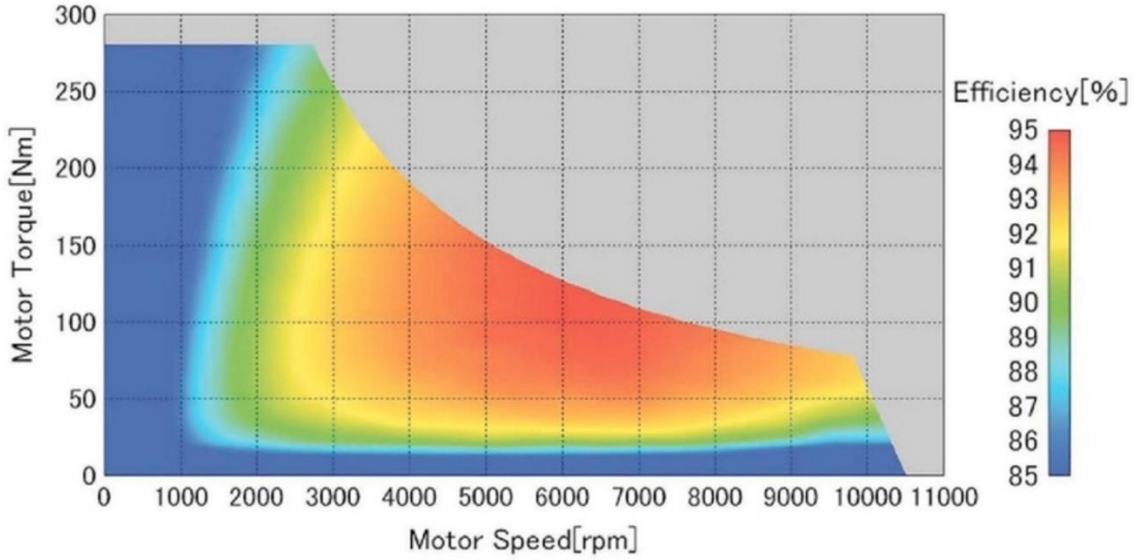

Figure 2.3 Efficiency map for a Nissan Leaf 2011 model motor (Source: [11]**)**

Meeting the cost reduction targets while achieving dramatic changes in performance poses numerous challenges. The wide reports which accompany the roadmaps anticipate cost reductions coming from a combination of scale-up in manufacturing volumes, emergence of improved material properties and improved design in particular thermal management [9].

In addition to headline performance factors in figure 2.1, there are numerous other requirements on electrical machines if they are to be competitive in future EVs, e.g. produce maximum torque from standstill, offer short-term overload capability above continuous rating, and be suitable for recycling or remanufacture [13].

As detailed in the previous chapter, this thesis is focussed on a pre-existing machine concept for a representative EV specification. This chapter covers the current state-of-the-art surrounding the different types of electric machines and their use in EVs, culminating in a more detailed review of machines that are close to the novel rotor concept at the heart of this project.

2.2. Types of Electric Machines used in Electric Vehicles

A 2021 review of electrical machines for the EV market [14] provides a useful breakdown of the motor type in vehicles which were on the market between 2010 and 2020. Figure 2.4 shows the resulting breakdown from which it can be seen that permanent magnet machines (designated as PM or PMSM) have dominated the market, at least in terms of the number of manufacturers that have adopted this technology. Of the 21 vehicle models captured in this review, 16 employed permanent magnet machine, 3 induction machines (IM) and one sole switch reluctance machine (SRM).

EV Model	Power (kW)	Motor Type	Year
Mahindra e2o Plus	19-30	IM	2016
Renault Kangoo ZE	44	PMSM	2011
Mitsubishi i-MiEV	47	PM	2010
Volkswagon E-up	60	PMSM	2019
Renault Zoe	65	PMSM	2012
LandRover	70	SRM	2013
Renault Fluence Z.E.	70	PMSM	2012
Nissan Leaf	80	PMSM	2010
BJEV EC5	80	PMSM	2019
Hyundai Ioniq Electric	88	PMSM	2016
Hyundai Kona	88-150	PMSM	2018
BYD E6	90	PMSM	2014
BMW i3	125	PMSM	2013
Xpeng G3	139	PMSM	2018
Mercedes-Benz EQC	150*2	IM	2019
BJEV EU5	160	PMSM	2018
Tesla Model X	193-375	IM	2015
Tesla Model 3	211-340	PMSM	2020
Tesla Model S	235-568	IM	2012
NIO EC6	320	PMSM	2020
NIO ES6	320	PMSM	2020

Figure 2.4: Survey of motor type on the market between 2010 and 2020 (Source: [14]**)**

There have been attempts to compare the suitability of different types of machines in terms of their effectiveness for EV traction. One useful comparison, albeit rather top-level and subjective, was published in [15]. Figure 2.5 shows a so-called relative qualitative indices assessment of several different types of machines for a small to medium EV specification, including many niche machine types such as flux-switching (FS) and traverse flux machines (TFM). In arriving at the final weighted total, the authors assigned a weighting of ×3 for cost, ×2 for mass and volume and ×1 for the remaining indices. Although subjective and based on the authors assessment of published designs, it nevertheless provides a useful indicator of perceptions of the strengths and weakness of different machine types. The highest total is achieved by interior PM machines in which the magnets are buried within slots in the rotor core. Surface mounted PM machines (SMPM) come joint second with induction machines (IM), with cost not unexpectedly being a weakness of PM machines. A particularly interesting outcome of figure 2.5 which is of relevance to the machines studied in this thesis, is the competitive position of synchronous reluctance machines (SYNCRELs). They come a close fourth in this ranking and not too distant from PM machines for the methodology adopted. It is worth noting in this is largely a consequence of cost being triple-weighted and synchronous reluctance machines are judged to be very competitive on cost.

Motor Type	Cost	Volume	Mass	Scalability	Equivalent fuel economy	Expected Life	Weighted Total
SMPM	5	9	8	8	9	7	73
IPM	6	9	9	8	9	7	78
IM	8	7	7	8	6	7	73
SR	10	3	4	7	4	7	62
SynRel	9	5	6	8	7	7	71
FS	7	6	7	7	5	7	66
FM	5	5	4	4	7	4	48
Homopolar	8	5	6	7	7	7	67
Axial	5	9	8	4	9	6	68
TFM	5	9	8	3	8	6	66
DS PM	4	10	7	6	10	6	68

Figure 2.5 Relative qualitative indices comparison of different machine types for EV traction applications (Source: [15]**)**

Despite the compelling evidence that PM machines are emerging as the dominant machine type in EV products and development programmes, and the general consensus that they offer the highest level of performance, there remains considerable interest and R&D activity in other machine types. Particularly those which have significantly reduced or zero permanent magnet content [16]. From a pure performance perspective, it is universally recognised that in the power ranges required for EV applications, brushless permanent magnet machines based on rare-earth magnets offer the best combination of power density and efficiency. The desire to eliminate rare-earth permanent magnets, even if this involves some performance penalty, is driven by a combination of costs concerns (the rotor magnets often being a high proportion of the overall cost), long-standing concerns over price and supply stability and geopolitical problems [17]. Neodymium (Nd) which is the key rare-earth material in permanent magnets for the EV market, suffered a ~25-fold price rise between 2009 and 2012 [16]. This was in large part a result of China controlling 97% of all the worlds rare earth element market in 2010 [18] and imposing export restrictions on rare-earth elements [19]. The demand for Nd is predicted to rise by ~2,600% by 2035 from a 2010 baseline [20].

Nd is a critically important material for the EV market. However, there is growing concern over supply capacity and the economics and environmental impact of new mining activities [17]. Therefore, there is growing interest in reducing the volume of magnets in future machines (including complete elimination), and increased recycling using dynamic substance flow in order to address this limited supply of new resources [21], [22]. With the supply risks and neodymium based magnet demand projected to rise in the future, recycling end of life magnets is an increasing priority [23]. Hence, the continued dominance of rare-earth based PM machines remains a highly topical issue while supply and price issues remain the key driver in terms of R&D into alternative machine types.

The following sections review the technical performance of both permanent magnet machines and competing magnet-free machine technologies, which are judged more favourably in figure 2.5. It is worth noting that although brushed DC machines found some applications in early and low-performance vehicle applications, their numerous performance limitations due to the presence of a mechanical commutators [24] means that they are very much a legacy technology for some low-power applications, and are not a serious candidate for the mainstream EV and hybrid market, and hence will not be reviewed in the following sections.

2.3. Brushless Permanent Magnet Machines

Brushless PM machines, which are also commonly referred to as PM synchronous machines and occasionally referred to as electronically commutated machines, have emerged over the past 30 years or so as the leading high performance machine type for applications which require the highest levels of power density or efficiency. A brushless PM machine has a rotor equipped with an array of permanent magnets, either on the surface of the rotor core or embedded into the core as shown in figure 2.6. As is the case with many types of electrical machines, the rotor can be mounted either inside or outside the stator as also shown in figure 2.6. The usual terminology for such arrangements are internal or external rotors. Internal rotors are far more common as they allow easier heat removal from the stator and a more straightforward mechanical arrangement. Within the EV sectors, external rotor motors have been proposed as attractive means of integrating in-hub direct drive machines. Brushless PM machines are usually equipped with a reasonably conventional multi-phase stator (almost always 3 phase although there are some 4 and 5 phase machines used in aerospace safety critical applications) [25].

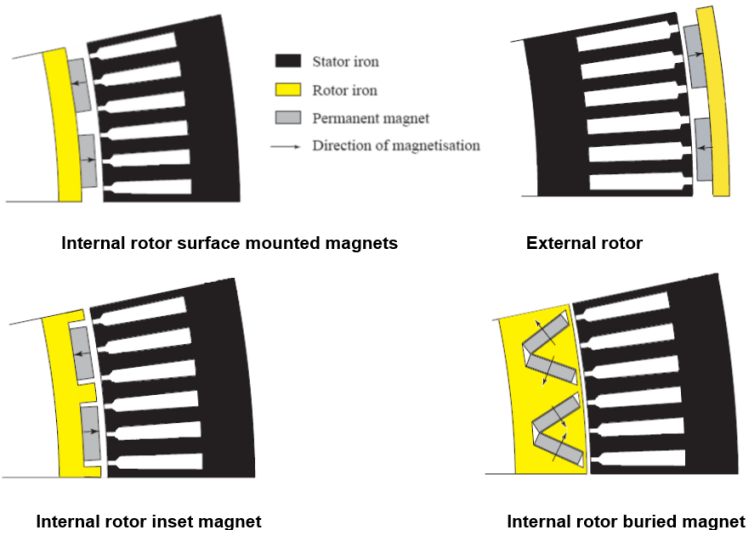

Figure 2.6: Schematic cross sections through different types of internal and external rotor PM machines

The key enabling development for power-dense PM machines was the emergence of rare-earth magnets, first with SmCo in the early 1970s and then NdFeB in the early 1980s [26]. These materials offered a step-change in the magnitude of the airgap magnetic field that could be produced in a PM machine compared to previous PM generations. Another important development was the advance in performance and cost reduction of power electronic inverters. Brushless PM machines are always used in combination with power electronic inverters in a configuration such as that shown in figure 2.7.

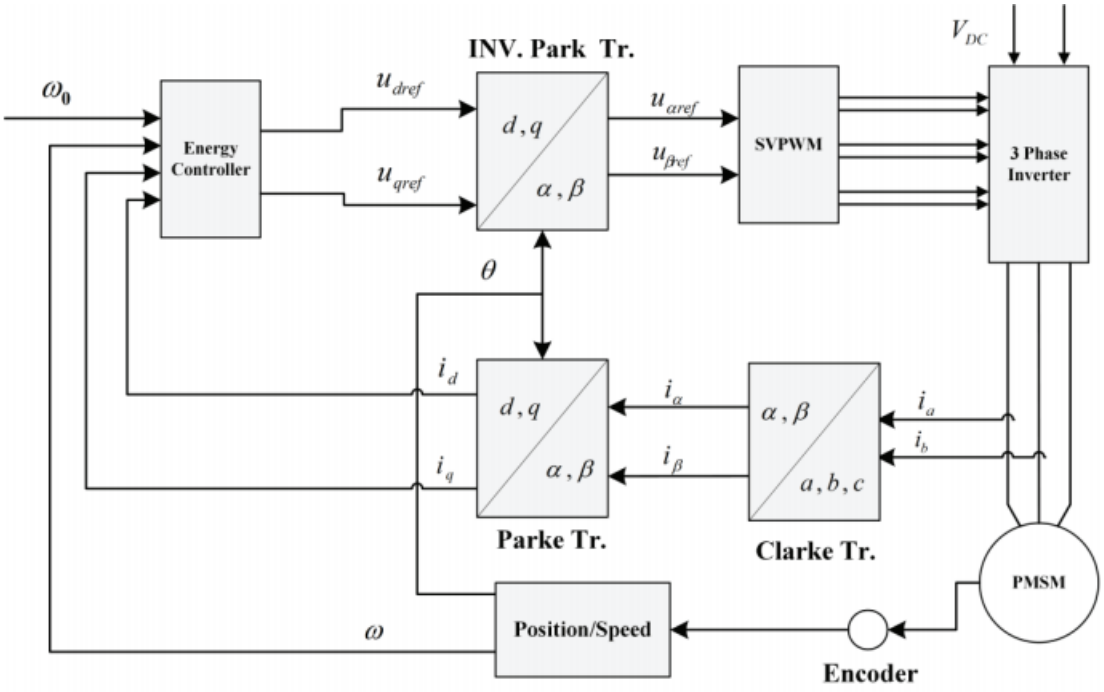

Figure 2.7 Typical 3 phase brushless PM machine drive system with angular position encoder, power electronic inverter and d-q axis based controller (Source: [27]**)**

The key to their operation is that the current pattern applied to the stator is varied as a function of rotor position and not time per se. Hence, the rotor is always synchronised with the stator field and therefore there are no concerns regarding loss of synchronism and stability. This will also allow full torque to be generated at standstill. This synchronisation of the stator rotating field with rotor position also allows the optimal angle between the rotor and stator field for maximum torque production to be maintained. This mode of operation relies on accurate information on instantaneous rotor position. In higher performance machines this is usually achieved with a position encoder or resolver, but in lower cost applications there is a growing use of so called sensorless position estimation which uses measurements of terminal currents and voltages to infer rotor position [28]. This has the advantage of eliminating the need for a position sensor, but does come with a performance penalty in terms of robustness of control, and introduces challenges when starting from standstill. Other types of

synchronous machines which operate with power converters to synchronise the stator currents with rotor position, such as synchronous and switched reluctance machines, have the same requirements for accurate position sensing.

Brushless PM machines can operate in either brushless AC mode or brushless DC mode, although the difference between these modes is not as significant as the terminology would suggest. Figure 2.9 shows schematic back-emf and current waveforms for both modes of operation. The difference between the machines is that machines intended for brushless AC operation are designed to produce a sinusoidal back-emf and operate with sinusoidal currents, whereas brushless DC machines have trapezoidal emfs and 120° quasi square wave currents. The vast majority of EV machines work in brushless AC mode.

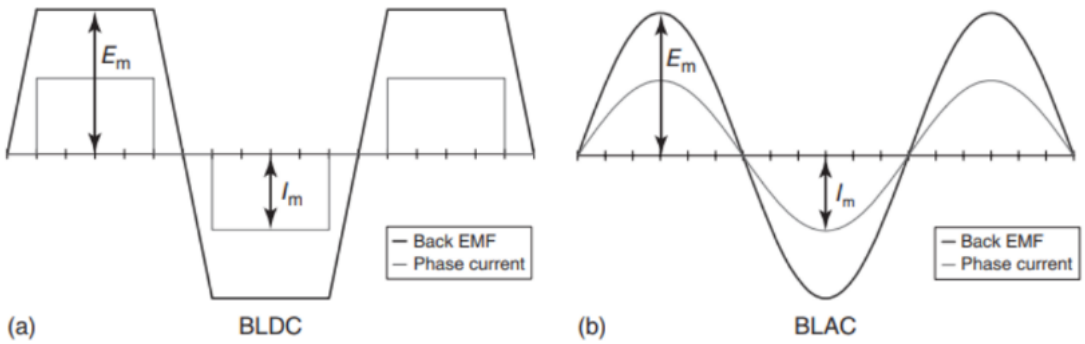

Figure 2.8 Schematic emf and current waveforms for brushless DC and brushless AC operation

An indication of the power density and efficiencies of PM machines aimed at the EV traction market can be obtained from various design studies undertaken to meet the target requirements set out in the US Department of Energy Freedom Car 2020 specification [29]. This is standardised specification which has provided a useful benchmark against which design studies and resulting prototypes can be compared on a consistency basis. The target specification is a 30kW continuous rating, increasing to 55kW for 18 seconds of overload capability. The operating speed range at this power is 2800-14,000rpm which corresponds to a maximum rated torque of 200Nm. The specification also sets out coolant temperature, maximum diameters, lengths and mass. Recent design studies using the Freedom Car 2020 specification have resulted in power densities of just under 1kW/kg for continuous operation with a maximum peak efficiency of 95.4% [30]. This modest power density is in part a reflection of the low speed of 2,800rpm at which the rated power is produced, and the focus on mass-market high volume applications. At the other end of the power density spectrum in automotive applications, small batch manufactured machines for high performance vehicles such as at the 220kW and 40kg APM200 from Equipmake [31] can achieved power densities in excess of 5kW/kg.

2.4. Induction Machines

Induction machines are by far the most commonly used machine type across many industrial sectors due to their combination of technology and manufacturing maturity, robustness, low cost combined with competitive power densities, competitive efficiencies and ability to self-start when line connected. They are far less prominent in the EV sector and despite some high profile US driven induction machine based EVs, such as Tesla vehicles prior to the recent Model 3, they have tended to be less favoured than permanent magnet machines in recent years by the majority of manufacturers, shown previously in figure 2.4. An induction machine of the type considered for EV traction applications consists of a 3 phase stator and so-called squirrel cage rotor, in which a series of conducting bars (often aluminium but sometimes copper) are incorporated into a rotor core and all connected with conducting end-rings. Figure 2.9 shows a cross-section through a typical design of 3 phase induction machine. The 3 phase stator winding generates a rotating field which induces emfs in the rotor bars, giving rise to current flow. The resulting rotor and stator generated fields interact to produce electromagnetic torque [32]. In order to induce an emf it is necessary to ensure some relative motion between the rotor and the rotating stator field, the speed difference being termed 'slip'. This slip accounts for the phrase 'asynchronous' often being used to describe induction machines.

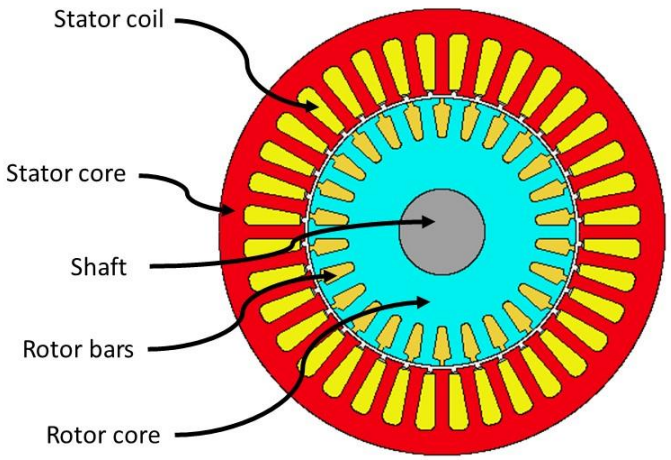

Figure 2.9 Cross-section through a typical 3 phase induction machine

Figure 2.10 shows the components of an induction machine with a copper cage which was designed specifically for EV traction applications [33], [34]. Induction machines tend to have a cost advantage over PM machines [35], particularly if an aluminium cage is employed although this gives a performance penalty compared to a corresponding copper cage. Induction machines are complex to control but modern control strategies and advanced controllers now allow precise control of speed and torque. The main drawback of induction machines is the lower efficiency and power density which arises due to losses in the rotor cage [24] [36]. Not only do these losses detract from the efficiency,

but removal of heat from the rotor is very challenging and often limits the power capability of these machines to be lower than that of a corresponding PM machine, as demonstrated in like-for-like design studies such as one reported in [37]. Overall, despite their low-cost and rugged construction the efficiency and power density penalty has resulted in a move away from induction machine for EVs in recent years, even amongst their original proponents such as Tesla. Nevertheless, induction machines continue to attract interest in lower power applications as a competitive magnet-free option, particularly amongst US manufacturers [38].

Figure 2.10 Components of a 26 kW induction machine producing 120 Nm at a base-speed of 2020 rpm (Source: [33]**)**

2.5. Switched Reluctance Machines

A schematic cross-section through a Switched Reluctance (SR) machine is shown in figure 2.11, in this particular case a 3 phase machine with 18 stator teeth (each equipped with a concentrated stator coil) and 12 rotor poles. This machine type is a doubly salient machine in which the rotor consists of a simple salient stack of electrical steel laminations with no magnets, coils or conductor bars. At a given starting position, forcing current into the appropriate stator phase causes the rotor to be drawn into a position of minimum reluctance and hence maximum flux. By selecting certain combinations of rotor and stator teeth number, and by appropriate sequencing of current pulses into the windings, continuous rotation in either direction can be realised. This type of machine operates via a series of discrete strokes and hence the torque is often very pulsed in nature.

SR machines have many potential advantages for EV applications when compared to other magnet-free machines, but they are not without their drawbacks. They offer competitive torque densities and efficiencies [24] although still some way behind permanent magnet machines [39]. These machines

have the potential to operate at high-speeds due to the robust single piece nature of the rotor [40]. They have the potential to be low cost with published estimates that the material cost of an SR machine is around half that of PM machine for a 30kW machine [14]. However, SR machines are well-known for suffering from high levels of vibration and acoustic noise in comparison with other machine topologies [24], [41], [42]. The acoustic noise problem usually occurs as a result of heavy saturation at the pole tips, and is influenced by the ratio of the number of poles on the rotor to the number on the stator, with an increasing ratio being claimed to reduce such vibrations [43], [36].

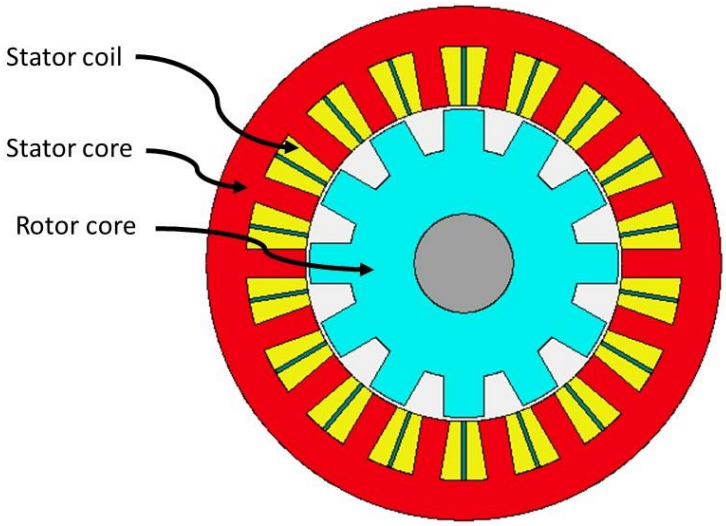

Figure 2.11 3 phase, 18-12 switched reluctance machine

SR machines have been heavily promoted as a competitor to PM machines for many years, with their slightly inferior torque density and efficiency (which is still very competitive with other magnet-less machines) being traded against their potential as a low cost machine. Despite these attractive features, as will be apparent from the list of machines adopted in vehicles shown previously in figure 2.4, they have very little impact in the EV market. This, in part, is a consequence of the large converter VA required for a given power (in effect the equivalent of a poor power factor), the complexity involved in their control, which is non-linear and often requires significant pre-characterisation, and the non-standard drives used [33].

2.6. Synchronous Reluctance Machines

2.6.1. Key Aspects of Geometry and Configuration

In common with SR machines, pure synchronous reluctance machines (which are commonly referred to as SYNCREL machines) exploit reluctance torque only. However, although they are based on a purely reluctance torque mechanism, there are several important differences from SR machines. A typical cross-section is shown in figure 2.12, in this case for a so-called 3 phase, 36 slot, two-layer stator

winding and flux barrier type rotor. As will be apparent, the stator is very similar to a standard 3 phase stator of an induction machine with limited saliency beyond the small and localised saliency contribution of individual slot openings. The manufacture of this kind of stator is highly optimised and mature to service the vast market for induction machines and hence it offers a relatively low cost stator. The role of the stator in a SYNCREL machine is to produce a smooth rotating magnetic field and not provide first-order stator saliency. Hence, SYNCREL machines are regarded in most cases as singly salient machines. The underlying operation is based on the rotor synchronously following the rotating stator field at some load angle which determines the torque produced. SYNCREL machines were first proposed in the 1920s [44]. However, whereas they can in principle be operated directly from the AC mains, in any application requiring robust synchronism and torque or speed control, operation with a power electronic inverter is necessary. Since SYNCREL machines operate with sinusoidal AC currents in all phases, they can use standard inverters. The rotor is designed to maximise the saliency ratio between the axis of high inductance (d-axis) and the axis of low inductance (q-axis) [45] [46] [47] [48]. Many different rotor constructions and design features have been studied to optimise this ratio.

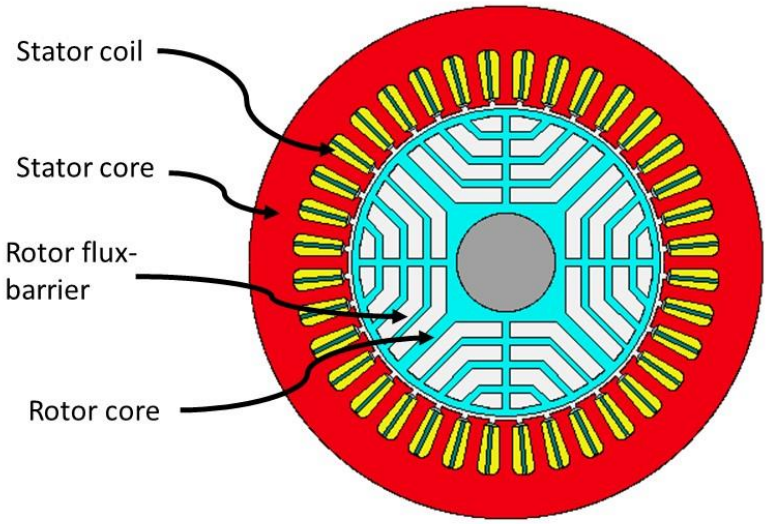

Figure 2.12 Typical 3 phase SYNCREL machine with flux barrier rotor

The rotors of SYNCREL machines are designed to maximise rotor saliency. Figure 2.13 shows 4 pole examples of the 3 main categories of rotors. Within these categories there are several variants. As an example, figure 2.14 shows several of transverse laminated rotors including so-called flux guide and flux barrier machines. The combination of a standard 3 phase stator and the simple stamped salient rotor make this type of machine a relatively low cost option [49], [16]. SYNCRELs have therefore attracted renewed interest as potential magnet-free option for EV drives, although it would appear that to date no commercially offered vehicles employ classical SYNCREL machines. This is in part a

consequence of their several key drawbacks, i.e. modest torque density [50], poor power factor [51] and tendency to saturate magnetically which limits the scope for short-term overload capability.

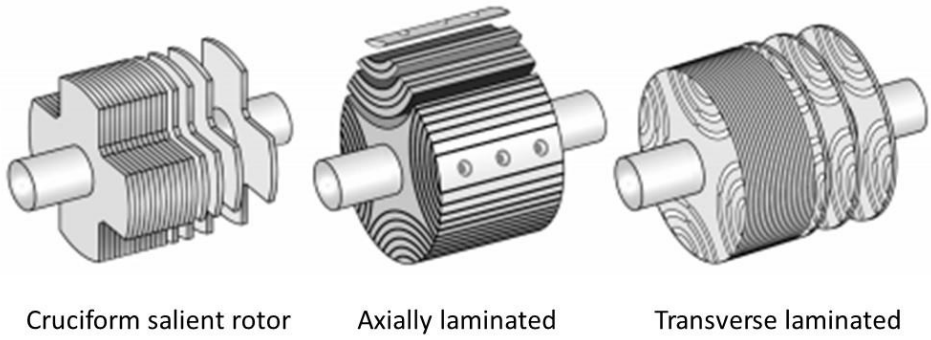

Figure 2.13 Main categories of SYNCREL rotors (Source: [50]**)**

(a) Curved flux barrier **(b) Angled U-shaped flux barriers** **(c) Cruciform or salient pole rotor**

Figure 2.14 Variants of transverse laminated rotors (Sources: (a) and (b) [52]**, (c)** [53]**)**

As will be apparent from figure 2.14, there are numerous types of transverse laminated topologies with numerous geometric parameters and features to select and optimise. The number of variables which define the rotor geometry of a complex flux barrier or flux guides rotor, and the number of operating points over which optimality can be established, has led to several studies on formal optimisation of rotor geometry including the use of combined finite element and genetic algorithms [52]. The rotor of figure 2.14(c), which is occasionally referred to in literature as 'massive' rotor, offers a very simple construction and good mechanical performance when the geometry is optimised to operate at high rotational speeds by incorporating an appropriate fillet radius such as the example shown in figure 2.15. In this case a degree of step-skew has been incorporated to reduce torque and emf harmonics, as large harmonics are a well-known drawback of simple cruciform type rotors [54].

Figure 2.15 4 pole salient pole rotor for high speed operation with 3-stage step-skew (Source: [54]**)**

In addition to a variety of different rotor structures, studies have been published into different winding configurations. A detailed design study supported by experimental validation is reported in [53] which covered combinations of 3 different rotor structures, 5 winding combinations, and two slot and pole number combinations. This study demonstrated that there is no single optimal winding arrangement for SYNCREL machines in terms of torque capability and efficiency, but that this varies for different slot / pole combinations and rotor geometries.

As noted previously, rotors of the type shown in figure 2.14(a) and (b) have very intricately designed flux guides and barriers to maximise the saliency ratio. In order to join the various regions of the rotor into a single-piece, there are bridging regions near the airgap. However, these act to reduce the saliency ratio by offering a magnetic circuit path. Their overall effect on the magnetic performance is usually limited by making them extremely thin so that they are readily saturated magnetically and hence no longer provide a low reluctance path. This necessarily means that the mechanical integrity of this type of rotor for high speed applications is often compromised by a trade-off in selecting these outer bridges [55]. The flux guides between the bridges acts as a beam in bending when subjected to centrifugal loading, and hence for long span flux barriers in low pole number machines, in some cases intermediate ribs are added such as those shown in figure 2.16.

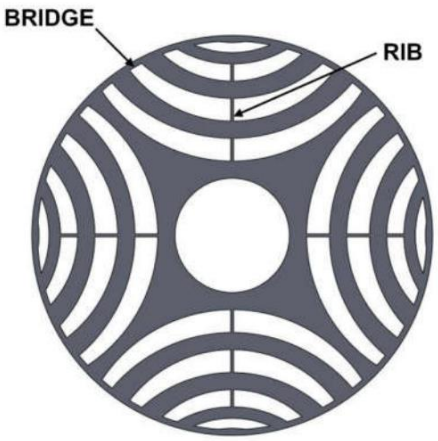

Figure 2.16 SYNCREL rotor with additional ribs to support flux guides (Source: [55]**)**

An alternative and potentially additional measure which can be taken to improve the mechanical integrity of such rotors is to fill the flux barriers with a high-strength resin, with the intention of resisting deformation of the flux guides [56]. The resin in this published study does not appear to be reinforced with a chopped fibre, and is described as 'Liquid aluminium-filled WEICON C'. It is claimed in [56] that this approach of resin infill allows operation of the rotor at 16000rpm with no intermediate ribs. A similar study in [57] with resin in-fill took this concept a stage further by relying on the resin bond to eliminate the ribs and bridge between flux guides as shown in figure 2.17. This study, which was published in 2020 (well after the start of this PhD thesis research) is the closest published concept to that proposed by Ricardo, and which underpins this thesis.

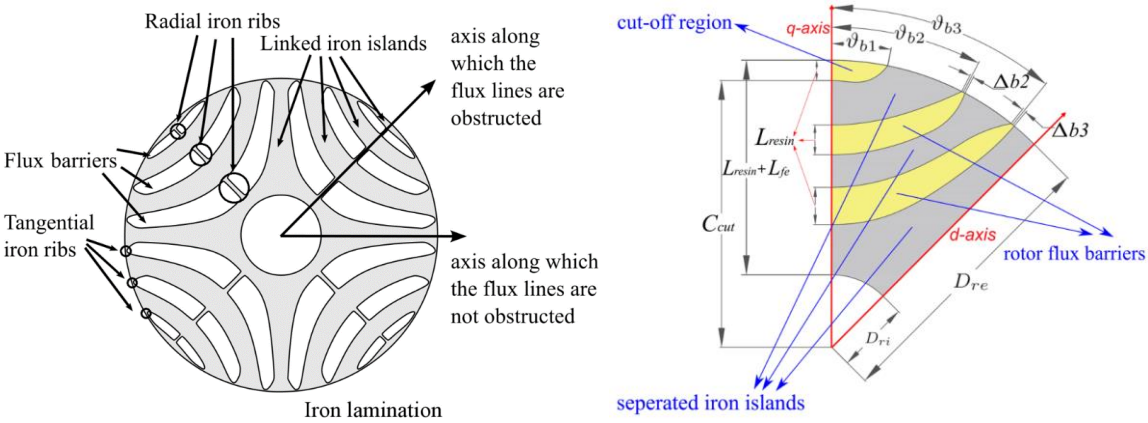

(a) (b)

Figure 2.17 a) original rotor structure with ribs and bridges b) Final test rotor segment with all ribs removed and epoxy resin in-fill (Source: [57]**)**

2.6.2. Fundamental Principle of Operation of SYNCREL Machines

The analytical equations for performance prediction of SYNCREL machine performance are often framed within the context of d-q axis theory in which a rotating reference frame is adopted to convert the time-varying sinusoidal currents to two orthogonal DC current components, i_d and $i_{q,}$ in the rotor reference frame. The underpinning theory of d-q axis theory is well covered in many standard textbooks and is not repeated here. Figure 2.18 shows the orientation relative to the rotor geometry of the d-axis and q-axis of a 4 pole synchronous machine [58], [53].

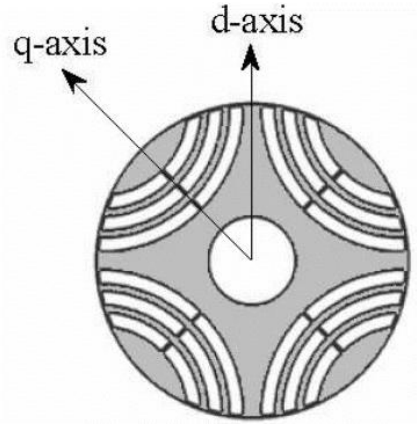

Figure 2.18 Definition of d-axis and q-axis in the rotor reference frame for a 4 pole SYNCREL machine (Source [53]**)**

The maximum torque these machines produce is directly dependant on the difference between L_d and L_q [59]. Standard d-q axis theory shows that the produced torque from this machine is given by equation 2.1 below [58].

$$T_{dq} = \frac{3}{2}p\left(\varphi_d i_q - \varphi_q i_d\right) \tag{2.1}$$

Where:

$$\varphi_d = L_d i_d \; and \; \varphi_q = L_q i_q \tag{2.2}$$

As there is no source of field excitation on the rotor, the flux on both the d and q axes is produced by i_d and i_q respectively;

$$T_{dq} = \frac{3}{2}p\left(L_d i_d i_q - L_q i_q i_d\right) \tag{2.3}$$

$$T_{dq} = \frac{3}{2}p\; i_d i_q\left(L_d - L_q\right) \tag{2.4}$$

Where;

$$i_d = i_s \cos\delta \;\; and \; i_q = i_s \sin\delta$$

where δ is the angle between the net current and the d-axis, and is also occasionally referred to as the load angle. Hence:

$$i_d i_q = i_s^2 \cos\delta \sin\delta = \frac{1}{2} i_s^2 \sin 2\delta \tag{2.5}$$

Substituting equation 2.4 into equation 2.3 for $i_d i_q$ gives the torque in terms of i_s and operating angle;

$$T_{dq} = \frac{3}{4} p\big(L_d - L_q\big) i_s^2 \sin 2\delta \tag{2.6}$$

As will be seen, the torque is proportional to the difference in inductances between the d and q axis, the square of the magnitude of the current and $\sin 2\delta$, which results in a maximum for $\delta = 45°$. When operated in conjunction with a power converter which is provided with angular position information, the current pattern in the stator can be synchronised to maintain $\delta = 45°$ for maximum torque. The key aspect in the magnetic design of a SYNCREL is achieving the highest possible difference between L_d and L_q , to achieve the maximum level of saliency. Most SYNCREL machines which are targeting applications in which power density is a requirement will usually have some level of localised magnetic saturation over their operating envelope [60]. Hence, the calculation of L_d in particular is likely to be a function of the magnitude of current. Values L_d and L_q for use in equation (2.6) usually requires finite element analysis either to establish a value for a particular current, or generate a characteristic which shows the variation of L_d and L_q with the magnitude of the current. There can also be a level of cross-saturation, [60], in which there is coupling between the magnitude of L_d and i_q but such considerations are usually set-aside in standard d-q axis theory.

The approach adopted in this thesis to calculate the L_d and L_q characteristic for phase A for example, is to orient the rotor relative to stator for the required component and then impose on phase A, a progressively increasing value of current whilst imposing currents in phase B and phase C that correspond to the values in those phases for the phase A current selected. An example of the resulting non-linear L_d and L_q characteristic is shown later in chapter 4.

The d- and q-axis current are related to instantaneous phase currents as follows [59], [58]:

$$\begin{bmatrix} i_d \\ i_q \end{bmatrix} = \sqrt{\frac{2}{3}} \begin{bmatrix} \cos(\theta) & \cos\left(\theta - \frac{2\pi}{3}\right) & \cos\left(\theta + \frac{2\pi}{3}\right) \\ \sin(\theta) & \sin\left(\theta - \frac{2\pi}{3}\right) & \sin\left(\theta + \frac{2\pi}{3}\right) \end{bmatrix} \begin{bmatrix} i_a \\ i_b \\ i_c \end{bmatrix} \tag{2.7}$$

Having established the relationship between the d- and q-axis currents, the phasor diagram of figure 2.19 (which neglects the resistive voltage drop) can be used to determine the underpinning voltage equations and power factor as:

$$V_s = \sqrt{(\omega \times L_d \times I_d)^2 + \left(\omega \times L_q \times I_q\right)^2} \tag{2.8}$$

$$\cos\theta = \frac{L_d I_d \sin\delta - L_q I_q \cos\delta}{\sqrt{L_q^2 I_q^2 + L_d^2 I_d^2}} \tag{2.9}$$

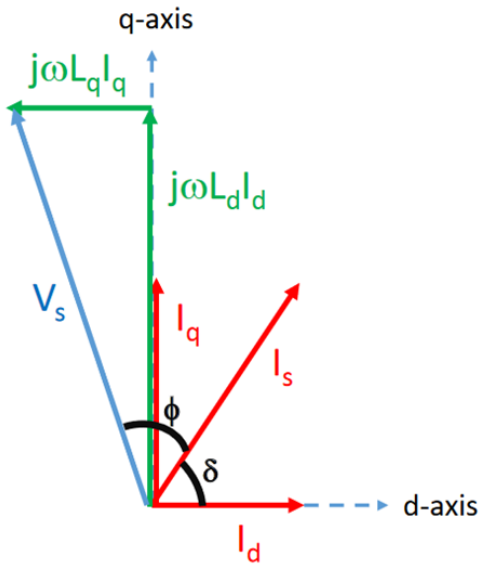

Figure 2.19 d-q axis phasor diagram for a SYNCREL machine (neglecting resistive voltage drop)

2.6.3. Permanent Magnet Assisted SYNCREL Machines

Some of the IPM machines of the type shown previously in figure 2.6 share many common features with SYNCREL machines in terms of their rotor core geometry since they are designed to produce a useful contribution from reluctance torque. A machine type that has attracted some attention in recent years with the price and supply pressure on rare-earth magnets are so-called reduced magnet IPM machines, and PM assisted SYNCREL machines. Although the exact geometry and feature may vary in emphasis, these types of machines form part of a continuum between the conventional IPM at one extreme, through to a pure SYNCREL at the other. At the permanent magnet assisted SYNCREL end of the spectrum, relatively small volumes of magnet (in some case low cost ferrite magnets rather than rare-earth magnets) are introduced to improve the power factor, as this is a well-recognised deficiency of conventional pure SYNCREL machines. Figure 2.20 shows a typical arrangement of a PM assisted SYNCREL in which an array of low-cost ferrite magnets within the flux barriers produce flux along the negative q axis to improve the torque capability and power factor [61].

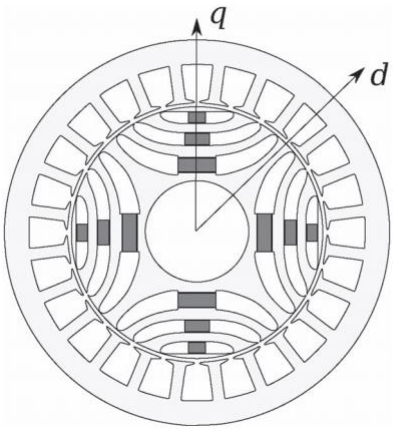

Figure 2.20 Typical arrangement of permanent magnets in a permanent magnet assisted SYNCREL machine (Source: [61]**)**

2.6.4. Doubly Salient Synchronous Reluctance Machines

There has also been growing interest in the use of doubly salient reluctance machines with standard sinusoidal converters. The terminology used in the literature is not entirely consistent, but in many cases the drive combinations are described as switched reluctance machine with sinusoidal current excitation [62], [63], [64]. From a construction point of view, these resemble SR machines with a highly salient stator and concentrated coils wrapped around a single tooth. These machines are an attempt to allow SR machines to operate with standard 3 phase converters, and yet exploit the potential torque benefit of being doubly salient. In some cases [62], this has included the adaptation of the rotor core from a single piece to a segmented rotor such as that shown in figure 2.21. In this case, the salient rotor poles are individual trapezoidal shaped poles, that are mechanically keyed into a non-magnetic structural hub for retention with potential for high-speed operation, at least from a mechanical perspective. A design study presented in [62] claims competitive torque densities with the PM machine from a Nissan Leaf, with torque densities between 9.5 Nm/kg to 11Nm/kg compared to 8.8kW/kg for the Nissan Leaf machine. However, these impressive torque densities are achieved in a series of designs which have rms current densities between 17.2 and 30.4 A/mm^2 while noting that no information on the Nissan Leaf was available for comparison. The use of highly compressed coils [65] to achieve high packing factors has been promoted as a means of addressing the high coil losses and heat transfer, but this technology is equally applicable to many PM machines and hence the margin is likely to remain. Whereas this shows that this configuration of machine has some potential to compete with PM machines on torque capability, it is unlikely to be on the basis of similar electric loadings and hence loss. On a like-for-like basis, PM machines are likely at have a higher torque and far superior power factor which has significant influence over the size and cost of the converter.

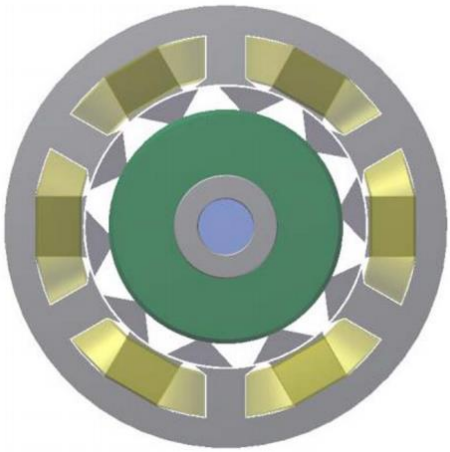

Figure 2.21 Segmented rotor doubly-salient 12-10 reluctance machine for use with sinusoidal excitation (Source: [62]**)**

2.6.5. Commercial Applications of SYNCREL Machines

Despite a great deal of on-going research and the pressure to eliminate permanent magnet materials, SYNCREL machines have made very limited impact commercially, particularly in applications requiring high torque density. ABB have been a strong advocate of SYNCREL machines as replacements for induction machines in many industrial applications such as fans and pumps which operate almost continuously. In this type of application, efficiency and hence energy consumption are the dominant considerations. Figure 2.22 shows a typical machine from the ABB industrial SYNCREL range which spans power from 5.5kW to 315kW. This series of SYNCREL machines can be operated direct on-line (in applications where the starting requirements are not onerous and the system moment of inertia is small) or via a power converter. Similar industrial sector SYNCREL machines are being offered as high efficiency alternatives to induction machines by other large manufacturers such as Leroy Somer. Despite some high profile demonstrators and niche product offerings, the presence of pure singly salient SYNCRELs in mainstream automotive traction machines is extremely limited with no major vehicle platforms adopting this technology. It is worth recalling that SR machines face a similar barrier to adoption for vehicles as noted earlier in this chapter. A high profile demonstrator programme involving Ricardo (the original industry sponsor of this PhD thesis) developed the machine shown in figure 2.23. Other than its headline specification of 85kW, there is no meaningful public-domain information readily available on this machine, and to date it does not appear to have need adopted in a vehicle platform.

Figure 2.22 ABB industrial SYNCREL machine (Source: [66]**)**

Figure 2.23 Ricardo 85kW SYNCREL demonstrator (Source: [67]**)**

Having examined current state of the art and background to the thesis, it is obvious that there is the start of a push into using composite materials to aid the mechanical strength, and achieve minor electromagnetic improvement in SYNCREL machines. This push for the use of composite materials in rotors fuels the research that will be discussed throughout this thesis, as it takes this work a step further. It has also been shown that there is a partial gap in the literature regarding the effects of higher pole numbers on SYNCREL machines. Over the course of this thesis the effect of different pole numbers on the performance of SYNCREL machines will be investigated. Therefore, the following chapter will initially examine in more detail the performance of several topologies of SYNCREL

machines to formulate a baseline design, to which higher pole number designs and composite material rotor designs may be compared.

3. Design Studies on Alternative Rotor Topologies

Having described the problem definition and current state of the art in previous chapters, this chapter is concerned with an assessment of the performance of several topologies of SYNCREL machines, covering both well-established topologies and newer rotor topologies based on the concept of embedding relatively small amounts of soft magnetic material in a composite rotor. This will allow for an initial concept test of the embedded flux guide designs as well as generating a baseline for torque output and torque ripple, against which future iterations of pole number and geometry can be compared. The assessment in this chapter is performed through a series of design and analysis studies which are underpinned by extensive finite element analysis. The finite element analysis package employed in these studies is Ansys Maxwell, as it is a solid finite element package, and employs the ability to use 2D and 3D analysis to solve a given problem. Ansys Maxwell is also a highly used and understood package, and therefore will be applicable to anyone following up on this work in the future. The topologies which are studied in this chapter are:

- 4 pole, single piece rotor with integral flux barriers
- Plain 4 pole, single-piece cruciform type rotor
- 4 pole flux guided rotor with flux guides embedded in a non-magnetic structure

In all cases, the designs were based on a 100mm long Silicon-Iron stator (M250-35A, magnetisation curve as used in the FEM analysis is shown in Appendix A [68]) with an outer diameter of 290mm and a bore diameter of 171mm, following on from the dimensions set out in section 1.2. Each machine was designed to operate with a working airgap (i.e. mechanical clearance) of 0.5mm. Initial stator designs were based around a 36 slot arrangement with a single-layer winding, although as will be shown later in this chapter, a 39 slot variant was also considered in order to reduce ripple torque. The arrangements of the coils in the 36 slot stator for a single-layer 4 pole winding is shown in figure 3.1. This winding has a fundamental winding factor of 0.96 and 5^{th} and 7^{th} harmonic winding factors of 0.217 and 0.177 respectively.

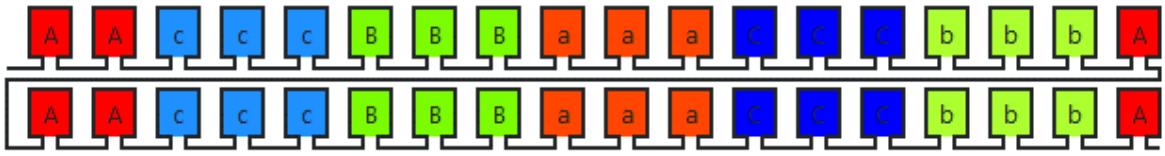

Figure 3.1 Winding layout for a 36 slot, 4 pole, single layer winding [69]

The leading parameters of the 36 slot stator are summarised in table 3.1. A close-up of one slot which serves to define the various slot dimensional parameters is shown in figure 3.2a.

Parameter	Measurement
Stator Outer Diameter (OD)	290mm
Stator Bore Diameter (BD)	171mm
Stator Axial Length (AL)	100mm
Tooth Pitch to Slot Pitch Ratio	1.58
Tooth Tip Height (H_1 in Figure 3.2a)	1.50mm
Tooth Body Width (Tw_2 and Tw_3 in Figure 3.2b)	9.47mm and 10.29mm
Tooth Tip Width (Tw_1 in Figure 3.2b)	13.14mm
Active Tooth Body height (Th_1 in Figure 3.2b)	14.00mm
Slot Opening Width (W_1 in Figure 3.2a)	2.04mm
Front Slot Width (W_2 in Figure 3.2a)	5.99mm
Back Slot Width (W_3 in Figure 3.2a)	7.85mm
Front Slot Spare Height (H_2 in Figure 3.2a)	2.96mm
Active Slot Height (H_3 in Figure 3.2a)	14.00mm
Back Slot Spare Height (H_4 in Figure 3.2a)	4.00mm

Table 3.1 Details of 36 slot stator geometry

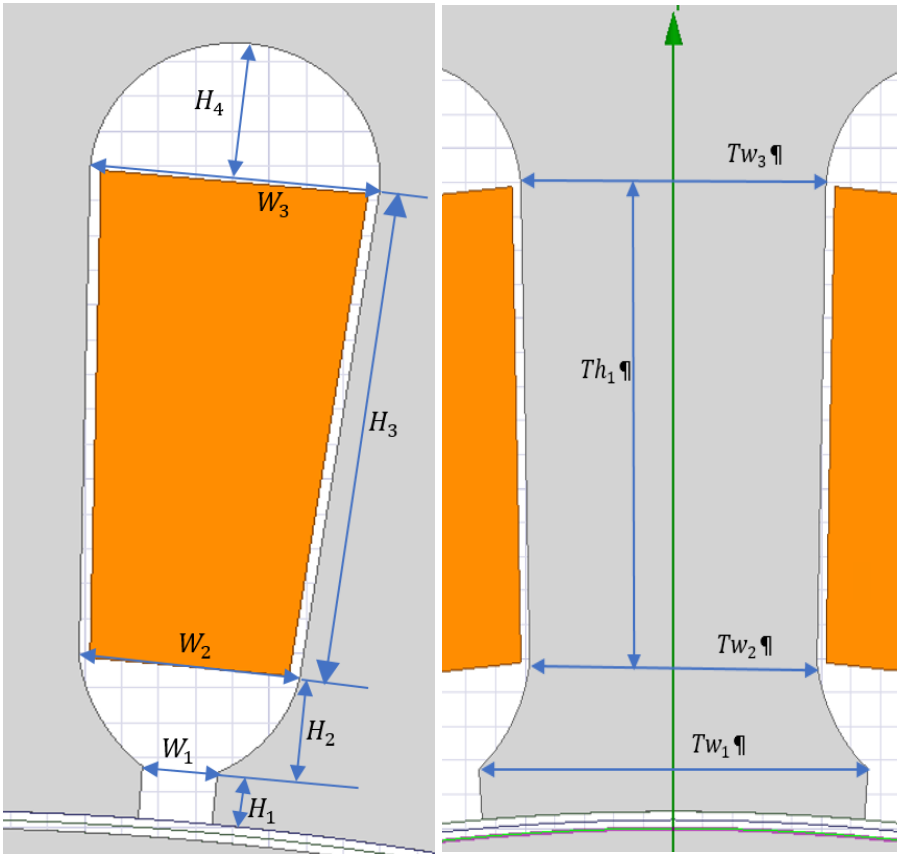

(a) **(b)**

Figure 3.2a, b: Details of slot and tooth geometry respectively.

Figure 3.1 is made up of multi-coloured boxes containing capital and lower case letters and are all linked together. These boxes represent the slots in the stator, and the adjoining 'links' are actually representative of the stator teeth. The upper case letters represent the positive coils of a certain phase, whereas the lower case letters represent the negative coils of that phase. Figure 3.2a shows the average design of the slots, the orange area is defined as the coil, and when discussing the packing factor throughout this thesis, it is based purely on this area, not taking into account the back of the slots.

3.1. Flux Barrier Rotor Design

The investigation that will be undertaken in this section is the initial design of a traditional SYNCREL rotor design. This will give a baseline design, to which the rest of the designs in this chapter can be compared. Later chapters will address the analysis of the stator design, for this section it is the rotor design that is under investigation.

The first rotor topology considered was the 4 pole flux barrier design shown in figures 3.3 and 3.4. Figure 3.3 shows the initial rotor topology for one pole, as well as the sizes of the different sections of the rotor geometry. This rotor consists of a laminated core in which a series of slots are introduced to act as barriers to magnetic flux, thus providing a low reluctance orientation in the rotor. The particular rotor geometry has 4 flux barriers per pole. The flux barriers are closed slots which do not extend all the way to the outer of the edge of the rotor, so ensuring that the cross-section is made up from a single piece. This leaves small joining bridges on the outer edge of the rotor which will reduce the effectiveness of the flux barriers by promoting flux-leakage through the bridges. Figure 3.3 shows a close-up of the rotor flux barriers in one quarter of the rotor which includes the key dimensions.

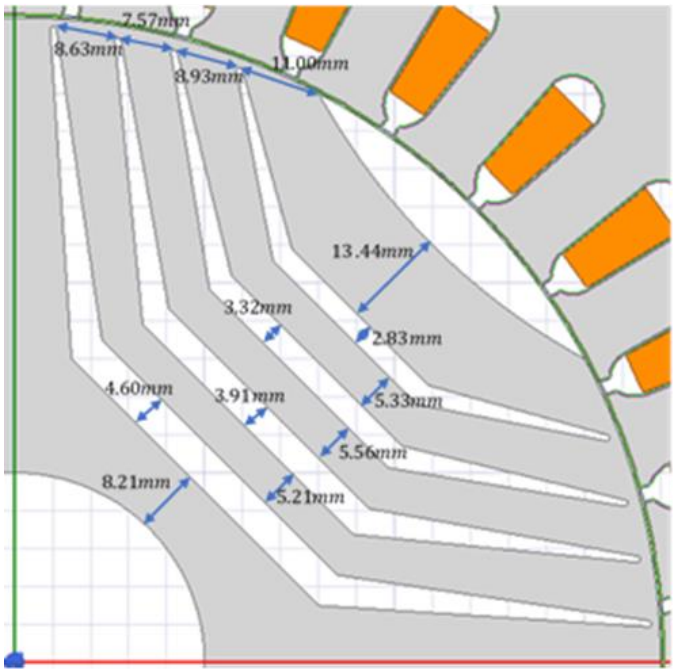

Figure 3.3 Detail of baseline design rotor flux barrier geometry

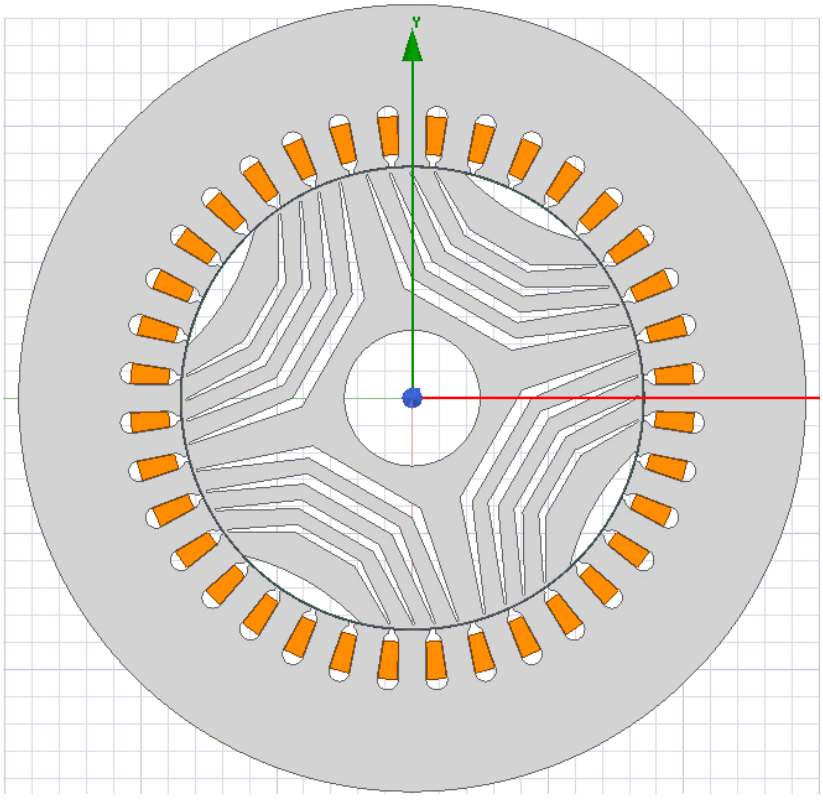

Figure 3.4: Cross-section through initial flux barrier baseline design (shown at 0° mechanical rotation angle)

Figure 3.4 shows a cross-section through the rotor core, the stator and the winding of which form the initial baseline flux barrier design for comparison with other designs. The torque waveform for this

first baseline design was calculated using two-dimensional, non-linear magneto-static finite element analysis. This use of 2D analysis allows complex designs to be run more efficiently instead of employing 3D analysis, as the torque production scales proportionally to the length along the Z axis, 3D analysis is therefore not required at this stage. Non-linear analysis is chosen as linear calculations wouldn't account for magnetic saturation. The magneto-static calculations are required to investigate the magnetic effects in the machines. In the analyses, 121 individual calculations were performed at 3° increments across one electrical cycle. The currents in each phase were synchronised to rotor position with an appropriate angular offset to ensure maximum torque production (the definition of the 0° reference rotational angle in the model was shown in the orientation of figure 3.4). The torque was calculated for sinusoidal phase currents which correspond to a rms current density in the stator winding of 10A/mm^2 for a coil packing factor of 0.5, which in turn corresponds to an mmf of 625A.turns per slot. Since ANSYS Maxwell solves such rotational problems in the time-domain as so-called 'transient solutions' (even though the magnetics are magneto-static), it was necessary to set a nominal rotational speed of 60rpm and hence an operating electrical frequency of 2Hz for this 4 pole machine.

A representative predicted flux design distribution in the machine at the rated rms current density of 10A/mm^2 is shown in figure 3.5, while figure 3.6 shows the calculated torque waveform for this baseline. At this rated current density, the average torque is 80Nm with a peak to peak torque ripple of 28.9Nm.

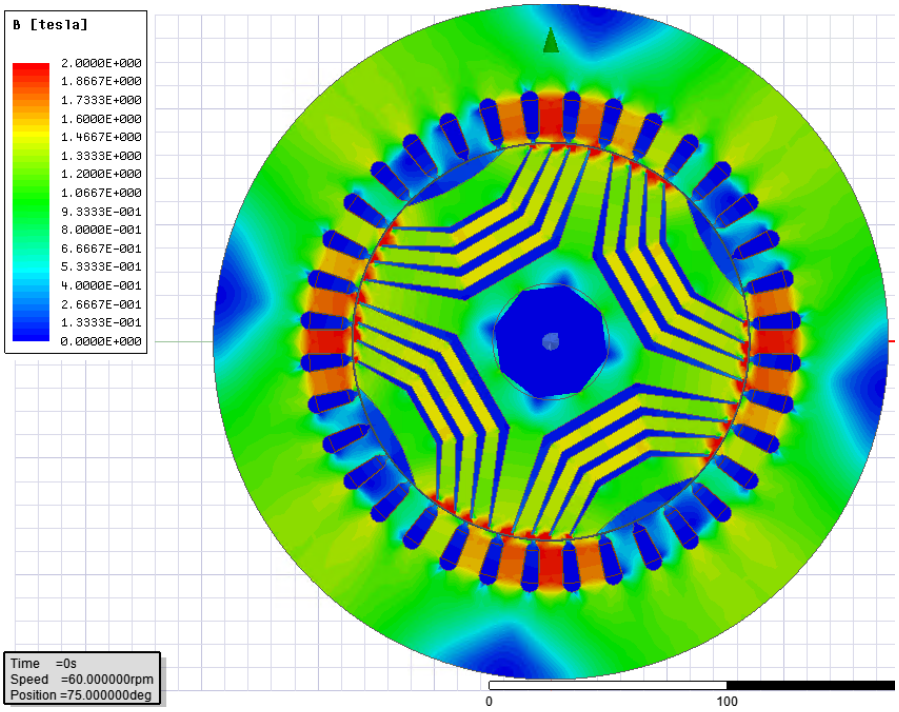

Figure 3.5 Finite element predicted flux density distribution for a rms stator current density of 10A/mm^2 (coil packing factor of 0.5) for the baseline flux barrier design

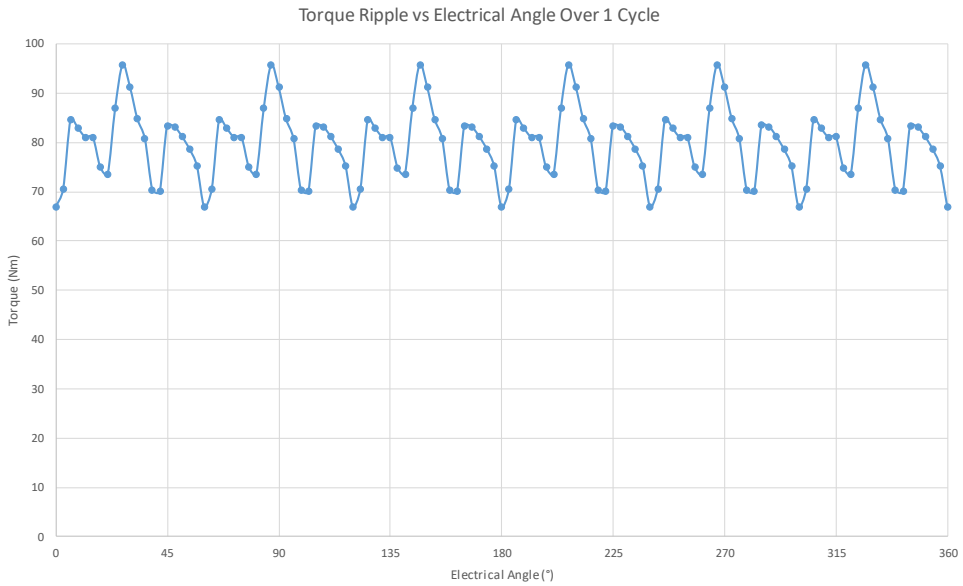

Figure 3.6 Calculated torque waveform for a rms stator current density of 10A/mm^2 (coil packing factor of 0.5) for the baseline flux barrier design

The predicted flux density distributions of figure 3.5 show that the highest level of flux density and hence magnetic saturation occurs in the rotor core, in particular in the regions between the flux barriers which are adjacent to the airgap. It is widely accepted that some saturation in the ribs between the edge of the flux barrier and the rotor outer diameter is acceptable. Additionally, in this design the saturation is shown to almost spread across the entire flux barrier. This will reduce the effective torque production as from a magnetic point of view it renders these sections invisible, and therefore act as though there is a larger airgap than there physically is. It also demonstrates the effectiveness of the flux barriers in promoting flux to pass through the preferred path within the rotor. However, these designs do show levels of saturation in the teeth that could be construed as unwanted, this will be addressed later in the thesis. In an attempt to improve the torque capability, the rotor design was revised to reduce the influence of magnetic saturation in the rotor. Figure 3.7 shows a close-up of one quarter of revised rotor design, designated 'FB2_4_36_10', in which the flux barriers have been modified as shown, specifically in terms of reducing the width of the flux barriers, and hence increasing the cross-section.

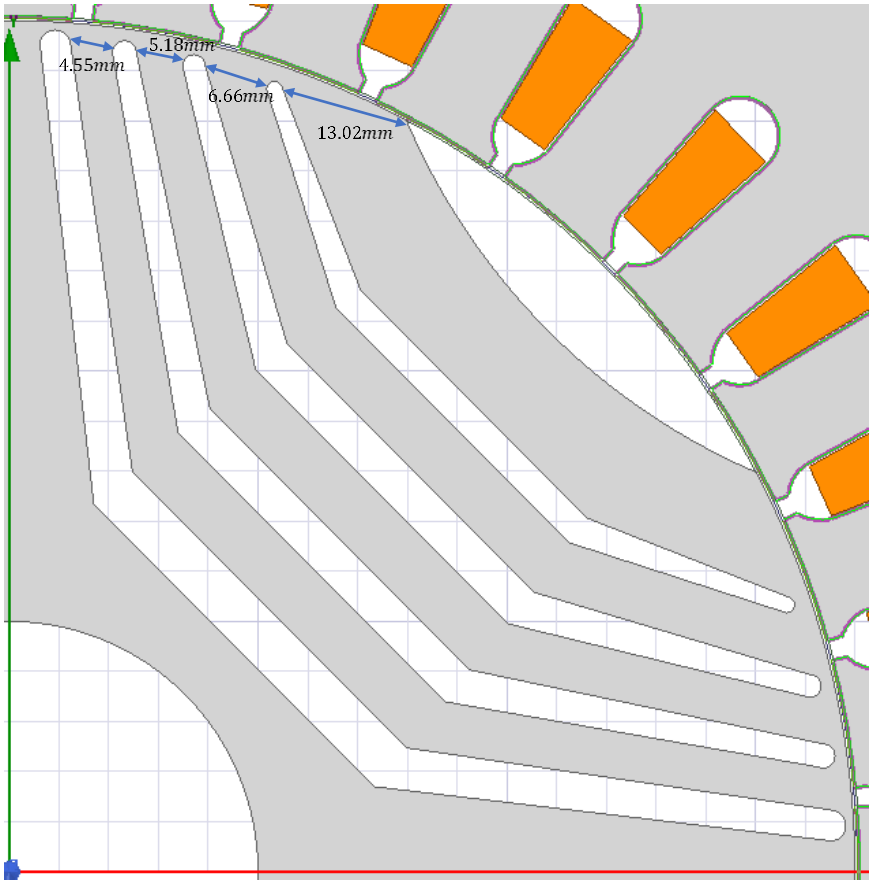

Figure 3.7 Detail of revised design rotor flux barrier geometry, shown is the alterations to the Flux barriers.

Figure 3.8 shows a predicted flux density distribution for this revised rotor design at the same stator rms current density of 10A/mm^2, and figure 3.9 shows the corresponding finite element calculated torque waveform with gives an average torque over one cycle of 83Nm, with a peak to peak torque ripple of 26.9Nm. This offers a modest improvement compared to the 80Nm average torque of the baseline design at the same stator current density. As will be apparent from figure 3.8, the levels of flux density in the rotor near the airgap still result in significant magnetic saturation, but as the levels of saturation here are more spread out along the lengths of the flux guides, this is a much more manageable design.

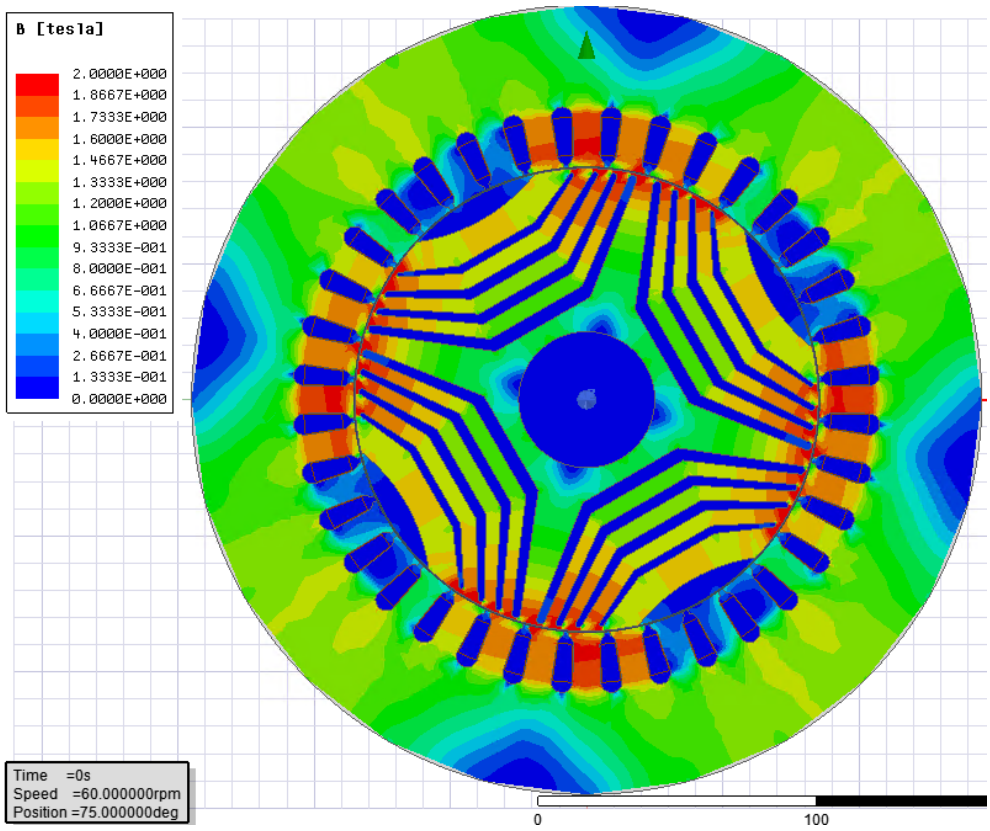

Figure 3.8 Finite element predicted flux density distribution for a rms stator current density of 10A/mm^2 (coil packing factor of 0.5) for FB2_4_36_10.

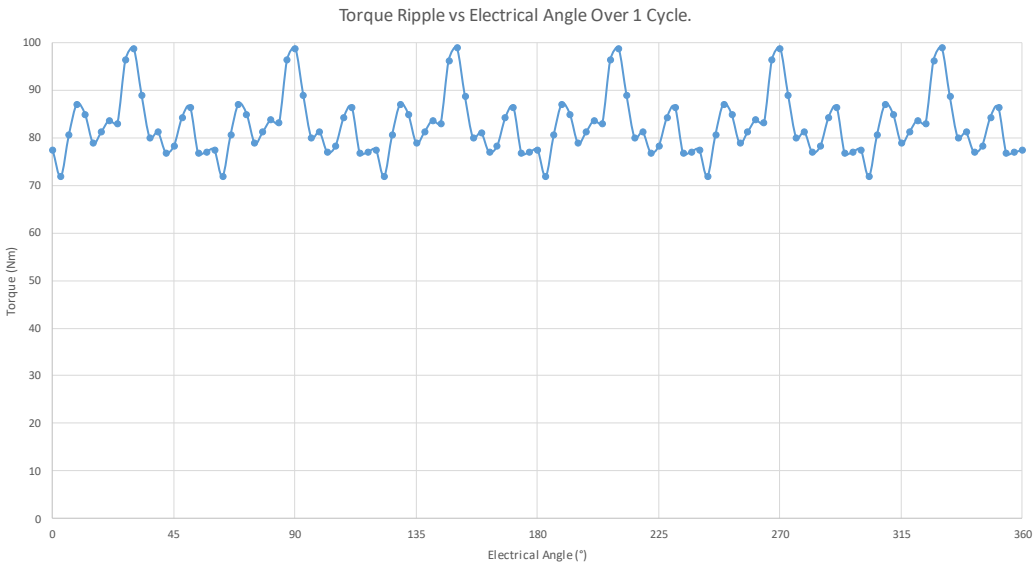

Figure 3.9 Calculated torque waveform for a rms stator current density of 10A/mm^2 (coil packing factor of 0.5) for Flux barrier design 2

Although the revised design (FB2_4_36_10) produced a higher average torque than the baseline design. A harmonic spectrum of the torque waveform for the revised flux barrier design, which was

calculated using an FFT, is shown in figure 3.10 (the dominant fundamental having been scaled down to allow a reduced scale to aid clarity of the harmonics). As is apparent, there is a significant 6th and 18th harmonic, which when normalised by speed of rotation, is due to the interaction of the spacing of the 36 stator slot openings and the flux barrier geometry.

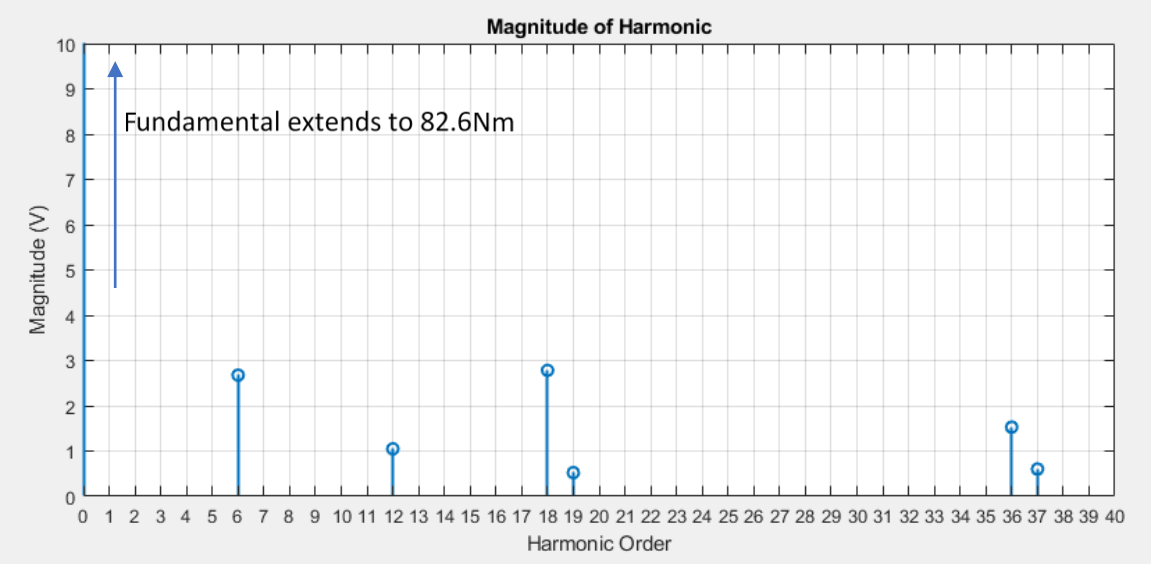

Figure 3.10 FFT of torque waveform of figure 3.9 for 36 slot revised rotor design (FB2_4_36_10)

In an attempt to reduce this torque ripple, a 39 slot stator variant with the two layer, fractional-slot winding arrangement of figure 3.11 was investigated with the same revised rotor, shown in figure 3.13. The slots were kept the same, with the teeth being slightly decreased in width to accommodate this increased slot number within the same stator core. Specifically, Tw_2 and Tw_3 are now changed to 8.49mm and 8.90mm respectively, down from those shown in table 3.1. This winding results in both a slightly different pitch of slot openings, and a reduced harmonic content in the stator field. This 39 slot winding has a coil span of 10 slots, and a pole-pitch of 9.75 slots. It has fundamental winding factor of 0.954 as compared to 0.96 for its 36 slot counterpart.

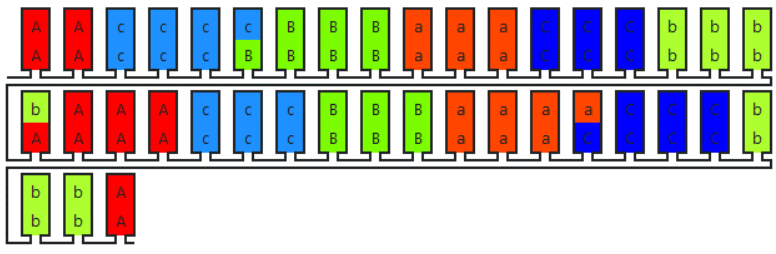

Figure 3.11: 39 Slot stator two-layer winding design

Figure 3.12 shows the finite element predicted torque waveform for the rated rms current density of 10A/mm^2 (at a packing factor of 0.5) which results in an mmf per slot of 625A.turns comparative to the previous 36 slot winding. As will be apparent, despite having a very similar winding factor as the 36 slot design (0.954 and 0.96 respectively), there is a very slight increase in the average torque produced by this winding from 83Nm for the 36 slot design (FB2_4_36_10) to 85Nm. However, the torque ripple is reduced significantly to 12.3Nm peak to peak.

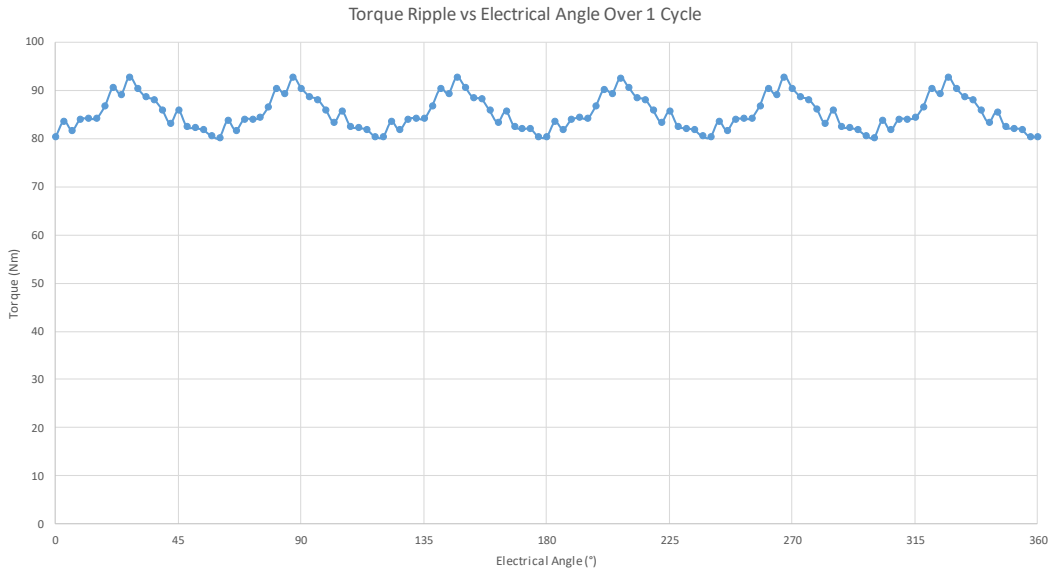

Figure 3.12 Calculated torque waveform for a rms stator current density of 10A/mm^2 (coil packing factor of 0.5) for Flux barrier rotor design 2 in a 39 slot stator (FB2_4_39_10)

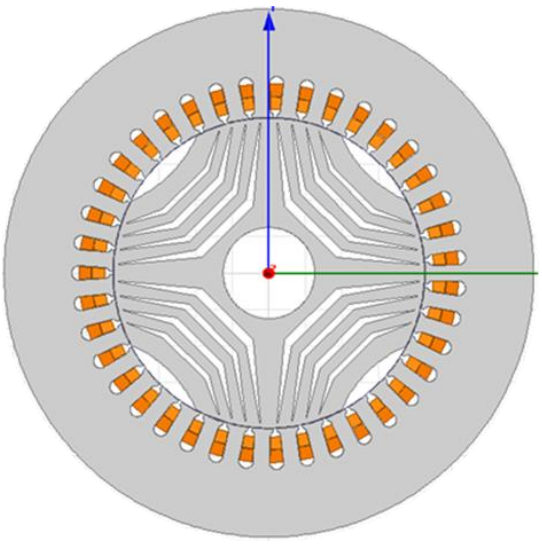

Figure 3.13: 39 Slot stator cross sectional design

3.2. Plain Cruciform Rotor Design

The next 4 pole machine variant considered is equipped with the plain cruciform shaped rotor shown in figures 3.14a-e. These particular designs (designated CF1_4_36_10 – CF5_4_36_10) were based on the same 36 slot stator with the same rotor outer diameter of 170mm and airgap of 0.5mm. For the first design (CF1_4_36_10), shown in figure 3.14a, the rotor pole arc spans 55° at each pole, and the inter-pole is 8.5mm deep at its centre.

Figure 3.15 shows the predicted torque waveform at the rated rms current density of 10A/mm^2 (at a packing factor of 0.5) for CF1_4_36_10. As will be apparent, many of the higher order harmonics in the torque waveforms seen previously are not present due to the absence of the modulating effect of the flux barriers. However, there is a marked reduction in the torque capability to a mere 44.8Nm in comparison with the best value achieved to date, at the same rms current density, i.e. 85Nm for design FB2_4_39_10.

Increasing the degree of saliency in this type of rotor was explored by maintaining the same pole arc but increasing the depth of the inter-pole. Increasing the inter-pole depth to 14.5mm, shown in figure 3.14b (CF2_4_36_10), and 20.5mm, figure 3.14c (CF3_4_36_10), increased the average torque at a rms current density of 10A/mm^2 to 48.3Nm and 49.5Nm respectively which remains some way short of the capability of a flux barrier design. Adopting the 20.5mm deep inter-pole (CF3_4_36_10), the effect of the pole-arc was investigated with 2 further designs having pole-arcs of 45°, figure 3.14d (CF4_4_36_10) and 35°, figure 3.14e (CF5_4_36_10). This resulted in average torque values of 60.1Nm and 60.2Nm respectively. The torque ripple in these designs are 46.1Nm and 55.2Nm peak to peak respectively.

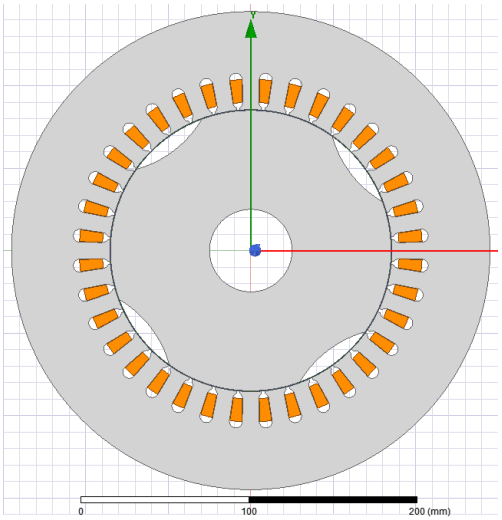

Figure 3.14a CF1_4_36_10

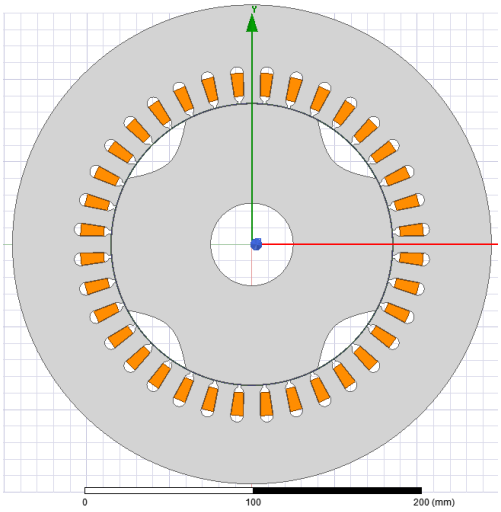

Figure 3.14b CF2_4_36_10

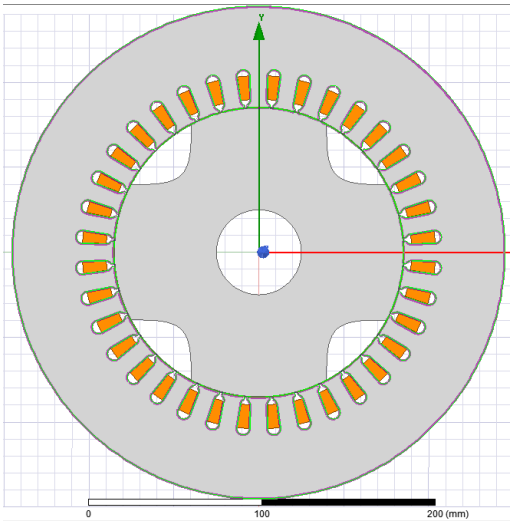

Figure 3.14c CF3_4_36_10

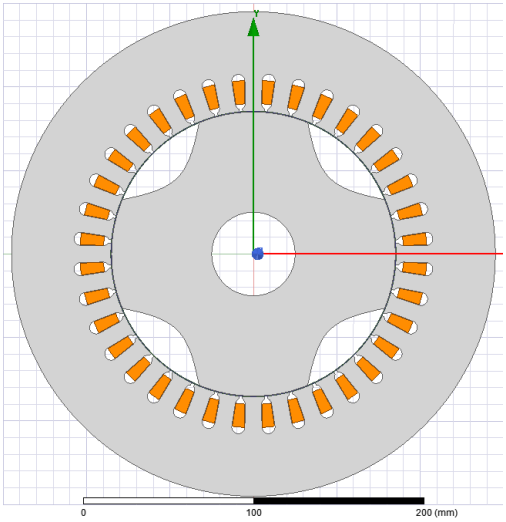

Figure 3.14d CF4_4_36_10

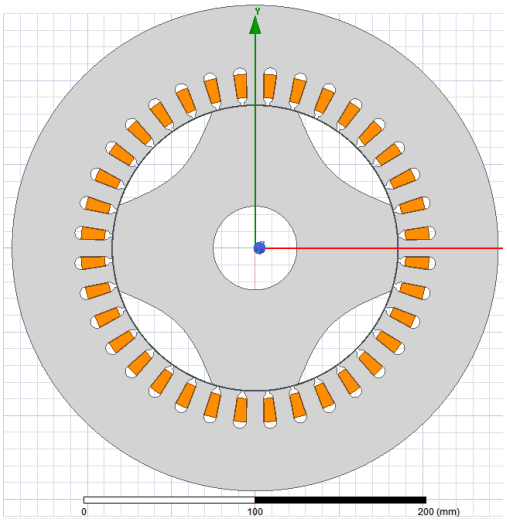

Figure 3.14e CF5_4_36_10

Figure 3.14a-e Cross-section through the 36 slot, 4 pole design with plain cruciform rotors.

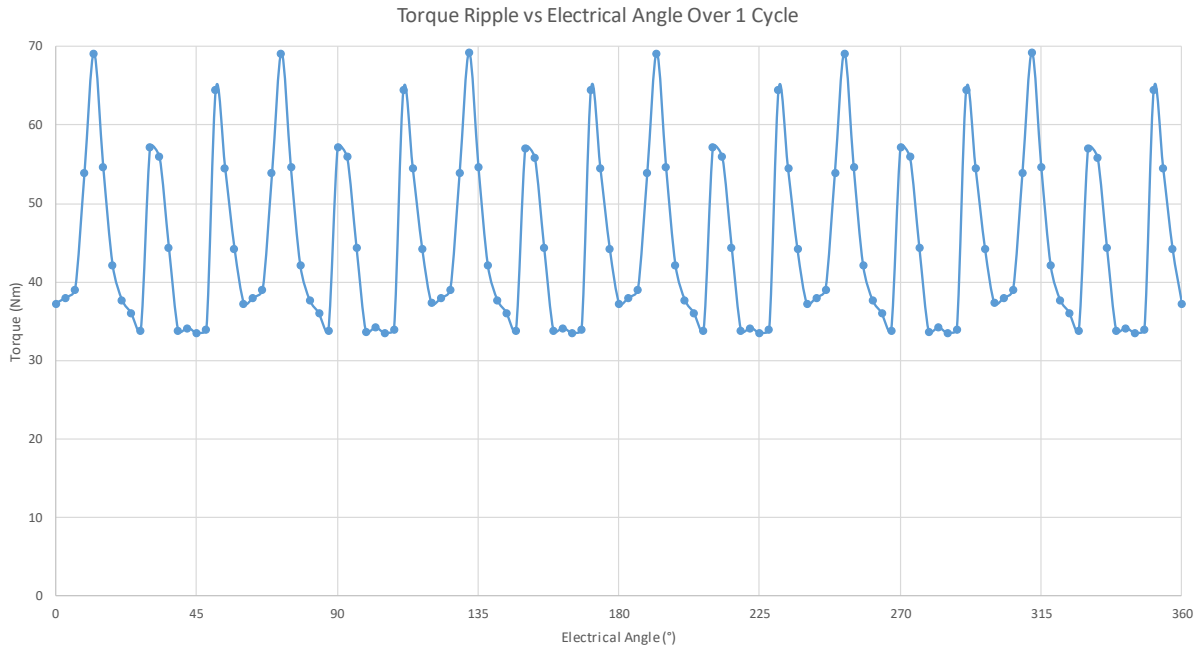

Figure 3.15 Calculated torque waveform for a rms stator current density of 10A/mm^2 (coil packing factor of 0.5) for the plain cruciform rotor design of figure 3.14a

3.3. Flux Guide Rotor Designs

As noted in section 1.2, the original machine concept set-out by the industrial sponsor was to embed a number of soft magnetic flux guides into a composite moulded rotor structure. In order to explore the torque capability of this approach a series of design based on different configurations and dimensions of flux guides were investigated. The initial design (designated FG1_4_36_10) is shown in figure 3.16 in which the grey regions represent M250-35A silicon iron flux guides and the yellow region the composite support structure.

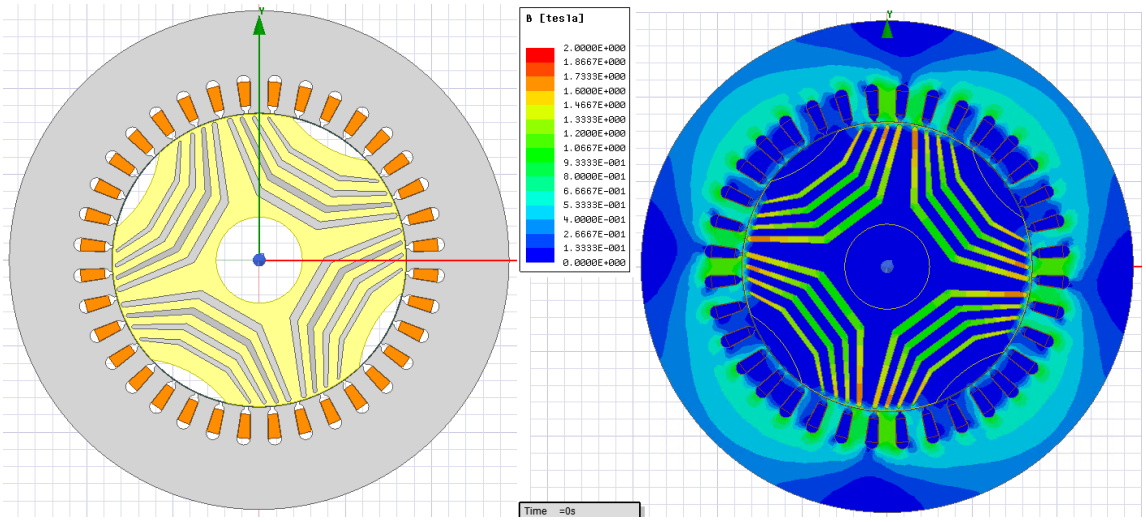

(a) **(b)**

Figure 3.16: Design FG1_4_36_10 and flux density plot.

Figure 3.16(a) shows this initial design concept. This design uses the same 36 slot stator and winding arrangement that was discussed in the last section. The orange sections are the copper windings with a packing factor of 0.5. The grey sections are at the moment a magnetic steel, M250-35A. This is an easily available, average magnetic steel that should be able to give a good baseline to start the investigation. The yellow part in the diagram is a non-magnetic compound that provides structural integrity, and aids with the saliency, as well as providing significant mass reduction when compared to a steel rotor. The initial idea is to use a chopped fibre composite material for the non-magnetic parts of the rotor that is of equal strength in all directions. This machine was simulated at a rms stator current density of 10A/mm^2 and produced a torque ripple as before. An FFT was performed on this torque ripple to give a peak fundamental torque of 27.6Nm. This highlights that the straight swap to flux guides has reduced the average torque output of the rotor considerably. The idea behind this rotor design was to keep the overall weight of the rotor down while still delivering a comparable torque output. Due to the reduction in the amount of magnetic material in this design, it was unlikely that this machine would perform to the same standard of torque as a more traditional rotor design. However, the mass difference and the easier manufacturability would provide other advantages.

The initial problem with only a straight swap of the material in the rotor occurs at the ends of the flux guides. The new flux guides have very sharp corners that also lead to a possible mechanical weakness of the rotor. These sharp ends were discussed, and it was decided that they would probably give rise to unwanted stress issues at higher speeds. If the design was to have any mechanical issues such as stress fractures or weak points, they could form around the sharp edges of the design where stresses

are more concentrated. Whilst figure 3.16(a) shows how the flux guides were originally derived from FB2_4_36_10, this section of the chapter will show how the rotor developed further to improve this 4 pole flux guide design to give a better torque to mass ratio.

3.3.1. Flux Guide Variant 'FG2_4_36_10'.

Moving forward with the design from FG1_4_36_10 (figure 3.16(a)), gives rise to rotor design FG2_4_36_10. This attempts to improve on some mechanical aspects of the previous design that was thought could potentially cause a problem. The first change is that the angular shape of the previous design has been changed to give a smooth, more flowing contour for the flux guides. This has been achieved by keeping the width of the flux guides the same all the way along their length. The ends of the flux guides have also been widened to allow more flux to link with the rotor at these points. The sharp 'elbow' corners have also been removed from the shape of the flux guides.

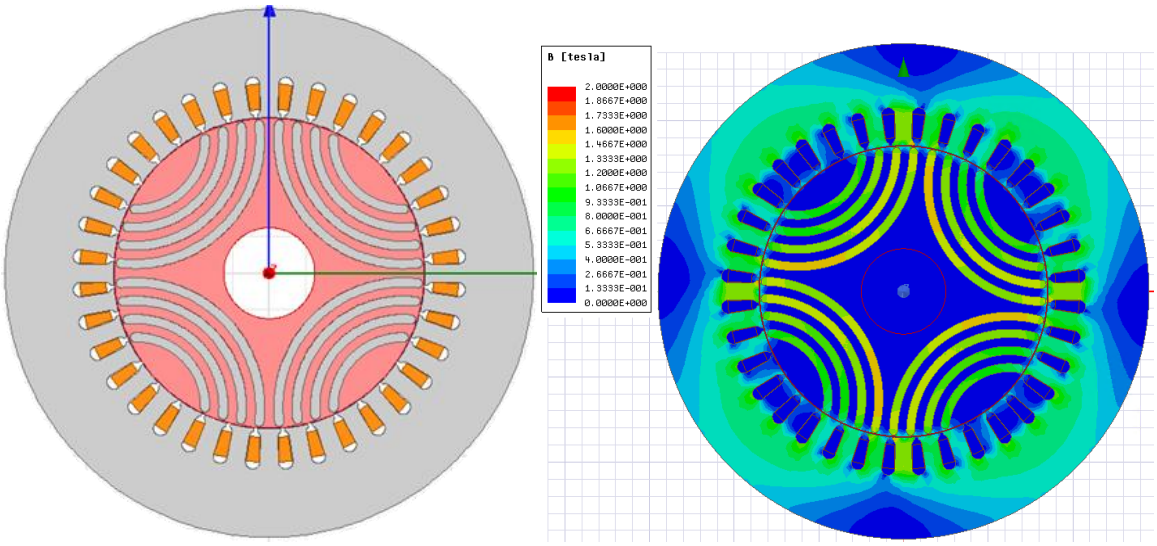

(a) **(b)**

Figure 3.17: Design FG2_4_36_10 and associated flux density plot.

Figure 3.17(a) shows the cross-section of design FG2_4_36_10. In the cross-section, the red material is the non-magnetic substance used for the structural support, as discussed previously. The flux guides were also brought closer to the edge of the rotor, this was to try and reduce the air gap, and increase the saliency. Bringing the flux guides closer to the edges of the rotor also allows more flux to link with the rotor from the stator. This can actually be seen in the flux density plot shown in figure 3.17(b) when compared to the same plot in figure 3.16(b) for the previous design. The smoothing out of the flux guides, pulling them slightly closer to the edge of the rotor and keeping them the same width all the way along has evened out the flux density through the flux guides in this design compared to the

previous. It also allows more flux to flow in the stator back iron. This design gave a max torque output of 36.9Nm when simulated with a packing factor of 0.5 and a rms current density of 10A/mm^2, which is better than FG1_4_36_10, shown in figure 3.16a (27.6Nm). This is due to the distance of the flux guides to the edge of the rotor. As well as the constant thickness of the flux guides, making the air gap smaller allows more flux to link from the stator to the rotor.

Figure 3.18 shows a close up of the flux density in the tips of the rotor flux guides and the teeth of the stator. The colours shown in the figure suggest that there is almost no flux above 1.6T in the rotor flux guides. This figure does show that there is a large amount of leakage flux in the nonmagnetic material at the ends of the flux guides. This would suggest that the flux guides may benefit from being moved closer to the outer edge of the rotor. This loss of flux-linkage implies that the machine is losing torque. Moving the flux guide ends to the very edge of the rotor will change the dynamic of this rotor greatly.

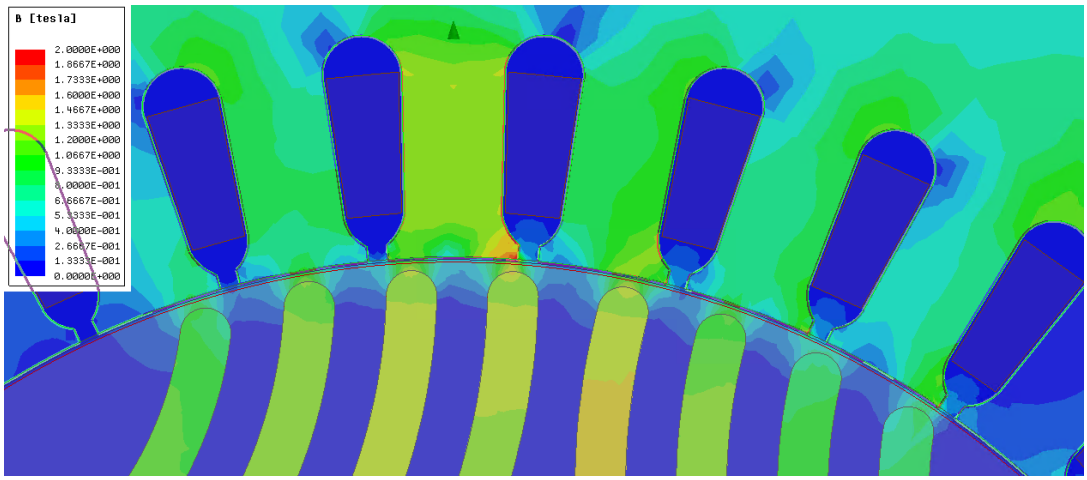

Figure 3.18: Flux Density of the FG Tips (FG2_4_36_10).

3.4. Parametric Investigation into the 4 Pole Flux Guide Machine.

This section is going to explore the iterative process of finding a more effective 4 pole flux guide rotor. FG2_4_36_10 has a ratio of 50:50, flux guide to nonmagnetic barrier design, where the flux guides have a width of 5mm and the nonmagnetic barrier also has a width of 5mm. This design has no saturation in the flux guides which suggests the machine could possibly take a higher current.

3.4.1. Initial Iteration, 'FG3_4_36_10'.

The first iteration of the design moving forward will address some issues that FG2_4_36_10 displayed. The aim was to reduce the distance that the flux has to travel in the air gap by adjusting the ends of the flux guides. The solution here was to extend the flux guides out, right to the edge of the rotor. Figure 3.19a shows this new cross-section of FG3_4_36_10. In figure 3.19a anything in the rotor that is blue in colour is the nonmagnetic material. The ratio between the flux guides and the nonmagnetic

flux barriers is 50:50. This means that it is still the same as the previous design at 5mm each. This iteration of the machine was first simulated to devise a torque baseline for the next set of design iterations. It was found to have a maximum torque of 60.4Nm, when simulated with a packing factor of 0.5 and a rms current density of 10A/mm^2. This was a large increase on FG2_4_36_10 (36.9Nm). The increase in torque can primarily be due to the decrease in the length of the air gap at the outer edges of the flux guides. This was a fairly common problem with the more contemporary designs, the flux barriers in those rotors could not extended too close to the edge of the rotor or the design would not be mechanically sound. This leads to a rotor design that sacrifices torque due to mechanical constraints. However, this leads to more problems for this rotor design, in finding a way to actually hold the rotor together with all of the nonmagnetic material parts not being attached together. This will be discussed later in this thesis. For now, the electrical performance of a rotor design is the focus for this chapter.

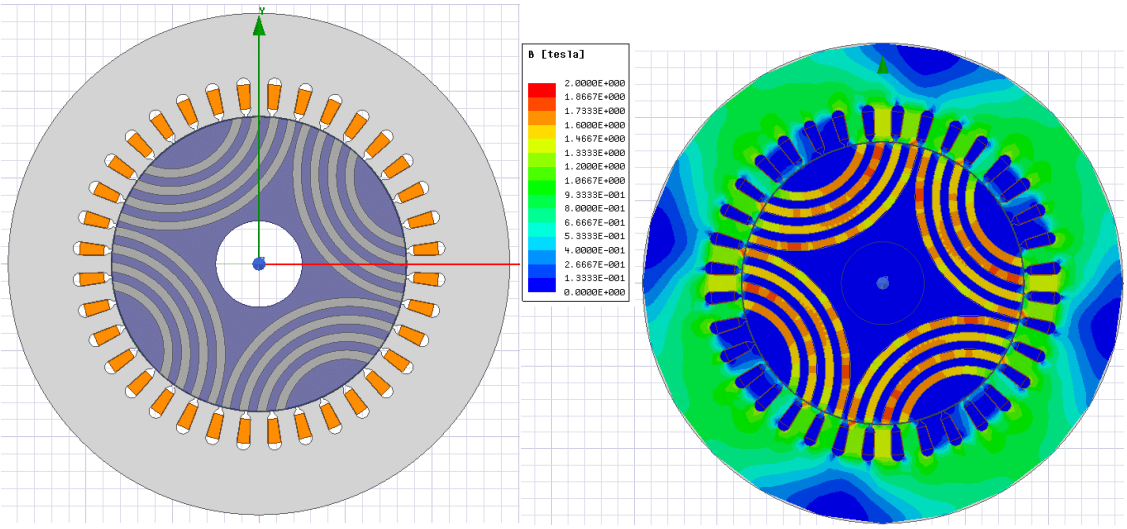

(a) **(b)**

Figure 3.19: Cross section of FG3_4_36_10 and flux density plot.

Figure 3.19b shows the flux density plot in the cross section of this machine design. As the parametric investigation for now is focused mainly on the rotor, looking at the flux guides themselves shows that the flux density here is an average of around 1.7T. This is quite high, and this design of machine has quite a bit of the flux guides near saturation, therefore adding to the thickness of the flux guides will hopefully reduce this effect. Over the next few sections this model will be developed further to try and push for a greater torque output, as well as to investigate how this effects the mass of the rotor and the overall machine. The results are presented in section 3.3.2 and the cross sections for reference in each of these machines is on the next page labelled as figures 3.20a-f.

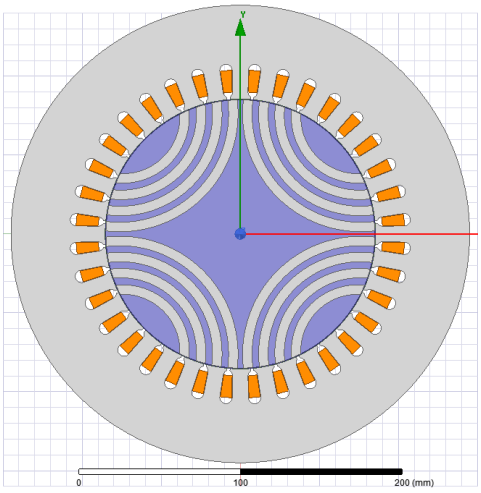

Figure 3.20a FG4_4_36_10

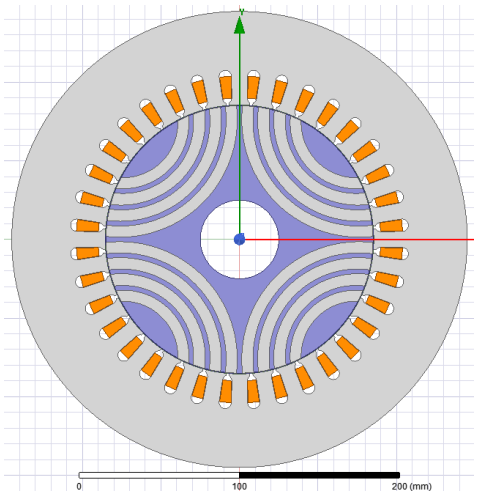

Figure 3.20b FG5_4_36_10

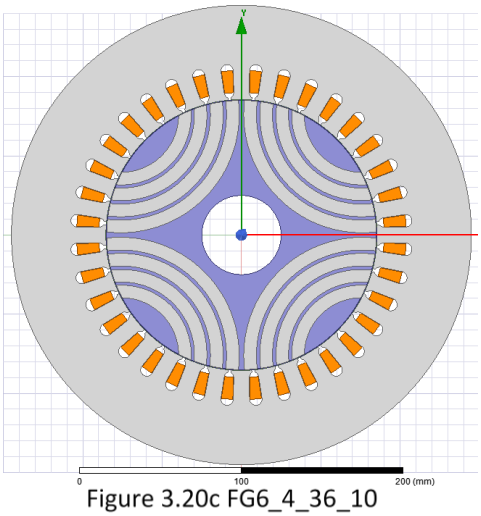

Figure 3.20c FG6_4_36_10

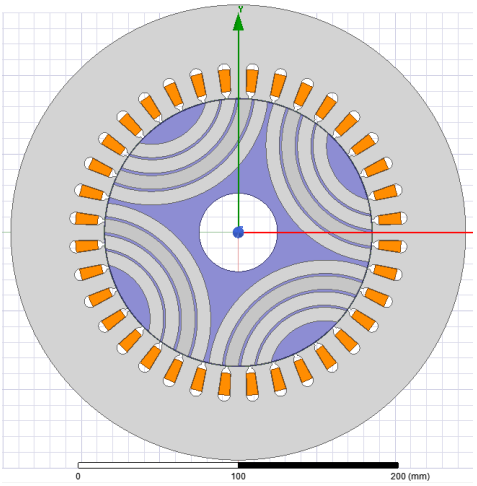

Figure 3.20d FG7_4_36_10

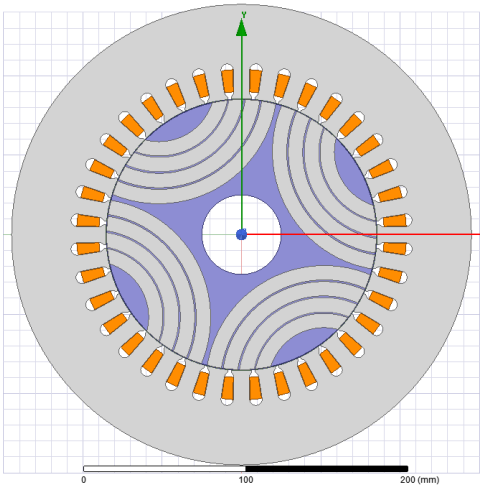

Figure 3.20e FG8_4_36_10

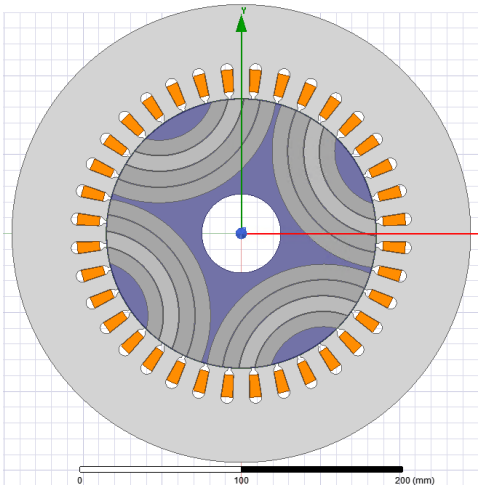

Figure 3.20f FG9_4_36_10

Figure 3.20a-f: Cross Sections used in this parametric investigation of the 4 pole design

3.4.2. Iteration Two, FG4_4_36_10.

The initial investigation was to be done on the thickness of the flux guides. This was to explore the effect that the ratio of the thickness of these flux guides verses the thickness of the nonmagnetic flux barriers. has on the mass and torque output of the machine. FG4_4_36_10 was this first machine iteration. All of these machines were run using a packing factor in the orange section of the slots of 0.5 and a rms current density of 10A/mm^2.

Using the previous model, FG3_4_36_10 (60.4Nm), as the baseline result, the thickness of the flux guides was increased from 5mm to 6mm. This leads to a corresponding decreased in all of the nonmagnetic material filling between the flux guides to a thickness of 4mm. Therefore, the ratio is now 60:40, flux guide to non-magnetic material, and this is shown in figure 3.20a, FG4_4_36_10. The 60:40 ratio gave an average torque of 71.2Nm, showing an increase from 60.4Nm with a 50:50 ratio.

The thicknesses of the flux guides and the non-magnetic material was further adjusted to give a change in ratio from 50:50 to 95:05, the last being a 9.5mm flux guide thickness. Figures 3.20a-f show the cross sections of these iterations;

Figure 3.20a: 60:40, FG4_4_36_10

Figure 3.20b: 70:30, FG5_4_36_10

Figure 3.20c: 80:20, FG6_4_36_10

Figure 3.20d: 85:15, FG7_4_36_10

Figure 3.20e: 90:10, FG8_4_36_10

Figure 3.20f: 95:05, FG9_4_36_10

It was predicted that the maximum torque should be achieved at some point within this range.

However, thickening the flux guides also impacts on the mass of the rotor, and overall machine mass. Throughout all this investigation there was no additional changes made to the rest of the model. Only the flux guides widths were varied.

3.4.3. Full Flux Guide Width Investigation.

This investigation includes the set of models that were designed after FG4_4_36_10 with different rotor cross sections. These models FG5_4_36_10, FG6_4_36_10, FG7_4_36_10, FG8_4_36_10 and FG9_4_36_10 can all be found labelled in the previous section. The maximum average torque output

was recorded from each of the simulations, and plotted for the different flux guide thicknesses, shown figure 3.21.

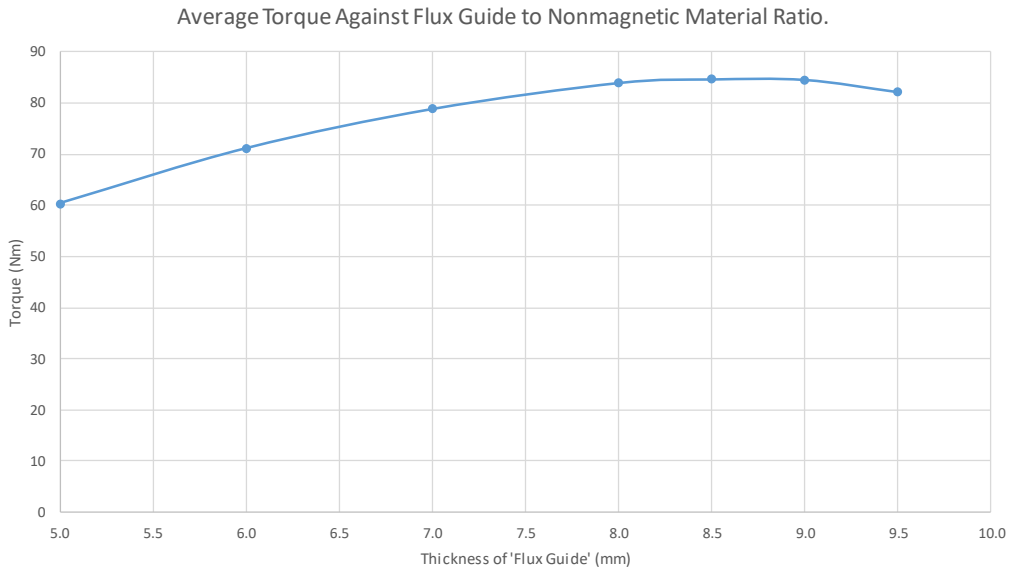

Figure 3.21: Torque as a Function of flux guide Thickness.

In figure 3.21, the torque has been plot against the thickness of the flux guides. This graph shows that the increase of flux guide does indeed allow for a higher amount of flux to link with the rotor. However, it also shows that too much flux guide and not enough nonmagnetic material gives a detrimental effect on the torque produced, due to leakage between the flux guides, showing a maximum torque produced at a thickness of 8.5mm (figure 3.20d, 85:15 ratio). This design peaked at 84.7Nm for a rms current density of 10A/mm^2 and a packing factor of 0.5. The rotor has a larger increase in torque output as the ratio is increased between a thickness of 5mm (60.4Nm) and 7mm (78.9Nm). Between 7mm (78.9Nm) and 8mm (84Nm) the increase in torque production slows down and between 8.5mm (84.7Nm) and 9mm (84.6Nm) the torque shows a maximum. The final iteration of 9.5mm (82.2Nm) shows that there is a torque drop, suggesting that there is now too much M250-35A in the rotor, and the non-magnetic material between the flux guides is not thick enough to reduce the leakage of flux between them. It is also leading to a higher mass rotor. A flux guide thickness of 8.5mm (84.7Nm) shows a maximum in torque production for this style of rotor. However due to how close the designs are between 7mm (78.9Nm) and 8.5mm (84.7Nm) the effect of the thickness on the mass of the rotor may change the current thinking that 8.5mm (84.7Nm) is the best option, with a lower overall machine mass being preferable, at the expense of slightly lower torque production.

Figure 3.22(a) shows the cross sectional area of FG7_4_36_10, the design iteration with the maximum output torque at this stage in the design (85:15). The output of this machine was just under 85Nm of torque.

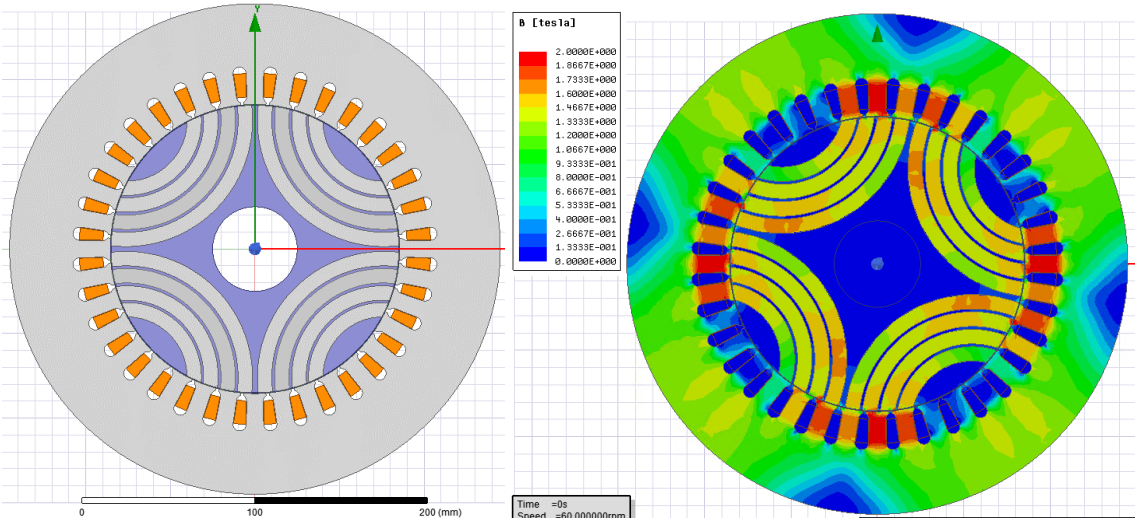

(a) **(b)**

Figure 3.22: Cross sectional area of FG7_4_36_10 and flux density plot.

Looking at figure 3.22(b) in comparison with figure 3.19(b) it is quite clear to see that the thickening up of the flux guides has had a large effect on the flux density in the rotor. Both figures are scaled to the same flux density. So the two graphs are directly comparable. The drop in flux density is from an average of 1.7T (FG3_4_36_10) to an average of 1.3T (FG7_4_36_10). There are still some investigations left to be performed on this machine. When the flux guide width was being investigated for maximum torque output, as well as a more acceptable flux-linkage with the stator, the mass of the rotor was affected. This was due to the amount of M250-35A in the rotor increasing, while the lighter nonmagnetic material was decreasing. This would suggest that FG7_4_36_10 is not the most effective design overall. It may be the case that a lower flux guide to nonmagnetic material ratio design might be preferential. A rotor which is slightly lighter but only had marginally less output torque could therefore be a better overall motor design.

3.4.4. Rotor and Machine Mass to Flux Guide Width.

Figure 3.23 shows how the mass of the rotor, in kg, changes with the flux guide width. The results here are as expected. The mass of the rotor increased linearly as the width of the flux guides increased. Therefore, there is a total mass increase across all of these designs of 3.79kg. The maximum value of

mass is 12.27kg, corresponding to a 9.5mm flux guide width. However, this actually past the torque maximum, with a 2.5Nm decrease on the maximum torque for these parameters.

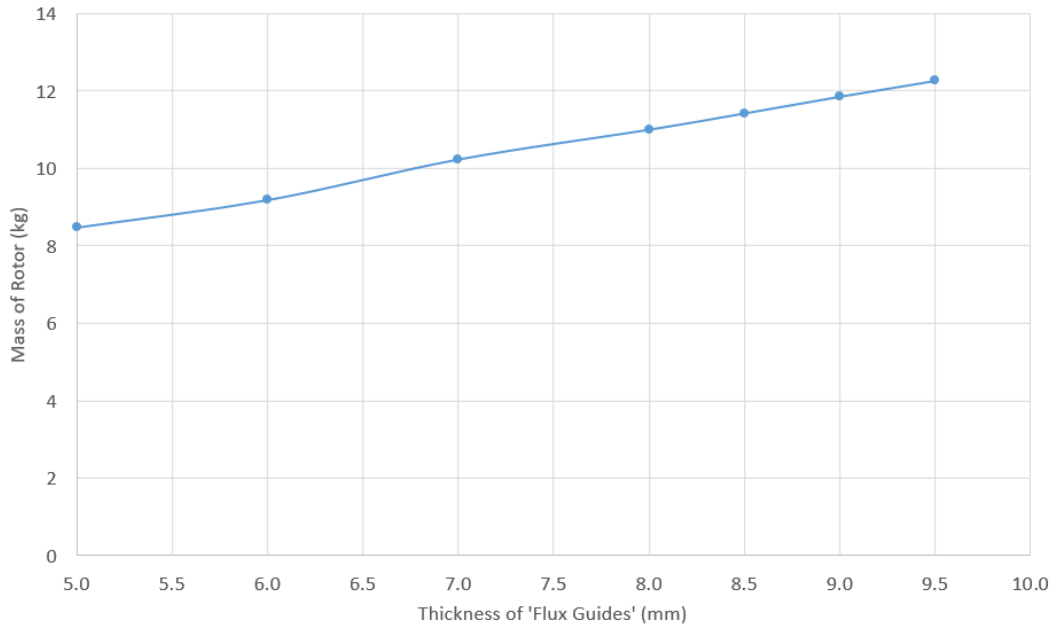

Figure 3.23: Mass of Rotor as a Function of the Thickness of the flux guides

As the current investigation is only concerned with the rotor, it would be of interest to see how these rotor design changes affected the overall mass of the machine. Figure 3.24 shows the overall mass of the machine varying with the flux guide width.

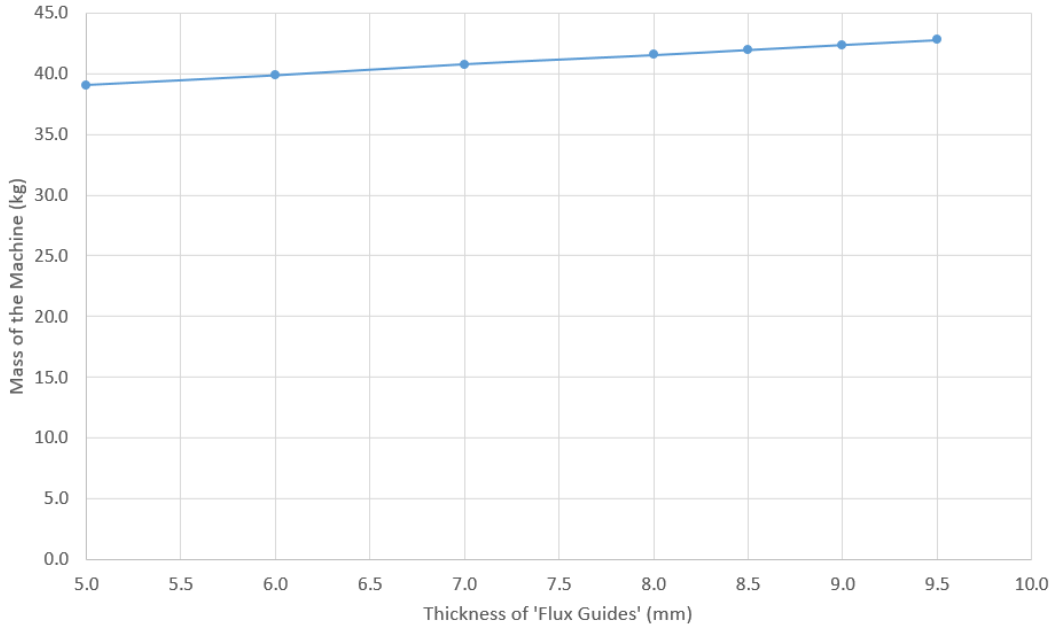

Figure 3.24: Overall Machine Active Region Mass (excluding End Windings) as a Function of width of the flux guides

A direct comparison between figures 3.23 and 3.24 shows the majority of mass in the machine is actually located in the stator, as can be seen in figure 3.24 the overall change in mass is rather insignificant in comparison. The overall increase in mass for the machine shows that there wasn't much change due to the parametric investigation of the flux guides and that there is scope for reducing the thickness in the back iron of the stator, assuming this does not lead to stator saturation. This will be investigated later in the thesis. The aim now is to find a flux guide width that gives a maximum torque to mass ratio. This shows that what was thought to be a good design torque wise, FG7_4_36_10, may not actually be the best option. Figure 3.25 shows the torque/mass ratio plotted against the flux guide thickness. The graph shows that actually the best torque/mass ratio is FG6_4_36_10 (8mm). This machine however may not give the best overall torque. The 7mm thick flux guide gives a torque/mass ratio of 1.9 whereas the 8.5mm gives only slightly higher with 2.0. Looking back at figure 3.21 shows that the torque difference between the two is 5.8Nm and the mass difference seen in figure 3.24 is 1.2kg. Therefore, as this machine (7mm, FG5_4_36_10) is so close to FG7_4_36_10, it might be considered to be a better overall machine as it is lighter than the higher torque machine for very little torque loss. However, as there is very little difference, FG6_4_36_10 is worth following through.

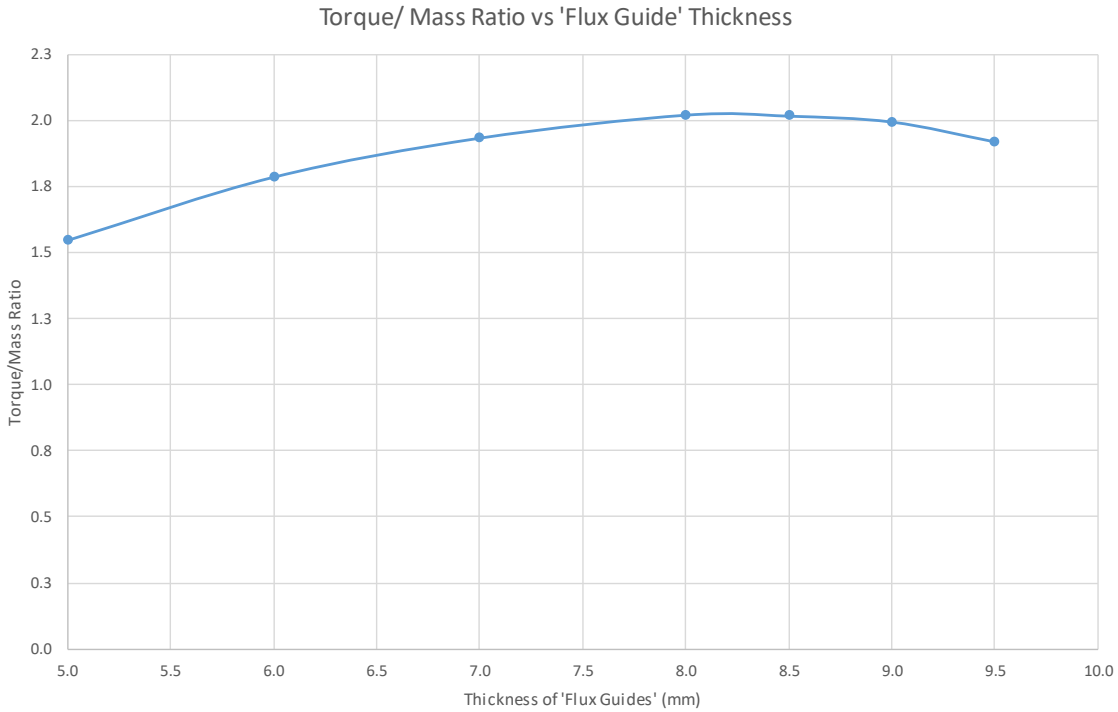

Figure 3.25: Torque/Mass as a function of flux guide Thickness

This parametric investigation showed that there may be more drastic results from squeezing the back iron in to give a higher mass reduction, and this will be examined further in a later chapter.

3.5. Chapter Summary.

After an extensive review of these 4 pole designs presented above, it was quite clear to see that there were a lot of areas to explore on the design of a new rotor and stator. Looking at the best designs from all of the above that were presented, FG6_4_36_10 was deemed to be the most suitable for the 4 pole machine. This design produced the best average torque output for the mass, in the 4 pole designs. There are still some issues that need to be addressed, mainly concerning the stator design to maybe lower the overall mass, and maybe maximise the torque output further. For now, this will be the baseline design to carry forward. This chapter has so far shown that it is indeed possible that the torque output from a traditionally designed SYNCREL rotor can be recreated, using a composite multipart rotor concept as proposed in this thesis. This chapter has laid the baseline work for further design studies and parametric investigation into stator design and pole number modification in the next chapter.

The preliminary studies in this chapter have highlighted a 4 pole design as a suitable machine for detailed investigation, which will be addressed in the next chapter. The following is a summary of the results in this chapter, corresponding to the rotor design designation and results.

Designation	Figure Showing the Machine Cross-Section	Predicted Average Torque at RMS Current Density of $10A/mm^2$ (Nm)	Predicted Torque Ripple (Nm pk-pk) at RMS Current Density of $10A/mm^2$ (Nm)	Overall Machine Mass (kg)
FB1_4_36_10	3.4	79.9	28.9	41.8
FB2_4_36_10	3.7	82.7	26.9	40.9
FB2_4_39_10	3.13(a)	85.3	12.3	40.7
CF1_4_36_10	3.14(a)	44.8	35.8	45.3
CF2_4_36_10	3.14(b)	48.3	44.3	44.8
CF3_4_36_10	3.14(c)	49.5	47.0	44.2
CF4_4_36_10	3.14(d)	60.1	46.1	43.6
CF5_4_36_10	3.14(e)	60.2	55.2	42.9
FG1_4_36_10	3.16(a)	27.6	13.1	37.4
FG2_4_36_10	3.17(a)	36.9	14.3	38.8
FG3_4_36_10	3.19(a)	60.4	31.8	39.0
FG4_4_36_10	3.20(a)	71.2	41.9	39.8
FG5_4_36_10	3.20(b)	78.9	35.7	40.8
FG6_4_36_10	3.20(c)	84.0	39.2	41.5
FG7_4_36_10	3.20(d)	84.7	47.2	42.0
FG8_4_36_10	3.20(e)	84.6	53.9	42.4
FG9_4_36_10	3.20(f)	82.2	65.6	42.8

Table 3.2: Final Design Summary for Chapter 3.

4. Investigation into Machine Pole Number

4.1. Introduction

The design study undertaken in chapter 3 demonstrated the advantages of machines based on flux guides within a non-magnetic structure, but only considered 4 pole designs. This reflects the fact that the majority of existing published designs of SYNCREL machines are based on 4 pole rotor, although it is far from a universally accepted principle that this pole number inherently produces machines with the highest torque density. This chapter explores the influence of pole number on torque density, starting with some top-level considerations which are then expanded with a detailed finite element study. This chapter will also run a short investigation into the iron losses in the chosen alternative pole number design and a 4 pole equivalent.

4.2. General Trends in Synchronous Reluctance Machines with Pole Number

The instantaneous torque produced by one phase of a SYNCREL machine is given by:

$$T = i^2 \frac{dL}{d\theta} \tag{4.1}$$

It is evident from equation 4.1 that increasing the pole number will reduce the angular excursion between positions of minimum and maximum inductance, which when considered in isolation would tend to increase the torque for a given current. The apparent benefit of increasing the pole number, at least when considered in isolation, is also evident in the well-established equation for torque with steady-state AC excitation in which the torque is proportional to the number of pole-pairs:

$$T = \frac{3}{4} p\left(L_d - L_q\right) i_s^2 \sin 2\delta \tag{4.2}$$

However, as the pole number is increased there will tend to be a decrease in the magnitude of the inductance change $\left(L_d - L_q\right)$, which will tend to reduce the torque. Hence, the relationship between torque and pole number in synchronous reluctance machines is far from straightforward, particularly when magnetic saturation is taken into account. As demonstrated in chapter 3, synchronous reluctance machine performance tends to be very adversely affected by magnetic saturation in the rotor and/or stator core.

Another factor which tends to drive up the pole number adopted in many high performance machines of all types is the scope to reduce the thickness of the stator back-iron or core-back since the level of flux passing through the back iron reduces more or less in direct proportion to the pole number for the same level of excitation.

The overall aim of this chapter is therefore to explore the influence of pole number on the performance of SYNCREL machines within the specific context of this performance specification and method of rotor construction. This includes consideration of much higher pole numbers (up to 14 pole) than is considered mainstream for SYNCREL machines, since as noted previously in this thesis, 4 pole machines tend to dominate in published designs.

4.3. Further Parametric Investigation of the Baseline 4 Pole Design

The baseline design which was established previously in chapter 3 and whose cross-section was shown previously in figure 3.20c was based on a 4 pole flux guide arrangement with a 36 slot stator. This baseline was established from an initial stator design, with the emphasis in chapter 3 on different rotor types rather than investigation of the stator, which other than consideration of a 39 slot version, remained fixed. The 4 pole baseline in figure 3.20c has a 290mm stator outer diameter and an axial length of 100mm, which results an estimated active mass of 44.04kg (including the end winding). This combination of dimensions results in a design, which closely produces the required average electromagnetic torque of 85Nm at a rms current density of 10A/mm^2. Several features of the design were explored in an attempt to improve the 4 pole design and these are considered in turn in the following sections

4.3.1. Proportion of the Stator Which is Occupied by the Stator Winding

As will be apparent from figures 3.20 shown previously, the slots in the machine only comprise a small proportion of the overall stator cross-section. In order to establish the merits of allocating a greater proportion of the stator volume to the coils, a series of further 4 pole designs with the same flux guide rotor was analysed. In this series of designs, the slot depth was progressively increased from an initial 22mm in the case of the machine from chapter 3 up to 40mm. In all cases the same overall outer diameter of 290mm was maintained, as well as the internal diameter. In all cases, the current density in the slot was set at 10 A/mm^2 rms with an assumed packing factor of 0.5. Any increase in slot depth has two effects. Firstly, it increases the stator mmf for the prescribed value of current density due to the greater coil cross-section, but it also reduces the thickness of the stator core back, recalling that the outer diameter remains fixed. The former will tend to increase the torque capability. However, this increase is achieved at the expense of an increase in the stator copper loss (since the current density remains fixed) while the reduced core back thickness is likely to lead eventually to a level of magnetic saturation which will impact on the torque capability. Given that these two factors work in opposition it is likely that there will be a peak slot depth for this machine within the given stator outer diameter constraint.

Figure 4.1 shows the finite element prediction of the average torque as a function of slot depth (expressed in terms of the overall slot area within the stator) for a machine with an axial length of 100mm, i.e. the same as the baseline. These torque values are predicted at a rms stator current density of 10A/mm^2, and in every case at a current load angle which results in maximum torque. As would be expected, there is a peak value of slot area, beyond which the effect of magnetic saturation in the stator back-iron more than outweighs the benefits of increased stator mmf. Hence, from the perspective of the imposed constraints on stator outer diameter and current density, the more effective 4 pole design has an overall slot cross-sectional area of ~7600mm^2 which in turn corresponds to an individual slot having a cross-sectional area of 212.9mm^2 and a slot depth of 36.3mm. Figure 4.2 shows a comparison between the original design and the design with the new revised slot depth of 36.3mm.

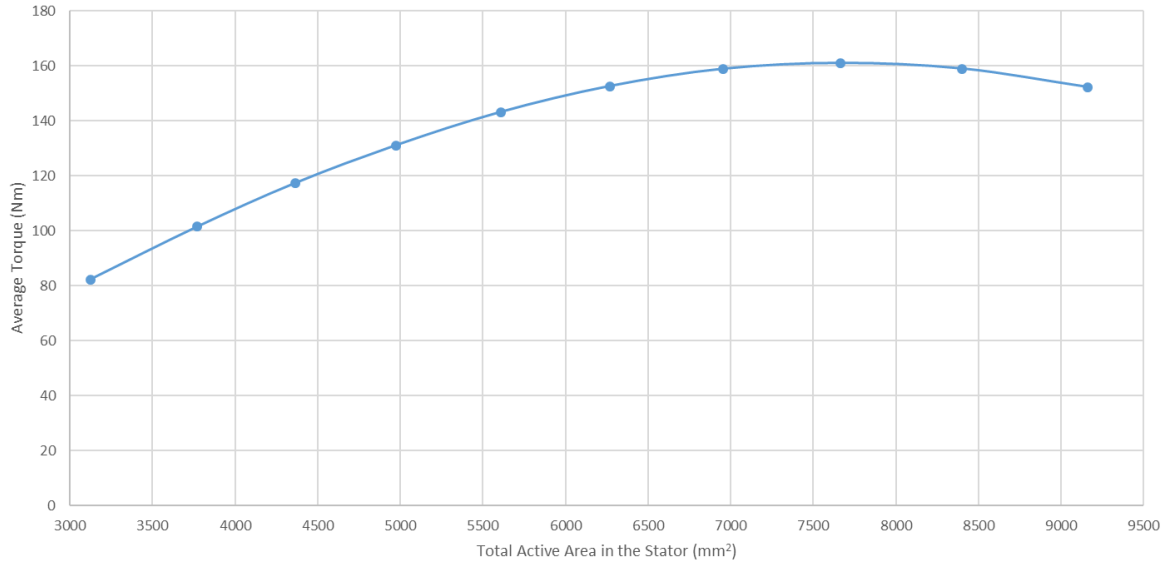

Figure 4.1 Finite element predicted variation in average torque as a function of total slot area for a 4 pole machines (all machines 100mm axial length and rms current density of 10A/mm^2)

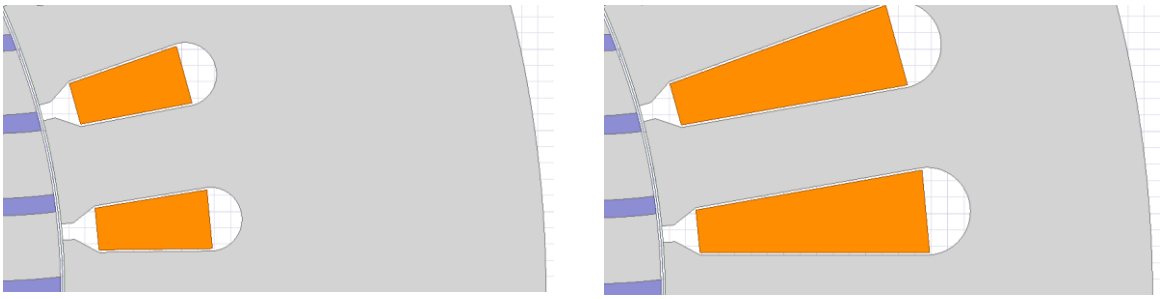

(a) Original slot geometry **(b) New revised slot geometry**

Figure 4.2 Comparison of original chapter 3 design and the new revised stator slot geometry

It is worth noting that this revised design, in terms of maximum achievable torque within the volume at the specified current density (and hence loss density), is not necessarily the most effective in other regards. For example, figure 4.3 shows the predicted variation in torque per unit copper loss for the same variation in slot area. Clearly, increasing the slot area reduces the volume of the core and hence reduces the iron loss, offering some amelioration of the increased copper loss which is evident in figure 4.3. Since the emphasis in this investigation is on torque density in order to minimise cost, the total stator slot area of ~7600mm^2 (slot depth of 36.3mm) was adopted as the preferred 36 slot stator design in this chapter, although as noted later in section 4.6 some minor revision of this were made in the demonstrator machine whose manufacture is described in chapter 7.

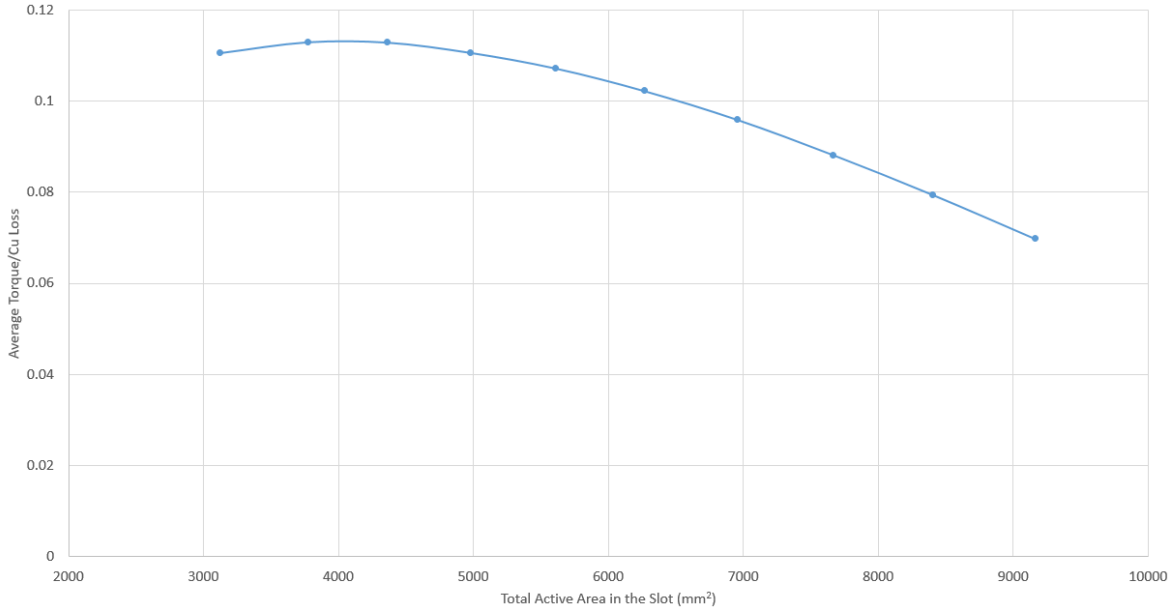

Figure 4.3 Predicted variation in torque per unit copper loss versus total active slot area

Since the torque produced by the revised design, with the same overall axial length (of 100mm) as the baseline, greatly exceeds the torque specification of 85Nm set out in section 1.2, the axial length of the design with the 36.3mm deep slots can be reduced to 52.8mm to meet the rated torque specification. This results in an active mass (i.e. excludes structural elements and including end-windings) for the 4 pole design with the revised slot-depth of 27kg, as compared to 44.04kg for the baseline design established at the end of chapter 3.

The ability to increase the slot depth to such an extent in figure 4.2 suggests that there is considerable scope in the original baseline design to improve its power density by drawing in the outer diameter to reduce the stator back-iron while maintain the original, (unrevised) slot shape and dimensions, although ultimately, there will be a limit in terms of magnetic saturation. Hence a series of further designs were considered, all based on the slot arrangement of the chapter 3 baseline but with

decreasing stator outer diameter. Figure 4.4 shows the predicted variation in average torque for a series of outer diameters from 290mm to the 255mm, in all cases for machine with an axial length of 100mm (which produces the rated 85Nm for the chapter 3 baseline) and at a current density of 10A/mm^2 rms. As shown, there is some potential to reduce the outer diameter without significantly reducing the torque. In all cases the original torque specification can be met by proportionally adjusting the axial length of each design. Figure 4.5 shows the axial lengths required to maintain 85Nm for each of the stator diameters considered, while figure 4.6 shows the calculated variation in mass for each of these 85Nm of designs.

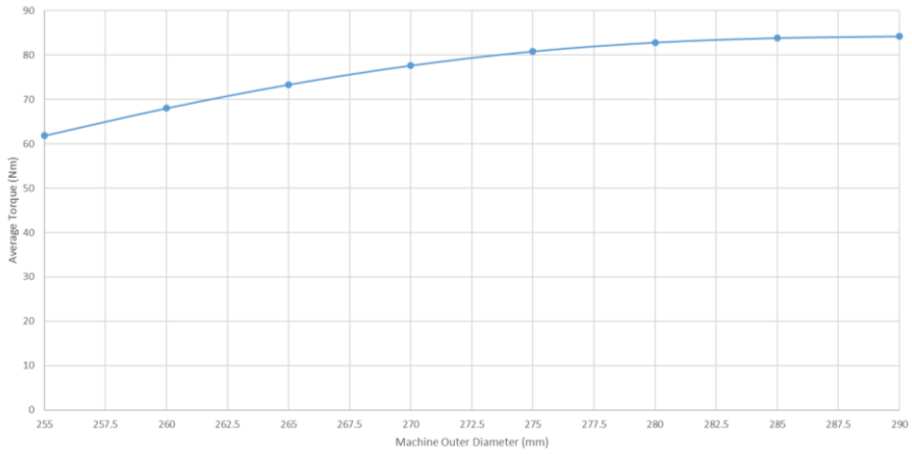

Figure 4.4 Predicted variation in electromagnetic torque as a function of stator outer diameter, in all cases with a rms current density of 10A/mm^2 and an axial length of 100mm.

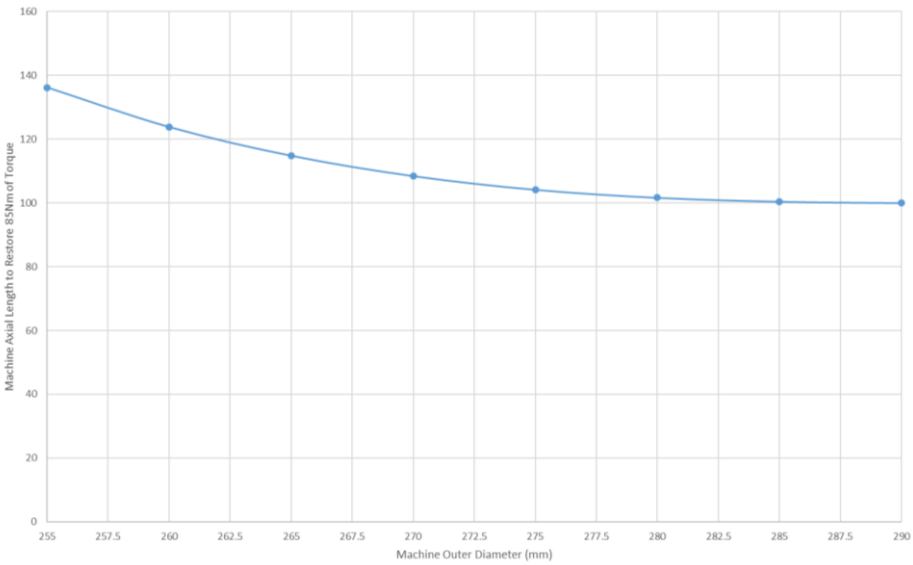

Figure 4.5 Calculated variation in machine axial length required to restore the torque to 85Nm (in all cases with a rms current density of 10A/mm^2)

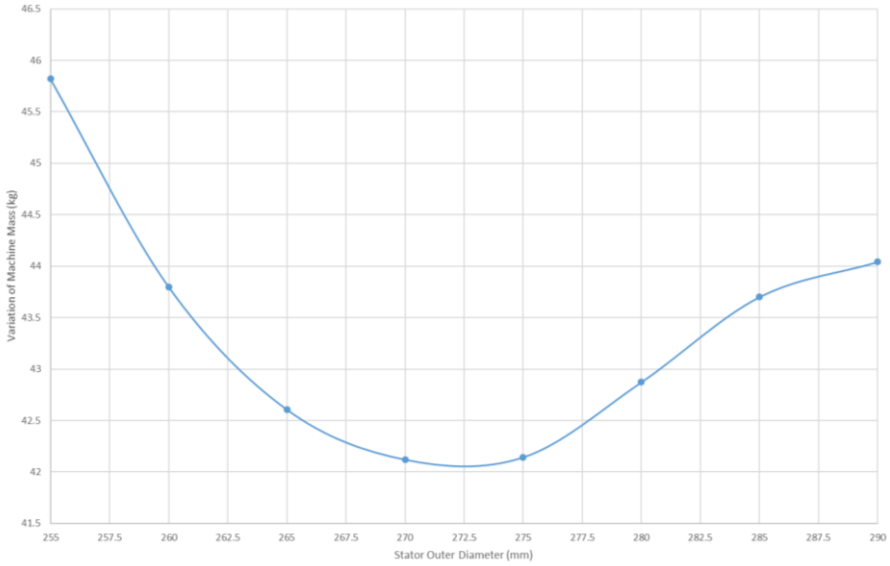

Figure 4.6 Calculated variation in machine mass for a function of stator outer diameter for machines capable of producing a torque to 85Nm at a rms current density of 10A/mm^2

This inevitably raises the question as to whether in a 4 pole configuration, there is also some scope to reduce the outer diameter in the revised, 36.3mm deep slot design, recognising that much of this opportunity may have been used up by increasing the slot depth. For the new slot depth of 36.3mm, the stator outer diameter was progressively reduced from 290mm to 265mm. The resulting variation in the torque for a stator current density of 10A/mm^2 rms as a function of stator outer diameter is shown in figure 4.7 while the corresponding variations in the axial lengths and resulting mass to maintain the rated torque of 85Nm are shown in figures 4.8 and 4.9 respectively.

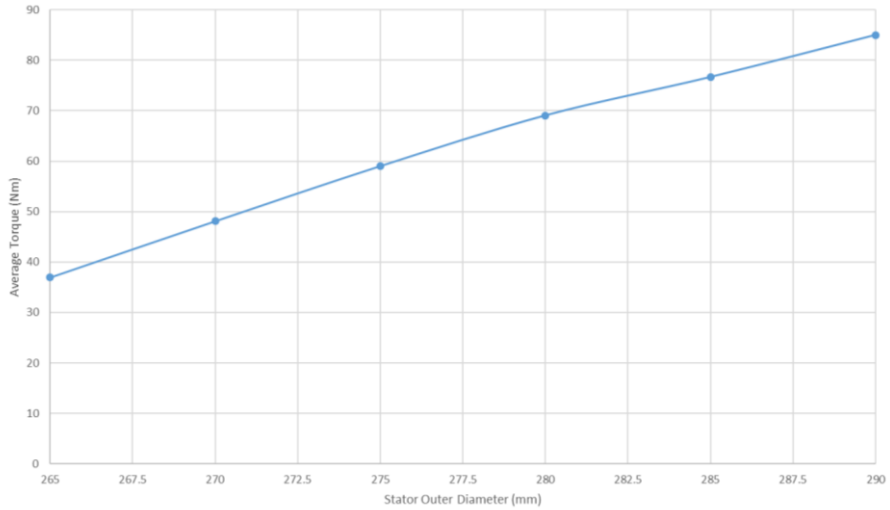

Figure 4.7 Predicted variation in electromagnetic torque as a function of stator outer diameter for the revised slot depth of 36.3mm, in all cases with a rms current density of 10A/mm^2 and an axial length of 52.8mm.

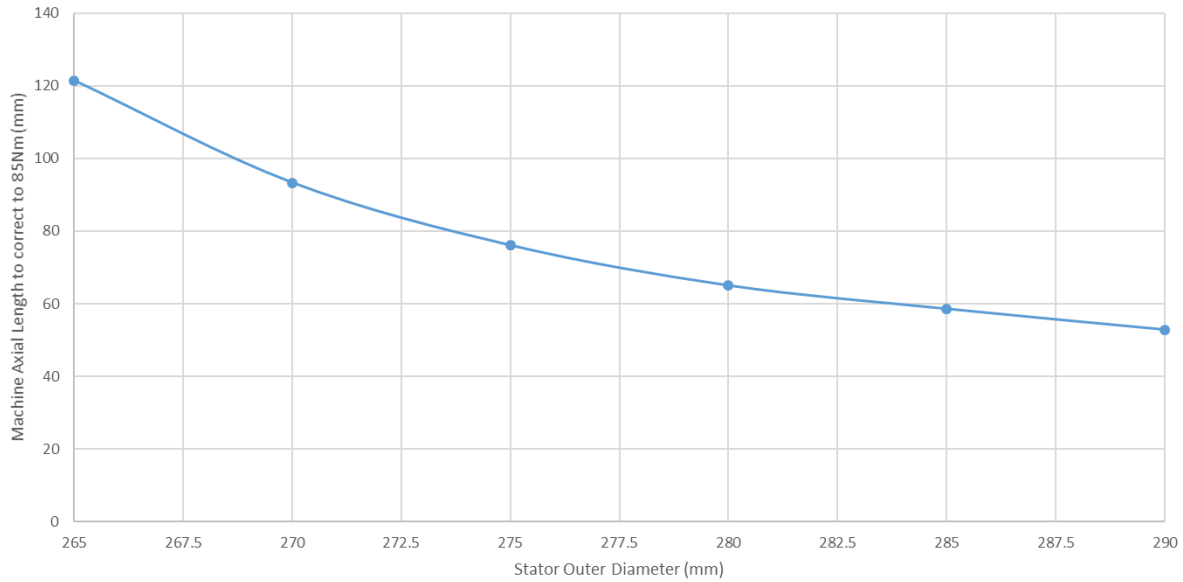

Figure 4.8 Calculated variation in machine axial length required to restore the torque to 85Nm (in all cases with a rms current density of 10A/mm^2)

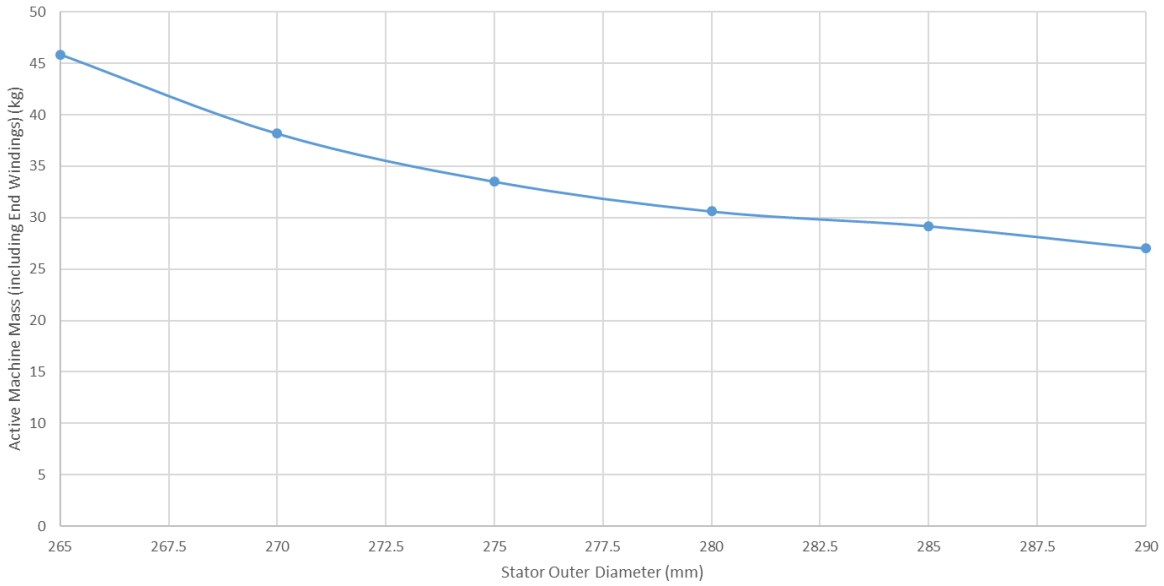

Figure 4.9 Calculated variation in machine active mass (excluding structural parts but including end windings) a function of stator outer diameter for machines capable of producing a torque to 85Nm at a rms current density of 10A/mm^2

A summary of the parametric investigation performed on the original baseline 4 pole design in figure 3.22a is shown in table 4.1. As will be apparent, the lightest 4 pole machine which meets the 85Nm rated operating point has a mass of 27.02kg and is achieved with 36.3mm deep stator slots and an outer diameter of 290mm. It will also be apparent that since the current density has remained fixed throughout this investigation, there is a significant difference in copper loss between the designs.

Quantity	Original baseline from chapter 3 shown in figure 3.22a	Design with parametrically investigated slot depth and 290mm stator outer diameter	Design with reduced stator outer diameter and original slot depth	Design with parametrically investigated slot depth and reduced stator outer diameter
Stator outer diameter (mm)	290	290	270	265
Axial length to produce rated 85Nm torque (mm)	100	52.8	108.45	121.5
Mass to produce rated torque (kg)	44.04	27.02	42.12	45.85
Copper loss (W)	761.85	1518.07	784.56	1960.26

Table 4.1 Comparison of various design (all dimensioned for rated torque of 85Nm at 10A/mm^2 rms)

4.4. Investigation into the Influence of Machine Pole Number

In order to explore the role of pole number in determining torque capability, a series of further designs were analysed with 6,8,10,12 and 14 poles. Not all of these pole combinations results in integer slot winding with a 36 slot stator and some modifications to the slot number may be required. In those combinations where a 36 slot stator could be used with an integer pole number, i.e. 6 and 12 poles, the revised 36 slot stator core geometry shown in figure 4.2(b) was initially used to assess the torque capability, although clearly with different coil arrangements in each case within this stator core to produce the required stator pole number to match the rotor. For other pole numbers considered, some modifications were required in terms of slot number and these are detailed as each design is considered in turn.

4.4.1. Analysis of 6 Pole Designs

The first option considered was a 6 pole design, which as a starting point used the same 36 slot stator as the 4 pole designs with 36.3mm deep slots, an outer diameter of 290mm and an axial length of 100mm. A cross-section through this machine is shown in figure 4.10 while figure 4.11 shows the single-layer, integer slot, 6 pole winding arrangement. One consequence of increasing the pole number is the need to adapt the rotor pole pieces as shown in figure 4.10. In this case there are three flux guides per pole, each 8.9mm wide at the airgap.

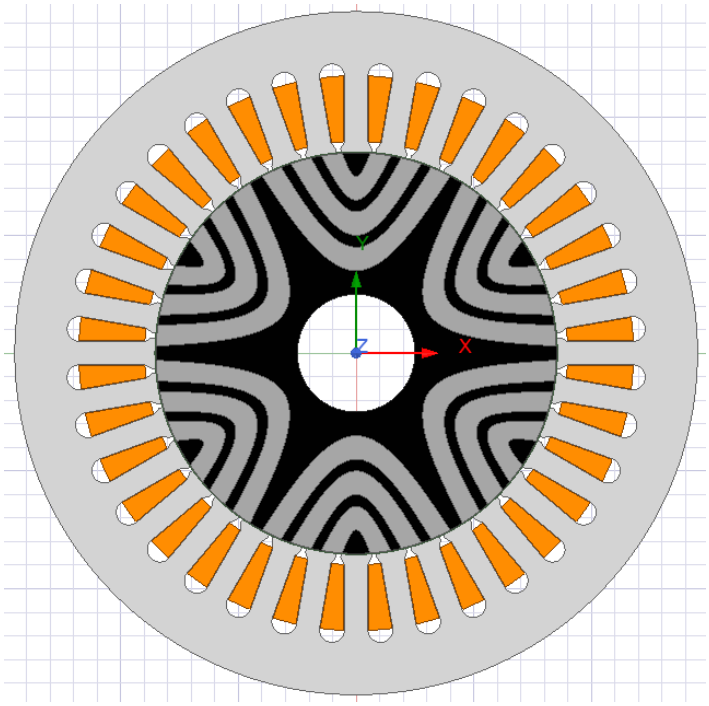

Figure 4.10 Cross-section through the initial 6 pole machine design

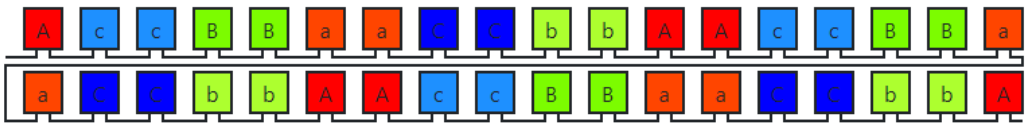

Figure 4.11 36-slot, single-layer, integer slot 6 pole winding layout

At the rated current density of 10A/mm^2 and a coil packing factor of 0.5, this machine produces an average torque of 181Nm with the optimum current angle, recalling that this calculation is based on a 100mm stack length. Although this average torque is impressive and would allow the stator axial length to be reduced to 46.96mm to meet the 85Nm specification, it does result in a very large torque ripple of 186Nm as shown in figure 4.12 at 100mm axial length.

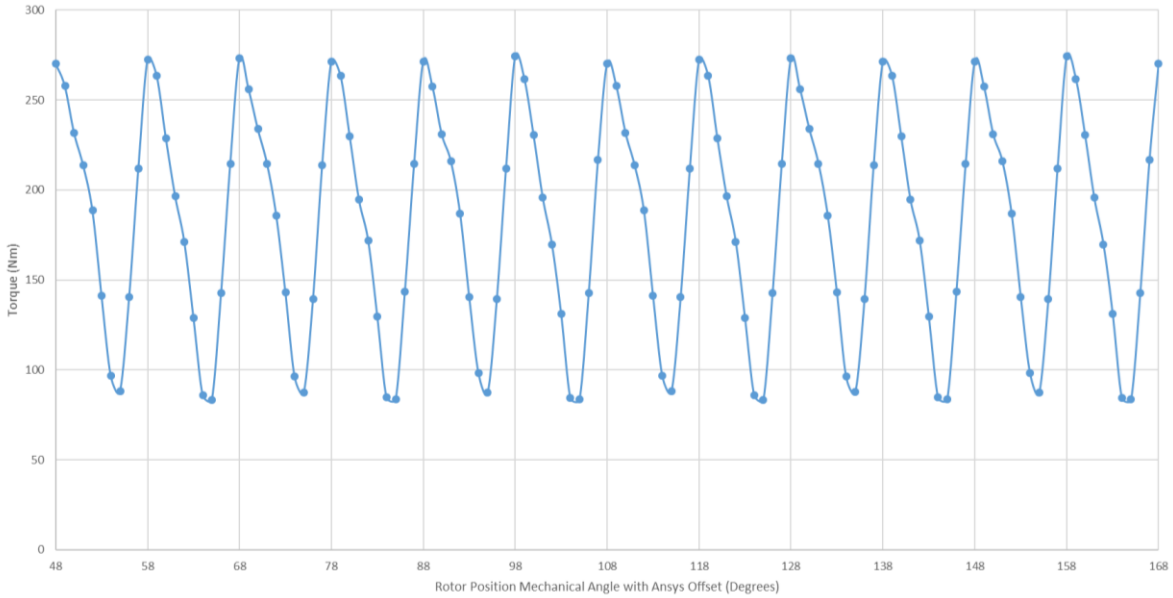

Figure 4.12 Finite element predicted torque waveform for a 6 pole design of figure 4.10 over 120° mechanical, 1 pole pair, (360° electrical) for a rms current density of 10A/mm^2 rms at 100mm axial length

This torque ripple corresponds to 12 pulsations per electrical revolution through a single pole pair, and as a result over the full cycle, the 36 rotor pole faces interact with the 36 stator slots to produce behaviour that resembles in some ways a doubly-salient machine with all the stator and rotor pole pieces coming in and out of alignment in near unison. On the one hand this results in a high average torque but at the expense of a large torque ripple. One means of attempting to mitigate the torque ripple is to reduce the number of rotor pole pieces per pole from 3 to 2 as shown in the design of figure 4.13. The corresponding predicted torque waveform for this machine is shown in figure 4.14 which shows the reduction in torque ripple from 186Nm to 106.85Nm but also the reduction in the average torque from 181Nm to 102.7Nm. For EV applications, where a suggested torque ripple value of around 1% to 20% of the average torque output is suggested [70], this pole number is a very poor contender. The method of removing one of the flux guides per pole was not the most effective method of torque ripple control, maybe a future look at this machine's stator slot number would be more effective as this was proven to reduce the torque ripple in chapter 3 when moving from 36 slots to 39 slots on the 4 pole machine. This isn't however, without its own draw backs.

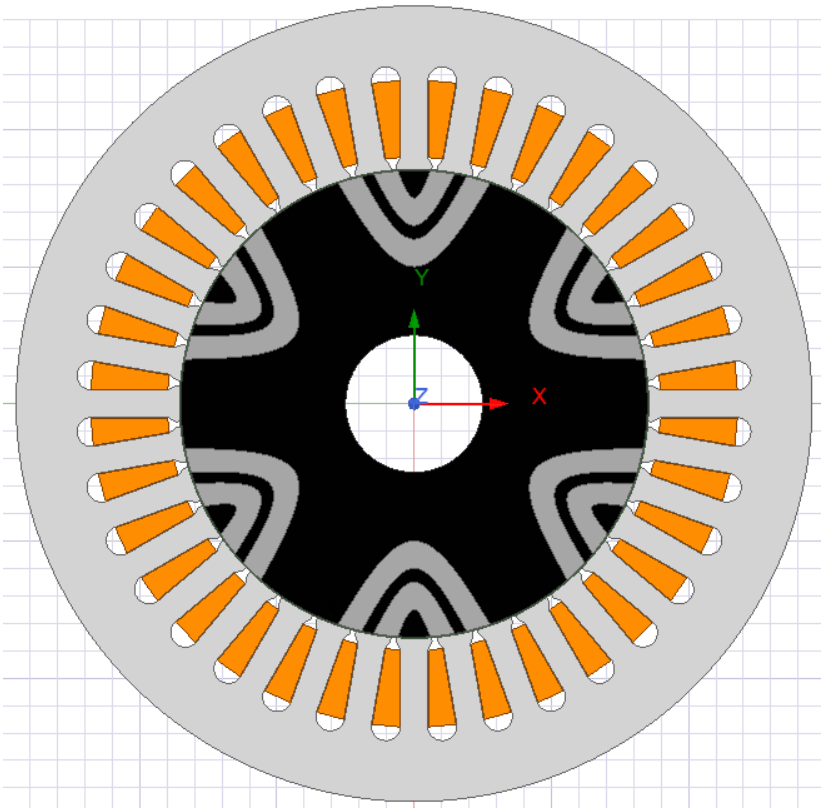

Figure 4.13 Alternative 6 pole design with 2 pole pieces per pole

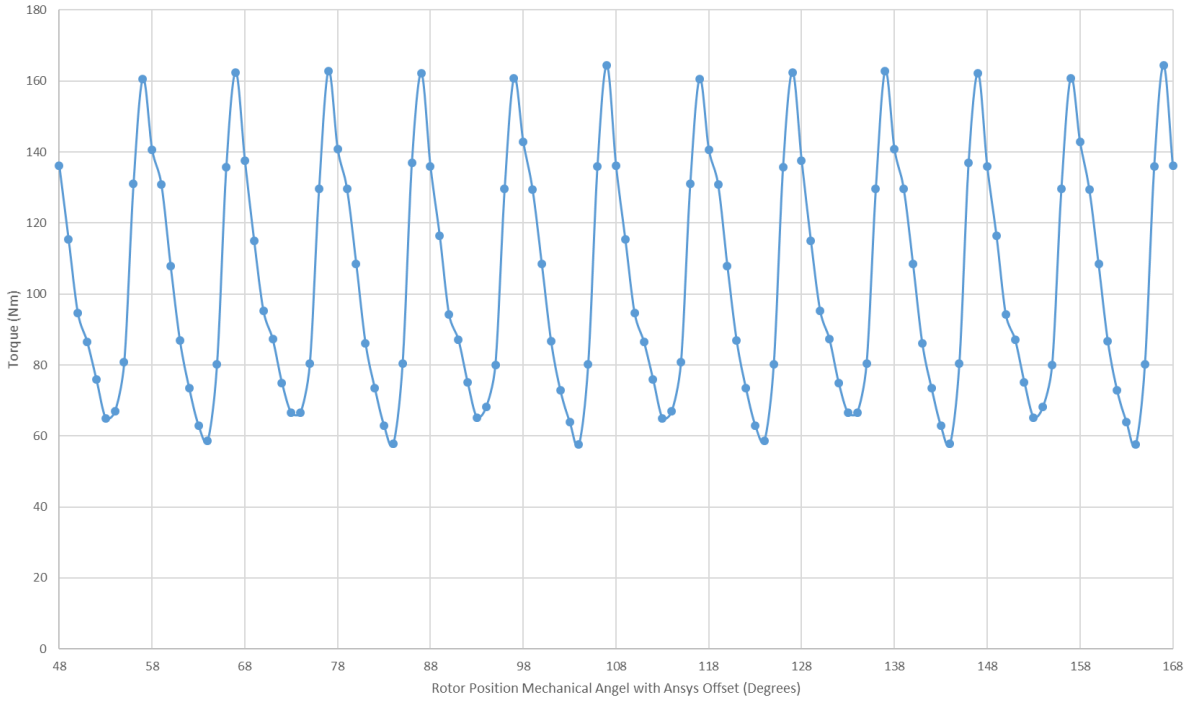

Figure 4.14 Finite element predicted torque for the 6 pole design with 2 pole pieces per pole (100mm axial length and a rms current density of 10A/mm^2)

4.4.2. Analysis of 8 Pole Designs

A 36 slot stator core design cannot be used in conjunction with an 8 pole rotor if a simple integer slot winding is to be used. A 36 slot, 8 pole machine would require a double-layer fractional slot winding with a pole-pitch equivalent to 4.5 slots. Whereas such a winding is entirely feasible, it would result in a reduced winding factor of between 0.831 and 0.945 depending on the coil span used, with a penalty in torque density as well as introducing potential asymmetry into the airgap field [70]. Hence, in order to maintain a comparison based on a single-layer integer slot windings, a 24 slot, 8 pole winding shown in figure 4.15 was adopted (the next integer slot option being 48 slots).

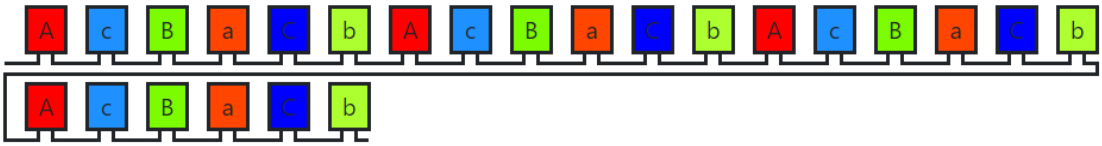

Figure 4.15 24-slot, single-layer, integer slot 8 pole winding layout

Such a significant change in slot number required some re-design of the individual stator slot geometry. A reasonable starting point was to establish a design with the same overall slot area of ~7600mm^2 as the revised 36 slot stator design of section 4.3, and with the same slot depth of 36.3mm. To a reasonable approximation, this will result in the same copper loss (which is proportional to the coil volume for a given current density). The initial 8 pole machine design which has a total slot area of 318.04mm^2 and an outer diameter of 290mm is shown in figure 4.16. This has 3 rotor pole-pieces per pole, which are each 6mm wide at the airgap.

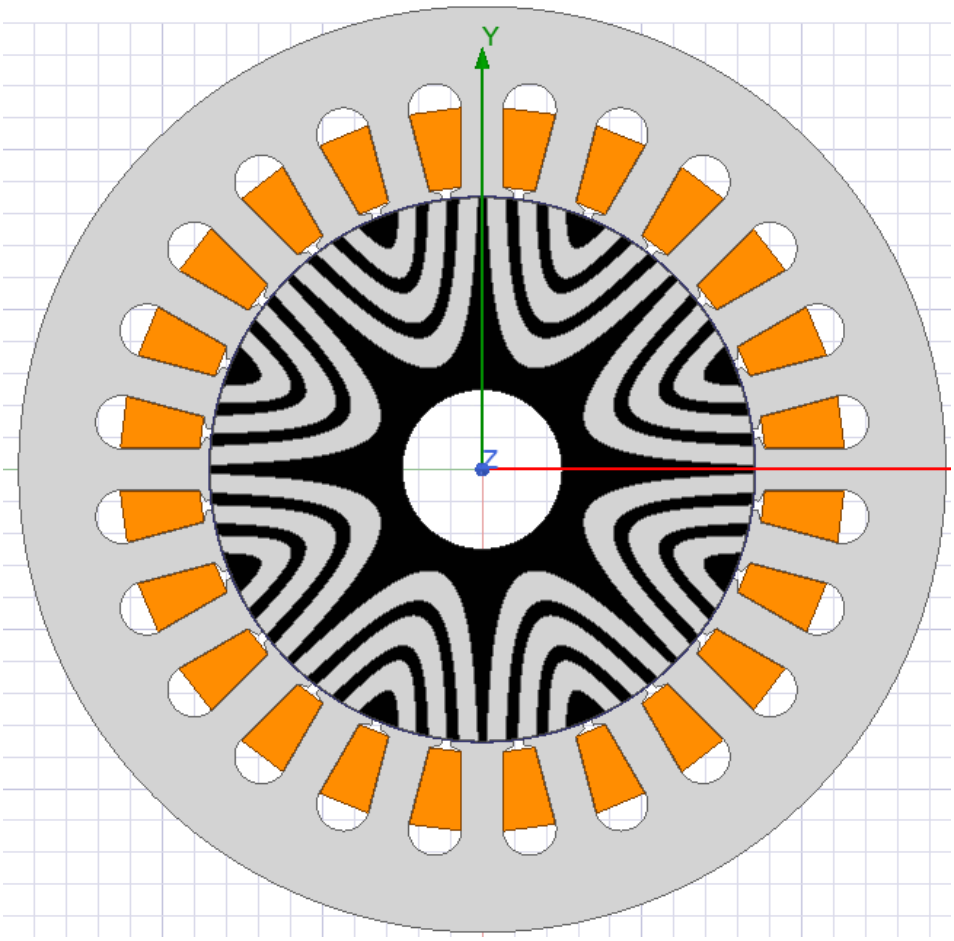

Figure 4.16 Cross-section through the initial 8 pole machine design with a stator diameter of 290mm

A 100mm axial length version of the 8 pole design of figure 4.16 produces the torque waveform shown in figure 4.17, which has an average value of 144Nm and a peak-to-peak torque ripple of 69.4Nm. This torque ripple is much reduced when compared to the 6 pole version, while the average torque is competitive with the 4 pole revised design, and would allow a reduction in axial length to 59.02mm to produce the 85Nm rated torque.

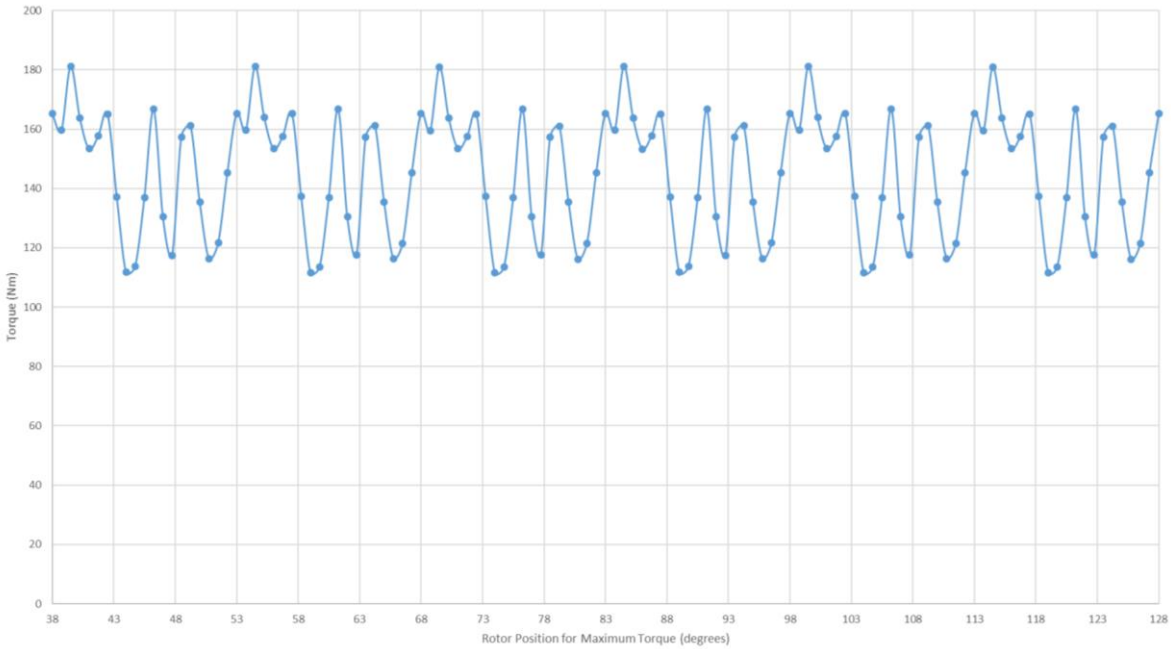

Figure 4.17 Finite element predicted torque waveform for an 8 pole design of figure 4.16 over a quarter of a mechanical revolution which constitutes to one electrical revolution for a rms current density of 10A/mm^2 rms at 100mm axial length.

One benefit of increasing the machine pole number is the opportunity to reduce the thickness of the stator back-iron since the flux per pole tends to drop with increasing pole number. In order to investigate the potential for reducing the back-iron thickness, the stator outer diameter was progressively reduced in steps of 5mm from the original 290mm down to 260mm. Figure 4.18 shows snapshots of predicted flux density distributions for machines with diameters of 290mm and 260mm diameter considered for the same angle of rotation and currents (corresponding to a rms current density of 10A/mm^2). As would be expected, the flux density in the back-iron increases significantly over this range of diameters. With levels that clearly exhibit significant magnetic saturation for a stator diameter of 260mm, with values of up to 2.82T in the region of the back-iron at the back of the slot, and much of the region behind the slot operating at ~2.5T. However, it is also clear from figure 4.18 that the back-iron in the 290mm diameter stator is more lightly fluxed, and although this is beneficial in terms of iron loss, there is scope to reduce the outer diameter with only a modest drop in torque.

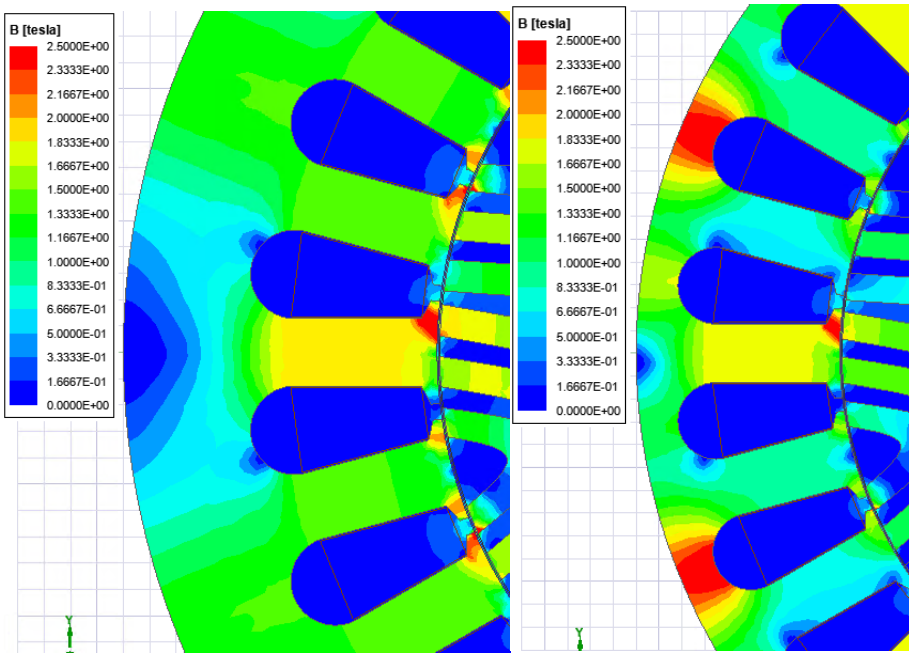

(a) 290mm stator diameter **(b) 260mm stator diameter**

Figure 4.18 Instantaneous flux density distributions for stator outer diameters of 290mm and 260mm at a rms current density of 10A/mm^2

Figure 4.19 shows the predicted variation in the maximum stator and back iron flux density as a function of the stator outer diameter at a rms current density of 10A/mm^2. It is worth noting that the average flux density (integrated over the entire stator annulus) can provide a useful indication of widespread magnetic saturation, but does not necessarily represent localised high flux densities. For example, the average value for flux density in the stator in figure 4.18(a) (the 290mm stator outer diameter) is 1.01T which although showing there is no overall saturation, the maximum back iron flux density shown in figure 4.19 shows a value of 1.39T. Similarly, for the 260mm outer diameter machine in figure 4.18(b) the average flux density in the stator is 1.24T whereas behind the slot, figure 4.19 shows a large increase to 2.82T which pushes the back of the slot into saturation.

Given that the M250-35A core material (magnetisation curve shown in Appendix A) shows signs of significant saturation at a flux density of ~1.5T, then figure 4.19 suggests that magnetic saturation becomes an important factor for stator outer diameters of 285mm and below. Although magnetic saturation is a concern in any machine, ultimately it is the effect on the torque that is the main design objective. Figure 4.20 shows the predicted variation in the average torque as a function of the stator outer diameter at a rms current density of 10A/mm^2. This demonstrates that there is only a marginal torque reduction when the diameter is decreased from 290mm to 280mm, but that this reduction

accelerates for further reductions below 280mm. The trend shows some consistency with the onset of significant magnetic saturation.

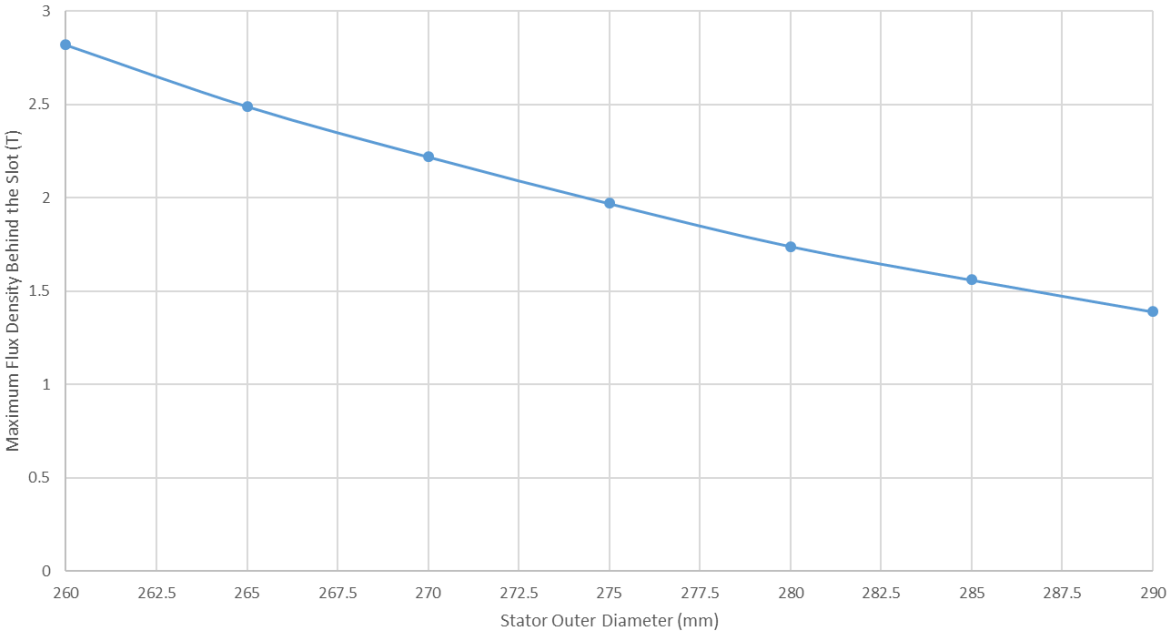

Figure 4.19 Finite element predicted variation in maximum back-iron flux density with stator outer diameter reduction for the 59.02mm axial length machine at a current density of 10A/mm^2.

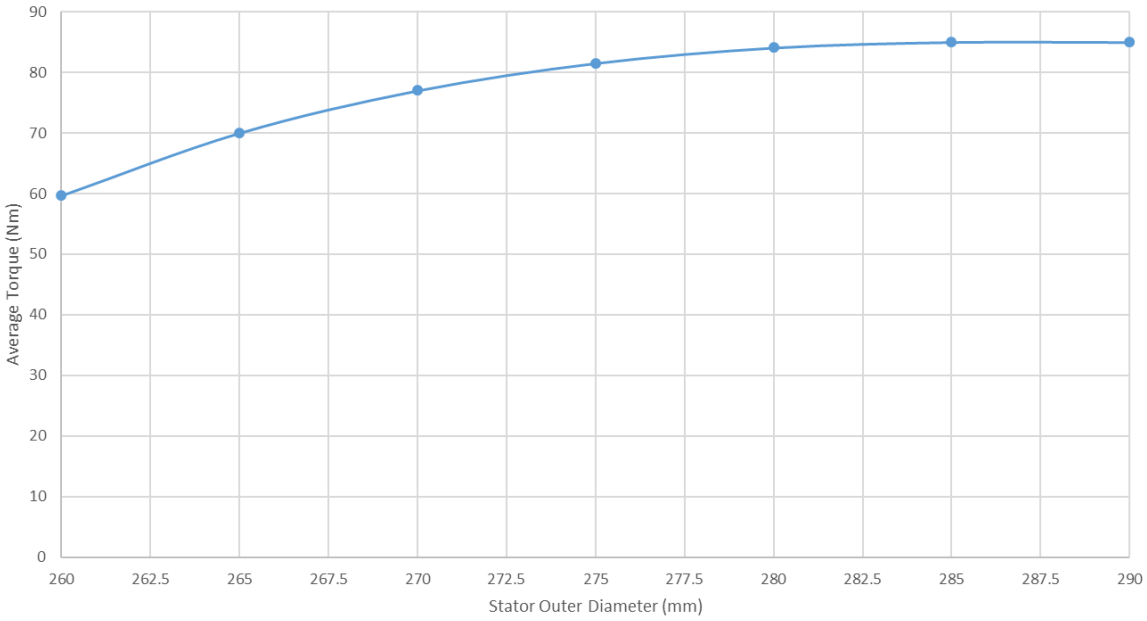

Figure 4.20 Finite element predicted variation in average torque with stator outer diameter

Although the torque produced by a 100mm axial length machine drops as the stator diameter is reduced, it is important to recognise that the mass is also dropping. The resulting variation in the

torque per unit mass of the designs is shown in figure 4.21. The mass shown is the total active mass, including the end-winding mass. The best torque density for this pole number occurs with a stator diameter of 275mm which produces a torque of 81.52Nm for an overall active mass (including end windings) of 23.14kg. This 275mm stator outer diameter design can be re-scaled to an axial length of 61.54mm in order to produce the rated torque of 85Nm at a new active mass of 23.97kg.

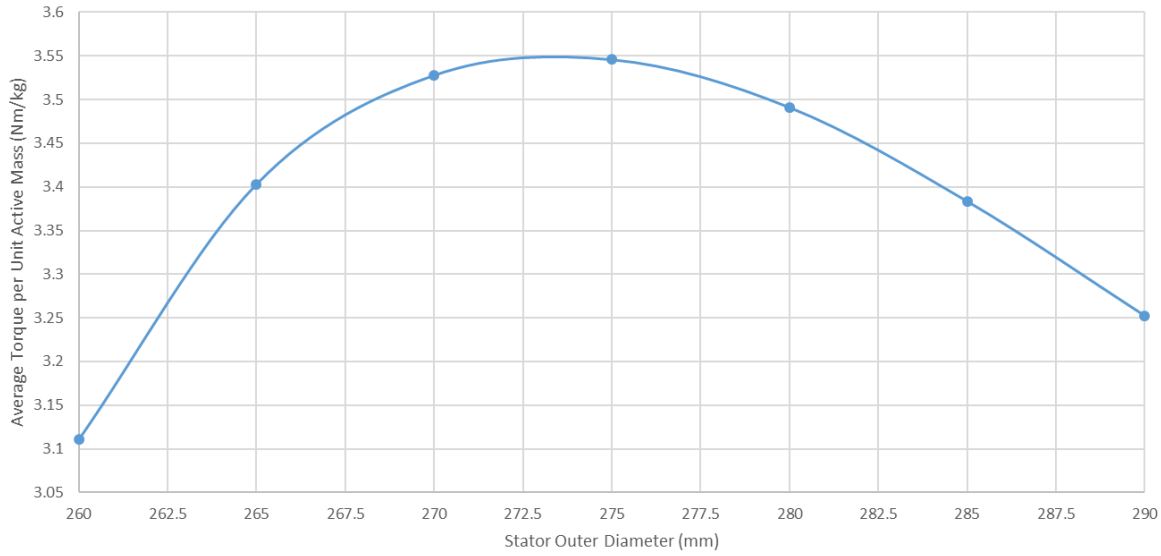

Figure 4.21 Finite element predicted variation in average torque per unit mass with stator outer diameter (including end windings) for axially scaled machines to produce 85Nm of Torque.

4.4.3. Analysis of 10 Pole Designs

A very similar analysis process was applied to a series of 10 pole designs as that adopted for the 8 pole designs. Again, in order to maintain a single-layer, integer slot winding, it was necessary to adjust the number of stator slots, in this case to a 30 slot stator with the winding arrangement shown in figure 4.22. As was the case with the other pole numbers considered, the slot geometry was adjusted to achieve an overall slot cross-sectional area of ~7600mm^2. A cross-section of the resulting design is shown in figure 4.23, in this case for the initial design with the 290mm stator outer diameter. This initial design with a 290mm stator outer diameter produces a torque of 144Nm (for a 100mm axial length) with an average flux density in the back-iron of 0.84T, which suggests considerable scope to reduce the stator outer diameter to improve the torque density. The same procedure of progressively reducing the stator outer diameter and calculating the torque was applied, but in this case down to 250mm as the higher pole number is likely to allow further reductions in the back-iron thickness. The machine is currently capable of producing 144Nm of torque at 100mm axial length, this means the axial length can be reduced to 59.03mm of axial length. Finite element predicted flux density distributions in machines with stator outer diameters of 290mm and 250mm are shown in figure 4.24.

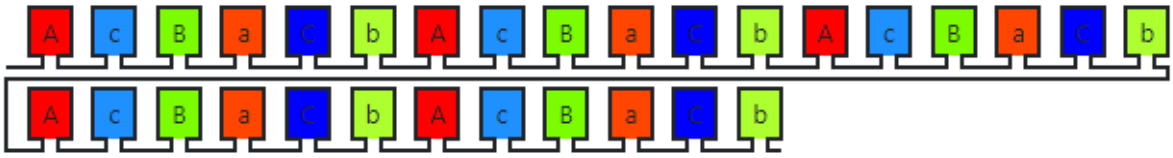

Figure 4.22 30-slot, single-layer, integer slot, 10 pole winding layout

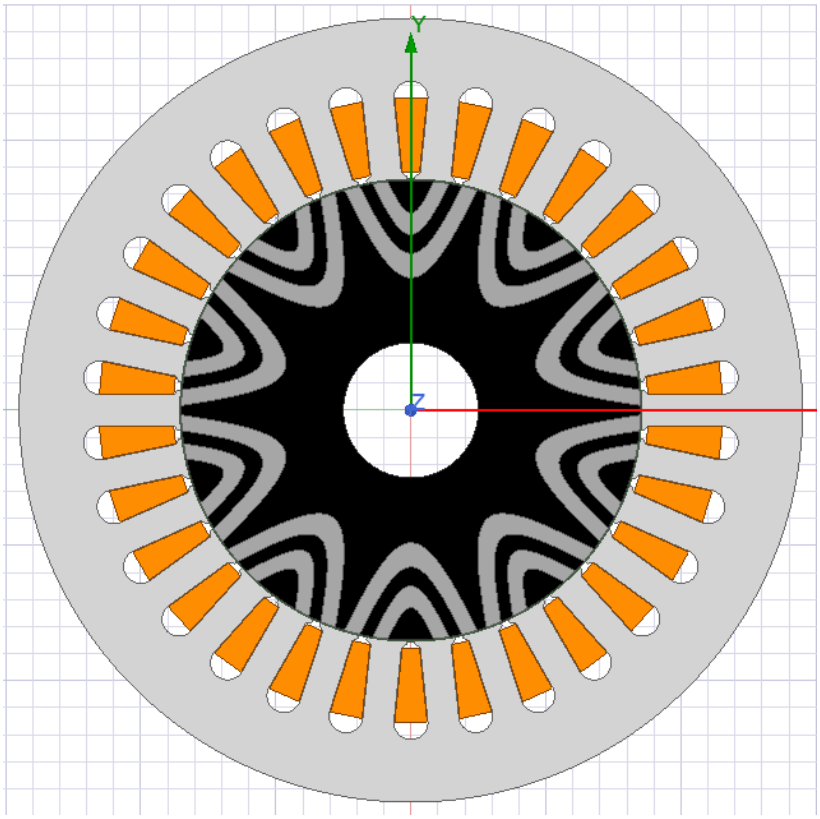

Figure 4.23 Cross-section through the initial 10 pole machine design

Figure 4.25 shows the predicted variation in torque with stator outer diameter, which again shows a similar trend to that observed with the 8 pole machine with no loss, a gradual reduction and then a steeper fall off in torque with the smaller stator outer diameter. The 250mm design shown in figure 4.24(b), produces a torque of 37.1Nm of Torque with an average flux density of 0.89T in the stator but with significant regions at this particular rotor angle in excess of 3.47T behind the slots.

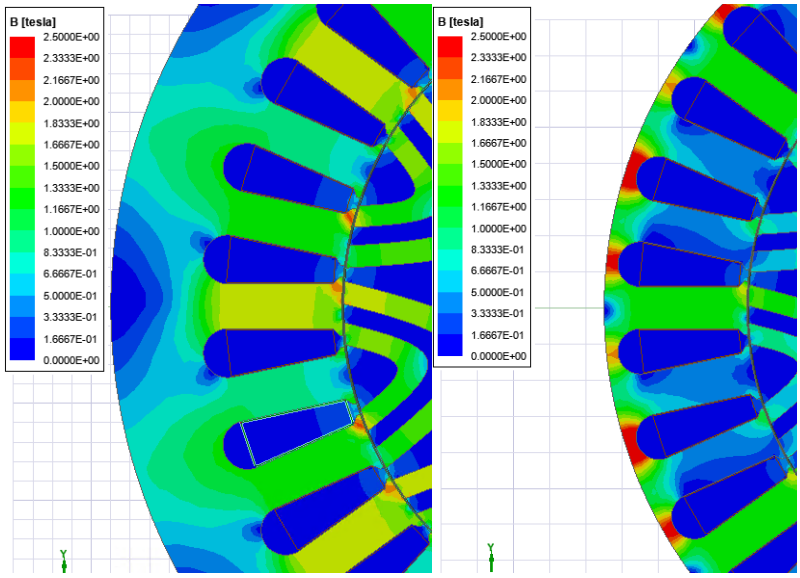

(a) 290mm **(b) 250mm**

Figure 4.24 Instantaneous flux density distributions for stator outer diameters of 290mm and 250mm at a rms current density of 10A/mm^2

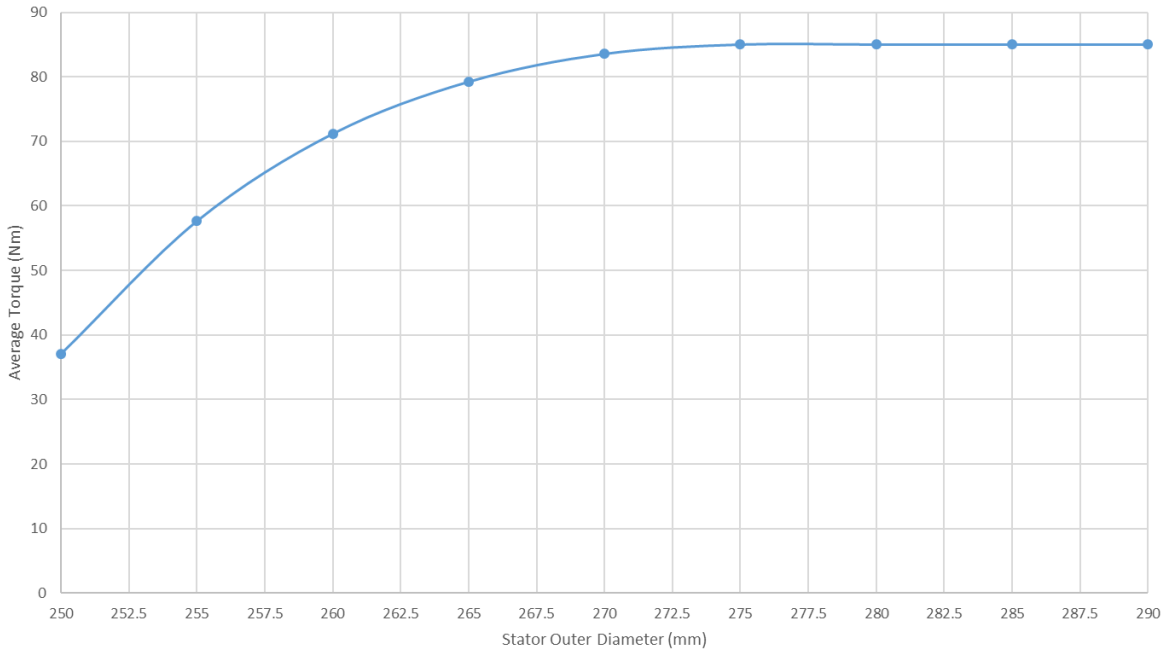

Figure 4.25 Finite element predicted variation in average torque with stator outer diameter at 59.03mm of axial length and a current density of 10A/mm^2

As was the case with the 8 pole designs there is some scope to trade off the mass reduction against the torque reduction which results from reducing the stator outer diameter. This is illustrated by figure 4.26 which shows the variation in the torque per unit mass as the stator outer diameter is reduced

from 290mm down to 250mm. On the basis of figure 4.26 a design with a stator outer diameter of 265mm would appear to be a favourable option, and this 265mm stator outer diameter design will be re-scaled to an axial length of 63.3mm in order to produce the rated torque of 85Nm.

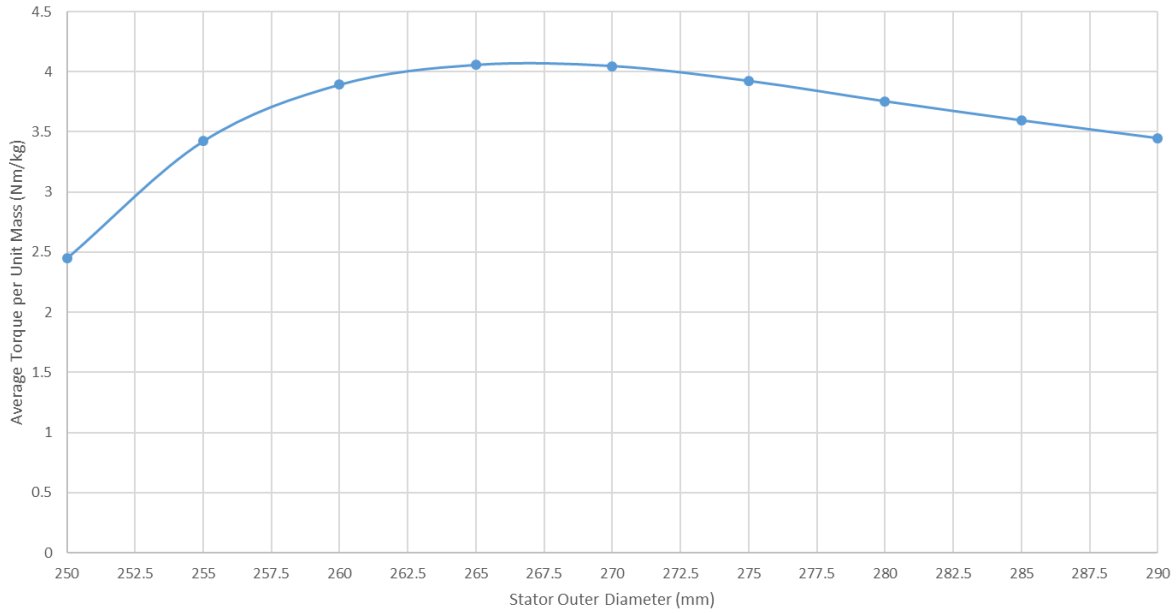

Figure 4.26 Finite element predicted variation in average torque per unit mass (including end windings) with stator outer diameter at a corrected axial length to give 85Nm of torque for a current density of 10A/mm^2

4.4.4. Analysis of 12 Pole Designs

A 12 pole rotor was designed initially for use with the same 36 slot stator as that established for the 4 pole machine and shown in figure 4.2(b). Initially, the same 290mm stator outer diameter was maintained to provide a direct comparison in terms of the influence of the rotor pole number change. However, there was an expectation that employing a higher pole number would be an opportunity to reduce the stator core outer diameter, as a thinner back-iron would be required. Figure 4.26 shows the 12 pole design, in this case with only 2 flux guides per pole. The stator coil arrangement shown in figure 4.27 is 36 slot, 12 pole, single layer, integer slot winding with a winding distribution factor of 1.0.

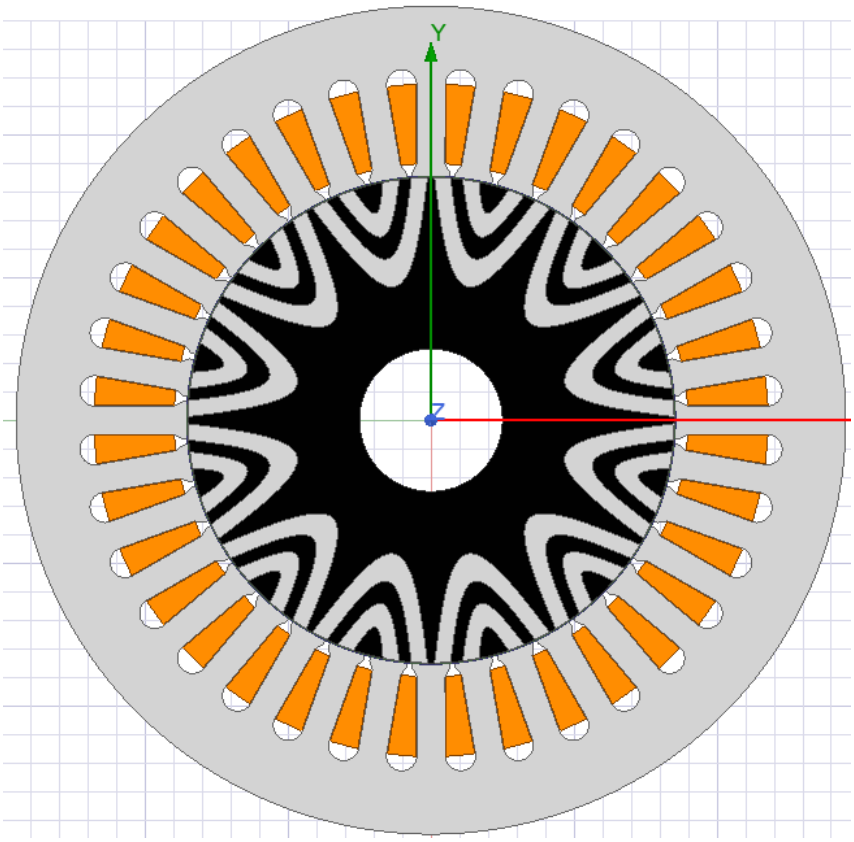

Figure 4.26 Cross-section of the 12 pole rotor

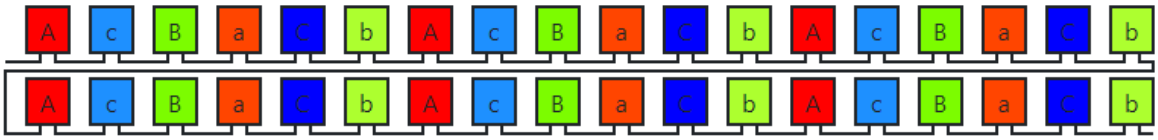

Figure 4.27 36 slot, 12 pole single layer, integer slot winding

This initial 12 pole design with a 290mm outer diameter stator and an axial length of 100mm has a finite element predicted average torque of 130.8Nm at a rms current density of 10A/mm^2. The torque waveform over one electrical revolution (60 degrees mechanical) is shown in figure 4.28 which demonstrates that this combination of 36 stator teeth and 48 rotor pole faces produce a peak-to-peak torque ripple of 125.26Nm. This average torque capability would enable the axial length to be scaled back to 64.98mm in order to meet the rated torque specification of 85Nm. This compares with an axial length of 52.8mm for the equivalent 4 pole design with a 290mm stator outer diameter. Hence, when using the same stator, and recalling that the back iron will be considerably over-sized for the 12 pole

variant, the revised 4 pole design (which produces 161Nm for an axial length of 100mm and the same current density) is more effective in producing torque.

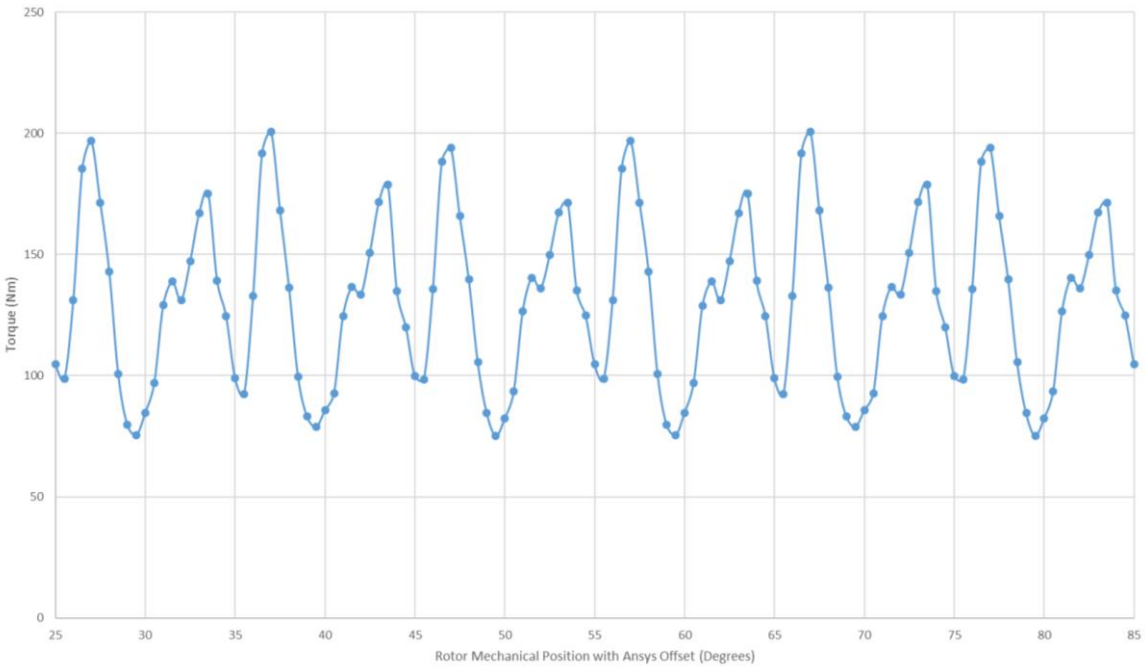

Figure 4.28 Finite element predicted torque waveform for the 12 pole machine design of figure 4.26 with a 290mm diameter stator

However, the flux density levels in the stator back iron in the 12 pole design with an outer diameter of 290mm are low, as shown in the predicted flux density snapshot of figure 4.29. Almost all the stator back iron is operating below 0.88T suggesting significant scope to reduce the stator outer diameter and hence reduce mass. A series of further designs were modelled with the stator outer diameter progressively reduced from 290mm to 255mm. The resulting variation in the average torque with stator outer diameter is shown in figure 4.30 while figure 4.31 shows the corresponding variation in the torque density.

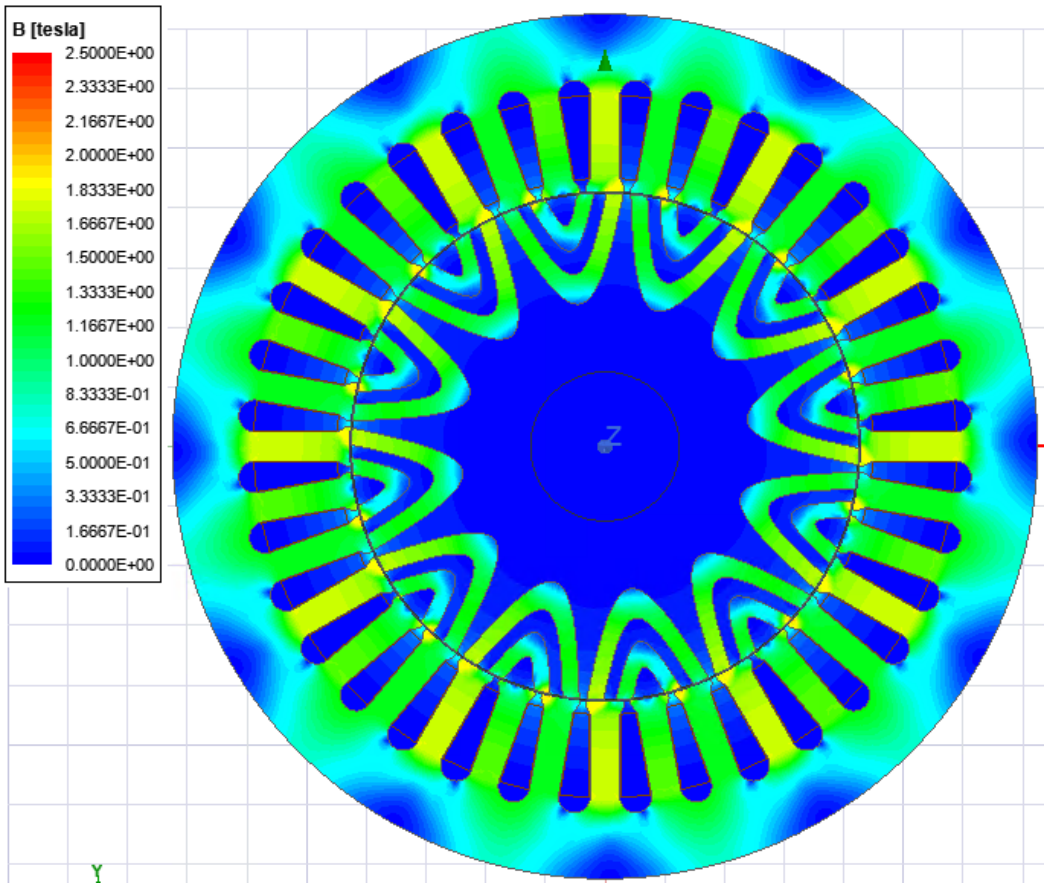

Figure 4.29 Finite element predicted flux density distribution when operating at a rms current density of 10A/mm^2 with a stator outer diameter of 290mm.

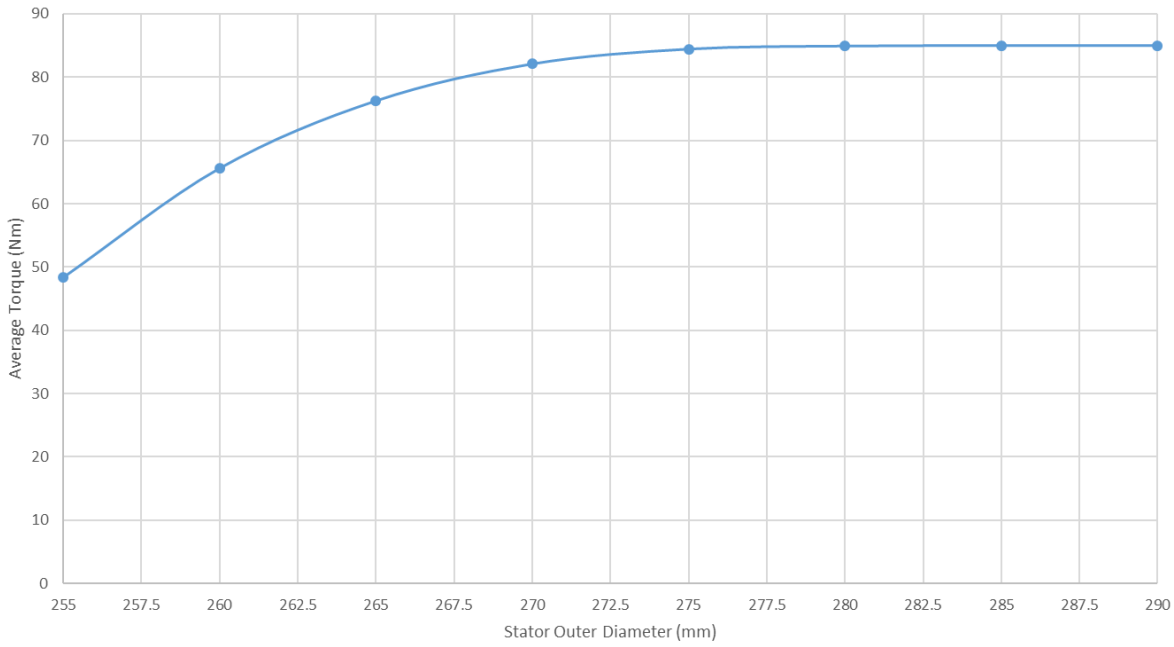

Figure 4.30 Finite element predicted variation in average torque with stator outer diameter (at an axial length of 65mm and a rms current density of 10A/mm^2)

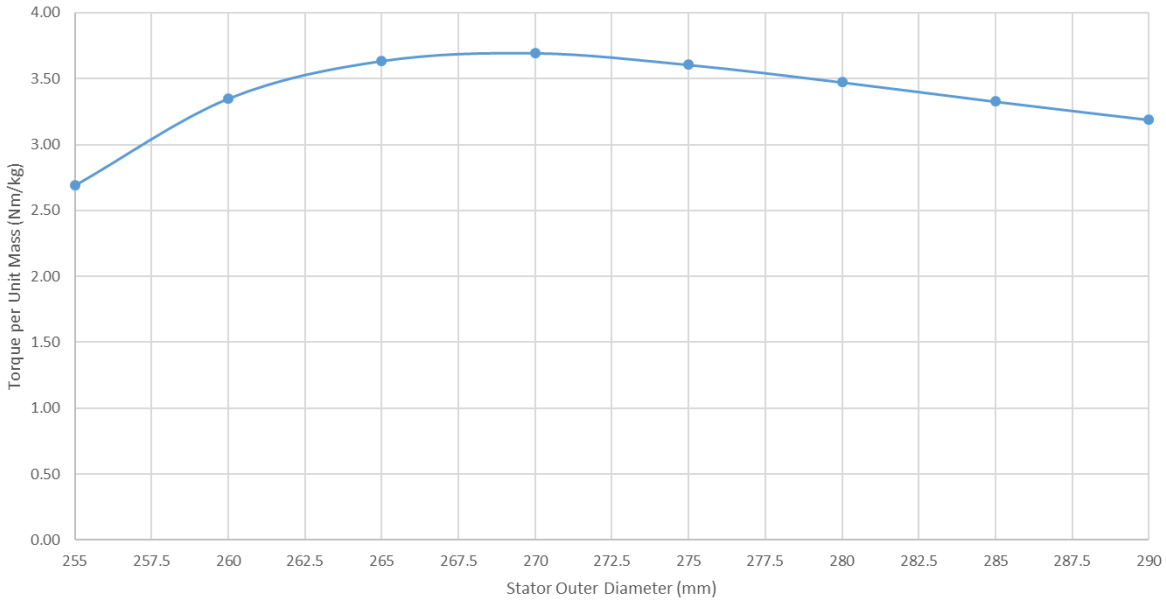

Figure 4.31 Finite element predicted variation in average torque per unit mass (including end-windings) with stator outer diameter (axial length corrected to give 85Nm of Torque at a rms current density of 10A/mm^2)

As will be apparent from figure 4.30, the torque capability holds up reasonably well until the stator outer diameter is reduced to 260mm, beyond which the influence of magnetic saturation on the torque capability becomes very pronounced, as evidenced by the predicted flux density distribution in figure 4.32. The drop in torque for reductions beyond 260mm are sufficiently large to outweigh the reduction in mass leading to a more effective stator outer diameter in terms of torque density of 265mm. The Outer Diameter gives a torque ripple of 86.3Nm. For this revised stator outer diameter, the axial length required to meet the 85Nm rated torque specification is 72.46mm, which results in an overall mass of 23.4kg which compares favourably with the 27.02kg for the revised 4 pole design whose length was scaled to 52.8mm to produce 85Nm.

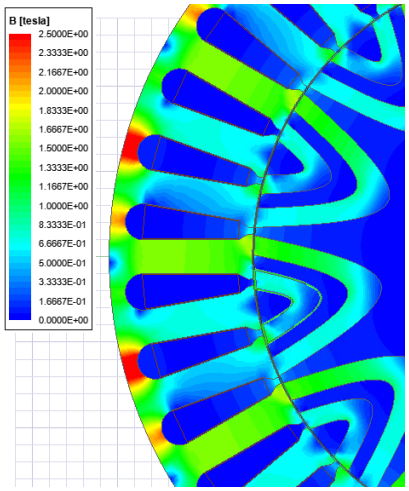

Figure 4.32 Finite element predicted flux density distribution when operating at a rms current density of 10A/mm^2 with a stator outer diameter of 255mm.

4.4.5. Analysis of 14 Pole Designs

The last pole number considered was a 14 pole design which required a 42 slot stator to accommodate a single-layer, integer slot 3 phase winding. The stator slots were again dimensioned to produce an overall slot area of ~7600mm^2 with 36.3mm deep slots. A cross-section through the 42 slot, 14 pole stator is shown in figure 4.33, in this particular case for a stator outer diameter of 290mm. Figure 4.34 shows the corresponding winding arrangement which has a winding factor of 1.0.

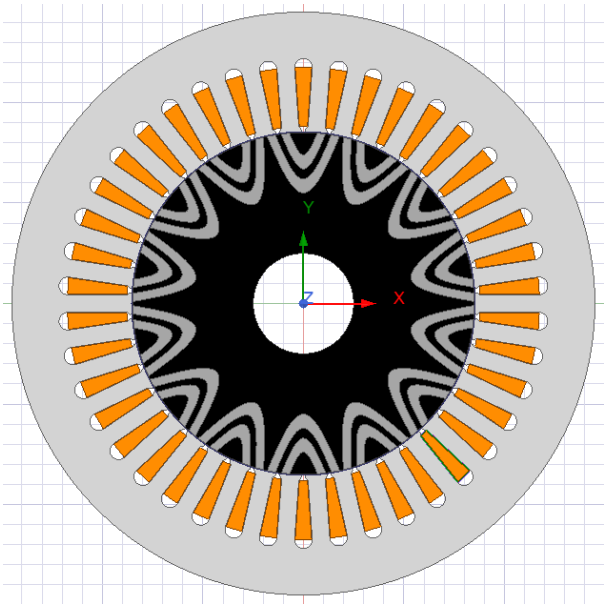

Figure 4.33 Cross-section through the 14 pole deign with a stator outer diameter of 290mm

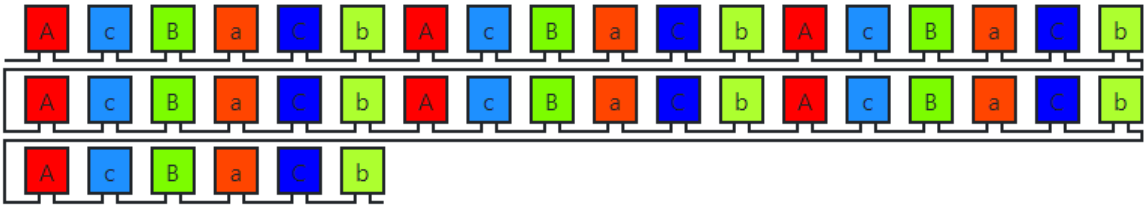

Figure 4.34 42 slot, 12 pole single layer, integer slot winding

The same process of starting with a 290mm stator diameter and progressively reducing this value was again employed for the 14 pole design, but in this case down to 250mm. The initial 290mm stator diameter design produced a torque of 129.55Nm for an axial length of 100mm and a rms current density of 10A/mm^2, which is marginally lower than its 12 pole and 4 pole counterparts. This means that the axial length can be scaled to 65.61mm to reproduce the required 85Nm.

The variation in the average torque as a function of the stator outer diameter (at 65.61mm axial Length) for the 14 pole design is shown in figure 4.35 while the corresponding variation in torque per unit mass for an axial length corrected stator is shown in figure 4.36. In this case, the stator outer diameter can be reduced to 265mm before there is a significant drop in the torque capability of the machine, although even below this value, there is still some marginal improvement in the torque density. For these 14 pole designs operating at the rated current density, the highest torque per unit mass is achieved with a 260mm stator outer diameter.

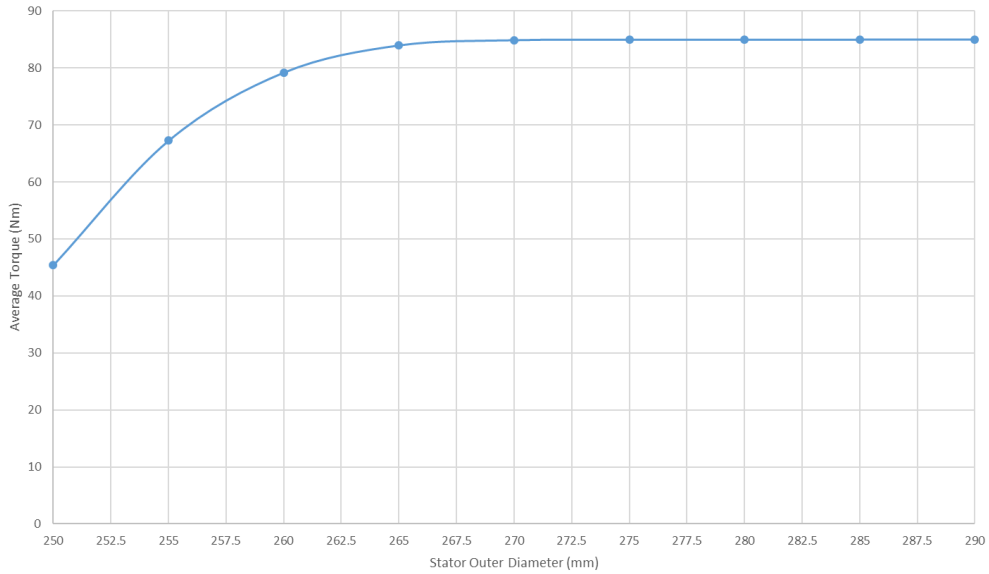

Figure 4.35 Finite element predicted variation in average torque with stator outer diameter for 14 pole design (axial length of 65.61mm and a rms current density of 10A/mm^2)

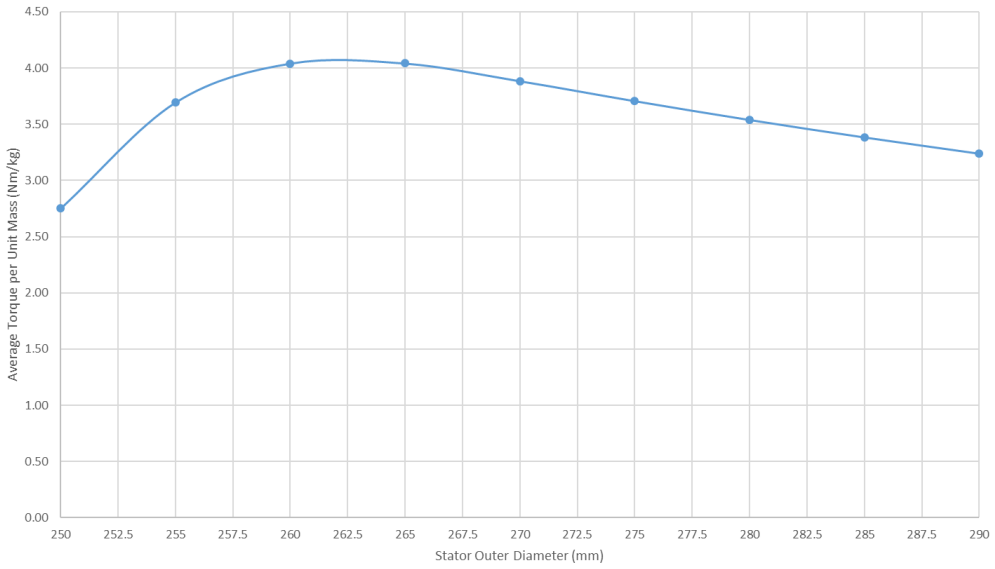

Figure 4.36 Finite element predicted variation in average torque per unit mass (including end-windings) with stator outer diameter for 14 pole designs (axial length corrected to give 85Nm and a rms current density of 10A/mm^2)

4.5. Summary of Torque Capability for Different Pole Numbers

A summary of the preferred designs for each pole number is shown in table 4.2. For each pole number, this is the design that yields the lowest mass to achieve the rated torque of 85Nm at the rated rms current density of 10A/mm^2. The copper loss for each design can be calculated without specifying the number of turns and wire gauge using:

$$P_{Cu} = J_{rms}^2 \rho_T V_{Cu} \tag{4.3}$$

where J_{rms} is the rms current density, ρ_T is the copper resistivity corrected for the operating temperature and V_{Cu} is the total volume of copper in the winding (including a representation of the end-winding length).

The resistivity can be corrected for a given temperature rise ΔT from a 20°C reference temperature by assuming a fixed temperature coefficient of resistivity α for the copper (0.00386 °C^{-1} [71]) using:

$$\rho_T = \rho_{20}(1 + \alpha \Delta T) \tag{4.4}$$

Since all the machines were designed for the same current density and slot area, the total copper loss at a prescribed temperature is only dependant on the axial length of the machine and the length of the external span of the end windings. On the basis of the static torque calculations undertaken in this chapter, designs with pole-numbers of 10 and 14 appearing the most favourable for the particular combination of rotor dimensions and current density set out in the specification, although the exact selection of the stator outer diameter (which has a significant effect on mass) and the 5mm increments used cause some perturbations in the general trends.

	4 pole	**8 pole**	**10 pole**	**12 pole**	**14 pole**
Most effective* stator outer diameter	290mm	275mm	265mm	265mm	260mm
Axial length to meet 85Nm rated torque	52.80mm	61.54mm	63.32mm	72.46mm	70.42mm
Active mass**	27.02kg	23.97kg	21.00kg	23.40kg	21.04kg
Copper loss at 20°C	1519 W	1115 W	1027 W	1025 W	959 W
Copper loss at 200°C	2623 W	1927 W	1774 W	1771 W	1657 W

* most effective in terms of torque density

** Excludes structural elements but includes end-windings

Table 4.2 Summary of different pole number preferred designs to meet 85Nm torque specification at a rms current density of 10A/mm^2

Table 4.2 shows that the two most favourable pole numbers, in terms of torque density and copper loss, were those with 10 poles and the 14 poles for the stator outer diameter increments selected. The 12 pole machine appears to be slightly out of step with the general trends in table 4.2, which may in part be due to the change in stator slot number and consequent impact on the slot opening and other stator proportions. Figure 4.37 shows the predicted instantaneous torque waveforms for 10, 12 and 14 pole machines (all adjusted to 360° electrical excursions) while the resulting peak-to-peak

torque ripple is shown in table 4.3. In all cases, the torque ripple is high with 12 peaks per electrical cycle.

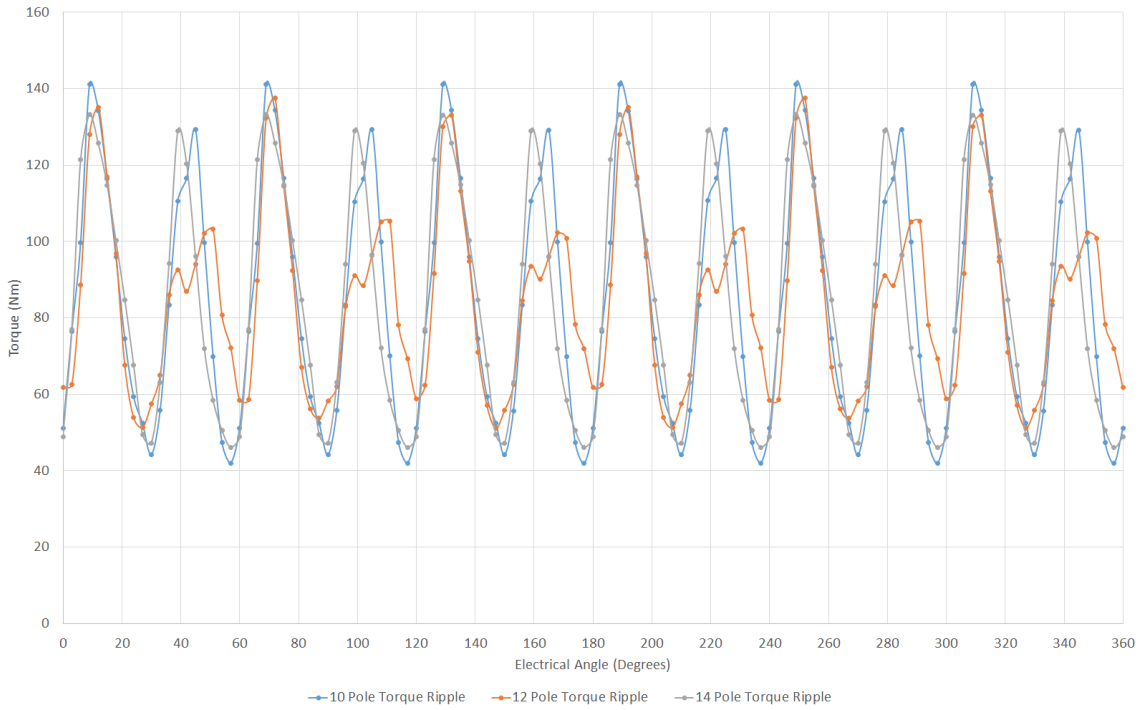

Figure 4.37 Instantaneous torque waveforms (plotted against electrical angle to allow a easier comparison) for 10,12 and 14 pole machines

	10 pole	12 pole	14 pole
Peak to peak Torque Ripple (Nm)	100.0Nm	86.3Nm	87.2Nm

Table 4.3 Predicted torque ripple

All three machines produce a high torque ripple, which can be attributed in large part to the slot-ripple. Although the differences across these pole numbers are fairly marginal, the exact best is influenced by steps adopted, i.e. there is a logic to suggest from table 4.2 that the 10 and 12 pole designs should have slightly different stator outer diameters (the higher pole number being the smaller of the two) which would eliminate much of the apparent mass difference. It is also worth noting that the 10 and 14 pole designs had stator core dimensions to suit the particular pole number while the 12 pole variant inherited the original 4 pole stator core, although the outer diameter was reduced. It was therefore concluded, due impart to this inherited and not custom stator, that there

were likely to be some further improvements to pursue in the 12 pole design and this was down-selected for further analysis, with the industry sponsors interest in a 12 pole design also being a factor.

4.6. Parametric Investigation of the 12 Pole Design

In common with the other pole numbers that could use the 36 slot baseline stator design, the only changes to the stator core made as the pole number was increased was a reduction in the stator outer diameter, and hence back-iron thickness. Figure 4.38 shows a close up of the flux density distribution in the 12 pole machine with a stator outer diameter of 265mm at a rms current density of 10A/mm^2. As will be apparent there is significant cross-slot leakage flux due to the narrow slot opening of 2mm. Since the d-axis flux in the stator core is by design much higher than that along the q-axis, then any leakage flux (which does not itself contribute usefully to torque production) causes a greater concern in terms of magnetic saturation for the d-axis flux than the q-axis flux, thus potentially narrowing the difference between L_d and $L_q$and so reducing the average torque produced.

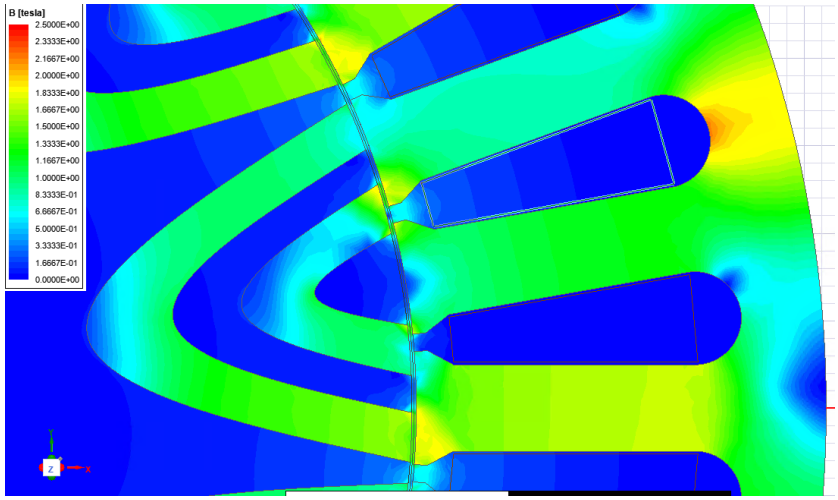

Figure 4.38 Finite element predicted flux density distribution at a rms current density of 10A/mm^2 for the 265mm stator outer diameter.

One means of reducing the leakage flux in the tooth tips is to open-up the slot opening, and adjust other dimensions in this region. Figure 4.39 shows a close-up of the slot opening region with various dimensions defined. It also worth noting that increasing the width of the slot opening would also ease the manufacturing challenges of the stator winding. It is also noticeable in figure 4.38 that the flux density in the back-iron at base of one of the slots is well into saturation whereas the maximum flux density in the main tooth body is lower. It is recognised that this is a single snapshot in time of the flux density distribution, but is does suggest that there is some scope to thicken up the back-iron within the same outer diameter and to compensate for the resulting loss of slot area by narrowing the stator tooth.

Following a series of iterations of the various slot parameters, the most effective stator geometry of figure 4.40 was established, which is shown alongside the original design. As will be evident, there has been significant change in the detailing around the slot opening and a significant increase in the thickness of the back-iron, recalling that the 265mm diameter was fixed. Table 4.4 summarised the main dimensions of the original and revised stator, from which it is evident that the various changes have only had a minimal effect on the total area of the stator with a reduction corresponding to 1.3% of the original slot area.

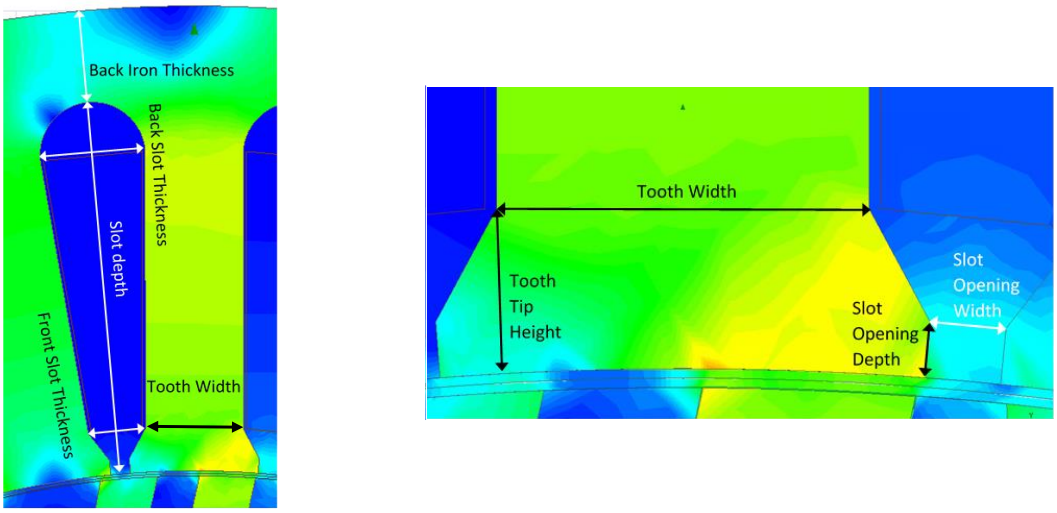

Figure 4.39 Close up stator tooth defining key dimensions

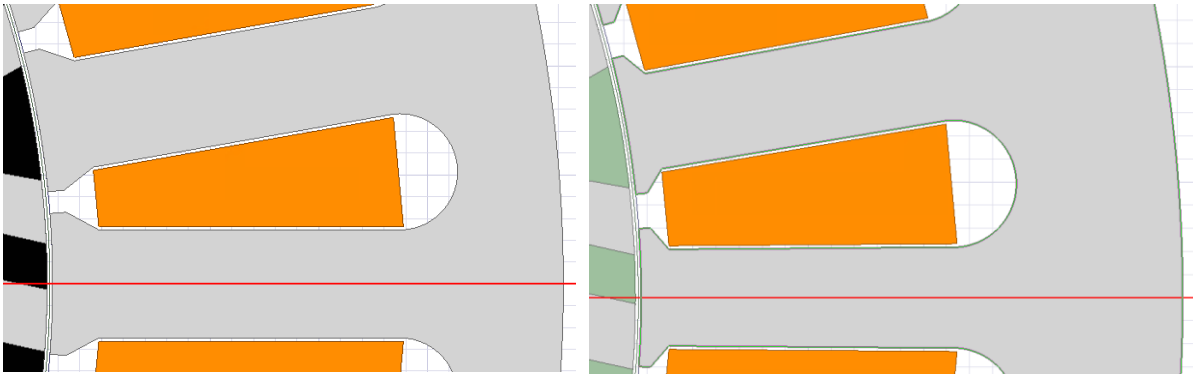

(a) Original design **(b) Secondary revised design**

Figure 4.40 Comparison of slot geometry for the original and the secondary revision designs

Parameters	Original Stator Design (Figure 4.40a)	Parametrically Investigated Stator Design (Figure 4.40b)
Back Iron Thickness (mm)	9.29	14.00
Slot Depth (mm)	37.70	33.00
Back Slot Thickness (mm)	10.65	11.00
Front Slot Thickness (mm)	5.78	7.00
Tooth Width (mm)	9.90	8.36
Tooth Tip Height (mm)	4.40	2.50
Slot Opening Depth (mm)	1.50	1.00
Slot Opening Width (mm)	2.00	3.00
Total Slot Area (mm^2)	~7600	~7500

Table 4.4 Key stator parameters of the original and the revised 12 pole designs.

This revised design shows a significant increase in torque density, allowing the stator core length required to produce 85Nm to be reduced from 72.5mm to 66.2mm with a consequent saving in mass. Figure 4.41 shows the flux density distribution for the same rotor position and current density as that used to generate the corresponding flux density distribution of figure 4.38 for the original design. As will be evident, there is reduction in the flux density in the back-iron and a better balance with the flux density in the main stator tooth body. The widening of the slot opening and the modifications to the tooth tips has also reduced the leakage flux across the slot opening.

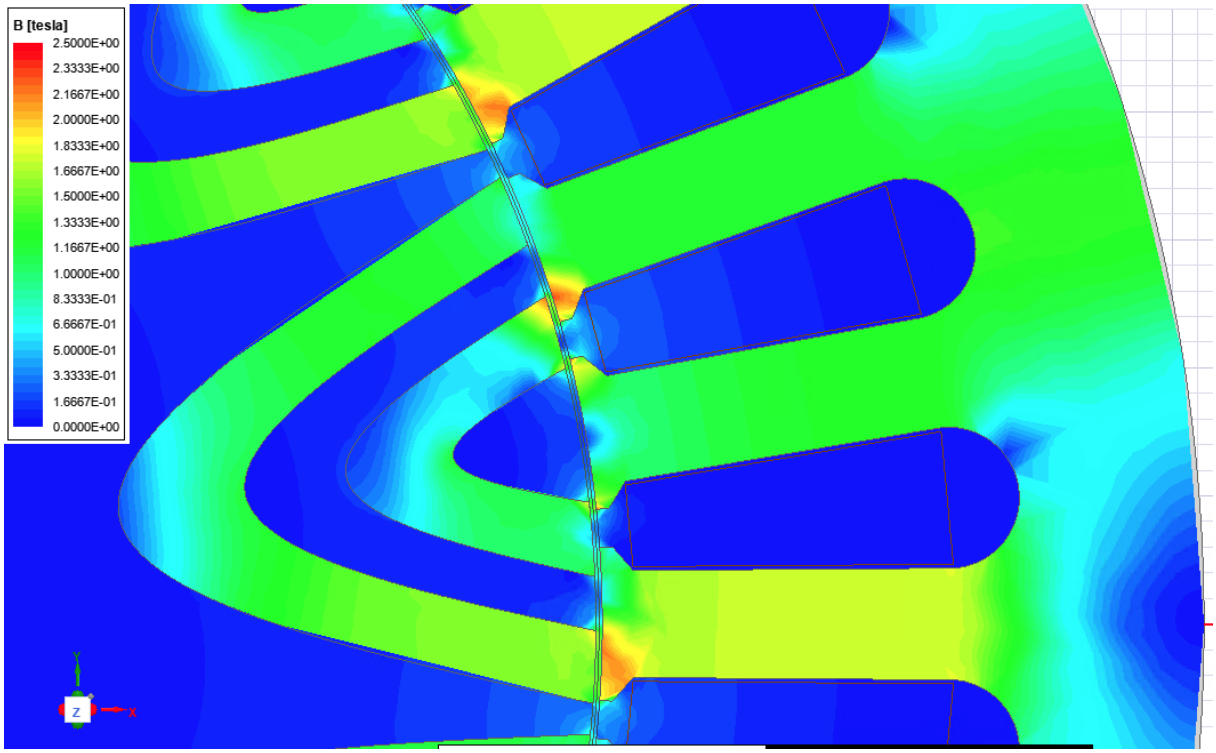

Figure 4.41 Finite element predicted flux density distribution in the parametrically investigated stator geometry at a rms current density of 10A/mm^2 (same rotor angular position as figure 4.39).

Table 4.5 shows a comparison between the headline performance value of the original and new revised 12 pole design from which a saving of almost 2kg is achieved while retaining the same rated torque. The combination of a reduced axial length and a slight reduction in the slot area has resulted in a lower copper loss since the coils at operated at a fixed current density and hence the loss simply scales with the coil volume.

	Original 12 pole design	Revised 12 pole design
Revised* stator outer diameter	265mm	265mm
Axial length to meet 85Nm rated torque	72.5mm	66.2mm
Active mass**	23.40kg	21.64kg
Copper loss at 20°C	1025W	970W
Copper loss at 200°C	1771W	1675W

* Revised in terms of torque density

** Excludes structural elements but includes end-windings

Table 4.5 Comparison of the original and revised 12 pole designs

4.7. D-Q Axis Inductances of the Revised 12 Pole Design

Having established the dimensions of the revised 12 pole design, the d and q-axis inductances were calculated to allow analytical checks on performance, including the winding design described later in chapter 6. As noted on several occasions in this chapter, and in chapter 3, magnetic saturation is an important consideration in SYNCREL machines, especially in designs targeting high torque density. Hence, as noted in chapter 2, it is likely that the d-axis and q-axis inductances will be functions of the magnitude of the d and q axis currents. The procedure adopted for calculating inductances followed that described in chapter 2.

Figure 4.42 shows the resulting variation in the d-axis and q-axis inductances with rms current magnitude for a single turn coil (which can be scaled by the square of the number of turns to obtain the actual distance). As expected the d-axis inductance is much more prone to the effects of magnetic saturation with a significant drop in inductance beyond 1000A rms or so (which corresponds to a current density of 9.6A/mm^2 rms). Since the q-axis inductance is largely insensitive to magnetic saturation effects, this illustrates the importance for torque capability of reducing flux-leakage, so as to maintain the gap between the two inductance values to be as high as possible. The characteristics shown in figure 4.42 can be used in combination with equation (2.6) to calculate the variation in torque with current, again assuming a single-turn per coil and using the appropriate values of L_d and L_q for

the current magnitude. This calculated variation in torque is shown in figure 4.43, alongside the corresponding values calculated directly from finite element analysis. As would be expected given that the L_d and L_q values contain all the non-linearity's in the field solution, there is good agreement between the methods even under heavily saturated conditions.

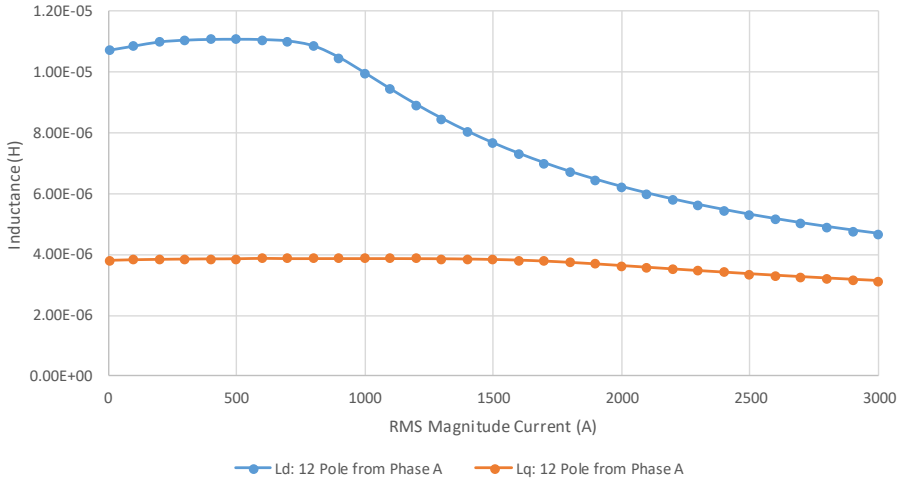

Figure 4.42 Variation in d-axis and q-axis inductance with rms current for a single-turn per coil in Phase A

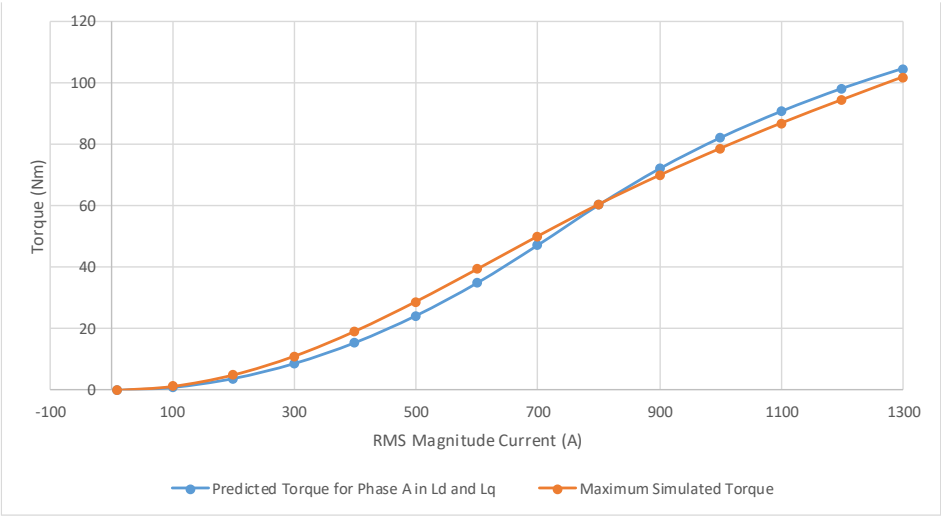

Figure 4.43 Comparison of direct finite element simulated torque and torque predicted using equation 2.6 and figure 4.42 for all three phases

4.8. Influence of Pole Number on Iron Losses

The analysis up to this point has focussed on static torque considerations. One drawback of increasing the pole number from the original 4 pole design at the start of this chapter, is the proportional increase in the electrical frequency for a given mechanical speed, and hence the frequency of the time varying fluxes in the stator and the rotor cores. Hence, the iron loss in these cores will increase with pole number. In order to investigate the magnitude of the iron loss penalty involved in adopting a 12 pole design, a series of calculations were performed which combined time-stepped finite element solutions over one electrical cycle with an existing in-house developed MATLAB based post-processor, for translating individual element-by-element flux density variations into iron loss for a specific set of material specific coefficients. The post processor runs a field solution under load and extracts the B_y and B_x for every element over the cycle of interest. Typically, it would be expected that the rotor is exposed to a near stationary field, but in practice the spatial harmonics in the stator field due to slotting effects, and the spatial harmonics inherent in the discrete nature of the coils, results in iron loss being present in the rotor core, hence the need to post-process the results.

The iron loss solutions were to start by using M300-35A as this was a pre-loaded material in the FEM solver, and as it is the same thickness lamination as used previously, also the difference in the magnetisation curves between M250-35A and M300-35A is negligible.

A typical post-processor output is shown in figure 4.44, in this case for the stator of the 12 pole machine at 10,000rpm. The total stator loss for this case is 3.52kW consisting of 630W of hysteresis loss, 316W of excess loss and 2575W of classical eddy current loss.

At 10,000rpm, the fundamental electrical frequency of the 12 pole machine is 1kHz, and it is therefore unsurprising that the eddy current loss dominates in a 0.35mm thick lamination. This suggests that using a thinner silicon iron lamination could yield significant benefits in terms of eddy current loss, even though it would have little effect on the hysteresis component. Two commercially available silicon iron lamination grades, of Cogent N020 and NO10 with thicknesses of 0.2mm and 0.1mm, were therefore investigated. For these two lamination grades the total stator loss at 10,000rpm is reduced to 1,706W and 1,013W respectively. Thinner laminations naturally incur additional manufacturing costs, not just in the original production of the thinner sheet but also in cutting and assembly where proportionally more laminations are required to make up a given stack length.

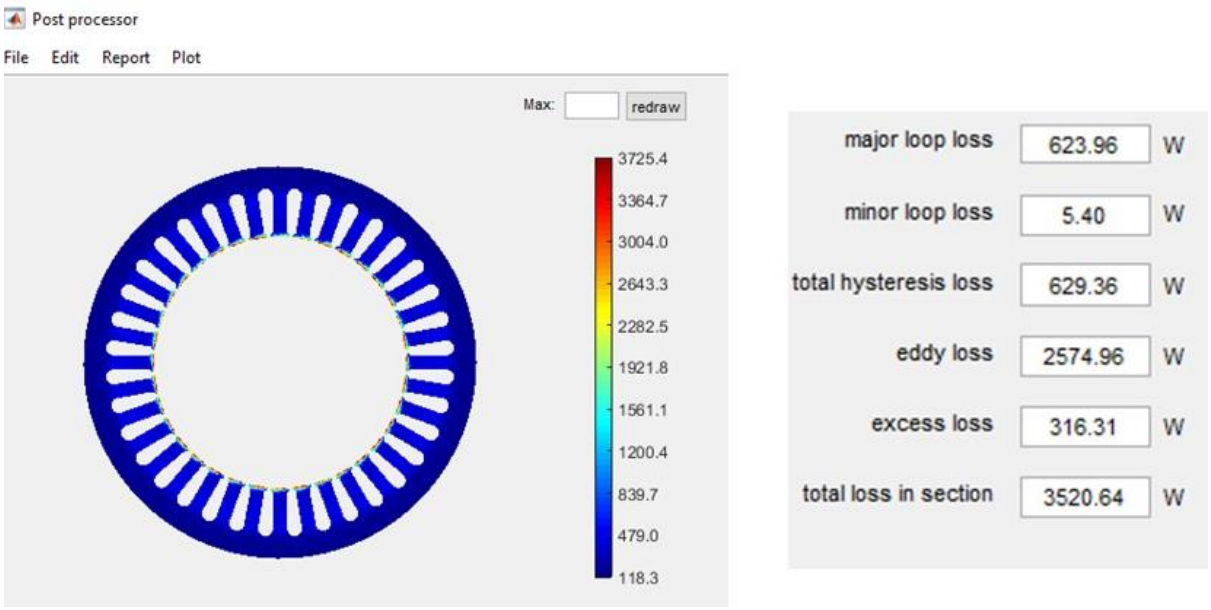

Figure 4.44 Typical output from an existing iron loss post-processing tool with loss density (W/kg) represented as shaded contours (case shown is M300-35A at 10,000rpm and rated current density)

A summary of the stator iron loss is shown in table 4.6 for speeds of 10,000rpm and 20,000rpm for these three silicon iron lamination grades. In all cases, these are for rated current and torque of 85Nm. Also shown in table 4.6 are the corresponding stator iron loss for the 4 pole revised design established at the start of this chapter, which has an axial length of 52.8mm. As would be entirely expected the loss in the 12 pole stator is much higher than the equivalent loss in the 4 pole design for the same combination of lamination grade and speed. However, the ratio between the losses, with different pole numbers, is far from straightforward and is dependent on both speed and grade. For example, at 10,000rpm with M300-35A laminations, the loss of the 12 pole machine is almost exactly 3 times the loss of its 4 pole equivalent. However, for NO10 at 10,000rpm the loss only increases by a factor of 1.56. It is worth noting that the combination of the loss formula employed in the calculation, which contains contributions which are proportional to f, $f^{1.5}$ and f^2, and the different core geometries, masses and nature of the flux density variation therein make the application of simple scaling rules with lamination thickness and speed very problematic.

It is useful to put the 12 pole loss values in table 4.6 into some context in relation to the output power. Taking the 10,000rpm operating point, which as will be shown in later chapter is close to the likely operating speed of the 12 pole machine, and recalling that the torque for the conditions in table 4.6 is 85Nm, then the mechanical output power is 89.0kW. Hence, the 1013W of stator loss produced with the thinnest laminations is 1.14% of the mechanical output which is reasonable in terms of anticipated efficiency for a SYNCREL machines. If the thicker 0.35mm lamination were adopted then

the stator iron loss would increase to 3,521W which corresponds to 3.96% which is beginning to impact significantly on the efficiency, let alone the difficulties of managing such heat loads in the stator when the copper loss is further added in. On the basis of the loss data in table 4.6, recourse to at least 0.2mm thick laminations is likely to be required to produce a competitive efficiency, and possibly even a thermally viable design. If a 4 pole machine were adopted and its size and weight penalty set-aside, then even the thicker 0.35mm lamination produces a likely acceptable loss at 10,000rpm, though again benefits would be significant if the lamination thickness were reduced.

Rotational speed	**Total stator iron loss (W)**					
	4 pole			**12 pole**		
	M300-35A	**N020**	**N010**	**M300-35A**	**N020**	**N010**
10,000rpm	1,222	763	649	3,521	1,706	1,013
20,000rpm	3,838	2,006	1,391	12,543	5,172	2,397

Table 4.6 Predicted stator iron loss for the 4 pole baseline and 12 pole revised machine for a range of core materials and speeds

Although first order considerations would suggest the rotor core should be exposed to a near stationary field in a SYNCREL machine, in practice spatial harmonics in the stator field due to slotting effect, and the spatial harmonics inherent in the discrete nature of the coils, results in iron loss being present in the rotor core. A corresponding table of rotor iron loss is shown in table 4.7. As was the case with the stator loss, there is a significant benefit from employing the thinner grades of laminations. As will be noted, these losses are far from insignificant being typically a quarter to a third of the corresponding stator loss. It is interesting to note that the proportions of hysteresis, excess loss and eddy current loss are different from stator breakdown shown in figure 4.44 at same operating point. As shown in figure 4.44 for this stator, the split between hysteresis, excess and classical eddy current losses are 18%, 9% and 73% respectively. In contrast for the same material grade and operating speed the corresponding breakdown in the rotor is 74%, 4% and 22% which is indicative of lower frequency field variations. This is understandable, at least for co-rotating fields, given that time-varying flux variations in the rotor are determined by relative speeds between the rotating field components, and the rotor.

This dominance of the hysteresis component of loss, particularly in the 4 pole variant explains some of the behaviour in table 4.7, such as the increase in loss when NO20 laminations are replaced by NO10 material at same speed in the 4 pole design, e.g. the increase in loss from 1208W to 1548W at 10,000rpm. In this case, the loss is dominated by hysteresis (>95% contribution in the case of NO10) and hence the small differences in hysteresis loss coefficients outweigh the influence of lamination thickness. NO10 by virtue of being a thinner material which has undergone more rolling and deformation has a slightly higher hysteresis loss than NO20. Although hysteresis plays an important role in the 12 pole designs, the higher frequencies in play mean that there are no instances where the loss increases with reduced lamination thickness. Although the benefits of a thinner lamination are less pronounced than in the stator. Rather unexpectedly, the rotor iron loss with the 4 pole rotor is higher than that with the 12 pole rotor at some of the operating points and similar at others. There are several contributing factors which act in combination to produce this somewhat surprising result:

- There is a significant larger quantity of magnetic material in the 4 pole rotor compared to the 12 pole rotor with masses of 5.04kg and 3.85kg respectively.
- A significant proportion of the loss in the rotor is likely to be caused by permeance modulation associated with the slotting. Since both pole numbers are rotating at the same mechanical speed, have similar stators with the same slot number, and the flux guide have comparable widths at the airgap, then the permeance modulation's contribution to iron loss density in the rotor will be similar and not directly dependant on the pole number.

Rotational speed	**Total rotor iron loss (W)**					
	4 pole			**12 pole**		
	M300-35A	**N020**	**N010**	**M300-35A**	**N020**	**N010**
10,000rpm	1635	1208	1548	1147	511	246
20,000rpm	4030	2674	3147	4177	1633	622

Table 4.7 Predicted rotor iron loss for the 4 pole baseline and 12 pole revised machine for a range of core materials and speeds

4.9. Summary of Final Design

Although the final 12 pole design has some shortcomings in terms of modest torque density and the need to use thin gauge laminations to manage the iron loss, it was selected as the basis for further

study. In comparison with the 4 pole baseline machine it has a lower mass (21.6kg versus 27.0kg), a lower copper loss (1.67kW and 2.62kW at 200°C in large part due to the end-windings) and a generally lower rotor iron loss (e.g. 511W versus 1208W at 10,000rpm with NO20). It has the drawback of a higher stator iron loss (e.g. 1706W versus 763W at 10,000rpm with NO20) and a larger torque ripple. It is likely that the additional flux guide mass of the 4 pole rotor and their greater span will pose challenges in terms of mechanical behaviour as well. On balance, the 12 pole design was down-selected as the preferred design for further investigations. Further considerations contributing to this decision were a combination of the 12 pole design being competitive with other pole numbers in terms of torque density, requiring relatively small individual rotor flux guides, and for reasons of novelty, since there is very little published literature on higher pole number SYNCREL machines. A cross-section through the final design is shown in figure 4.45, while table 4.8 summarises predicted performance at rated torque and at speeds of 10,000rpm and 20,000rpm for the case of NO20 stator and rotor cores.

Despite the large iron loss in both the stator and rotor of this machine, particularly at 20,000rpm, the efficiency is respectable at >95% at both speeds (neglecting mechanical losses and any AC winding loss). Moreover, the power density, even at 10,000rpm is competitive at ~4kW/kg although this is likely to reduce by a factor of ~1/3 to ~1/2 or so, once allowance is made for casing and a shaft etc. Hence, from an electromagnetic performance point of view, this 12 pole design looks promising. However, thermal management of the rotor may require some further attention or the adoption of very thin 0.1mm laminations which would detract from the low cost aspect of the proposed concept.

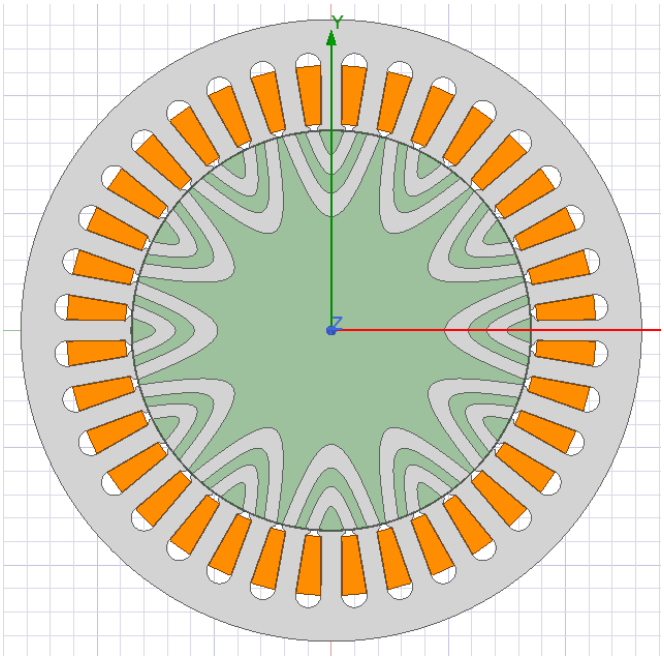

Figure 4.45 Cross-section through the final down-selected 12 pole machine design

	10,000rpm	20,000rpm
Rated power at 85Nm	89.0kW	178.0kW
Overall active mass (includes end windings but excludes structural elements)	21.64kg	21.64kg
Power density based on active mass	4.12kW/kg	8.24kW/kg
Total iron loss (rotor and stator) based on NO20	2.22kW	6.80kW
Total copper loss at a winding temperature of 200°C (based on assumed end-winding length – see chapter 6 and neglects any AC losses)	1.67kW	1.67kW
Total of copper + iron loss	3.89kW	8.47kW
Efficiency	95.8%	95.4%

Table 4.8 Summary of performance for down-selected design

5. Investigation into Rotor Mechanical Behaviour

5.1. Introduction

The preceding chapters have considered the electromagnetic merits of different pole numbers, rotor configurations and flux guide geometry in various combinations. At the conclusion of chapter 4, a 12 pole design was down-selected for further investigation. However, if the final design is to meet the performance objectives set out in chapter 1, in particular achieving a high power density by means of operation at high rotational speed, the rotor must be capable of remaining within acceptable mechanical stress limits at the maximum operating speed. As noted in chapter 1, the point of departure for this study did not have a specific speed in mind, with a key outcome of the research being a well-founded investigation into the speeds that can be achieved with this rotor concept while retaining competitive torque densities.

In this chapter, the focus in on the mechanical analysis of the candidate 12 pole rotor design, in order to establish a detailed understanding of the factors that influence its mechanical capability. Features which will be explored include the selection of rotor structural materials, and the refinement of the geometry to reduce radial growth of the rotor at speed, avoiding the separation of components and manage localised stress. In order to determine the maximum operating speed of a given rotor design, or to incorporate features that will meet a particular specification, it is necessary to consider two factors that can limit the operating speed of the rotor:

i) Structural integrity of the rotor - Centrifugal loading of the rotor components will generate a stress distribution within the rotor structure. These stresses must remain below the material design stress limits (which are often specified as some fraction of the yield stress or ultimate tensile stress) in order prevent failure of the rotor during operation. The design stress usually includes some form of safety factor to allow for deterioration in material properties with ageing and thermal cycling.

ii) Rotor-dynamic behaviour of the rotor – A rotor can fail or cause other systems elements to fail though excessive vibration due to rotor-dynamic effects, and therefore the rotor must perform within certain criteria. From these factors, the practical operating safety margin, below the first critical speed of the rotor needs to be determined.

One of these two factors will ultimately determine the maximum operating speed of a rotor. It is worth noting that in many high-speed machines, it is not necessarily clear in advance of analysis which of these two factors will ultimately limit the speed. This said, rotors with short lengths and larger diameters tend to be limited by structural integrity conditions while long, thin rotors tend to run into rotor-dynamic concerns. It is worth noting that for this topology of rotor being considered, the soft

magnetic regions are limited to a small proportion of the rotor cross section, as most of the rotor is made up from a high strength, and much less dense, fibre composite. This means that the rotor weight is relatively low in comparison to a more conventional synchronous machine rotors of similar overall dimensions, and yet may well prove to have a comparable or even greater stiffness.

5.2. Rotor Construction and Manufacturing Methods

As discussed previously in chapter 1, one of the key attractions of the proposed rotor concept investigated in this thesis, is the ability to use advanced moulding methods to rapidly produce cost-effective, lightweight and high-strength rotors. The 12 pole stator core design established in chapter 4 would be manufactured in volume production from a bonded stack of laminations of non-orientated electrical steel. Each individual lamination would be cut from the sheet by a stamping process for high volume production, or from laser cutting for small to medium batch production where the large one-off capital cost of the stamping tooling could not be justified. One feature of any electrical machine stator core manufacturing process, irrespective of the cutting method selected, is the relatively poor utilisation of the sheet material from which is it cut. This is due to both the unused region within the bore of each stator, and the fit of the circular stator lamination within rectangular sheets of the starting material. One attractive feature of the design of the 12 pole machine is that the flux guides can be arranged and positioned such that they can be easily cut from the inside offcut created during the stator stamping process. In volume manufacturing, this could be done after or at the same time as the stator lamination stamping. Hence, manufacturing the flux guides out of the same material as the stator, using the same adhesive bonded stack approach, would be beneficial.

Material	Density (kg/m3)	Ultimate Tensile Strength (MPa)	Young's Modulus (GPa)
FR4	1900	250	200
Menzolit© BMC 0200	1900	30	13
NO20	7600	535	185
30% Loaded Short Glass Fibre / Polyamide Composite	2500	69.5	3.26

Table 5.1 Material properties [72], [73], [74], [75].

The key manufacturing innovation and challenge with this rotor is the method for manufacturing the non-magnetic composite hub which locates the flux guides, and retains them during rotation. As discussed in chapter 1, high-strength fibre composites were identified as the key enabler of this rotor geometry, but it was also noted that for cost reasons these would be glass fibre, and not carbon fibre based, despite their inferior mechanical properties. There are a variety of different candidate material types which exhibit high-strength, good temperature resistance (~150°C service temperature capability), low mass density and good formability.

One proposed manufacturing route is over-moulding an array of precisely positioned pole pieces with a chopped glass fibre composite in form of a Bulk Moulding Compound (BMC) or Chopped Glass Fibre Reinforced Plastic (CGFRP), to create the rotor body in a single net-shape process. As with all moulding processes involving fibre reinforcement, selecting the fibre volume fraction and length involves a trade-off between the flow characteristic and the mechanical strength of the finished composite. BMCs based on glass fibre are widely used in the automotive industry for complex moulding of high strength parts and would, from a volume production perspective, be good candidates to create the body of the rotor in this application. However, the manufacturing process requires a high pressure and precise heat to soften the compound sufficiently to allow the BMC to flow into all of the gaps. Typically, the tool is heated to around 140-165°C and the BMC is compressed at around 100 bars [76].

Using a high pressure and temperature would require the flux guides to be held firmly in place so that there could be no movement when the BMC is added. The BMC is a pre-loaded fibre paste material of relatively high viscosity. Another option would be to use the same mould and fill the rotor body with short pre chopped fibres and then add in the resin and curing agent through injection moulding. This could allow for an easier moulding process in which the material could more easily find their way between the flux guides. However, achieving an even distribution of chopped fibre throughout the entire rotor volume could be problematic.

The feasibility of manufacturing a one off prototype using a moulding approach and a BMC was discussed with composite manufacturing experts at the Advanced Manufacturing Research Centre (AMRC). It was concluded that this approach to manufacturing would not be cost effective to only produce a single prototype of this size. The tooling costs were deemed excessive for prototype manufacturing, although the concept may well be amenable to bulk manufacturing with appropriate tooling. Therefore, for a single prototype, a new manufacturing approach for the final rotor was required. The proposed approach was to use a stack of FR4 (commercial grade of woven glass-fibre epoxy composite) sheet material, with slots cut for flux guides into a pre-formed sheet using a CNC milling machine. These FR4 sheets, which are readily available commercially in sheets up to 20mm

thick, could then be bonded to form the overall rotor. A more detailed description of this approach is contained in chapter 7. This method of manufacturing would create a viable prototyping design as it does not require large and expensive tooling for manufacture. From a design and analysis point of view, given that FR4 board and BMCs have similar volume fractions of glass-fibre reinforcement (although one is a based on woven fabric which has a higher strength along the direction of the fabric ($0^o/90^o$) and the other is chopped fibre which has strength in all directions due to the randomness of the fibre orientation), the key material properties in terms of stiffness and density are very similar and hence a single set of material properties which would be representative of both approaches was used as detailed later in section 5.3.6.

5.3. Rotor Stress Analysis

5.3.1. Introduction to Stress Analysis

An essential requirement for any viable machine rotor design is that the levels of mechanical stress in its constituent materials remain below a specified threshold in order to prevent immediate or premature failure of the component. There are two key factors in ensuring that this requirement is met:

1. A reliable means of calculating localised mechanical stress throughout the rotor, with due account of various material physical properties and manufacturing factors.
2. A reliable means of specifying the maximum design stress for the materials in the rotor.

This section is concerned with the application of various stress calculation techniques to a range of rotor geometries, with a view to parametric investigation of the rotor geometry in terms of mechanical stress, hence allowing the maximum possible rotational speed to be realised for the proposed rotor topology.

5.3.2. Analytical Calculation of Stress in Various Simplified Rotor Representations

The centrifugal stress distribution in some simple component geometries can be calculated from well-established analytical expressions. Although these involve simplification of the rotor geometry, they still play a useful role in providing an indication of possible performance, and a useful check for more advanced models based on finite element analysis. In the case of the rotor type being considered in this chapter, a useful starting point is the equation for the stress in plain rotating disk of diameter *D* and mass density m_v.

$$\sigma_{max} = 0.2\, m_v \omega^2 D^2 \tag{5.1}$$

Which can be rearranged to:

$$\omega_{max} = \sqrt{\frac{\sigma_{max}}{0.2\, m_v D^2}} \tag{5.2}$$

The first calculation performed with this simple disk equation was the maximum speed for a bulk moulding compound composite rotor with an outer diameter of 170mm. A mainstream glass-fibre strand filled BMC such as Menzolit® BMC 0200 [75] has a typical density of 1900kg/m^3, a Young's modulus of 13GPa, and a manufacturer specified UTS of 30MPa. Setting a stress limit of 50% of UTS for a plain moulded disk, to provide a safety margin, yields a maximum rotational speed of 1169rad/s which corresponds to a modest 11,160rpm, which only increases to 14,116rpm for a stress limit of 80% of the UTS. For the 30% by volume fraction loaded short-glass fibre / polyamide resin composite, detailed in table 5.1, which has a density of 2500kg/m^3 and a UTS of 69.5MPa, set at a 50% stress limit as before, gives a maximum rotational speed of 1550rad/s which corresponds to 14,800rpm, and only increases to 18,640rpm for a stress limit of 80% of the UTS.

As noted earlier in this chapter, FR4 which has a manufacturer specified UTS of 350MPa may be the only viable option for a prototype because of tooling, even though it would not be suitable for cost-effective volume production. With this in mind, a 170mm diameter plain disk of FR4 operating at 50% of UTS could sustain a maximum speed of 38,120rpm.

Another useful preliminary calculation which can be performed, with the simple expression for a disk, is to apply it to the 4 pole cruciform rotor of the type shown previously in figure 3.14 in chapter 3. This is the rotor geometry which most closely represents a plain disk. Although it contains a series of scalloped regions to provide the necessary rotor magnet saliency, it was demonstrated in [77] that the factor 0.2 in equation (5.1) for this kind of rotor does not vary significantly for most salient rotors, and hence the stress predicted for the plain disk provides a good approximation to the stress in a corresponding salient rotor. In the case of the 4 pole cruciform rotor of the same outer diameter 170mm, with a density of 7600 kg/m^3 and a UTS of 535MPa [74], while taking a result at 50% of this stress gives a speed of 23565rpm.

Although the simple analytical expression of equation (5.2) provides a useful indicator of the upper ceiling on mechanical performance, the various rotor flux guide arrangements considered in this investigation contain complex geometry. The location of high density materials at the outer edges of the rotor is likely to both increase greatly the complexity of the stress distribution, and markedly reduce the maximum speeds that can be achieved. Hence, in order to model practical SYNCREL rotors, recourse to finite element analysis is necessary.

5.3.3. Finite Element Modelling of Mechanical Stress

The finite element modelling undertaken during this research was all done within the ANSYS environment. Since some of the mechanical behaviour involves three-dimensional effects, e.g. bending of rotor tie-rods, the modelling throughout was performed using three-dimensional structural models. The models were formulated and solved within the ANSYS work-bench environment and the models were all linear models (i.e. fixed Young's modulus) to help with the scale of computational resources required to calculate these designs, and to allow a full range of speed tests of the simulated design, with the exception of the adhesive bond modelling in section 5.4.5. One consequence of this linear modelling approach is that some of the calculated localised stresses may be beyond the yield or ultimate tensile stress of the materials, and yet the model will still solve and produce a result. It is important to recognise this, and set-aside such solutions when assessing viable designs.

5.3.4. Overview of von Mises Stress and Principal Stresses

The calculation of mechanical stresses using finite element analysis generates a wealth of stress information. In order to interpret the results and to use the results to aid design it is necessary to adopt some useful measures of stress to summarise the performance of a given design. Normal and shear stresses can be made up of two or three principal stresses, that represent the maximum to minimum stresses in the local coordinate system of a plane. The definition of a normal principal stress uses the normal stress calculated at an angle, θ, when the shear stress to the plane is considered as zero. This is considered to be the two-dimensional principal stress, but there is also a three-dimensional principal stress. For the two-dimensional principal stress, the normal stresses in the plane will be on the X and Y axis. In the case of three-dimensional principal stress, the normal stresses would be on the X, Y and Z axes. From [78], the expression for the 2-D principal normal stress is:

$$\sigma_{1,2} = \frac{\sigma_{11}+\sigma_{22}}{2} \pm \sqrt{\left(\frac{\sigma_{11}-\sigma_{22}}{2}\right)^2 + \tau_{12}^2} \tag{5.3}$$

Where σ_1 is the maximum and σ_2 is the minimum principal stresses when τ_{12} is considered to be zero [79]. Here, τ_{12} will go to zero when the stress element is rotated to θ_p, which is the principal angle that produces the maximum and minimum [80]. The solution resulting from the positive sign in equation 5.1 gives the maximum principle stress, while that resulting from the negative sign is the minimum. In finite element analysis, the maximum principal stress is generally used both in analysis on brittle materials, and in fatigue studies.

For ductile materials, the measure of stress which is preferred for linear static analysis is the so-called von Mises stress, which is often also referred to as the effective stress. The von Mises stress can be calculated using the 3 principal stresses calculated in a 3-D element according to:

$$\sigma_{vm} := \frac{1}{\sqrt{2}} \times \sqrt{(\sigma_1 - \sigma_2)^2 + (\sigma_2 - \sigma_3)^2 + (\sigma_3 - \sigma_1)^2} \quad (5.4)$$

The maximum to minimum principal stress is again defined as $\sigma_1 > \sigma_2 > \sigma_3$.

Ansys can give out both the von Mises and maximum principal stresses [81]. Whilst the von Mises stress analysis gives an excellent method for easily visualising the overall stresses within a structure, an example of which is shown later in the chapter as figure 5.4, it does not easily show whether stresses are tensile or in compressive in nature as visually, it only shades the colour of the stress by magnitude. However, it does allow a machine designer to visualise the locations of high stress within the mechanical design, which can then be further investigated. Both of these will be compared in this chapter with von Mises will be the initial test bench design.

5.3.5. Formulation of the ANSYS Structural Model

By exploiting the geometrical symmetry in the cross-section of the rotor, the finite element problem domain can be reduced to 1/12th of the rotor cross-section, corresponding to one rotor pole. This significantly speeds up computation and/or allows a much finer mesh to be used in the reduced problem domain. Figure 5.1 shows the symmetrical section of a single pole piece in the rotor for analysis, in this case for a design with a carbon fibre tie-rod running the length of the rotor. In order to represent the symmetry in the reduced 1/12th section model, appropriate boundary conditions must be applied to link the symmetry surface, in order to ensure that the problem domain is constrained correctly to reflect the influence of the remainder of the rotor.

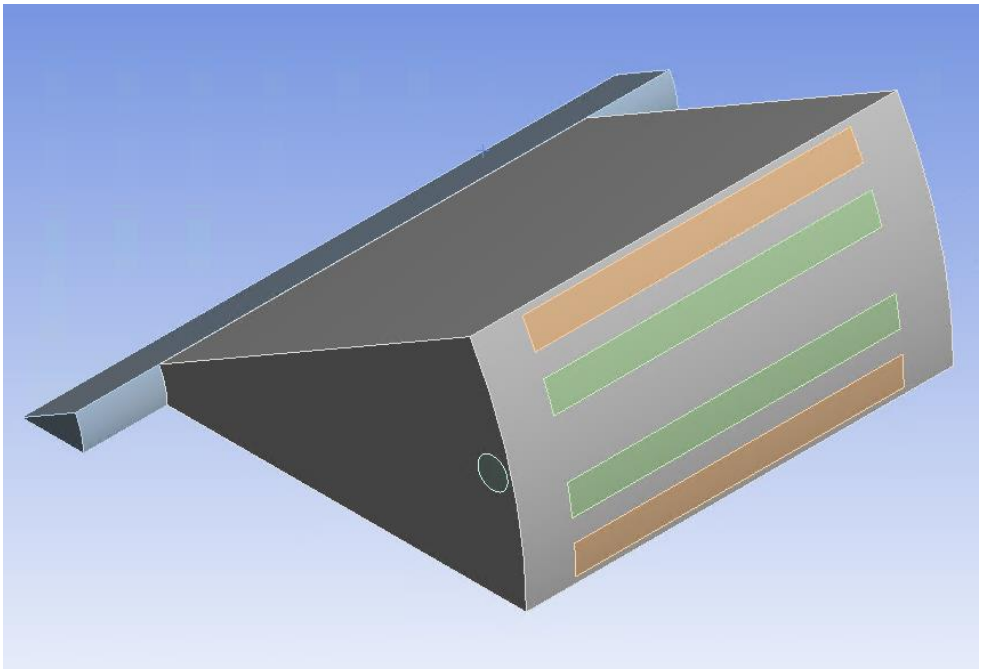

Figure 5.1 Three-dimensional rotor finite element model domain in ANSYS

5.3.6. Material Properties for Finite Element Structural Models

The rotors considered in this analysis consist of the following components and materials:

1. **Non-magnetic glass-fibre composite hub** – Options for manufacturing a glass-fibre reinforced hub were discussed in detail previously in section 5.2 of this chapter. For the purposed of finite element modelling, the composite hub was assigned an isotropic Young's modulus of 13GPa, representative of the chopped fibre composite, bulk moulded structure that is proposed for industrial manufacture. This will however mean that the results for the FR4 board are going to slightly differ from this, as the woven FR4 material is anisotropic.
2. **Array of 24 flux guides manufactured from bonded stacks of N020 Silicon iron sheets** - These laminations are bonded to each other to form a stack with Surlac 9000 adhesive, which is a coating applied during manufacture of the sheet, and is activated by heat and pressure to bond the individual cut laminations together. The manufacturer quoted Young's modulus of the material in the plane of the sheet as 200GPa, which is typical of a low alloy steel. Modelling each individual lamination and its adhesive bond would be prohibitive in terms of solution time and problem size, and it is common practice to represent the core as a bulk region with anisotropic properties. Assigning a bulk Young's modulus to a built-up stack in the direction of lamination is a well-recognised problem in the mechanical analysis of stator cores for predicting vibration and acoustic noise. Published studies [82] and [83] suggest that value of

5-10% of the in-plane modulus correlates well with observed vibration modes. Hence, for this study a modulus of 5% of the in-plane modulus of NO20 was assigned to the rotor cores, with these modelled as anisotropic regions

3. **Carbon fibre rod** – Some later developments of the rotor include a pultruded carbon fibre rods with fibres aligned along their length to act as tie-bars and reinforce the outer supporting section of the rotor hub. In the direction of the fibre, the manufacturer quoted modulus is 230GPa.

A summary of the densities and Young's modulus values used in the ANSYS modelling is shown in table 5.2.

	Young's modulus (GPa)	**Density (kg/m^3)**
Bulk epoxy / glass composite	13	1900
NO20	200 in plane 10 inter-laminar (5%)	7600
Carbon fibre rod	230	1700

Table 5.2 Key material properties for ANSYS structural modelling

5.3.7. Contact Types for Structural Modelling in ANSYS

With many simple rotating components such as shafts or solid rotor induction machines, the rotors are manufactured from a single-piece of material and there are no interfaces or contacts which need to be taken into account. The resulting problem simply involves calculating the stress in this single-body. However, for many of the rotors considered in this chapter there are numerous separate parts and hence interfaces or contacts between different materials and components of very different densities, modulus etc. Interestingly, having multiple parts in a rotor construction means that using different materials for the rotor nonmagnetic material will have different methods of holding the flux guides in place. Using a bulk moulded compound with added chopped fibres will lead to a bond forming between the flux guides and the bulk moulded compound as it cures. This is different if the nonmagnetic material is made using FR4 sheet, as these sheets do not cure and will not 'stick' under

its own effect. Therefore, using this material will require the use of a glue being added between the flux guides and nonmagnetic material. This glue will have a different strength composition to the natural adhesion of the bulk moulded compound. The different contact types in ansys will help model these differences. The means by which these contacting surfaces are modelled will have a profound effect on the mechanical behaviour of the rotor, and in particular, on the relative movement of components in the rotor. As will be demonstrated in this chapter, it is separation and relative movement within the rotor that ultimately causes as much concern as the stress levels in the materials. ANSYS provides a number of alternative representations of contact behaviour within a finite element model, as summarised in table 5.3. This sets out the nomenclature of the different representations and the normal and tangential behaviour at the interfaces. It is worth noting at this point that these models do not provide a particularly good representation of practical adhesive bonds. The various contact representations have to be mixed within a particular model to reflect the nature of the individual interfaces between materials in the model.

Name	Separation of parts allowed	Sliding of parts allowed
Bonded	No	No
Rough	Yes	No, $\mu = ?$
No Separation	No	Yes, $\mu = 0$
Frictionless	Yes	Yes, $\mu = 0$
Frictional	Yes	Yes, if Friction > μ

Table 5.3 ANSYS Contact Types [84]

The first contact model in table 5.3 is a 'Bonded' contact, which is the default contact between faces or objects in ANSYS. It does not allow any sliding or separation between mating surfaces. This is akin to a perfect bond between objects. The second contact type 'Rough' allows for separation of the parts, i.e. displacement normal to the contact surface but does not permit sliding at the interface, i.e. the coefficient of friction between two objects in a 'Rough' contact boundary is infinite so the parts will not slide over one another, only pull apart. The 'No Separation' is a contact type that does not allow the contact surface to separate from one another as is the case with 'Bonded' contact but unlike 'Bonded', this constraint does allow the contacted parts to slide with a coefficient of friction between the two surfaces of zero. This contact type only applies to face contact regions, unlike 'Bonded' that can be applied to any contact region. 'Frictionless' is a self-explanatory contact type in that it allows the contact regions to move freely in all directions, all contact regions that are defined as frictionless will be allowed to separate and slide as the coefficient of friction between the parts is equal to zero. One recognised problem with this type of contact boundary is that it can lead to nonlinear solution

types, as the contact area between regions can change over time as the simulation progresses. To aid model convergence, 'Weak Springs' should be added between regions to help better constrain the solution when this contact type is used.

The last type of contact boundary in table 2 is the 'Frictional' boundary that allows for separation of regions that are initially in contact, and also allows for the sliding of the parts across each other but with a specified 'coefficient of friction' (CoF) at the boundary. This is known as a 'Sticking' state, in which a certain shear stress is defined and when this shear stress is exceeded, the two geometries that are constrained by a frictional boundary will start to slide over each other. The coefficient of friction can be set to any positive value [84]. Whereas this may appear to be a model that is suited to most geometries and cases, it is recognised that the specification of the frictional behaviour is challenging. It is worth noting that many published studies on mechanical stress in electrical machine rotor pay little, if any attention, to the definition and significance of contact modelling despite many rotors such as permanent magnet rotors being made up of many different components. Given that the mechanical behaviour of this rotor is likely to be dominated by the behaviour of the numerous contacting regions within the rotor, a systematic study of rotor models with different contact models was undertaken.

5.3.8. Frictionless Contact Models

This contact model is in many respects the opposite of the bonded method, and will tend to be a worst case and overly pessimistic in terms of the relative motion between the different rotor parts since there is no form of join at each interface to hold them together. This is clearly not representative of a rotor manufactured by moulding, or by adhesive bonding, but an attempt was made to model the rotor with frictionless contacts for completeness. However, despite incorporating 'weak springs' into the model, and adding into the solver constraints and damping coefficients, no convergence or stability was achieved and no meaningful results obtained.

5.3.9. Frictional Contact Models

In this model of the rotor the components can separate, i.e. motion normal to the contract surface is permissible, but only allows sliding if the shear stress limit set by the coefficient of friction between the materials is overcome. The coefficient of friction is set by the user based on representative values from published data. In the absence of specific data on the coefficient of friction between a reinforced composite and the laminated pole pieces, a sensitivity approach was adopted in which a series of simulations were performed for coefficients of friction of 0.5 and 0.75. Frictional contacts do not provide a useful contact representation for the interface between the shaft and the rotor hub since radial growth of the hub bore results in detachment from the shaft. In practice, this could be avoided

by introduction of a level of interference between these components, but for the purposes of this series of frictional contact simulations, the contact was represented by a bonded contact recognising that there will some be some additional stress around the hub bore from the interference. From a practical point of view, the frictional model provides a good approximation to a rotor which is assembled as a 'dry' structure, i.e. with no adhesive applied, and is reliant on the structure to retain the various elements in place under centrifugal loading. It also provides a worst-case in terms of long-term deterioration of adhesives to the point where they provide very little useful bond strength.

5.4. Analysis of Different Rotor Concepts

5.4.1. Modelling of a Single-Piece Composite Hub with no Flux Guides

The original concept for the rotor construction was a fully over-moulded structure in which the iron flux guides were retained within a glass fibre reinforced composite hub. As shown previously in section 5.3.2, a plain cylindrical rotor of this composite material has a maximum operating speed of 38,120rpm. The first set of simulations performed were for a rotor structure consisting of only the composite regions, i.e. the iron flux guides were removed from the model with the apertures they leave behind being left as voids. This provides an indication of the ability of the composite hub to support itself against centrifugal loading. The composite hub, which includes 10mm thick continuous integral end-caps at each end was modelled by exploiting the symmetry to again reduce the problem domain to one $1/12^{th}$ of the periphery, and half the axial length. The resulting displacement of this rotor at four speeds up to 20,000rpm are shown in figure 5.2. As with all such deformation plots from finite element analysis, the graphical representation is greatly exaggerated to aid visibility of the deformation, since true-scaling would provide little visual insight into the nature of the deformations. The resulting variation with rotational speed of the maximum deformation, which occurs at the mid-point of the outer supporting section, is shown in figure 5.3.

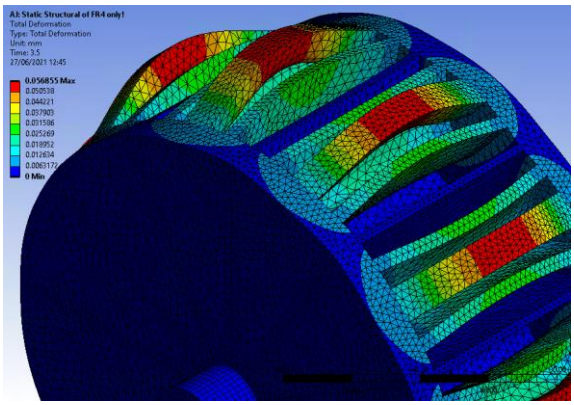

(a) 5,000rpm

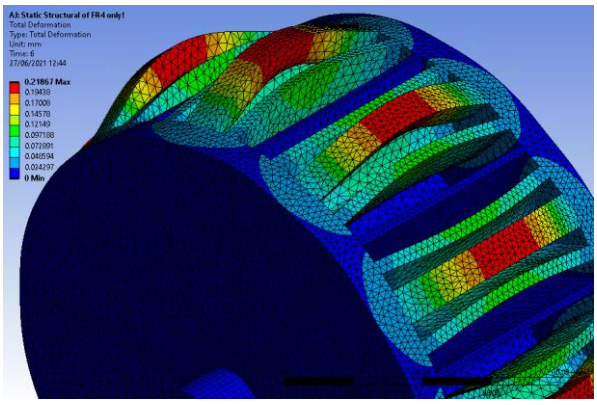

(b) 10,000rpm

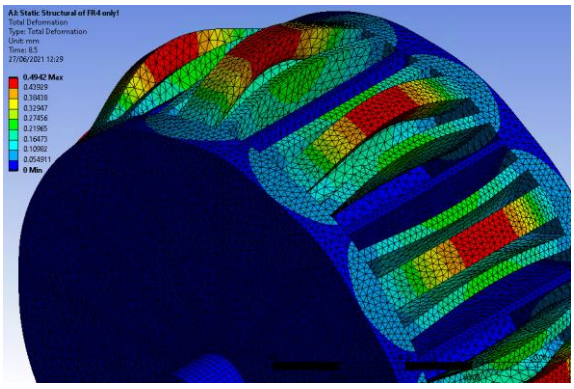

(c) 15,000rpm

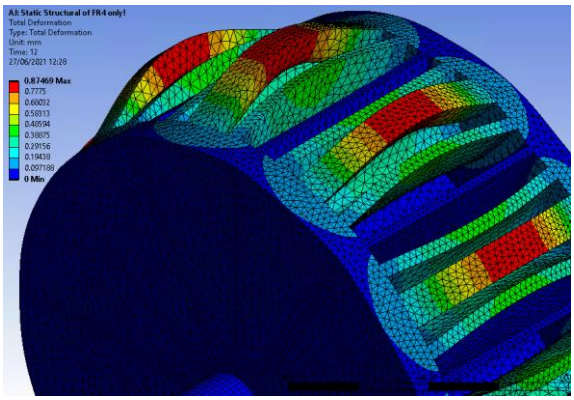

(b) 20,000rpm

Figure 5.2 Finite element predicted deformations at a series of rotor speeds for a single-piece composite structure with no pole pieces in place

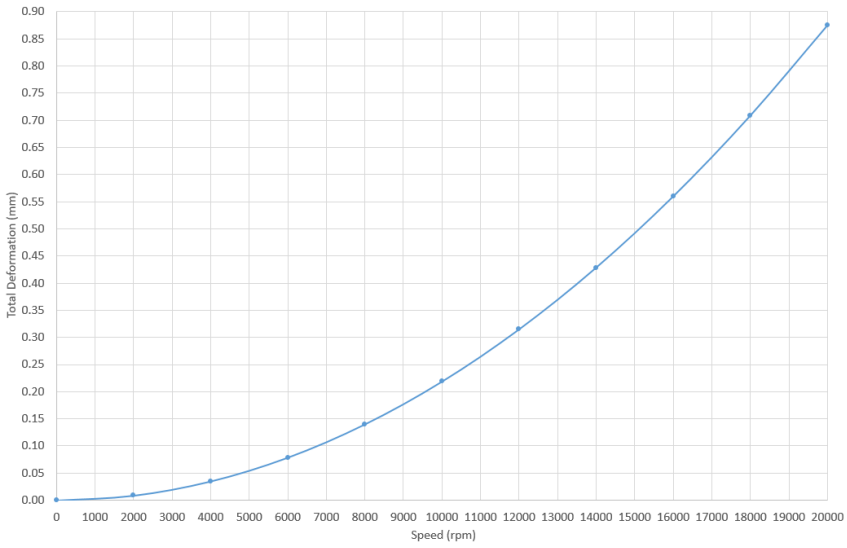

Figure 5.3 Finite element predicted variation with of the maximum deformation with rotational speed for a single-piece composite structure with no pole pieces in place

Figure 5.4 shows the predicted von Mises stress distribution in the rotor at 20,000rpm. The maximum localised stress of 205MPa (corresponds to red stress region on the scale) is very localised and located around the region in which the outer support structure joins the main end cap and is not visible in this view.

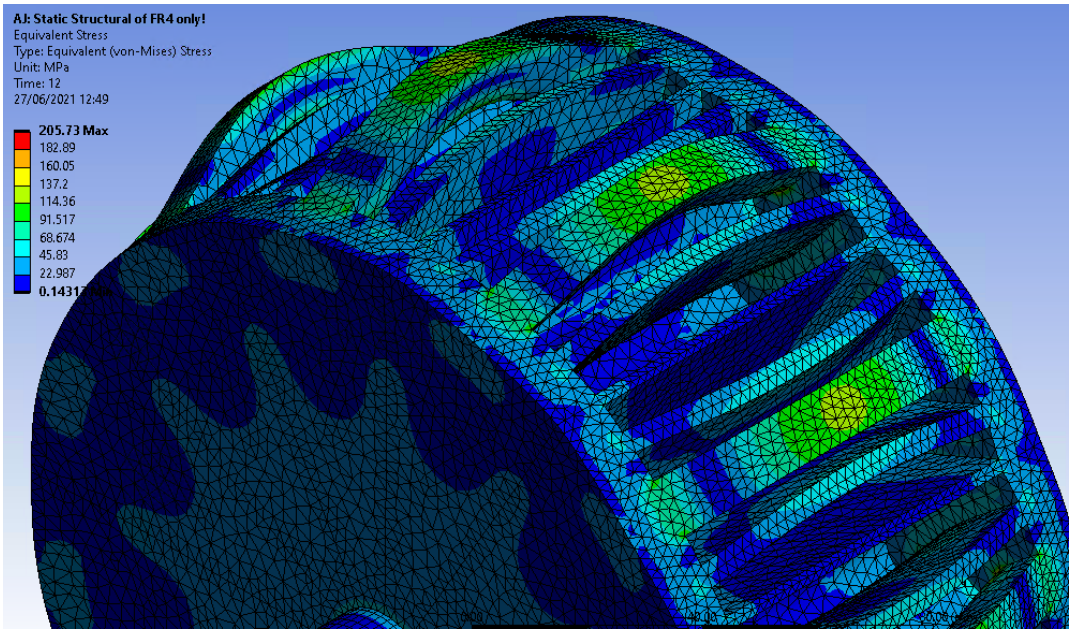

Figure 5.4 Finite element predicted von Mises stress distribution at 20,000rpm in a composite hub with no flux guides fitted

The following observations can be made from the results shown in figure 5.2 to figure 5.4:

- Even without the loading imposed by the presence of the flux guides, which would act as a dead-weight on the sections of composite rotor which retain them, the deformation in the outer supporting section which would normally retain the outer pole pieces is excessive given the 0.5mm airgap.
- The inner supporting section, which is located between the pole-pieces, is much less prone to a beam bending behaviour, as it has much larger second moment of area and is hence a much stiffer structure than the outer supporting section while also being exposed to a lower self-loading due to its reduced distance from the axis of rotation.

5.4.2. Incorporation of Tie-Rods

As noted in chapter 1, glass-fibre is the only viable reinforcement fibre for the main hub section due of cost considerations. It is clear from the predicted deformations in figures 5.2 and figures 5.3, for the single-piece composite hub, that the outer composite supporting structure is not stiff enough to

prevent a large beam-bending type deformation along its length due to centrifugal loading even when just self-loaded. One means of reducing the deformation is to introduce a tie-rod through this section using a much stiffer material. Since tie-rods are small components comprising of a few percent of the overall composite volume in the rotor, then a change to carbon fibre tie-rods with the fibre aligned along the length of the rods may well be a viable commercial proposition, and a significant boost to the stiffness of the outer supporting regions. The aligned carbon fibre tie-rod selected for this study is based on data for commercially available rods from [85].

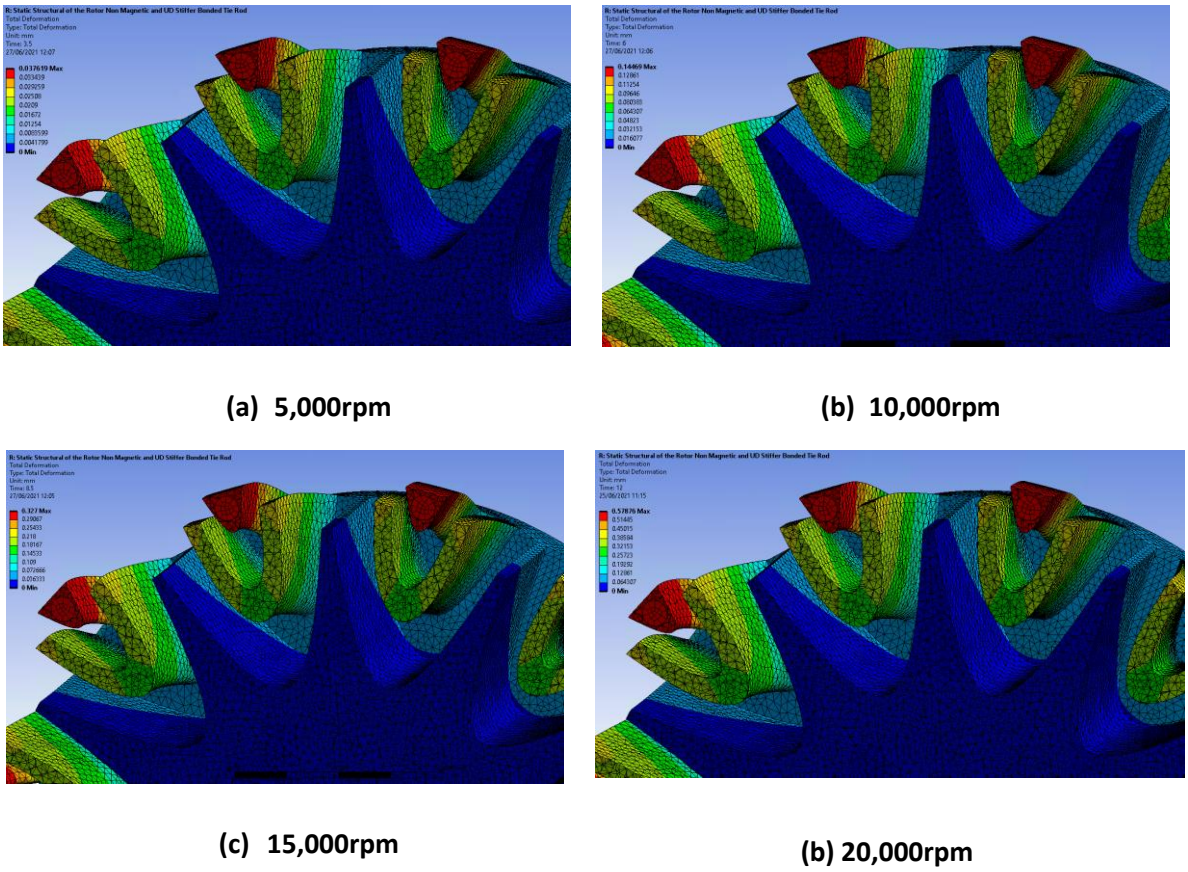

(a) 5,000rpm **(b) 10,000rpm**

(c) 15,000rpm **(b) 20,000rpm**

Figure 5.5 Finite element predicted deformations at a series of rotor speeds for a single-piece composite structure with no pole pieces in place and directionally oriented carbon fibre tie-rods in outer supporting structure

A summary of the key physical properties components of the selected carbon fibre rod compared to the glass-fibre composite / BMC was shown previously in table 5.2. It is worth noting that the main advantage of carbon fibre rods for this particular application is the greatly increased stiffness rather than the increased strength. A 6mm diameter tie-rod at each pole was fixed in place in the end-cap with an ideal bonded contact to prevent any separation from the end-cap. The exact means by which

the tie-rods would be fixed to the end-cap, e.g. flaring of the rod ends after assembly, would require further considerations.

Figure 5.5 shows the resulting finite element predicted deformations at a series of rotational speed with a cut-plane mid-way along the rotor length (noting that the geometry is symmetrical about this cut plane. As will be apparent from close inspection of the scales, the deformation is, as expected, smaller with the carbon fibre rods, e.g. 0.145mm at 10,000rpm compared to 0.219mm for the same speed with a solid single-piece composite hub. The corresponding variation in the maximum deformation with rotor speed is shown in figure 5.6.

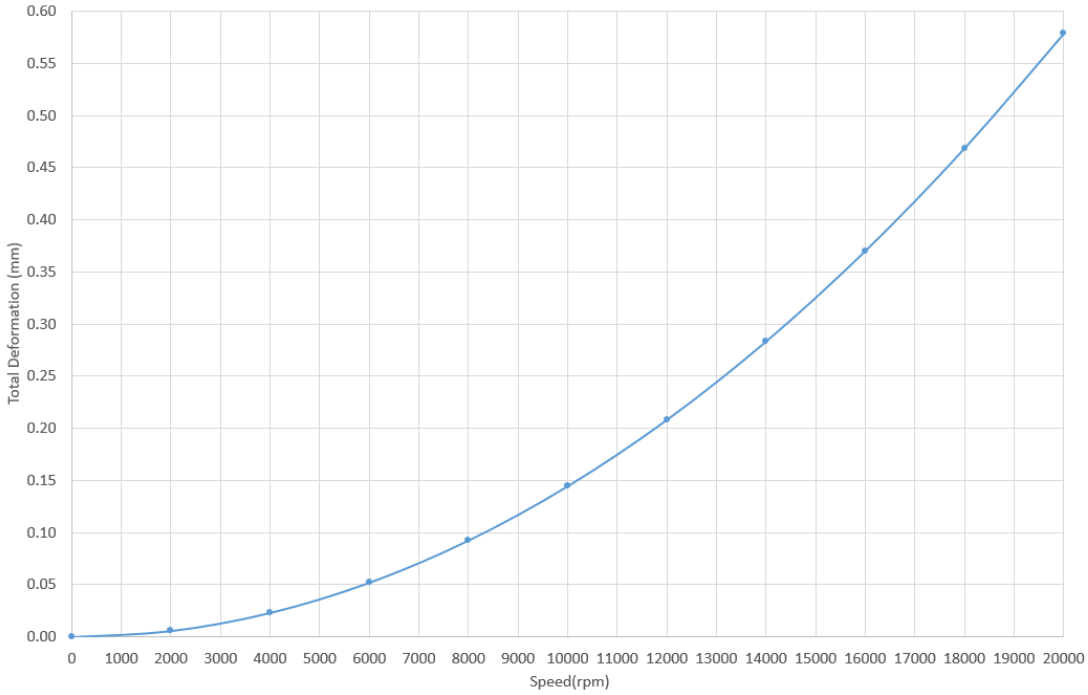

Figure 5.6 Finite element predicted variation with of the maximum deformation with rotational speed for a single-piece composite structure with no flux guides in place and directionally oriented carbon fibre tie-rods in outer supporting structure

As was the case with the solid single-piece composite hub, the problem area remains deformation of the outer supporting limb, which would retain the outer flux guide if it was in place, with an already excessive deformation. The carbon fibre tie-rod is effective up to a point in both reducing deformation and stress within the remainder of the hub, but the benefits are modest and largely a consequence of the limited contribution of the 6mm diameter rod in terms of second moment of area (a critical factor in beam bending) despite is high stiffness. Hence, even with carbon fibre tie-rod stiffening, the external support is still unlikely to be able to provide useful retention of the outer flux guide. Figure 5.7 show the variation in stress throughout the rotor at 20,000rpm from which it can been seen that

the maximum stress is on the outer edge of the carbon fibre tie-rod. Figure 5.8 shows the corresponding stress variation in the tie-rod alone, in which the effect of the large end-cap is evident in resisting deformation over the last 10mm or so at each end of the tie-rod.

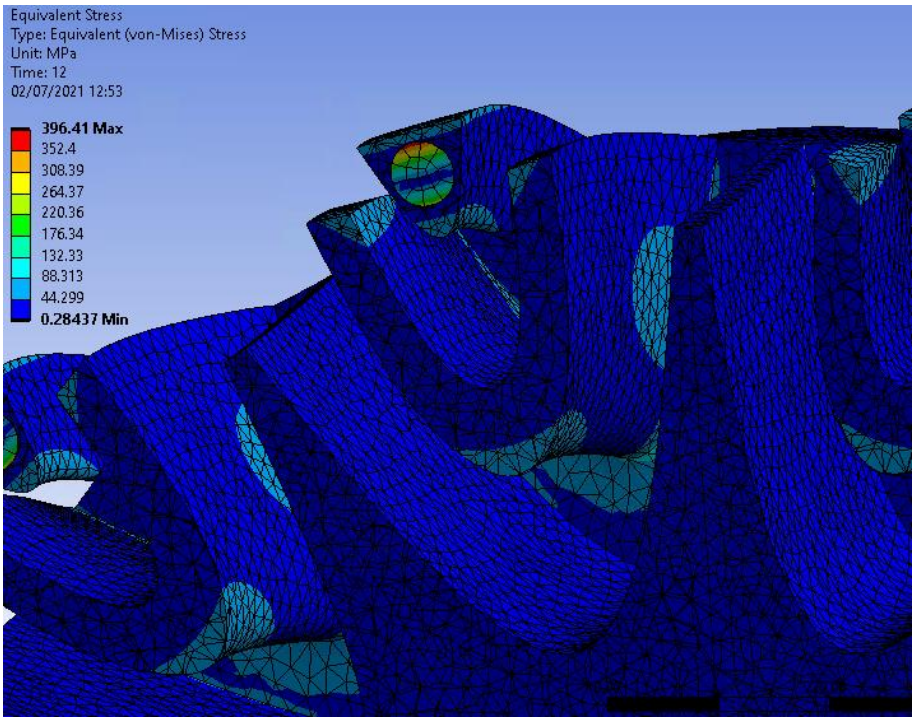

Figure 5.7 Finite element predicted von Mises stress distribution in the rotor at 20,000rpm

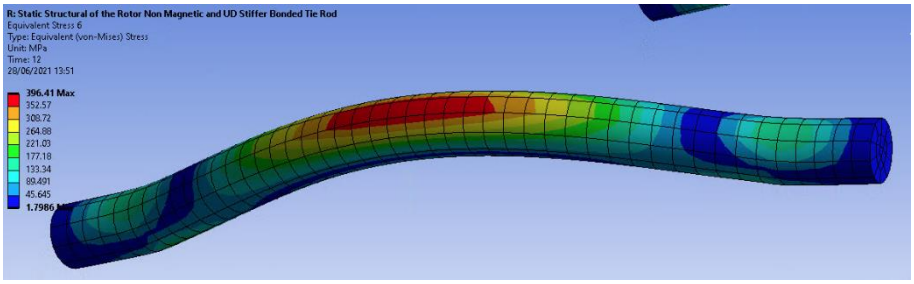

Figure 5.8 Finite element predicted stress in the carbon fibre tie-rod at 20,000rpm

5.4.3. Modelling of a Complete Rotor with an Ideal Bonded Contact Model

A rotor including the flux guides, tie-rods and shaft, was initially modelled with every contact interface set as bonded contacts, which would be the default setting in ANSYS. This model provides a representation of a best case scenario, where all the components of the rotor are perfectly joined and unable to move relative to each other. The rotor in effect behaves like a single body, albeit with density and modulus variations throughout the structure. Figure 5.9 shows the predicted von Mises stress distribution on the surface of the rotor at 20,000rpm on a cut-plane which is located at the centre of the rotor. The mesh was initially set to have elements no bigger than 0.1mm, this value required a lot

of computational analysis to solve and was too fine for the model. The mesh was brought up to elements smaller than 2mm, as this was close to the boundary where the results were affected by the mesh being too large, and helped in the length of time it took to solve the model.

Figure 5.10 shows the corresponding deformation of the rotor (scaled to make it visible) at 20,000rpm which shows a maximum deformation of only 106 microns. It demonstrates that since the rotor elements are ideally bonded and act as a single-piece structure, the deformation of the outer supporting structure is greatly reduced compared to the hub without the flux guides despite the centrifugal loading of the flux guides. Despite being an idealised representation of the rotor, these result demonstrate that finding a method for making the rotor behave as close as possible to a bonded single part is likely to be productive in terms of maximising the rotational speed at which the rotor deformation of localised peak stress crosses a threshold.

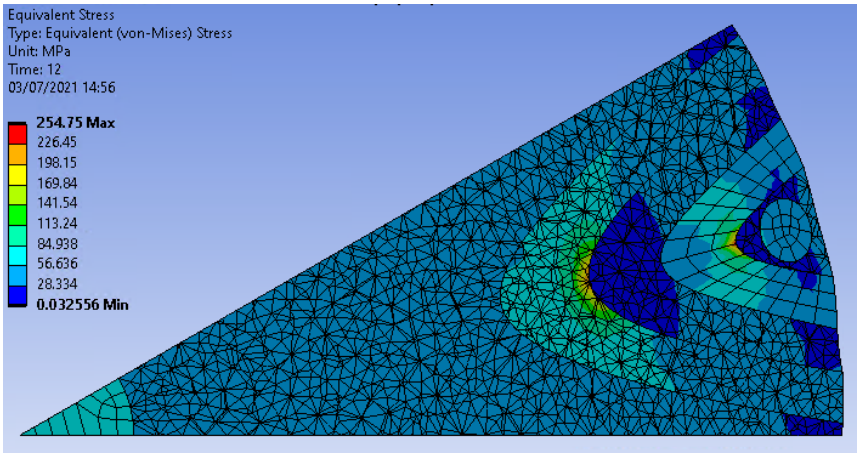

Figure 5.9 Finite element predicted stress distribution in a fully bonded model of the rotor at 20,000rpm

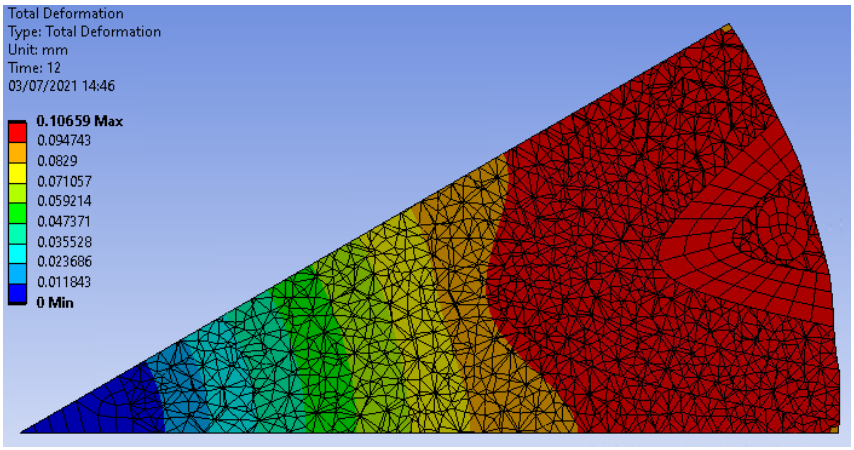

Figure 5.10 Finite element predicted rotor deformation in a fully bonded model of the rotor at 20,000rpm

5.4.4. Modelling of a Complete Rotor with Frictional Contacts

Although the ideal bonded model is section 5.4.3 is useful in terms of understanding the likely upper limit on performance for a rotor which acts as a single-piece, it is not representative of an actual rotor in which the contacts between different regions would allow some degree of relative motion under load. The first non-ideal case considered was the use of frictional contacts on all surfaces. As noted previously, this type of contact surfaces offers no opposition to normal separation but does generate a reaction force governed by the coefficient of friction to oppose slipping. As a consequence, this model resembles a rotor in which the flux guides are retained solely by their captive location in the hub rather than with any adhesive bonds which would oppose separation. As noted in the earlier discussion on friction contacts, it also provides a useful worst-case for adhesive that has degraded over the service life to the point where it offers little resistance to contact separation.

Figure 5.11 shows the resulting variation in the finite element predicted deformation for a model with ideal bonded carbon fibre tie-rods and central shaft and frictional contacts (coefficient of friction of 0.75) on all other surfaces. As would be expected, the deformations observed with the flux guides in place are much larger than the corresponding deformations of the composite hub and tie-rods with no flux guides, e.g. deformations of 2.57mm and 0.578mm respectively at 20,000rpm. It is worth noting that these models are based on linear analysis (i.e. fixed value of Young's modulus) and hence predicts stress and strain levels which may well be beyond failure in practice. Even setting aside concerns over stress levels, the deformations are far greater than could be tolerated from the point of view of the airgap clearance of 0.5mm between the rotor and the stator. The deformation plots in figure 11 demonstrate some interesting features in terms of understanding the shortcomings of a rotor design that relies on fit and captive element with frictional contacts:

- Even at the lower speed of 5,000rpm, the load on the outer supporting structure cause significant bending and separation between the outer flux guide and inner U-shaped composite region. There is also evidence of separation between the inner flux guide and the main section of the hub
- The outer flux guide bends significantly along its length to remain in contact with the outer composite support over its entire length, despite the significant curvature and deflection of the support. This is useful in terms of avoiding point loading at a point of separation if the flux guide were much stiffer than the outer support.

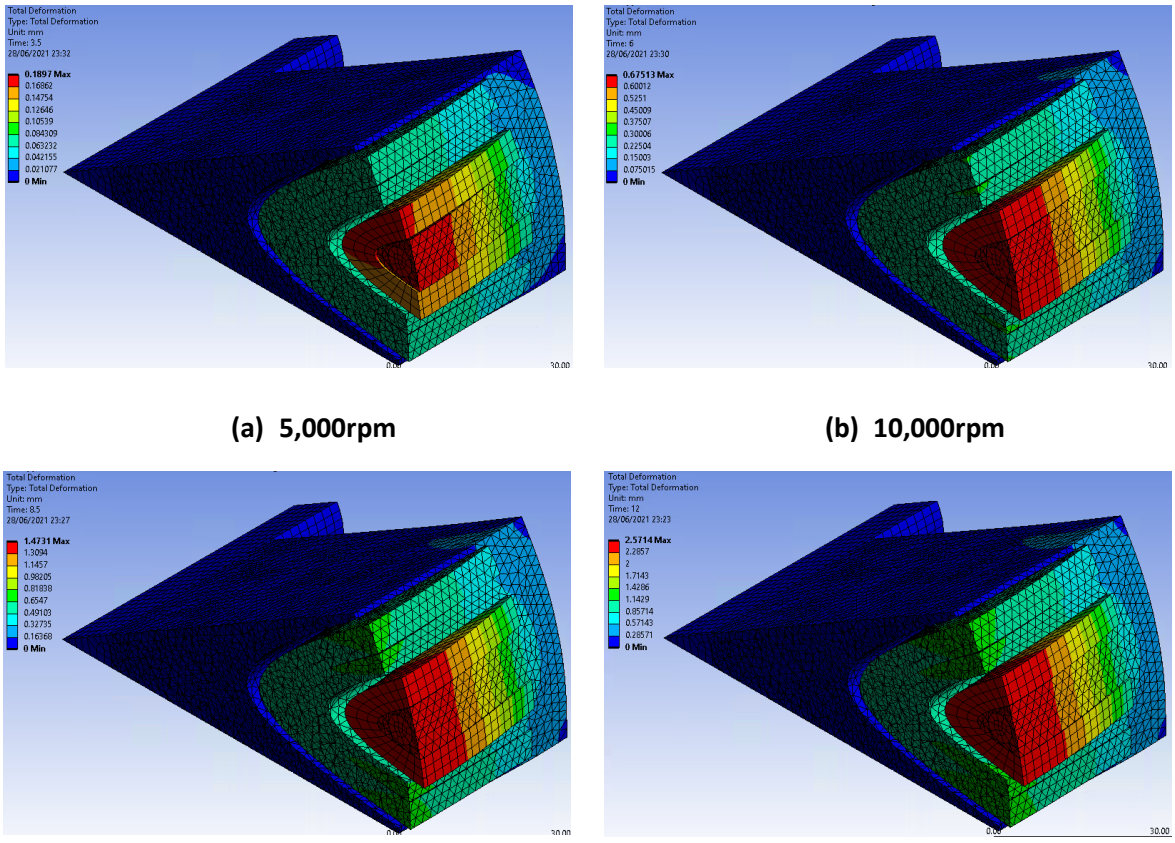

(a) 5,000rpm **(b) 10,000rpm**

(c) 15,000rpm **(b) 20,000rpm**

Figure 5.11 Finite element predicted deformations for a composite hub with flux guides and tie-rods– model based bonded tie-rods and central shaft and frictional contacts on all other surfaces (coefficient of friction 0.75)

Figure 5.12 shows the corresponding variation in deformation across the full-speed range, from which it can be seen that the airgap is breached at a speed of ~8,400rpm and the rotor would contact the stator bore around this speed.

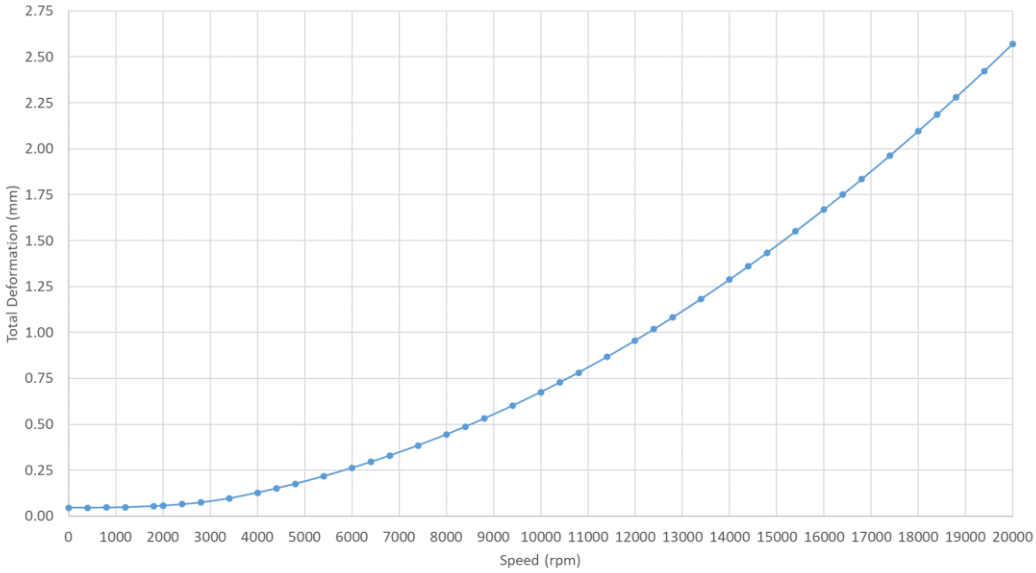

Figure 5.12 Finite element predicted variation in deformation with rotor speed for a coefficient of friction of 0.75

The corresponding von Mises stress plots for the particular cases of 5,000rpm and 20,000rpm are shown in figure 5.13. As will be seen, there are raised stress regions visible in these plots within the carbon fibre tie-rod which is evidence of its usefulness in stiffening the outer support and at the point at which the outer support blends into the end-cap. The maximum stress levels shown in scales, i.e. up to 2296MPa in the 20,000rpm case, are at points which are not visible, but are at the interface between the outer flux guides and the outer supports at a location adjacent to the end-cap region.

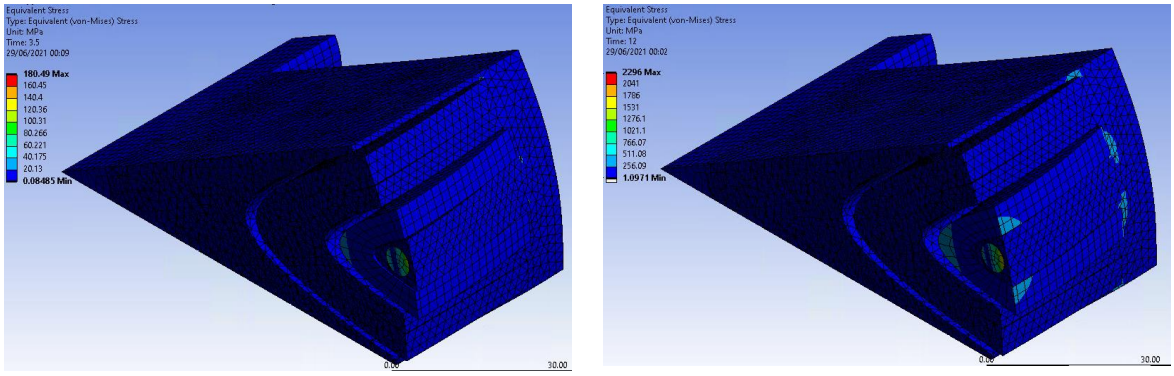

(a) 5,000rpm **(b) 20,000rpm**

Figure 5.13 Finite element predicted von Mises for a composite hub with flux guides and tie-rods – model based bonded tie-rods and central shaft and frictional contacts on all other surfaces (coefficient of friction 0.75)

The predicted variation in the von Mises stress with rotor speed is shown in figure 5.14. Although the main glass-fibre composite could sustain the peak localised stress of 180MPa at 5,000rpm in figure

5.13(a) (manufacturer specified UTS is ~500MPa), it would fail at around 9,000rpm and would result in a design maximum speed of ~6,000rpm if a safety factor of 2 were applied to limit the stress loading to 50% of the UTS, i.e. 250MPa. As shown previously in figure 5.12, at 6,000rpm the predicted deformation of the rotor outer surface is ~0.25mm and although this would halve the running airgap it would not result in contact. Hence, in this case with a safety factor of 2.0 applied to the stress limit, the design pinch-point is stress and not closure of the airgap. However, with a less conservative safety factor, the deformation becomes the pinch-point on the design. In either case, this rotor construction with a coefficient of friction of 0.75 has an upper speed limit of around 6,000rpm.

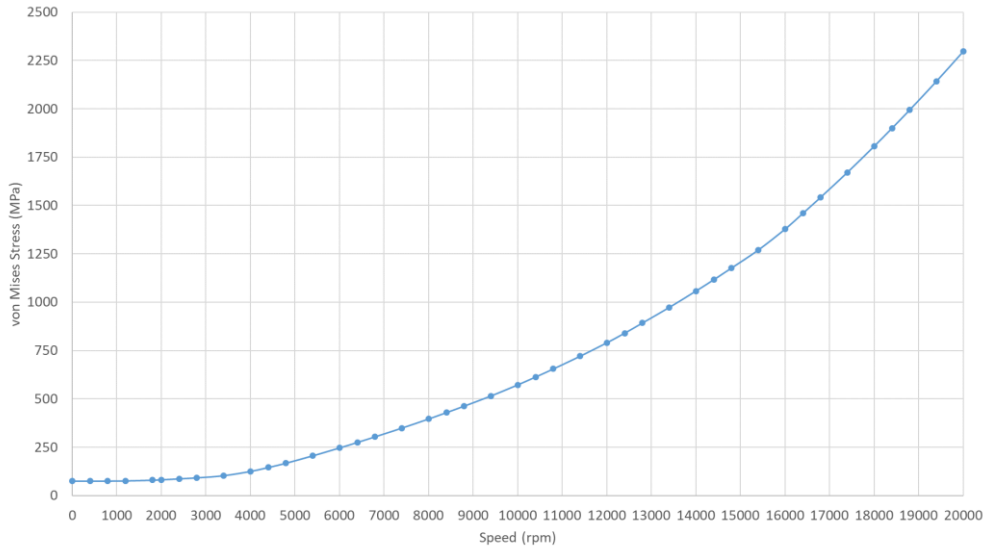

Figure 5.14 Variation with rotor speed of the predicted maximum localised stress in composite hub

The same modelling was taken with a reduced coefficient of friction of 0.5. Figure 5.15 shows the predicted deformation with this reduced coefficient of friction for the particular speed of 10,000rpm. This results in a near maximum deformation of 0.681mm as compared to 0.675mm for a corresponding speed with a coefficient of friction of 0.75 and shown previously in figure 5.11(b). This insensitivity to the coefficient of friction demonstrates that frictional sliding is not of major significance in determining the overall deformation, which is unsurprising given that bending of the outer support and separation of components are the primary causes of the deformation.

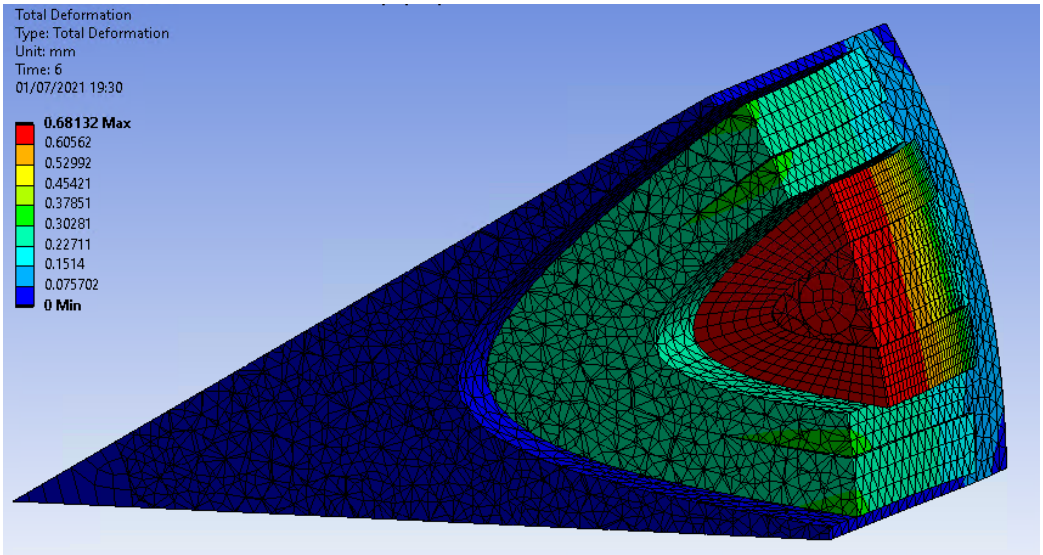

Figure 5.15 Finite element predicted variation in deformation with rotor speed for a coefficient of friction of 0.5

5.4.5. Modelling of Adhesive Bonds with a Cohesive Zone Model (CZM)

As noted at the conclusion to the frictional model analysis, separation of the rotor components from each other is the major contributor to deformation of the rotor. The use of a high strength adhesive to achieve strong and stiff bonds between the different component should offer a route to reducing deformation and stresses within the rotor in closing the gap to the performance predicted with the original perfectly bonded model. The modelling of realistic adhesive bonds in finite element models is far from straightforward, with the most common approach being the adoption of so-called cohesive zone models. A cohesive zone model, which is commonly referred to as a 'CZM' model, is an additional mathematical feature that can be added to a bonded contact interface between two regions, and offers a more realistic representation of the separation behaviour of adhesively joined materials. This is achieved by introducing a model of the fracture zone between two connected parts. In this way, the CZM model can behave as a strong adhesive holding the rotor parts together [86].

A CZM model was set-up using datasheet properties for Permabond TA439 [87]. This is a toughened and non-corrosive acrylic adhesive that has a rapid contact time of between 20-40 seconds. For full strength, the material should be left for 24 hours to cure, but it will set in around 75 seconds. This is representative of a high performance adhesive, but has the key advantage of having published data values for integration into a CZM model. A summary of the key physical properties for this material is shown table 5.4 which also contains the manufacturer supplied CZM parameters. Figure 5.16 shows the resulting stress versus displacement characteristic generated by using these parameters.

Properties of Outline Row 5: CZM Material

	A	B	C	D	E
1	Property	Value	Unit		
2	Fracture-Energies based Debonding				
3	Debonding Interface Mode	Mixed			
4	Tangential Slip Under Normal Compression	No			
5	Maximum Normal Contact Stress	25	MPa		
6	Critical Fracture Energy for Normal Separation	15	mJ mm^-2		
7	Maximum Equivalent Tangential Contact Stress	20	MPa		
8	Critical Fracture Energy for Tangential Slip	15	mJ mm^-2		
9	Artificial Damping Coefficient	1E-08	s		

Table 5.4 Key physical properties and CZM parameter models for Permabond TA439

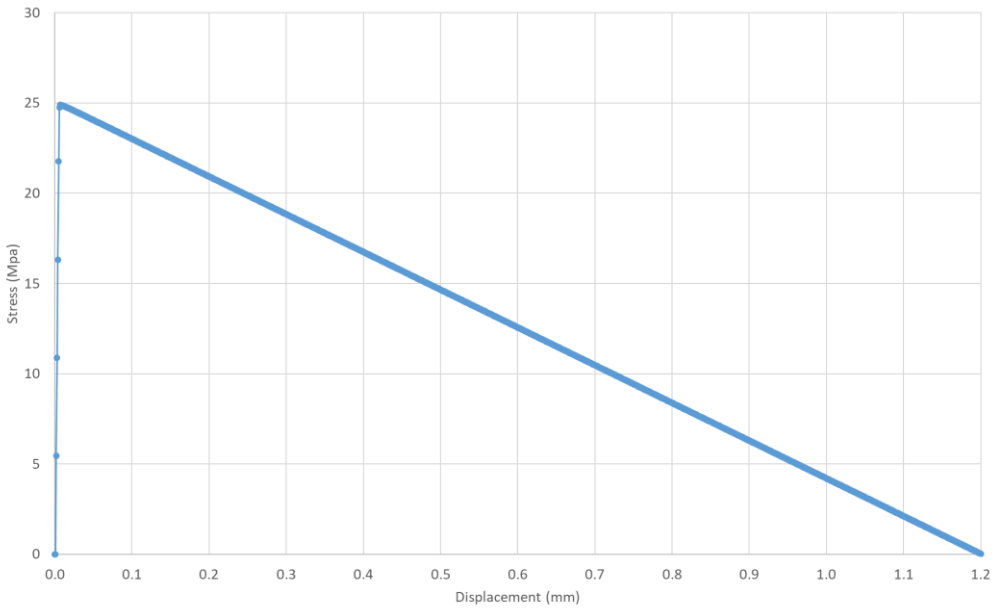

Figure 5.16 Stress versus displacement characteristic for CZM model of Permabond TA439.

The CZM characteristic assigned to the Permabond TA439 allow an adhesives joint of thickness 0.1µm while still providing some useful stiffness, but eventually the maximum stress limit is exceeded and the adhesive fractures. The mode fracture in this contact representation involves de-bonding of the faces. The adhesive at the interface needs to be defined as a Fracture-Energies based de-bonding material, and is assigned the model parameters shown previously in table 5.4. Once the adhesive material has been fully defined, the contact is implemented as a bonded contact which is set as a 'Pure Penalty' system in order for the CZM to take effect at the contact. The resulting contact de-bonding regions will sustain a level of normal stress up to a specified level for the particular adhesive employed, beyond which the two element held in a CZM will fracture apart as though the adhesive holding them together has failed.

5.4.6. CZM Simulation of the Baseline 12 Pole Rotor with no Tie-Rods or End-Caps

The first simulation using a Permabond TA439 CZM representation of the contacts between the flux guide did not include tie-rods and rotor end-caps in order to provide a better insight into the influence

of the stiffness and strength of the adhesive bonds without the complicating factor of the tie-rod reaction forces and bending. A cross-section through this simplified rotor model is shown in figure 5.17.

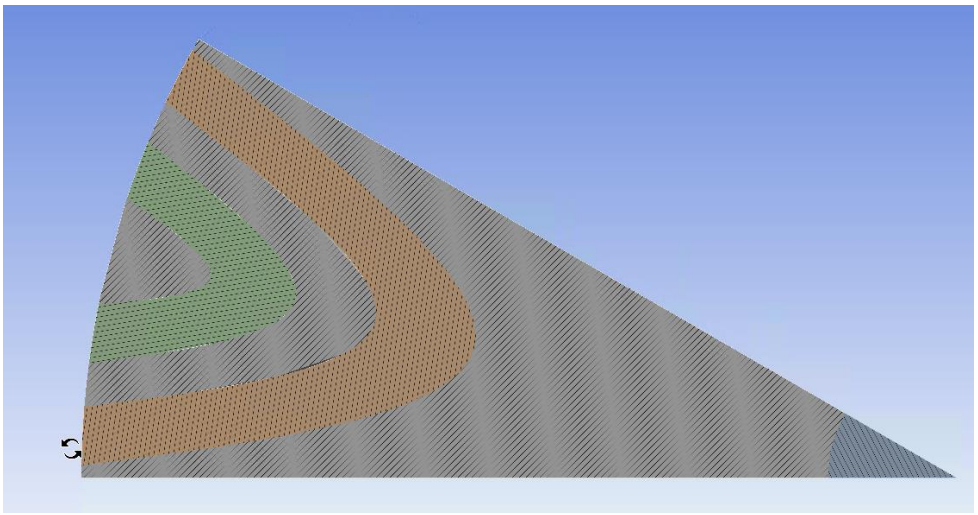

Figure 5.17 Rotor geometry with no tie-rods for initial CZM modelling.

This model allows the flux guides and/or the intermediate U-shaped section of the composite hub to come away from the main central section of the hub if the CZM model limits are exceeded. In this model there is potential for the components to come apart and for the simulation to fail to produce a viable solution at and beyond a certain speed. A series of solutions was therefore undertaken with the rotor speed varying from standstill with an initial target speed of 20,000rpm. For this particular combination of geometries and adhesive properties, the finite element solver failed to produce results beyond 18,400rpm since the flux guides become completely detached, and the integrity of the rotor is entirely lost. Figure 5.18 shows the resulting predicted deformations at 4 discrete speeds up to 18,400rpm. As will be apparent, there is no evidence of separation at the adhesive bonds at 5,000rpm or 10,000rpm but there is partial separation between the inner flux guide and the hub at 15,000rpm, with complete separation at 18,400rpm.

There are many measures of stress which could be used to summarise the behaviour of the adhesively bonded rotor as the speed is increased. A useful measure which was adopted in this case is the maximum stress at the interface between the inner most section of the inner flux guide and the composite hub, as this is likely to be the location of the highest stress on a bonded interface, and the first point of failure. As an example, figure 5.19 shows the stress distribution at the contact surface for 12,000rpm from which a maximum value of 21.6MPa can be extracted. This is a comparable value to the stress in the adhesive properties at which fracture begins to have an influence.

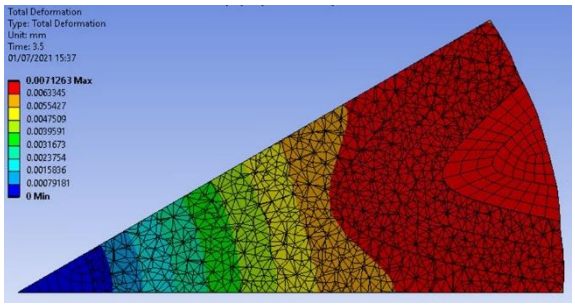

(a) 5,000rpm

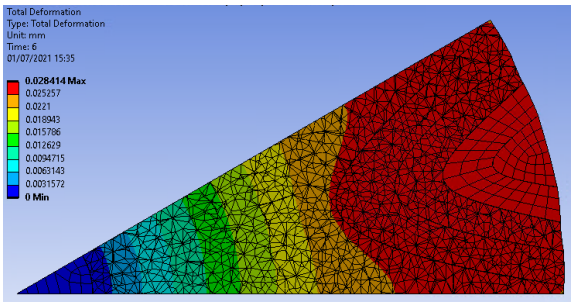

(b) 10,000rpm

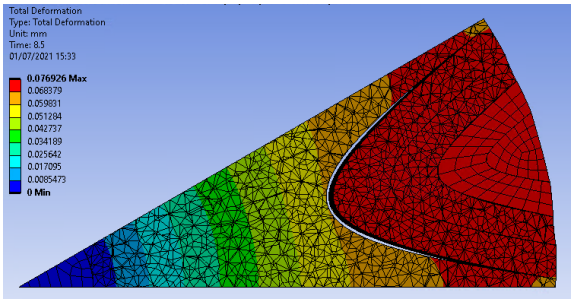

(c) 15,000rpm

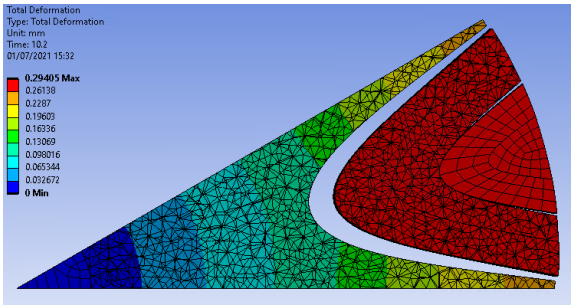

(b) 18,400rpm

Figure 5.18 Predicted deformation in a rotor with adhesively bonded flux guides but no tie-rods or end-cap regions

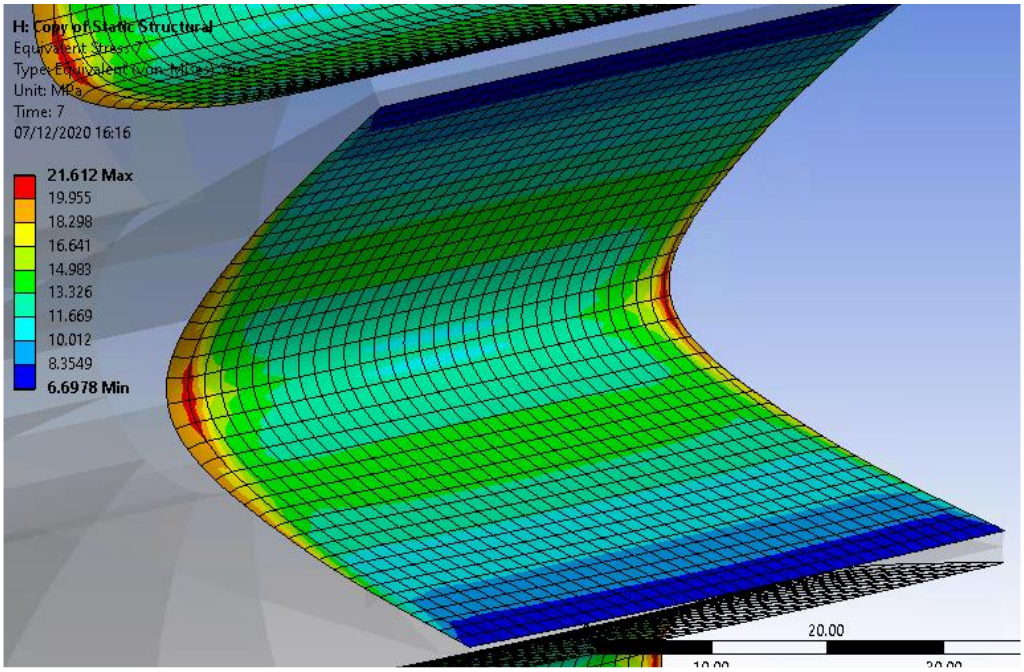

Figure 5.19 Predicted von Mises stress at 12,000 rpm on the interface between the inner flux guide and the main rotor hub

Figure 5.20 shows the variation in the maximum stress level at the CZM contact interface between the hub and the inner flux guide as the rotor speed is increased. As will be noted, the increments in speed are not exactly uniform, this being a consequence of the auto-time stepping feature within ANSYS which adjusts the time interval to aid convergence (and hence the speed intervals when a constant ramp rate is applied). As will be apparent, the behaviour looks predictable up to ~13,000rpm with the magnitude of the stress increasing with the square of speed, behaviour which is similar to that expected of a single-piece disk. However, beyond 13,000rpm the stress in this region starts to deviate from this straightforward behaviour, indicating the onset of some levels of adhesive failure. Beyond around 14,000rpm, the flux guide is detached from lower end of the U-shaped void in the hub in which is sits but remains partially attached via the sides.

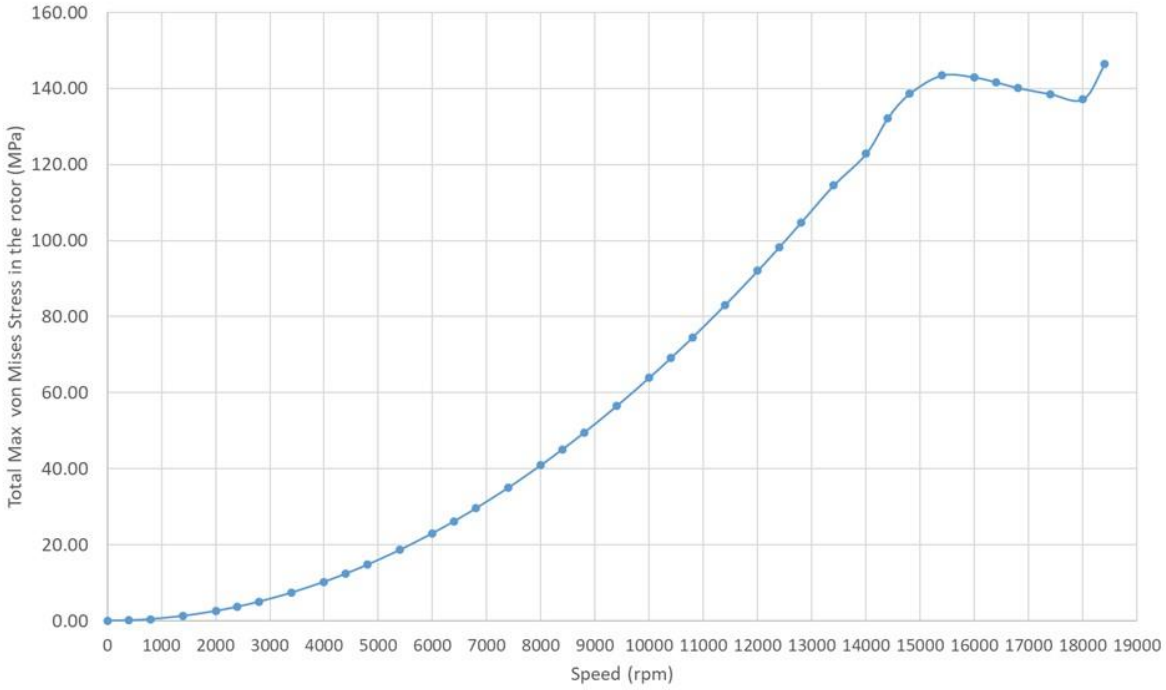

Figure 5.20 Finite element predicted variation with speed of the von Mises stress in the composite hub at the contact interface with the bottom of flux guide

The corresponding variation in the deformation of the outer surface of the rotor is shown in figure 5.21. As will be apparent this starts to show a marked increase in deformation beyond 14,000rpm due to the partial failure of the adhesive bond between the flux guide and the U-shaped void in the hub in which it sits.

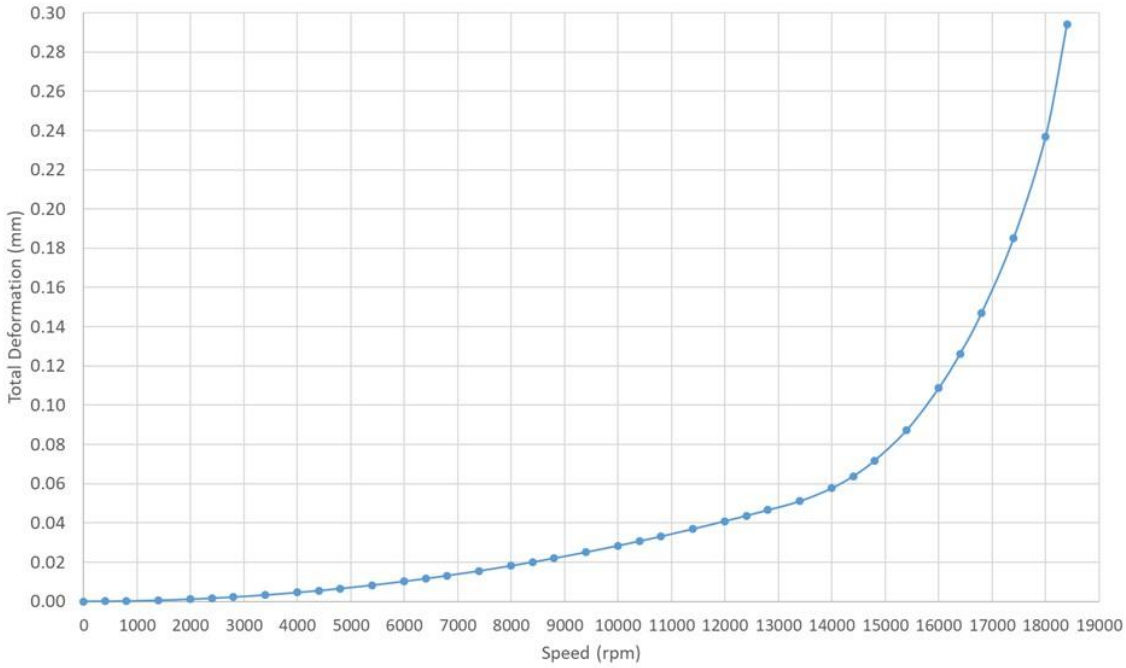

Figure 5.21 Finite element predicted variation with speed of the overall deformation at the outer surface of the rotor

This analysis demonstrates both the benefits of adhesive bonding in reducing the deformation compared to an un-bonded rotor, at least up to the point at which the adhesive fails. It also shows the insight which can be obtained into detailed adhesive fracture behaviour from finite element analysis with CZM contacts.

5.4.7. Rotor with Adhesive Bonding of all Flux Guides and Ideal Bonded Carbon Fibre Tie-Rods and Shaft

A series of simulations were performed for a rotor which combined the carbon fibre tie-rods with adhesive bonding of the flux guides. This rotor included the same 10mm thick end-caps to retain the tie-rods. Figure 5.22 shows the finite element predicted distribution of deformation in the rotor at a series of discrete speeds, in this case only up to a maximum of 16,000rpm since solutions beyond this point did not converge due to complete separation at the adhesive interface despite the external support still retaining the flux guides. It is interesting to note that the deformation of the rotor outer diameter with the carbon fibre tie-rods is marginally lower than the corresponding simulations of section 5.3.6 for the plain CZM model with no tie-rods or end-caps, e.g. at 10,000rpm the deformations are 27.7 and 28.4 micron respectively. Hence, the tie-rods offer modest benefit on this measure. As will be apparent, there is evidence of some separation of the inner flux guide from the main central hub in the 15,000rpm plot. The corresponding variation in the deformation over the speed range 0-16,000rpm is shown in figure 5.23. As shown, there is some deviation in individual

points from a smooth curve. This is due to the allowable convergence criteria and some difficulties in achieving convergence at some points. As will also be apparent, there is a marked up-turn in deformation for speed of ~15,000rpm and above.

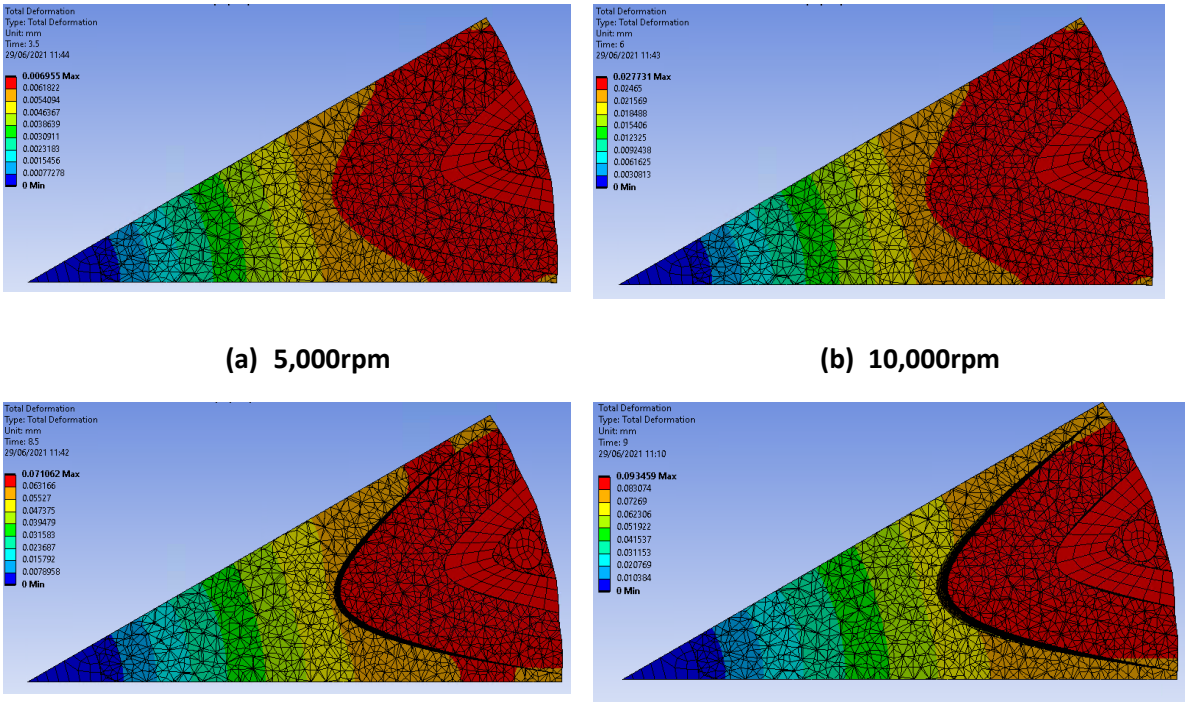

(a) 5,000rpm **(b) 10,000rpm**

(c) 15,000rpm **(d) 16,000rpm**

Figure 5.22 Finite element predicted deformations in the at a series of discrete speeds – section taken at mid-point of rotor axial length

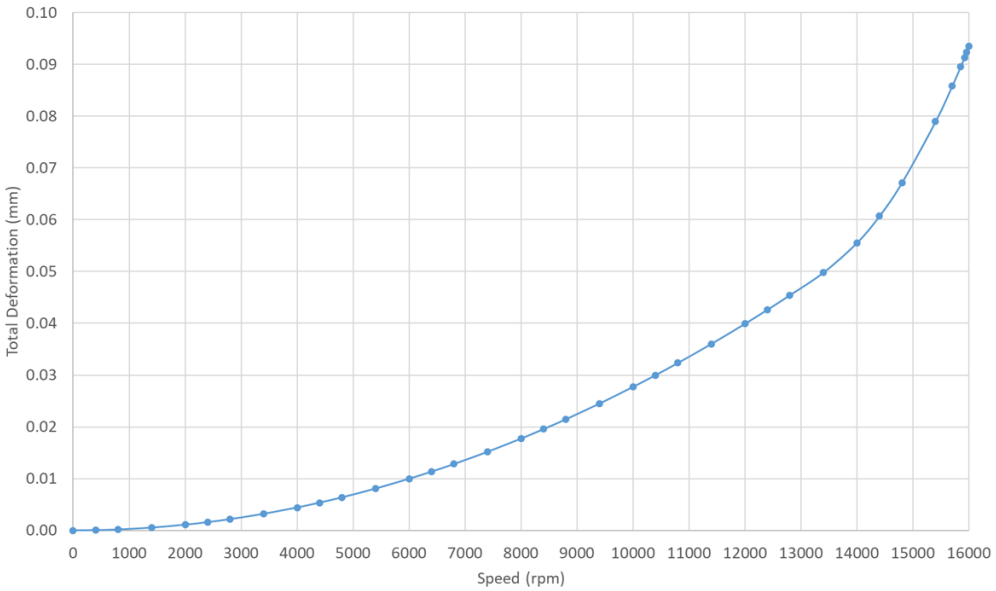

Figure 5.23 Finite element predicted variation of total deformation with rotor speed

Figure 5.24 shows the predicted von Mises stress distribution at 16,000rpm with a peak localised stress of 182MPa, which demonstrates that this rotor design is well within the stress limits of composite hub, the flux guides and the tie-rods. Indeed, the deformation of the rotor is only 94 microns at this speed, but as shown in figure 5.22, there is clear failure of the adhesive bond between the inner flux guide and the main hub and hence 16,000rpm is not a viable operating speed.

As was the case with the rotor considered previously in section 5.4.6, in which the flux guides were bonded but did not include a tie-rod or end-caps, a useful indication of mechanical performance is the maximum value of the stress at the contact interface between the inner flux guide and the main hub. The variation in localised stress at this location, with rotor speed, is shown in figure 5.25 from which it is evident that at speeds beyond ~13,000rpm there is a discernible change in the slope of the characteristic, which is indicative of some separation. This is consistent with the deformation plot at 14,000rpm which shows the onset of separation and the fact that the stress level at the adhesive bond location in figure 5.25 at this speed is ~20MPa which is the limiting stress of the CZM model of the adhesive.

On the basis of this analysis, this rotor is capable of operation up to 12,000rpm with no safety factor applied. However, some level of speed de-rating would be required in practice to allow for bonding imperfections, ageing effects etc. Adopting a commonly used safety factor of 2 on the stress applied to the most critical element, i.e. the adhesive bond on the inner flux guides, allows the maximum speed to be determined from figure 5.25. In this case, a design stress of 10MPa results in a maximum speed of 9,500rpm as shown in figure 5.25.

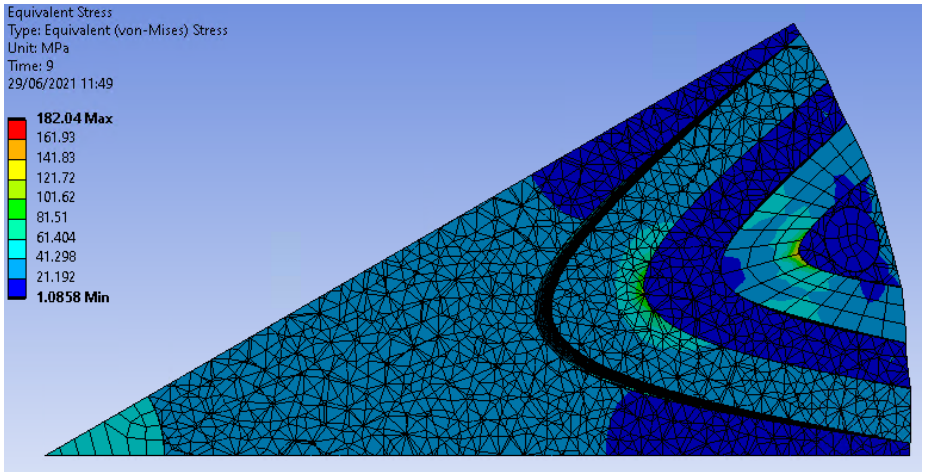

Figure 5.24 Finite element predicted von Mises stress distribution at 16,000rpm

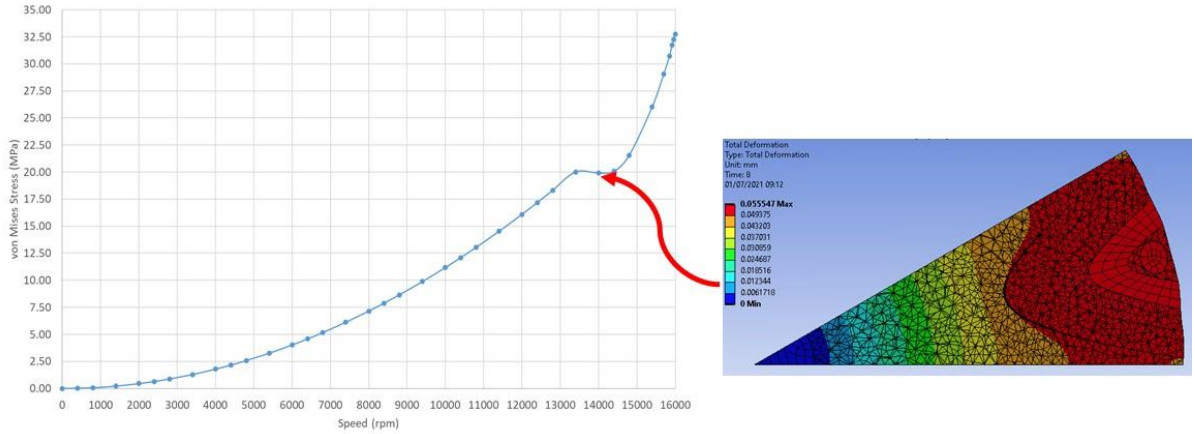

Figure 5.25 Finite element predicted von Mises stress at the contact interface between the base of the flux guide and main hub

5.4.8. Modification of Flux Guides Geometry to Include Captive Projections

The flux guides considered up to this point have been based on the electromagnetic derived designs established in chapter 4. One feature of these flux guides which might be important in terms of displacement within the rotor during rotation is the absence of any geometrical feature which keys the flux guide into the main hub section. To explore whether such features would be beneficial a series of further simulations were performed. The initial analysis that took place in this section before this style of key shape was adopted took on a fir tree/screw fitting shape. However, these designs were rejected early on due to electromagnetic issues (leakage between poles) and mesh/analysis errors that caused the solutions to be invalid or to not even start/finish. The first modification was the incorporation of circular projections at the base of both flux guides as shown in figure 5.26 which are then captive within the surrounding main hub. The geometry for these captive elements was decided to be circular for a number of reasons. The first being that the shape of these is basic and doesn't interfere too heavily with the solving of the simulations unlike the 'fir tree' styles that were rejected. This less complex shape also reflected positively on the manufacturability of the flux guide laminations. Too complex a design would lead to expensive tooling, unreliable stamping or the need to use more expensive methods of cutting, such as laser or water jet, to gain that accurate and complex shape required. The first case considered, which is shown to scale in figure 5.26, includes a 5.9mm diameter (d_{ci}) circular projection on the inner limb which in combination with the original flux guides results a neck width (w_{ni}) of 5.3mm. The outer flux guides are modified to include a similar circular projection with d_{co} and w_{no} values of 12mm and 10.5mm respectively. There are matching projections on the composite hub and a further small projection with a diameter of 2mm on the outer

supporting section of the hub. As will be apparent, in order to retain the two U-shaped composite sections adjacent to the flux guides, it is also necessary to incorporate matching cut-outs in the flux guides.

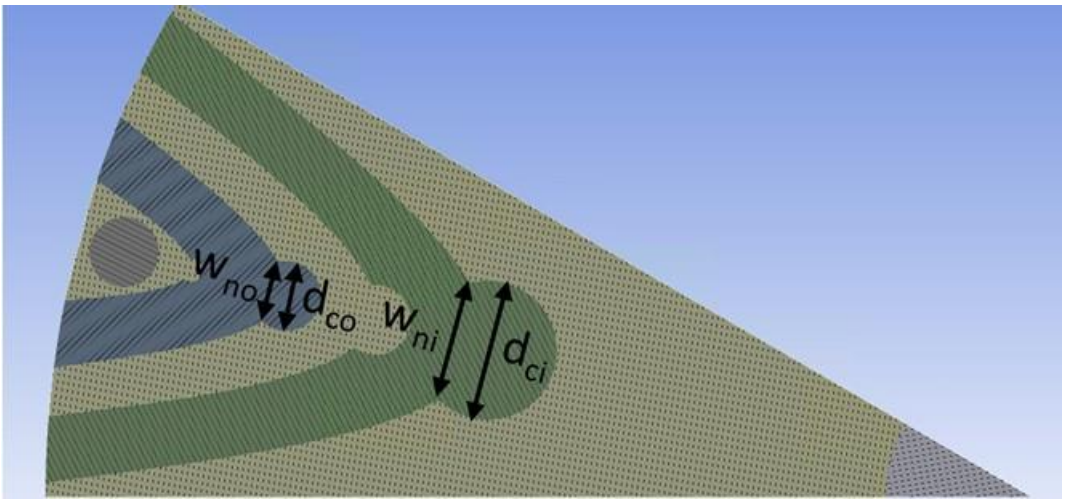

Figure 5.26 Rotor with captive flux guides showing definition of key captive projections dimensions.

The performance of the rotor shown in figure 5.26 was modelled using a CZM model based on Permabond TA439 with the ideal bonded carbon fibre rods in place. Figure 5.27 shows the predicted deformation at four discrete speeds up to 15,400rpm which was the maximum speed at which solution convergence was achieved. As was the case with the other tie-rod simulations with the plain flux guides, the failure to converge is related to the complete failure of the CZM bond and not necessarily unconstrained separation of the rotor and catastrophic failure (as was the case with the plain rotor with no tie-bars in section 5.4.6). As will be apparent up to 10,000rpm there appears to be no discernible failure of the adhesive bond at 10,000rpm, but there is very significant failure of the bond between the inner flux guide and the main section of the composite at 15,000rpm and near full failure of this bond at 15,400rpm.

Figure 5.28 shows the variation with speed of the localised stress at the contact between the innermost point of the captive section of the inner flux guide and the composite hub (shown at point ‘P’) which is the first point at which the onset of failure in the composite is most likely. As will be apparent, there is some deviation in the von Mises stress at a speed of ~12,800rpm which again is indicative of the onset of local failure and corresponds to a stress in the adhesive bond of ~20MPa which is consistent with the material properties adopted for Permabond TA439. It is interesting to note that this is a very similar separation speed to that which predicted for the plain flux guides and tie-rods in figure 5.25.

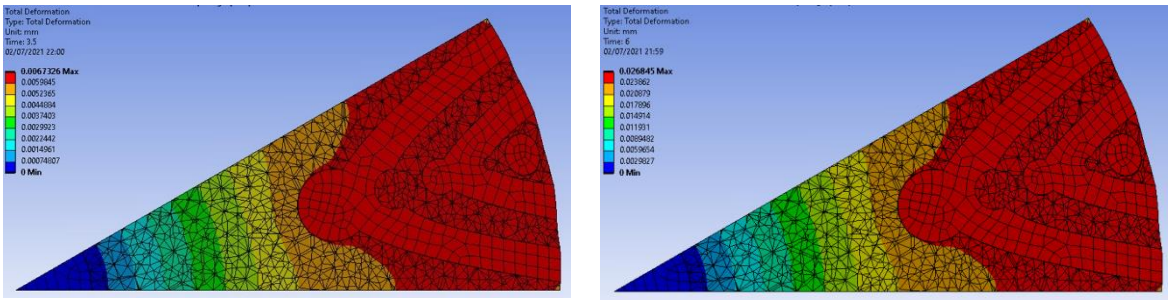

(a) 5,000rpm **(b) 10,000rpm**

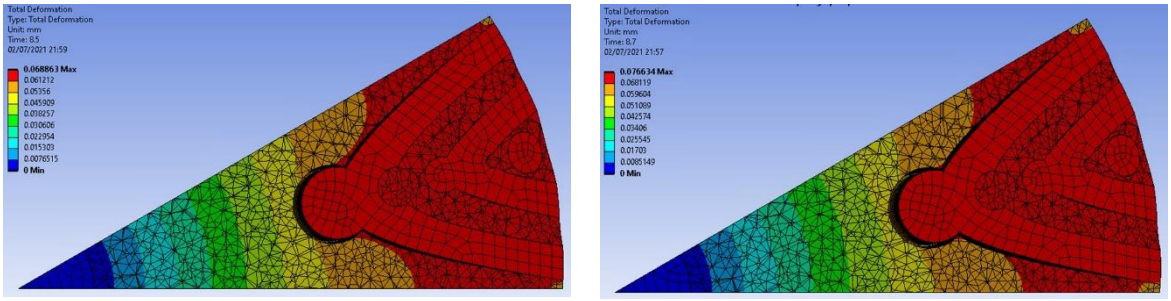

(c) 15,000rpm **(d) 15,400rpm**

Figure 5.27 Finite element predicted deformation of the rotor of figure 5.26

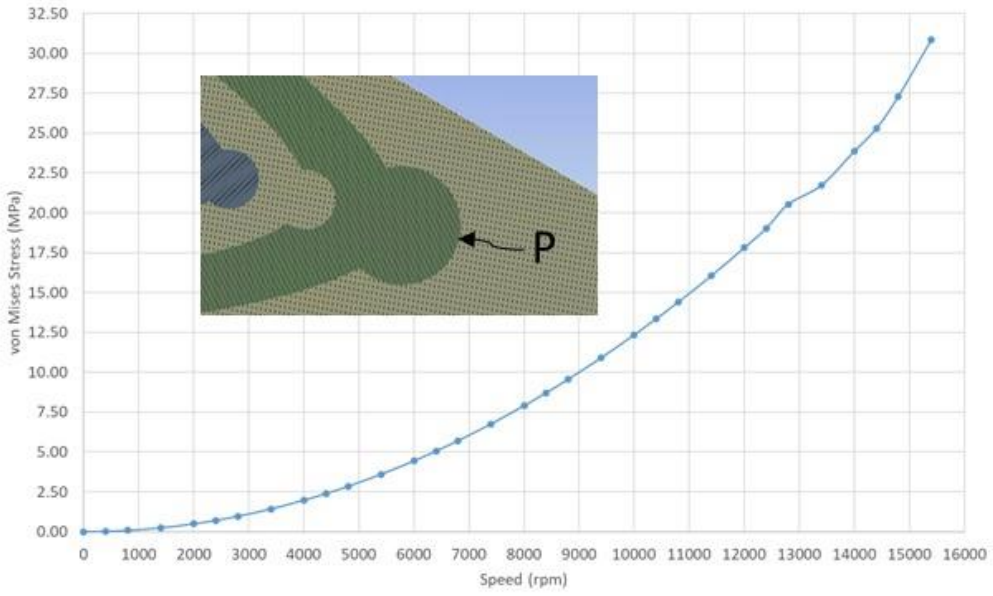

Figure 5.28 Finite element predicted variation in von Mises stress at a point P with rotor speed for the first captive flux guide design

When the bond at point P begins to separate at ~12,800rpm, there is an increasing stress in the region of the composite hub which makes the flux guide captive, although this region does not react to the full centrifugal force on the flux guide as it remains attached for much of its periphery until 14-

15,000rpm or so. Figure 5.29 shows a predicted von Mises stress distribution at 15,400rpm, a speed at which the bond between the inner flux guide and the main composite hub region has fully separated and the flux guides are being retained by a combination of the captive projection and the outer supporting region (which includes the carbon fibre tie-rod). As will be apparent from this stress distribution, there is some localised stress concentration around the captive elements but the stresses are well within the capability of the composite hub.

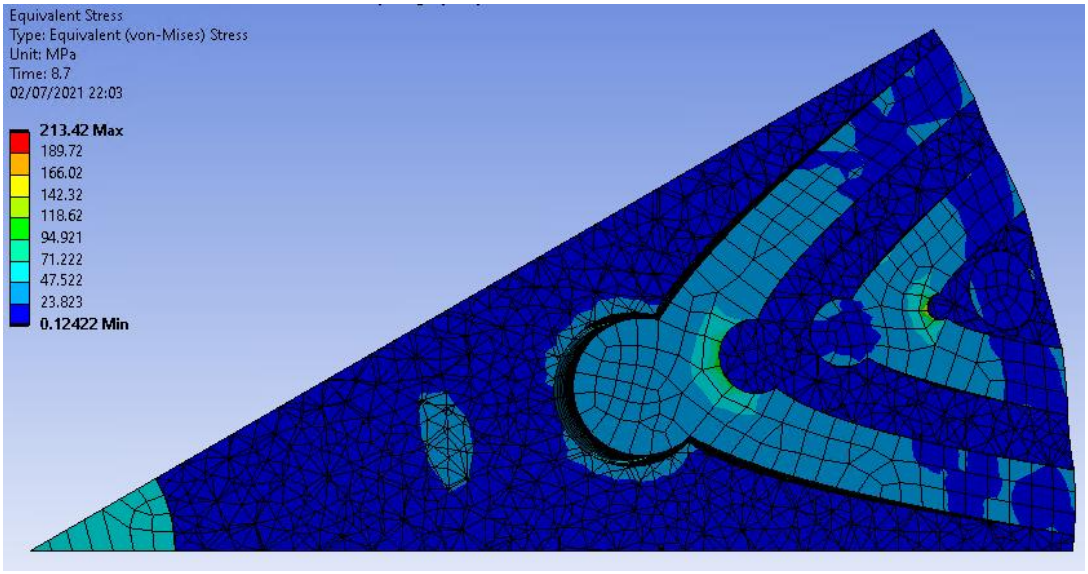

Figure 5.29 Finite element predicted von Mises stress distribution at 15,400rpm

Although the first captive projection design showed little, if any advantage, over a plan flux guide, it was recognised that this may in part be a consequence of the detailed geometry of the captive projection, and in particular the diameters of the projections and the neck widths as defined in figure 5.26. A second captive design was modelled where the effective captive circles were pulled backwards to decrease the two 'w_n' widths while keeping the 'd_c' values the same, in this case with d_{ci} = 12mm, w_{ni} = 8.2mm, d_{co} = 5.9mm and w_{no} = 4.6mm. Figure 5.30 shows the finite element predicted deformations for this modified projection at four discrete speeds up to the maximum speed of 16,400rpm at which convergence was achieved. As shown, there is evidence of separation of the inner-flux guide from the main section of composite hub around the base of the captive in the 15,000rpm simulation.

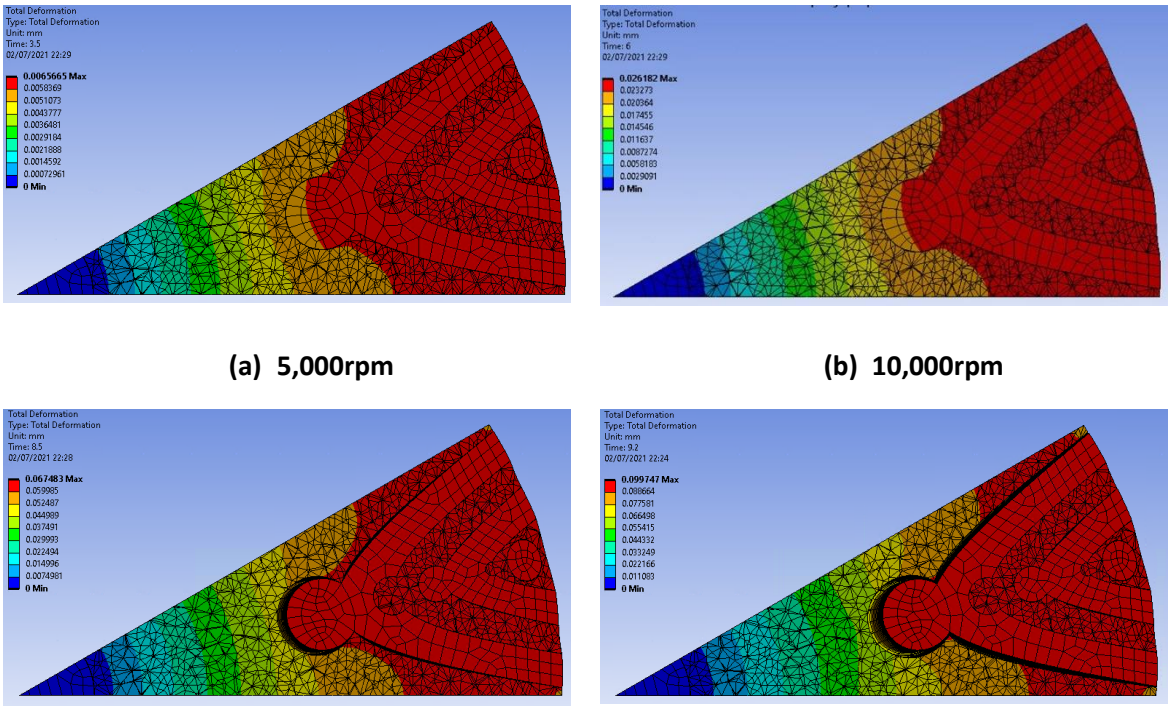

(a) 5,000rpm **(b) 10,000rpm**

(c) 15,000rpm **(d) 16,400rpm**

Figure 5.30 Finite element predicted deformation of the 2nd rotor design with captive flux guides (d_{ci} = 12mm, w_{ni} = 8.2mm, d_{co} = 5.9mm and w_{no} = 4.6mm)

Figure 5.31 shows the corresponding variation with speed of the von Mises stress at the contact between the point at the base of the inner flux guide projection and the main section of the composite hub (equivalent of point 'P' in figure 5.26). This variation in stress at the interface of the inner flux guide suggests that the onset of some localised failure of the adhesive bond occurs at ~13,000rpm, which is very similar behaviour to that observed with the smaller captive projection. At this speed the maximum rotor deformation at the outer surface is 0.045mm.

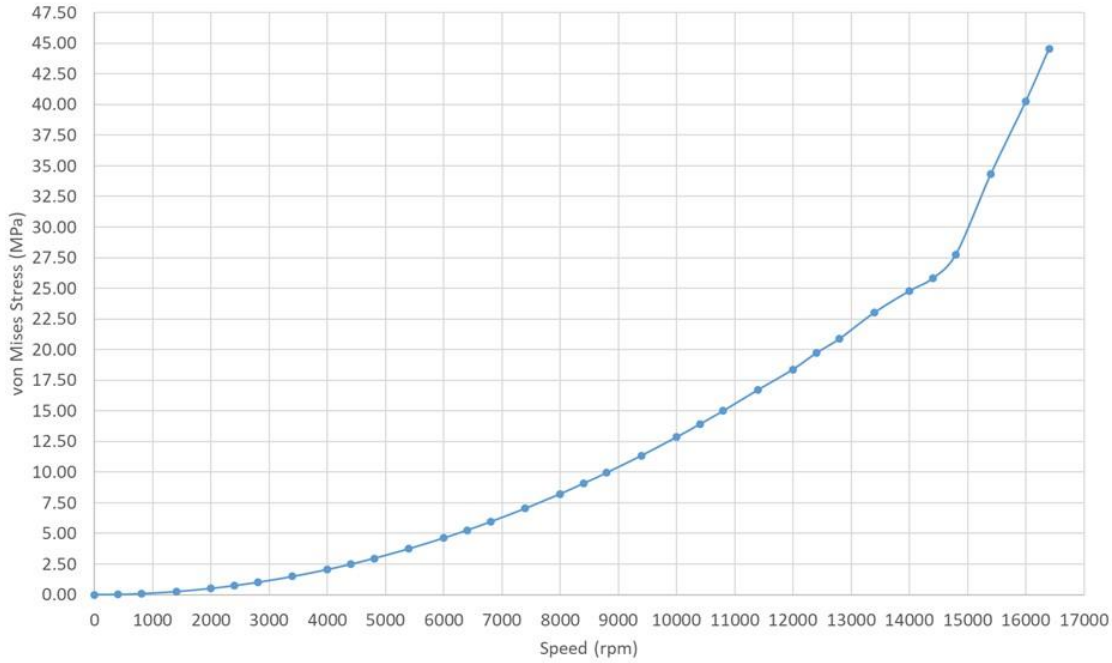

Figure 5.31 Finite element predicted variation with rotor speed of von Mises stress at a location corresponding to point 'P' for the second captive flux guide design

Although the incorporation of captive projections on the flux guides does not have an influence on the geometry of the magnetic circuit near the airgap, there is a possibility that the incorporation of the projections does have some influence on the electromagnetic behaviour. To assess this, two-dimensional finite element electromagnetic torque calculation was performed for the second captive design projections considered. The average torque produced at the rated rms current density of 10A/mm^2 for this configuration is 78Nm which compares with 85Nm for the plain flux guides in the design established at the end of chapter 4. This drop in torque is due to increased leakage between the flux guides and some additional magnetic saturation. Overall, the inclusion of captive elements on the flux guides provided no meaningful improvement in the mechanical performance of the rotor as judged in terms of speed at which the flux guides start to separate from the main composite hub, but do incur an electromagnetic torque penalty.

5.4.9. Incorporation of a Carbon Fibre Overwrap Sleeve

It is apparent from the investigation into the incorporation of captive projections that ultimately trying to restrain the flux guides from the inside of the rotor offers very limited scope to enhance mechanical performance. A design feature that will improve mechanical integrity of the rotor under load but at the inevitable expense of electromagnetic performance is to incorporate a filament wound composite overwrap / sleeve onto the outer surface of the rotor. Given the relatively thin sleeve that will be

interest (~1mm thick given the likely electromagnetic penalty) then a high-strength and high-stiffness carbon fibre composite could be an economically viable option.

The use of a carbon fibre sleeve was first explored on a rotor with plain flux guides. A 1mm thick sleeve was added to the rotor with the overall diameter maintained at 170mm, and the remainder of the rotor elements having a reduced rotor diameter of 168mm to accommodate the sleeve. In this model, an additional coordinate system was introduced to allow the modelling of the directional properties of the filament wound carbon fibre overwrap. The overwrap was assigned a circumferential stiffness of 121GPa, and 8.6GPa in the remaining orthogonal directions. This design was simulated with CZM representation on all contact boundaries except the shaft and hence assumes that the overwrap is adhesively bonded to the underlying rotor components. There was no pre-stress introduced into the overwrap.

A series of simulations were performed with a target maximum speed of 20,000rpm. However, as the speed was stepped up the solver failed to converge and generate solutions beyond 18,400rpm. The finite element predicted deformation at 4 discrete speeds up to 18,400rpm are shown in figure 5.32. At the maximum speed of 18,400rpm, there is only a small region near the outer edge of the rotor in which adhesive bond between the flux guide and the hub has not separated. This confirms that the failure to produce solutions beyond 18,400rpm is a consequence of complete separation of the flux guides from the hub, which would occur beyond this speed. As will be apparent from figure 5.32, the bond between the base of the inner flux guide and the main hub is intact at 10,000rpm, but shows evidence of separation at 15,000rpm. Despite this separation at 15,000rpm, the overall deformation of 63.5 microns at this speed remains small in the context of the 0.5mm radial mechanical clearance between the rotor surface and the stator bore. Figure 5.33 shows the variation with rotor speed of the stress at the contact between the innermost edge of the inner flux guide and the hub, from which is can be seen that there is evidence of some separation at ~13,000rpm with a deviation in the stress. It is interesting to note that in this rotor, although the inner-pole pieces completely separate from the hub at 18,400rpm, the rotor is still fully contained within the carbon fibre sleeve. The maximum stress in the sleeve is 232MPa as shown in figure 5.34 which shows the predicted von Mises stress distribution in the rotor at 18,400rpm. This is well within the stress capability of a typical carbon fibre composite and would ensure no catastrophic failure of the rotor at speeds beyond 20,000rpm or so. However, operation with completely separated elements within the rotor does not offer a viable option for long- maintaining rotor balance and hence reliable operation. Hence, for this rotor, the limiting speed to void failure of the adhesive bond is only ~13,000rpm with a deformation on the outer surface of 44micron, which are both very similar to the other adhesive bonded variants considered up to this point.

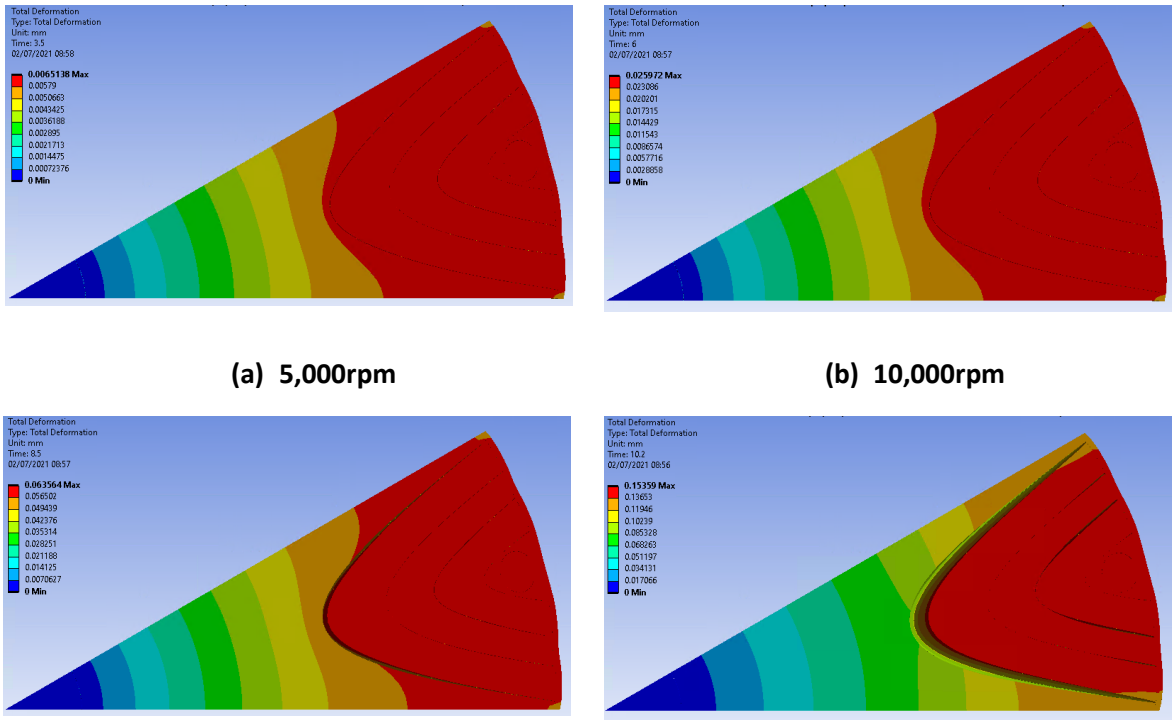

(a) 5,000rpm **(b) 10,000rpm**

(c) 15,000rpm **(d) 18,400rpm**

Figure 5.32 Finite element predicted deformations for a composite hub with a 1mm thick carbon fibre overwrap, adhesively CZM bonded flux guides and tie-rods

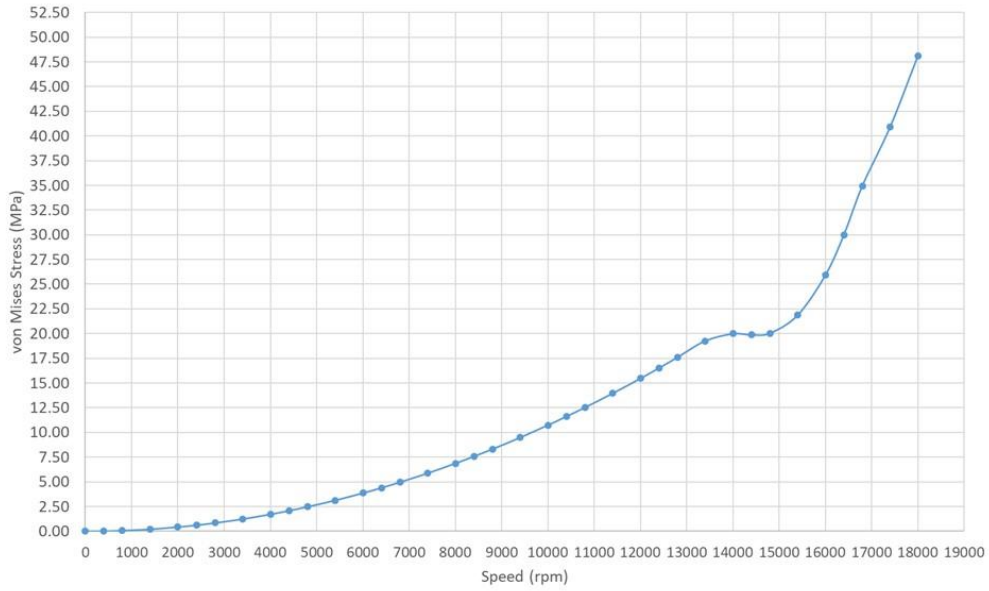

Figure 5.33 Finite element predicted variation with speed of the maximum stress at the contact between the inner flux guide and the hub

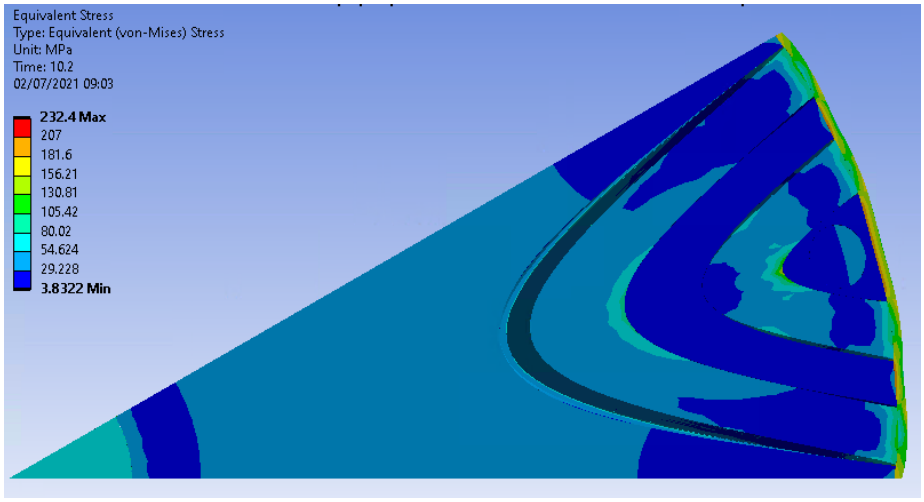

Figure 5.34 Finite element predicted von Mises stress distribution in the rotor at 18,400rpm

5.4.10. Combination of Captive Flux Guides, Carbon Fibre Tie-Rod and a 1mm Carbon Fibre Overwrap

The final rotor variant with a carbon fibre overwrap sleeve combined the second captive flux guides, with a 1mm thick carbon fibre sleeve. As was the case with earlier sleeved designs the overall diameter was again maintained at the same 170mm which required a reduction in the diameter at which the outer edges of flux guide are located to 168mm. Figure 5.35 shows the predicted deformation of the rotor of the rotor at four discrete speeds up to 16,800rpm, beyond which convergence was not achieved due to complete separation of the adhesive bond between the inner-flux guide and the rotor hub.

As shown in figure 5.35, there is almost complete separation of the adhesive bond on the innermost surface of inner flux guides at 16,800rpm although the flux guides remain contained with the rotor due the carbon fibre sleeve. It is interesting to note that at 16,800rpm the captive projection makes no contact with the main hub-section even at front end of the projection which would normally be expected to be the region which is constraining the flux guide. This is a result of the flux guide radial movement being constrained by the outer sleeve while deformation of the main composite hub (which has a much lower modulus than the flux guides) opens up the aperture in which the projection sits. It is also interesting to note that in common with the other sleeved rotor design, even with full detachment of the adhesive bond, the deformation of the rotor outer surface at 16,800rpm remains comparatively small at ~98 micron while the stress in the carbon fibre sleeve, as shown in figure 5.36 has a maximum of ~200MPa which is well within the material limit of 800-1000MPa or so.

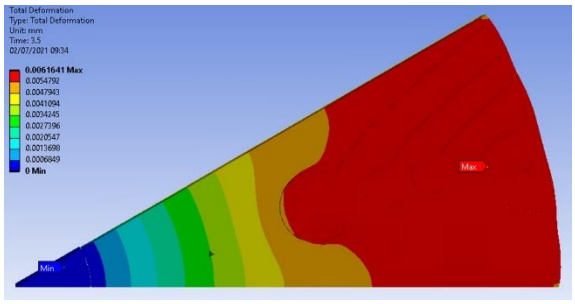

(a) 5,000rpm

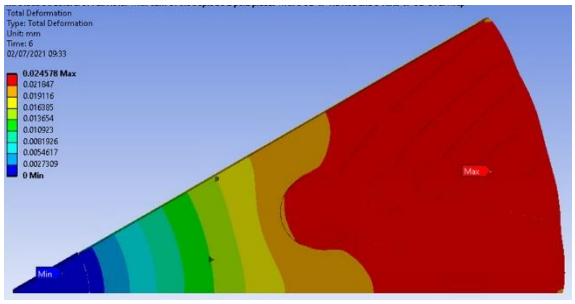

(b) 10,000rpm

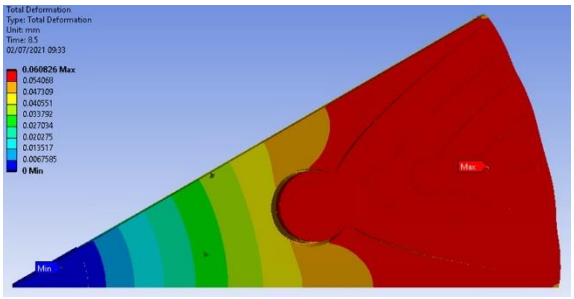

(c) 15,000rpm

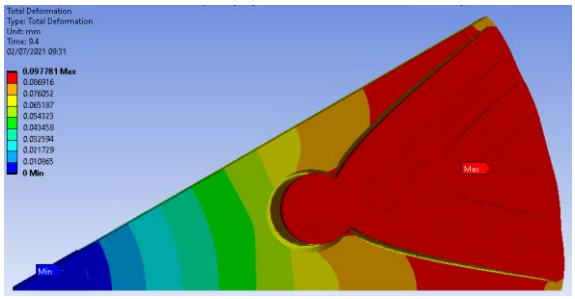

(d) 16,800rpm

Figure 5.35 Finite element predicted deformations for a composite hub with a 1mm thick carbon fibre overwrap, adhesively CZM bonded captive flux guides and tie-rods

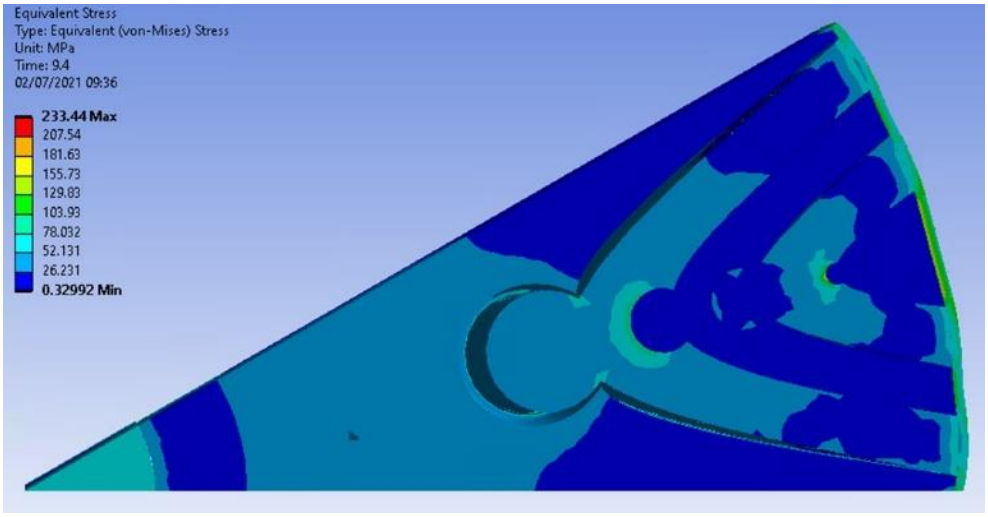

Figure 5.36 Finite element predicted von Mises stress distribution at 16,800rpm

Figure 5.37 shows the variation with speed of stress at the interface between the inner flux guide circular projection and the main section of the composite hub (i.e. a point analogous to point P shown previously in figure 5.26).

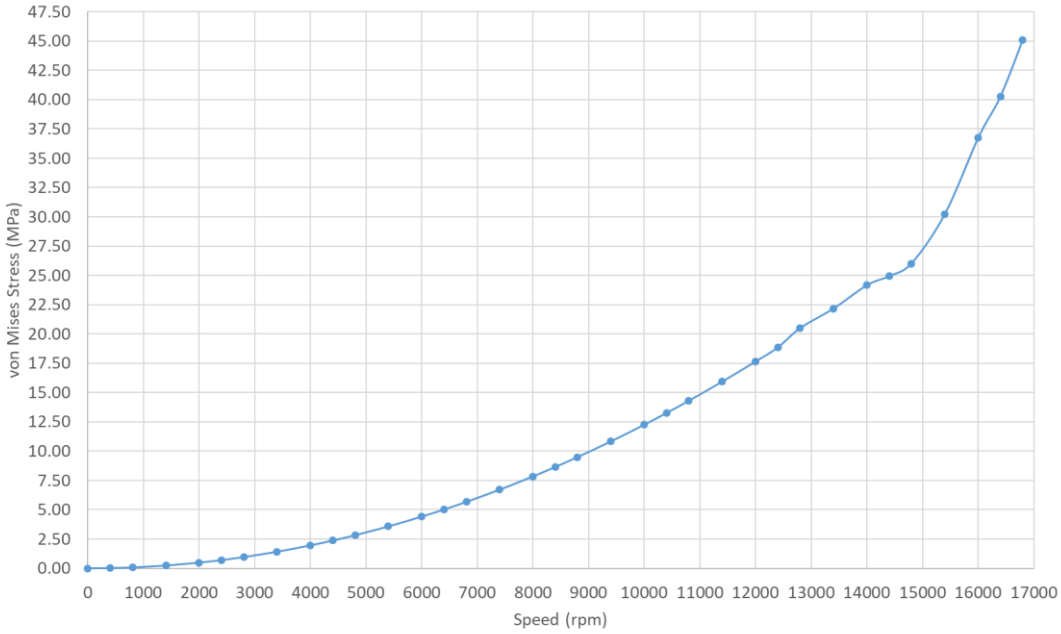

Figure 5.37 Finite element predicted variation with speed of the maximum stress at the contact between the inner flux guide and the hub

As will be apparent, there is a discernible change in the rate of increase of stress at a speed of ~13,000rpm which is indicative of some level of fracture. The predicted localised stress level of ~20MPa at 13,000rpm is consistent with the fracture stress of the Permabond TA439. The predicted deformation on the outer surface of the rotor at 13,000rpm is again ~44micron.

5.4.11. Electromagnetic Impact of Incorporating a Carbon Fibre Overwrap Sleeve

Whereas the incorporation of a carbon fibre sleeve has some benefits mechanically, this is at the expense of an increased effective magnetic airgap in the machine. As noted previously in chapter 2, the performance of SYNCREL machines, in common with all singly-excited machines, tends to deteriorate rapidly as the effective magnetic airgap is increased. In order to understand the reduction in the level of electromagnetic performance that a 1mm thick carbon fibre sleeve would introduce, the torque was calculated using the same two-dimensional magneto-static approach used throughout chapter 4.

For an axial length of 66.2mm (the length required to meet the rated torque requirement of 85Nm with the 12 pole design established in chapter 4) a 170mm diameter rotor with a 1mm carbon fibre sleeve, results in a predicted average torque at a rms current density of 10A/mm^2 of only 42Nm. As will be evident, the incorporation of this sleeve has had a severe effect on the torque capability of the machine with a halving of the torque capability of the corresponding machine with no sleeve. It is recognised that some parametric investigation into sleeve thickness might improve the trade-off

marginally. To assess the benefits of thinner sleeves the variation of the predicted electromagnetic torque with the magnitude of the effective airgap is shown in figure 5.38 for both plain and the second captive flux guides. The effective magnetic airgap quoted in figure 5.38 includes the 0.5mm radial clearance and the sleeve itself and hence a 1mm sleeve corresponds to an effective airgap of 1.5mm. As will be apparent, even a 0.5mm thick sleeve results in a very significant penalty in torque capability for both plain and captive flux guides. It is recognised that pre-stressing of the sleeve could further enhance the mechanical performance by applying a significant inward compressive force on the flux guides to avoid detachment but given that even very thin overwrap sleeves incur such significant torque penalties, these were not explored further.

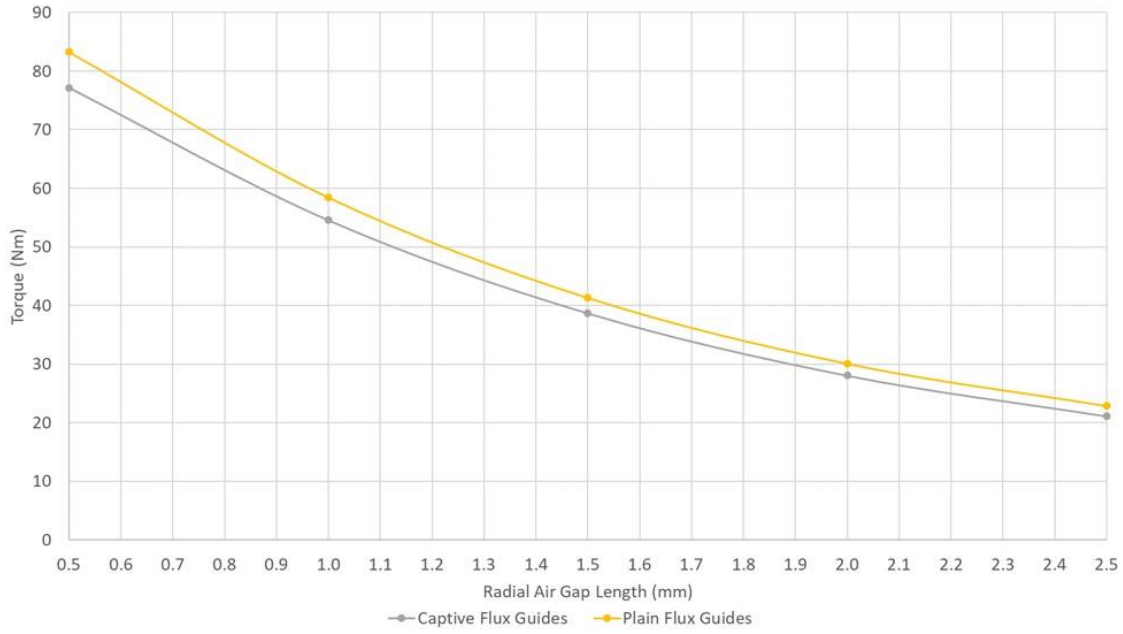

Figure 5.38 Finite element predicted variation in torque with effective magnetic airgap length for machines of axial length 66.2mm and a rms current density of 10A/mm^2

5.4.12. Removal of Outer Support and Tie-Bar

As shown previously in section 5.4.2 when the composite hub and tie-rods alone were modelled, i.e. with no flux guides in place, the main problem was deformation of the outer supporting structure despite the presence of the high stiffness carbon fibre tie-rods. However, once adhesive was introduced in the structure, the problem region became the interface between the inner flux guide and the main section of the composite hub. The outer support did not separate from the outer flux guide but the degree to which it provides useful restraint against separation of the inner flux guide cannot be readily determined without further simulations. Hence, a further series of simulations were

performed for a rotor with plain flux guides but no outer support region and no tie-bars. The resulting rotor deformation at four discrete speeds up to 16,400pm (maximum speed at which solution convergence was achieved) are shown in figure 5.39. As is evident from figure 5.39, in this case there is evidence of significant separation of the inner and outer flux guides in the 15,000rpm plot. This contrast with the corresponding deformation shown previously in figure 5.22 for a rotor with an outer support element with tie-rods where there is no evidence of separation between the outer flux guide and the U-shaped section of the composite hub between the flux guides.

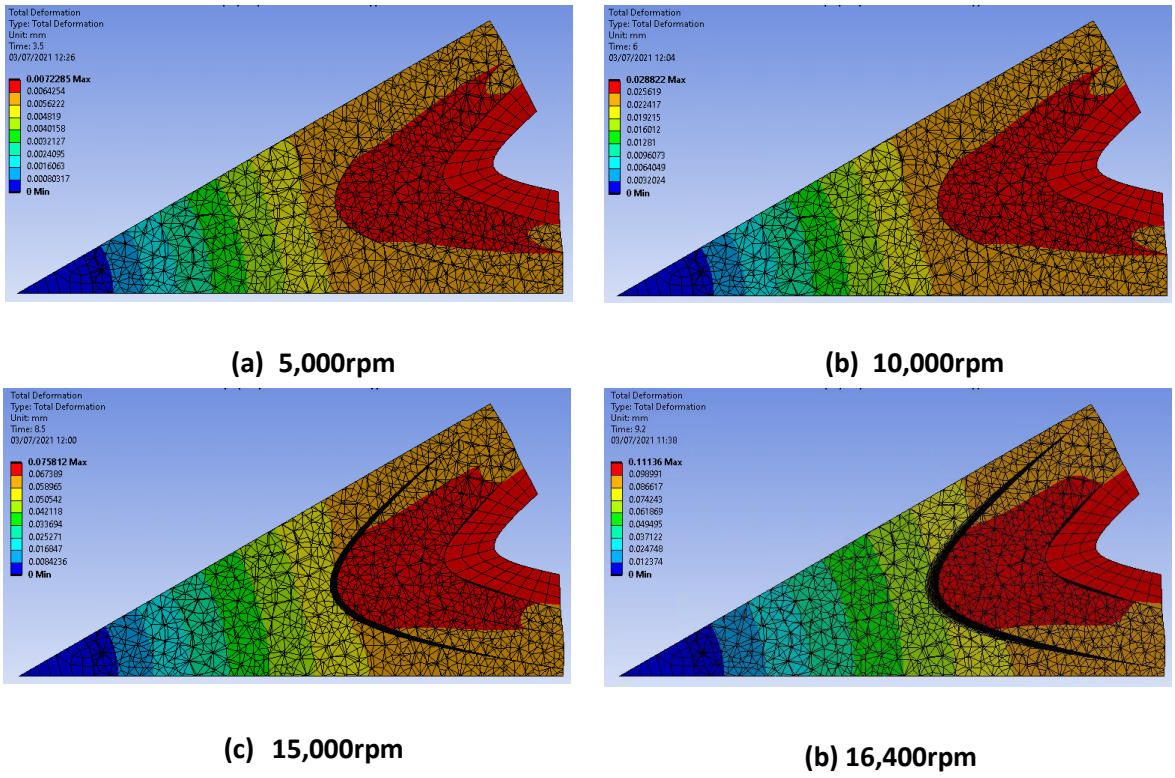

(a) 5,000rpm **(b) 10,000rpm**

(c) 15,000rpm **(b) 16,400rpm**

Figure 5.39 Finite element predicted deformations for a composite hub adhesively CZM bonded plain flux guides and no outer supporting region

The variations in stress at the innermost point of both flux guides is shown in figure 5.40, which demonstrates that although it is the innermost flux guide that shows the first sign of some deviation in the stress variation at ~13,000rpm, the outer flux guide is not far behind. The variation in the deformation of the outer surface with speed is shown in figure 5.41 noting that in most of the other rotor designs, it is the outer supporting region that exhibits the highest deformation. In this case, it is the outer flux guide that experiences the largest movement with a maximum deformation on the outer surface of ~48micron. Given the that limiting speed and deformation values are very close to those of the corresponding rotor with an outer support, it is entirely appropriate to question the value of the outer support. Whilst is may not increase the limiting speed, when the definition is based on failure of the internal adhesive bonds, it does provide retention of the flux guides, albeit with large

deformation, and could prevent catastrophic failure in the event of glue failure below the design stress due to ageing effects. Hence, it provides some back-up to the adhesive bond even though in normal operation it does little to prevent facture of the adhesive bond since it so heavily loaded itself and has modest resistance to beam-type bending.

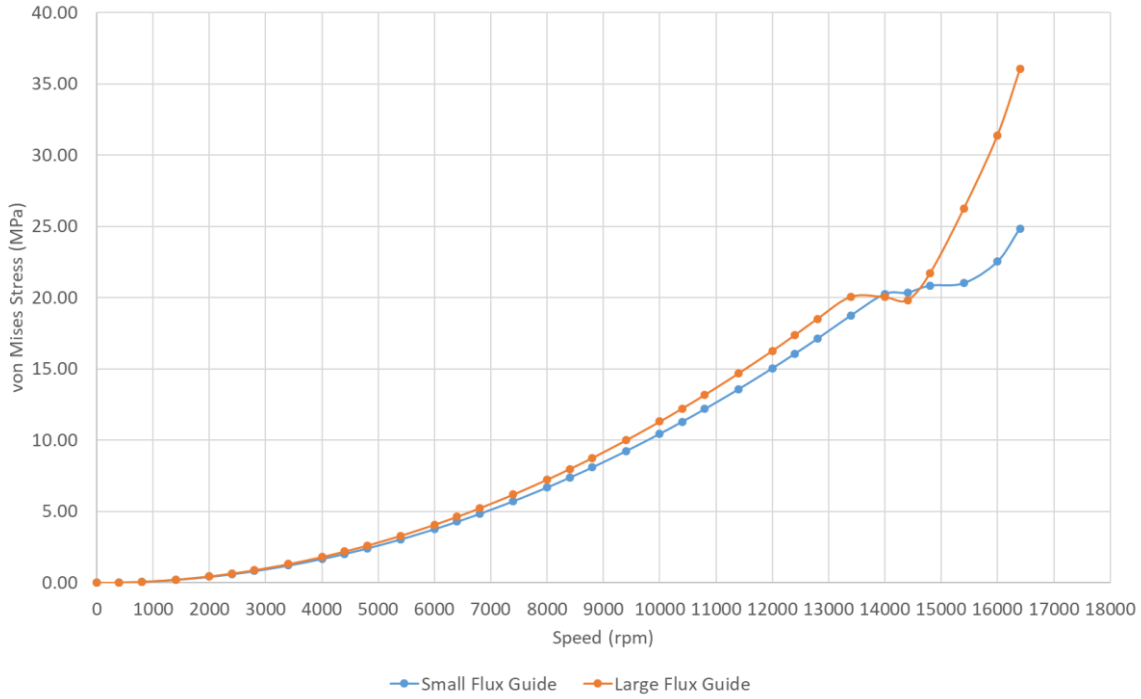

Figure 5.40 Finite element predicted variation with speed of the maximum stress at the contact between both the inner and outer flux guides and the hub

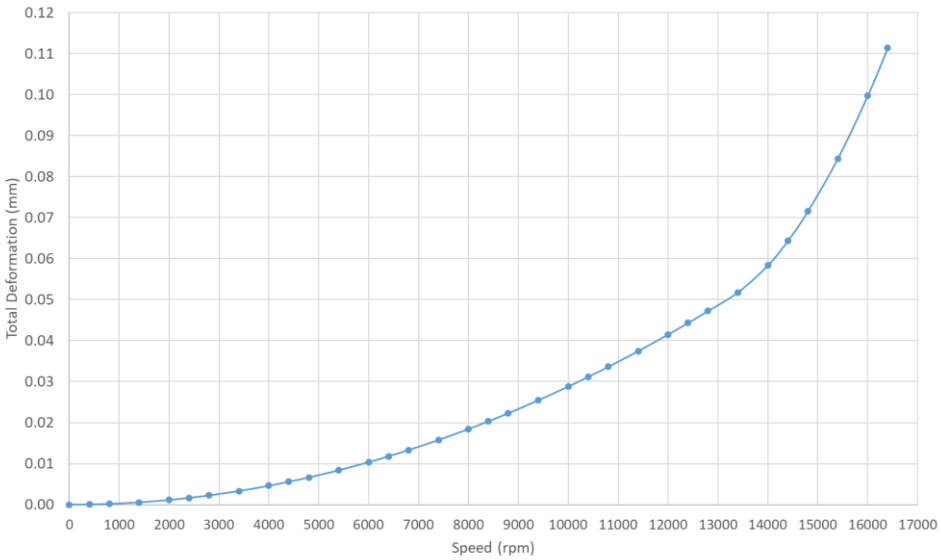

Figure 5.41 Variation in outer surface rotor deformation with rotational speed

5.4.13. Single-Piece Rotor Flux Guides

Further alternative configurations which were explored consisted of various single-piece rotor core constructions in which the individual flux guides are all joined via a central continuous ring and radial bridges between the inner and outer flux guides at each pole. Examples of which are shown in the close-ups of various individual pole configurations considered in figure 5.42. These single-piece flux guides configurations were chosen to provide some anchoring of the individual flux guides, and hence when used in combination with adhesive bonding of the flux guides, may have allowed some increase in the maximum speed. However, joining the individual flux guides was likely to have an effect on the electromagnetic performance of the rotor since the previously uncoupled flux guides now have numerous shared flux paths through both the central ring and the individual bridges between flux guides.

The first assessment performed on this series of rotors was the calculation of the electromagnetic torque at the rated current density of 10A/mm^2. In all cases, the radial airgap to the stator was fixed at 0.5mm to provide a direct comparison with the machines considered in chapter 4, and the torque was calculated in each case for a 66.2mm axial length. Table 5.5 shows the calculated torque at the rated rms current of 10A/mm^2 along with the axial lengths that would be required to produce the rated torque of 85Nm. It is useful in assessing these torque and axial length values to note that the machine design established at the end of chapter 4 was capable of producing the rated torque of 85Nm with an axial length of 66.2mm, and the same stator arrangement and current density. As will be apparent, these single piece flux guide rotors, at best only produce half of the torque of the original design.

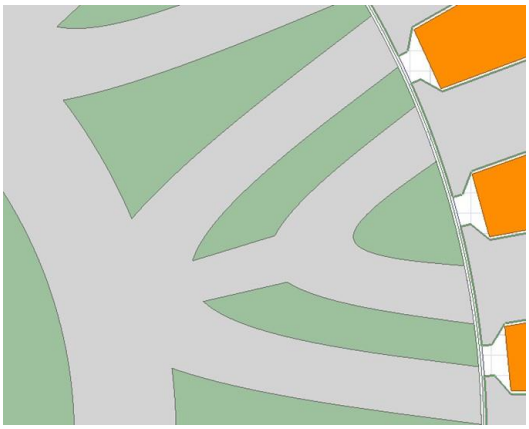

(a)

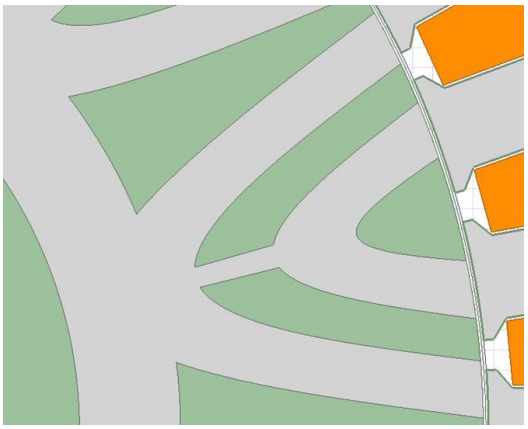

(b)

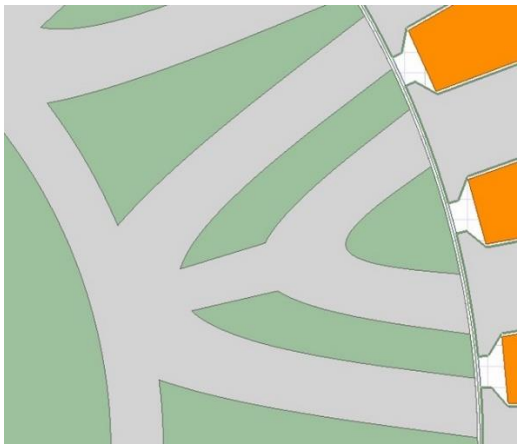

(c)

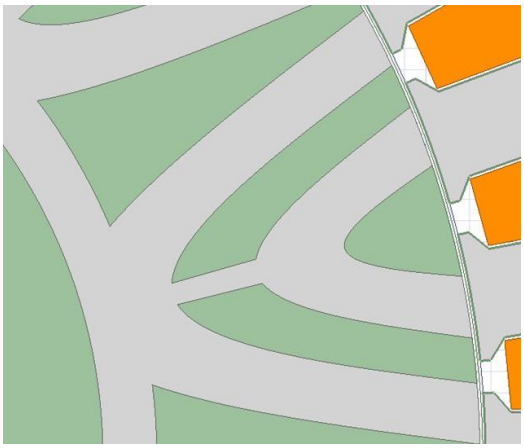

(d)

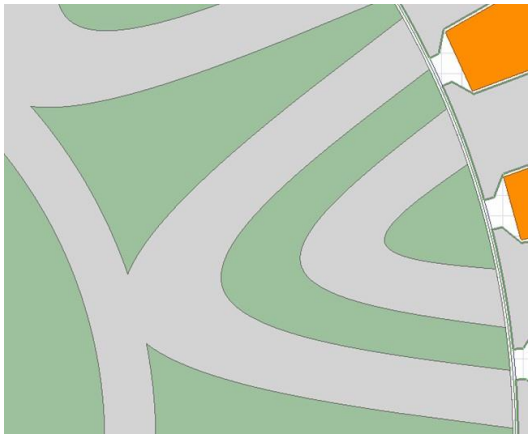

(e)

Figure 5.42 Close up of rotor pole geometries for variety of different single-piece flux guide arrangements considered

Rotor geometry	Torque for 66.2mm axial length (Nm) at a rms current density of 10A/mm^2	Axial length required to produce 85Nm (mm)
Baseline design	85.0	66.2
Figure 5.42(a)	29.5	190.7
Figure 5.42(b)	41.9	134.3
Figure 5.42(c)	33.8	166.5
Figure 5.42(d)	42.7	131.8
Figure 5.42(e)	56.9	98.9

Table 5.5 Finite element calculated average torque for different single-piece rotor design variants

One last variant considered was the rotor geometry shown in figure 5.43. This is not a single piece rotor, but it does incorporate a connection between the inner and outer flux guides. In this, the machine produces a torque of 72.5Nm at a rms current density of 10A/mm^2, which is 12.5Nm below the capability of the baseline design.

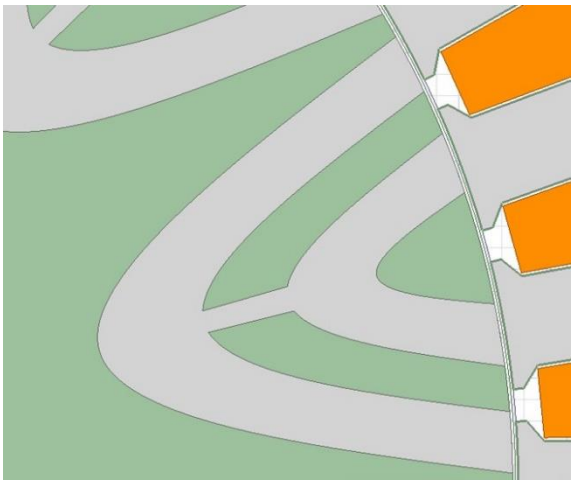

Figure 5.43 Rotor geometry with joined inner and outer flux guides but no mechanical connection between successive poles

Given the significant torque drop in all these rotors with some form of connection between flux guides, these were not pursued through to mechanical analysis. In the case of the bridged flux guides in figure 5.43, although the torque reduction was not so dramatic, the mechanical benefits are likely to be marginal given that the main challenge in the rotors analysed previously in this chapter is retaining the inner flux guide in contact with the central hub.

5.4.14. Summary and Rotor Design Selection

The analysis described in this chapter has considered numerous designs of rotors with a variety of features to accommodate the resulting radial growth of the rotor, relative motion and separation of components and stress levels. It has been demonstrated that the proposed concept of a series of embedded flux guides in a composite hub poses many challenges in terms of realising a high integrity rotor capable of operating at high-speeds. Table 5.6 shows a summary of the limiting speed without the application of a safety-factor, in which the definition adopted for the limiting speed is the rotational speed at which there is evidence of facture and separation of the adhesive bonds within the rotor or, in the case of the rotor designs with no adhesive, radial growth that exceeds 0.25mm (which is half the mechanical clearance between the rotor or stator). In some cases, the automatic speed increments used by Ansys to solve the structural model, and which are related to convergence issues, can limit the resolution of the limiting speed and the increments are not necessarily consistent. Hence, quoted limiting speeds of 12,800rpm may in practice be the same as those quoted as 13,000rpm, the difference being simply the nature of the speed increments used in that particular simulation.

Description of rotor	Chapter section	Limiting speed (rpm)	Deformation of outer diameter at limiting speed (mm)
Non bonded component with frictional contacts – coefficient of friction of 0.75	5.4.4	8,400rpm*	0.25
Non bonded component with frictional contacts – coefficient of friction of 0.5	5.4.4	8,400rpm*	0.25
Adhesive bonded rotor with plain flux guides	5.4.6	13,000rpm	0.044
Adhesive bonded flux guides and tie-rods	5.4.7	13,000rpm	0.044
Adhesive bonded rotor with the first captive flux guides and tie-rods	5.4.8	12,800rpm	0.043
Adhesive bonded rotor with the second captive flux guides, tie-rods	5.4.8	13,000rpm	0.044
Adhesive bonded rotor with plain flux guides, tie-bars and 1mm carbon composite overwrap sleeve	5.4.9	13,000rpm	0.044
Adhesive bonded rotor with the second captive flux guides, tie-bars and 1mm carbon composite overwrap sleeve	5.4.10	13,000rpm	0.044
Adhesive bonded rotor with plain flux guides and no outer support or tie-bar	5.4.12	13,000rpm	0.048mm

* -speed limited by deformation

Table 5.6 Summary of rotor performance

There are several key outcomes from this study:

- The use of adhesives to retain the flux guides offers a much more viable route to ensuring mechanical integrity than reliance on the structure alone.
- Whereas making the flux guides fully enclosed on the outside of the rotor would be beneficial, the associated electromagnetic torque penalty in excessive.
- The criterion used to set an upper limit on speed, i.e. onset of fracture of the adhesive, means that the various designs are clustered around 13,000rpm with many of the differences in their behaviour only apparent at higher speeds where the nature of structural features such as projections, sleeve and tie-rods in limiting deformation comes into play.

Of the numerous rotor considered, the design from section 5.4.7 was selected for further investigation as this matched the performance of all other variants from a mechanical perspective, retained the full electromagnetic torque capability, and included a means of restraining the flux guides in the event of an adhesive failure. As noted in section 5.4.7, applying a safety factor of 2 to the stress at failure reduces the design speed to 9,500rpm. It is recognised that this falls well short of the ambitions set out at the start of this project for speeds of 20,000-30,000rpm in order to achieve competitive power densities. However, it has been demonstrated by evaluating many different concepts and design features, that the specification of a 170mm rotor diameter at the outset and the significant penalty in torque which is incurred by placing any retaining structures between the flux guides and the airgap, are the main reasons for such modest speed capability. It is interesting to note that the strength requirements for the composite are not particularly onerous, since apart from the overwrap sleeve designs (which was uncompetitive in terms of torque rating) the composite components takes modest loads relative to their capability.

5.5. Rotor Dynamic Analysis

5.5.1. Fundamentals of Rotor Dynamic Analysis

Having identified a preferred rotor design on the basis of structural analysis, it is necessary to consider its rotor dynamic behaviour in order to ensure that the maximum speed is not further restricted by rotor-dynamic factors. Rotor dynamics is the study of rotating components which are subject to complex mechanical excitations. These excitations can be caused by mass imbalance, or finite stiffness of the rotor. These factors can cause vibrations in the rotor, which usually fall into two categories: synchronous vibrations, which are caused by the mass imbalance in the rotor, and nonsynchronous vibrations, which are caused by the self-excited whirling of the rotor. Therefore, in any in-depth study of rotor dynamics, there are three main areas of interest; the rotor critical speed, system stability and the unbalanced response. The most important area of interest to this project is the critical speed,

which is linked to the un-damped natural frequencies of the rotor system. It is important to manage these frequencies, since whereas the final rotor design may be able to manage the centrifugal loading encountered in operation, it could still suffer a catastrophic failure due to running through a critical speed. Therefore, wherever possible, it is desirable to avoid encroaching on the first critical speed in operation [88]. It is worth noting that in some very high-speed applications it is not possible to place the first critical speed beyond the required operating range and in such applications it may be necessary during run-up to quickly traverse the critical speed recognising for a short duration the rotor and the remainder of the machine will be subject to excessive, but short-lived vibration.

The rotor dynamic considerations in this chapter are largely focused on establishing the first critical speed of rotor designs in order to provide an upper limit on the operating speed of the rotor from the perspective of rotor-dynamics. In any practical design it is necessary to maintain some margin between the maximum operating speed and the predicted first critical speed of the system by an acceptable margin. This margin is a safety factor to ensure that the rotor can be safely run at its operating speed. The critical speed criterion adopted in this study to indicate safe operation is based on setting a maximum operating speed at no more than 75% of the first critical speed. This value has been adopted on the basis of an approach described in [88] which states that critical speeds should be 10-20% above the operating speed while [89] states that the critical speed should be 15% above the maximum operating speed. One important feature of this rotor which warrants some extra margin is the need to allow for uncertainties of fit and adhesive bonds in the multi-component rotor.

5.5.2. Calculation Methods for Establishing Critical Speeds

There are several approaches to calculate the critical speed of a particular rotor design which involve various levels of complexity and computational effort. The most straightforward analytical methods allow rapid calculation of critical speeds and provide direct insight into the role of different material properties and dimensions, but are based on simplifying assumptions regarding the rotor geometry. The reasonableness or otherwise of these assumptions depends strongly on the rotor geometry with simple cylindrical and single material rotor being most appropriate. It is inevitable that a complex rotor such as this will have a different performance than can be accurately calculated using these simplified assumptions.

Numerical methods based on various approaches to finite element analysis allow the full geometry to be captured. However, these are both time consuming to formulate and solve, and the results usually require several variations of parameters to be explored to extract meaningful insight into the role of different dimensions and properties. In this chapter, a classical analytical method is first considered followed by two finite element numerical approaches.

5.5.3. Jeffcot Rotor Analysis

The Jeffcot rotor is an important and fundamental building block of rotor-dynamic analysis which lends itself to analytical solutions of some key aspects of rotor-dynamic behaviour. A Jeffcot rotor consist of a simply supported 'mass-less' shaft with a thin but rigid disk at the centre point of the shaft [90], which in effect acts as point mass. The dynamic response of the Jeffcot rotor is determined entirely by the ability of the shaft to resist bending. Although based on a simplified geometry which cannot represent the complex geometry of the proposed 12 pole rotor, it is nevertheless a useful tool to provide order of magnitude level checking of calculations on more complex geometries, and more importantly in this study provides some on-going verification of modelling approaches by comparisons back with standard Jeffcot model predictions. This deflection of the shaft in fact moves the centre line down and therefore impacts the rotor dynamics by creating forward and backward whirl effects that impact the critical speeds of the rotor. Figure 5.44 shows a schematic of a Jeffcot rotor with a shaft radius r and axial length L between the bearings.

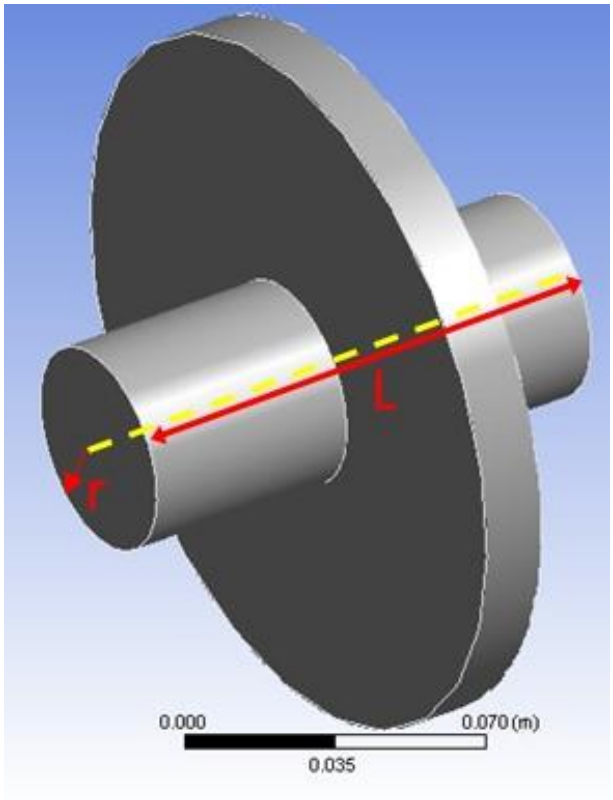

Figure 5.44 Jeffcot rotor

A standard expression for the calculation of critical speed (in rev/s) for a Jeffcott rotor with bearings that can be represented as having zero axial lengths themselves is given in [91] as:

$$N_c = \frac{\sqrt{\left(\frac{48EI}{ML^3}\right)}}{2\pi} \quad (5.5)$$

Where *E* is the Young's modulus of the disk material, I is the second moment of area of the disk, *M* is the mass of the disk and *L* is the distance between the bearings. The second moment of area can be calculated [92] using:

$$I = \frac{\pi d^4}{64} = \frac{\pi r^4}{4} \quad (5.6)$$

The material selected for the analysis was carbon steel SAE 1045 with modulus of 201GPa as this commonly used shaft steel [93]. The shaft diameter was set to 25mm and the distance between the bearings was set to 230mm which provides ~82mm of casing overhang at each end of the stator to accommodate end-winding and terminations. If equation (5.5) is applied to a Jeffcot rotor manufactured from a composite with the properties summarised in table 5.7, then the analytically calculated critical speed based on equation 5.5 is 384rev/s which corresponds to 23,055rpm.

Shaft diameter	25 mm
Distance between bearings	230 mm
Shaft Young's modulus	201 GPa
Composite density	1900 kgm^{-3}
Mass	2.86 kg

Table 5.7 Baseline composite Jeffcot rotor

Repeating this process for the same diameter disk but with a weighted average density of 3420kgm^{-3} which reflects the relative proportions of the rotor occupied by the composite and the flux guides gives an analytically calculated Jeffcot first critical speed of 17,655rpm.

5.5.4. Calculation of Critical Speeds from Static Deflection of the Actual Rotor Geometry

Whereas the Jeffcot rotor provides a straightforward means of calculating rotor critical speeds, it necessarily is limited to very simple rotor geometries. An alternative method for predicting critical speeds, which is suitable for more representative models of rotor geometry and can be readily used in combination with finite element analysis, is described in [91]. This is based on calculating the critical speed from the static deflection, which is in turn calculated from beam-bending type consideration in which the rotor is supported at positions which correspond to the location of the bearings. Having calculated the static deflection, the critical speed can be calculated straightforwardly from:

$$N_c = \frac{\sqrt{\left(\frac{g}{y}\right)}}{2\pi} \tag{5.7}$$

where y is the maximum static deflection and g is the acceleration due to gravity (9.81ms^{-2}).

Figure 5.45 shows the finite element predicted static deflection for the down-selected rotor with adhesive bonded flux guides and the composite hub attached via an ideal bonded interface to a long carbon steel SAE 1045 steel shaft with the same diameter of 25mm. This is then supported by ideal representations of bearings, spaced 230mm apart.

As shown in figure 5.45, the static deflection for this rotor with this particular bearing separation arrangement is 0.000676mm. Substituting this static deflection into the expression for the critical speed yields a critical speed of:

$$N_c = \frac{\sqrt{\left(\frac{g}{y}\right)}}{2\pi}$$

$$N_c = \frac{\sqrt{\frac{9.806}{0.676\times10^{-6}}}}{2\pi}$$

$$N_c = 608\, rev.per\ second\ (36{,}530rpm)$$

As will be apparent, on this basis the first critical speed, even with a margin, is considerably higher than that predicted for a Jeffcot rotor with the same overall mass. The reason for this higher critical speed is clearly apparent from the deflection plot in figure 5.45 since the composite rotor section (which spans the central 86.2mm of the rotor when the end-caps are included) significantly stiffens the central section of the rotor, and therefore reduces the static deflection appreciably.

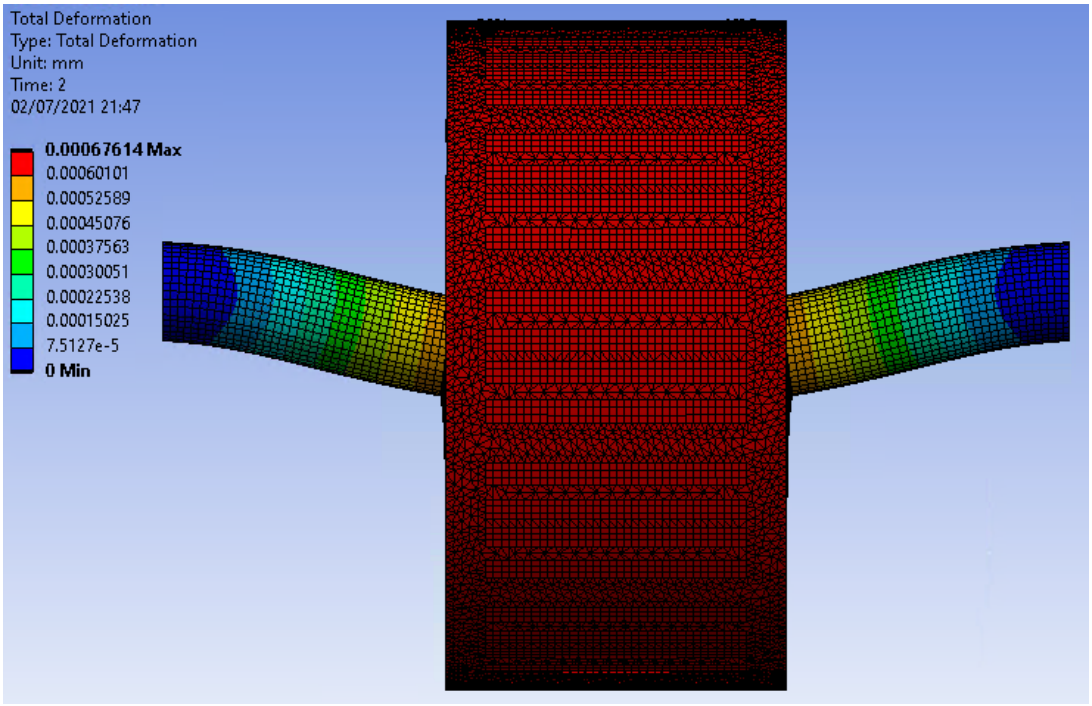

Figure 5.45 Finite element predicted static deflection for a rotor with adhesive bonded flux guides, an ideal bonded 230mm long steel shaft and ideal bonded carbon fibre tie-rods

5.5.5. Calculation of Critical Speeds using the Modal Analysis Capability within ANSYS

Within its many tools, ANSYS has a modal analysis capability to examine, amongst other things, whirling modes of rotors and shafts, and the dynamics of the modelled systems. This modal feature can also be used to calculate the first critical speed of rotors. In order to set up a model for modal analysis it is necessary to apply constraints to the displacement. In the model employed, the z-axis of the model was oriented along the length of the shaft and model was fixed in the z-axis for translational movement, with rotation fixed to be about the z-axis. The other factor in setting up the modal analysis is that that the bearings can be have finite stiffness and hence their effect can be included in the analysis. It is also possible to that the bearing stiffness can be set to a very high value within the context of the other stiffness's in the system, to approximate infinitely stiff bearings. This allows exploration of the behaviour of the rotor in isolation. Figure 5.46 shows the ANSYS modal model in which the

bearing (which are separated by 230mm) are clearly apparent at either end of a carbon steel SAE 1045 shaft.

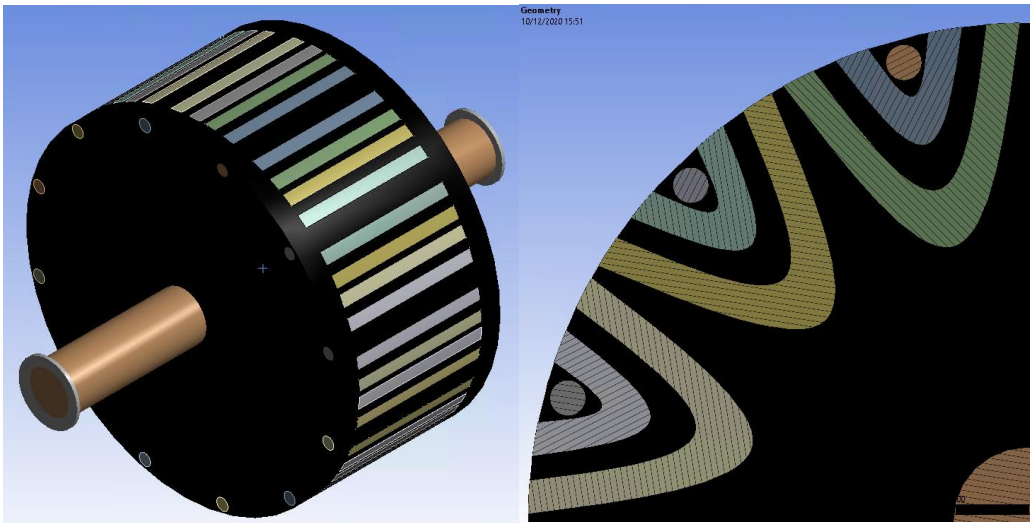

Figures 5.46 Geometry of the preferred rotor design

For an essentially infinite bearing stiffness (value set to $1 \times 10^{11}\, N/m$), the modal analysis features in ANSYS generated the following critical speeds, which are shown in terms of their order and whether they are co- or contra-rotating. Table 5.8 shows the various critical speeds (in rpm) identified from ANSYS for this rotor with essentially infinite stiffness. As would be expected the first critical speed is the lowest speed and hence the speed of interest in terms of design. This is at 47,801rpm, which compares with the 36,530rpm identified using the static deflection methods.

Critical speed order	Speed (rpm)	Resonant Frequency (Hz)	Co- or contra rotating
1	47,801	797	Co-rotating
2	74,538	1956	Contra-rotating
3	135,460	2258	Contra-rotating
4	353,230	5901	Co-rotating

Table 5.8 Critical speeds for the rotor shown in Figure 5.46 for infinitely stiff bearings

5.5.6. Representation of Finite Bearing Stiffness

The calculations up to this point in the analysis have been based on an idealised infinitely stiff bearings and hence that the first-critical speed has been determined solely by the properties of the rotor and its associated shaft. However, in many electrical machines rotors, the finite stiffness of the bearings can play a significant, and in some cases dominant, role in determining the overall rotor dynamic response. This is not to forget the role of the shaft diameter on determining the critical speed of a rotor. The length, diameter, material and stiffness of the shaft can all change the dynamic response of the rotor. This was not really an important factor in this thesis, but should perhaps be visited at some point in the future work. As noted previously, the modal analysis feature within ANSYS section is capable of calculating the critical speeds of a rotor while setting realistic values of bearing stiffness. This allows for a more realistic and accurate representation of rotor behaviour within a practically realisable machine. Following a search of candidate bearings, SKF 61905 deep groove ball bearings [94] were selected on the basis of speed rating and ability to accommodate the shaft. Data on the non-linear radial stiffness as a function of radial load was provided by the manufacturer [95] and is shown in table 5.9. As shown, depending on the radial load applied, the stiffness can range from 3.35 $\times 10^7 N/m$ under light radial loading to $1.6 \times 10^8 N/m$. In terms of the minimum critical speed, this would be achieved with the stiffness at the lower end of the range. An initial indicator of the significance of the bearing stiffness on the likely critical speed can be established by calculating the resonant frequency of the bearing when supporting the rotor mass. Neglecting gyroscopic effects, the resonant frequency is given by:

$$f = \frac{1}{2\pi}\sqrt{\frac{K}{m}} \tag{5.8}$$

Radial load [N]	Radial stiffness [N/m]
30	3.45E+07
100	5.15E+07
500	8.81E+07
1000	1.11E+08
2000	1.40E+08
3000	1.60E+08

Table 5.9 Stiffness data provided by SKF for SKF61905 deep groove ball bearing [95]

Figure 5.47 shows the variation in this resonant frequency as a function of bearing stiffness for a mass of 7.41kg. As will be apparent, for the worst case stiffness of 3.45×10^7 N/m, the resonant frequency is 486Hz which is lower than the frequency equivalent of the critical speed i.e. 797Hz as shown in table 5.8. Even at the highest stiffness in table 5.9, the resonant frequency introduced by the bearing is still likely to contribute to the rotor dynamic response.

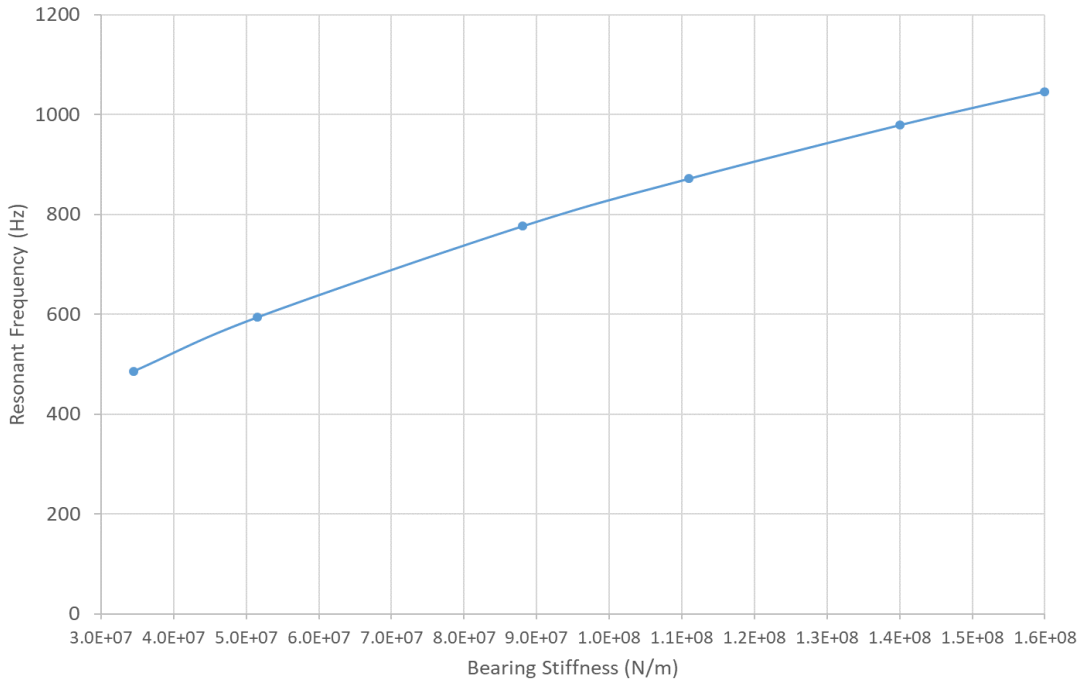

Figure 5.47 First resonant frequency of the SKF61905 bearings calculated by equation 5.8 as a function of bearing stiffness for a rotor mass of 7.41kg

For the minimum bearing stiffness of $3.45 \times 10^7\ N/m$, the critical speeds were calculated using the modal analysis feature in ANSYS and the resulting variation in the various orders of critical speeds are summarised in table 5.10

Critical speed order	Speed (rpm)	Resonant Frequency (Hz)	Co- or contra rotating
1	28,851rpm	481	Contra-rotating
2	47,801rpm	797	Co-rotating

Table 5.10 Critical speeds for the rotor shown in figure 5.46 for a bearing stiffness of $3.45 \times 10^7\ N/m$

5.5.7. Summary of Rotor Dynamic Modelling

Table 5.11 summarises the first critical speeds calculated by the various methods considered in this chapter. As noted previously given that the rotor hub extends for some 1/3 of the span between the bearings, the Jeffcott analysis is a little pessimistic. These results also show the significant influence of bearing stiffness on the first critical speed. Although these critical speeds may have become problematic if the structural behaviour had proved more promising, as shown there is ample margin

from a rotor dynamic perspective given that maximum speed established for the down-selected rotor design is only 9,500rpm when a safety factor is applied to manage adhesive failure with ageing.

Method	**Geometry and materials**	**Bearing stiffness**	**Calculated critical speed**
Jeffcott rotor analysis	170mm glass-fibre / epoxy composite disk	Infinite	23,055rpm
Jeffcott rotor analysis	170mm rotor disk with weighted mean density of the flux guides and composite	Infinite	17,655rpm
Static deflection from ANSYS structural model and application of equation (5.7)	Full model of rotor geometry	Infinite	36,530rpm
Modal analysis with ANSYS	Full model of rotor geometry	Infinite	47,801rpm
Modal analysis with ANSYS	Full model of rotor geometry	3.45×10^{7}N/m	28,851rpm

Table 5.11 Calculated first critical speeds by different methods and various bearing models (all case based on a bearing separation of 230mm)

Having now discussed the electromagnetic and mechanical design of the machine, the following chapter will examine the electrical characteristics and the winding design.

6. Dynamic Simulation and Winding Design

6.1. Introduction

The previous chapters have been concerned with electromagnetic and mechanical analysis of a wide variety of SYNCREL machine designs resulting in the down-selection of a 12 pole machine with a maximum operating speed of 9,500rpm. The electromagnetic torque calculation up to this point has been based on specifying a current density and packing factor in each stator slot rather than the definition of a specific winding with a combination of series turns and current. The design of a winding which is matched to a particular supply voltage and draws the correct current to produce rated torque is often amongst the last stages of electromagnetic design of a machine. Indeed, a particular combination of stator core and rotor can be wound with a variety of different winding arrangements to match any value of supply voltage, the key requirement being that the voltage is of sufficient magnitude to draw the correct current in the chosen number of turns to produce the required torque. If the number of turns selected is too high then the supply will run out of available voltage before the required current is drawn, whereas if the number of turns is too low, the machine draws a very large current resulting in a very large converter VA rating, and hence size and cost.

A reasonable estimate of the preferred number of series turns in a winding can often be derived from a phasor diagram approach which is inherently based on a consideration of the fundamental frequency. Although this approach is used in this chapter for initial estimates, as will be demonstrated in this chapter, harmonics in the induced winding voltage and the presence of magnetic saturation are both major issues, and a more detailed model of the machine is required. In this chapter, a dynamic SIMULINK model of the machine is developed in order to allow for the selection of an appropriate number of turns to match a representative converter voltage. The SIMULINK model developed is based on a detailed look-up tables of the flux-linkage derived from finite element analysis, to capture the full effects of harmonics and non-linearity.

6.2. Model General Architecture and Operation

Although the machine would be operated in practice from a voltage source converter, in this model, the machine is fed with sinusoidal currents as the input, and the resulting output voltage at the terminals is the model output. By adjusting the number of turns in the SIMULINK model, the various flux-linkages, currents and resistances are simply scaled to generate terminal voltage waveforms required to produce the specified sinusoidal currents, and hence rated torque. This allows the relationship between the number of series turns and the required supply voltage to be determined so that the upper limit of turns for a given supply can be established by iteration. It is important to note

that the machine model is entirely a mathematical block diagram type model and does not include any electrical circuit representations. The overall structure of the model is shown in the simplified block-diagram of figure 6.1.

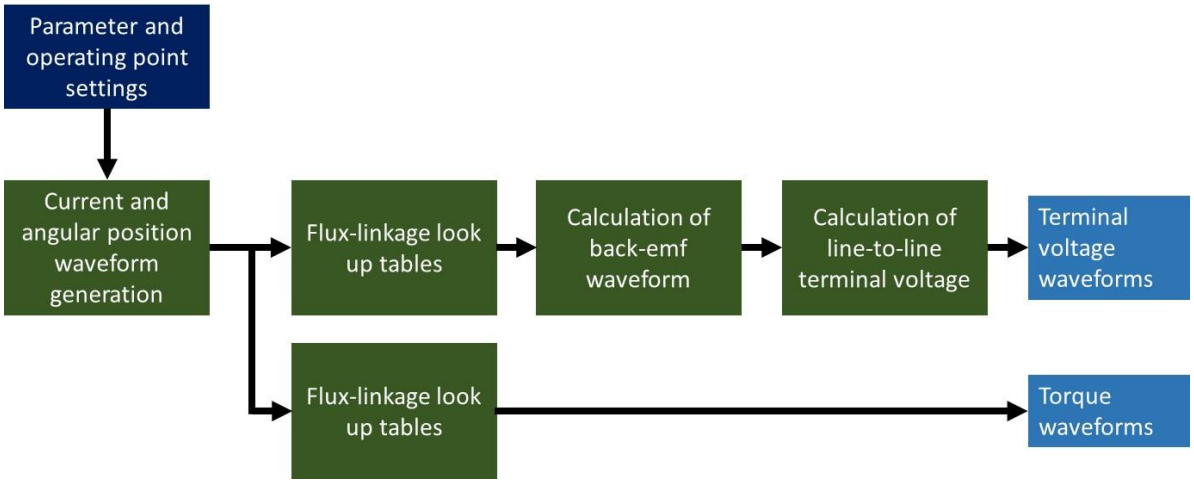

Figure 6.1 Simplified top-level block diagram of the model

6.3. Description of SIMULINK Model Sub-Systems

The various sub-systems and parameter calculation methods used to build-up this simulation model are described in the following sections.

6.3.1. Calculation of End-Winding Inductance

The end-winding inductance plays little, if any, role in determining the torque as it remains essentially fixed with rotor angular position. However, given that the stator core is relatively short in axial length in comparison to its diameter, the end-effects are likely to make some contribution to the overall winding voltage drop which needs to be taken into account. An estimate of the end-winding inductance for this stator core and winding design was calculated using MOTOR-CAD, which is a machine design package based on a combination of analytical design equations and an embedded two-dimensional finite element solver. Three-dimensional features such as end-winding inductance are calculated from various analytical equations and correction factors. Specifically, it employs a long-standing and classical analytical approach from [96].

The dimensions and winding arrangement for the 36 slot stator was input into the SYNCREL MOTOR-CAD module and resulted in a calculated end-winding self-inductance per phase of 0.47µH for a one-turn coil. The significance of this fixed inductance in the overall model can be judged by noting that the d-axis and q-axis inductances of the active regions of this machine (derived from two-dimensional finite element analysis) are 10.9µH per turn and 5.4µH per turn respectively. Despite the end-winding

inductance being small in comparison to the main active region inductances, a representation based on a fixed single-value of inductance to represent each phase winding was included in the model. The instantaneous flux-linkage per phase from the end-winding regions can be simply calculated from the product of the end-winding inductance (suitably scaled for the number of turns) and the instantaneous current. This is then added to the active region flux-linkage to obtain the overall phase flux-linkage with the arrangement of blocks shown later in figure 6.10.

6.3.2. Calculation of Stator Winding Resistance

Although the impedance of SYNCREL machines, particularly those operating at high power tends to be dominated by the reactance of the active region, it can be important to account for resistive voltage drop which also allows a prediction of the winding losses. Given that the number of series turns is a variable for this series of simulations, it is necessary to calculate the mean path length and cross-section of one turn which allows the resistance per turn at a specified temperature to be calculated. This single-turn resistance can then by simply scaled by the square of the number of turns within the SIMULINK model to obtain the winding resistance.

The cross-sectional area of the coil can be calculated from the slot dimensions and the coil packing factor. The length of the section within the stator slot is straightforward to calculate given the stator core length. However, the mean path length of the end-winding is more difficult to calculate as this requires some assumption about the geometry of the end-winding. Using the simplified coil geometry of figure 6.2, an approximation to the end-winding length can be obtained by dividing it into 3 distinct segments:

Short straight extension beyond the core – This is a fixed length, (l_{ext}) and is included to both space the end-winding away from the core and prevents the curvature in the remaining section of winding from forcing the conductors on the inner edge onto the edge of the tooth at the end of the core so as to improve the reliability of the insulation. In the initial estimate of the winding used in this analysis, this section was a fixed length of 10mm

Right-angled bend – This section is required to transition between the axial orientation of the winding as it leaves the core to a circumferential orientation to pass to the slot around the periphery through which the conductor returns. Setting the bend-radius on the inner edge to be equal to the mean coil width (w_c) results in a mean path length for a single right-angled bend of:

$$l_{bend} = \frac{\pi}{4}(1.5 \times w_c) \tag{6.1}$$

Circumferential arc which passes to the next slot for the coil – The length of this path is determined by the slot separation and the coil throw. In the case of this 12 pole, 36 slot stator with a single-layer winding, the coil conductors from one slot pass back through a slot which is 3 slot pitches away. Hence, for a slot whose mean diameter is at d_{mean} the length of a single section of this end winding component with allowance for the contribution to this span from the right-angled bend is:

$$l_{circ} = \frac{3}{36} \times \pi d_{mean} - 2 \times (1.5 \times w_c) \quad (6.2)$$

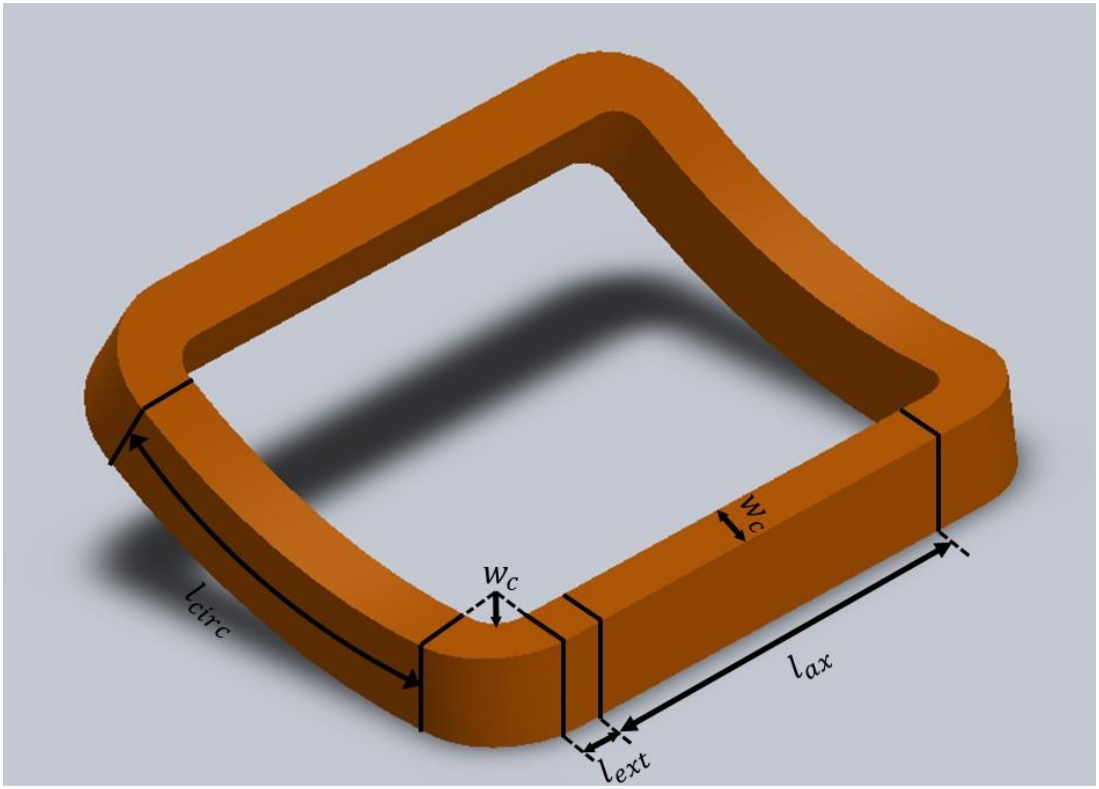

Figure 6.2 Simplified coil geometry for calculating the mean length per turn

Hence the mean length per turn for a single coil, which includes an active section in the slots of length l_{act} and equations 6.1 and 6.2 is:

$$l_{1turn} = 2l_{act} + 4l_{ext} + 4l_{bend} + 2l_{circ} = 2l_{act} + 4l_{ext} + \pi(1.5 \times w_c) + \frac{6}{36}\pi d_{mean} - 4 \times (1.5 \times w_c) \quad (6.3)$$

Substituting in values for the 36 slot, 12 pole machine into equation 6.3 yields a mean path length per turn and per coil of:

$$l_{1turn} = 2 \times 0.0662 + 4 \times 0.01 + \pi(1.5 \times 0.0084) + \frac{6}{36} \times \pi \times 0.202 - 4 \times 1.5 \times 0.0084$$

$$l_{1turn} = 267.8mm$$

Of this 267.8mm mean length per turn, only 132.4mm is contained by the active section, with 135.4mm contributed by the various components of the end-winding. In terms of copper loss, this illustrates the significant impact of end-windings and the practical importance of making them as compact as possible.

The cross-sectional area of the slot is 209mm^2, which with the application of coil packing factor (also known as a slot fill factor) of 0.5, results in a copper cross-sectional area, $A_{cu,}$ of 104.5mm^2. Hence, for a room temperature resistivity of $\rho_0 = 1.68 \times 10^{-8}$ Ωm, the resistance per turn per coil is given by:

$$R_{coil\ 1turn} = \frac{\rho_0\, l_{1turn}}{A_{cu}} \tag{6.4}$$

$$R_{coil\ 1turn} = \frac{1.68 \times 10^{-8} \times 0.267}{104.5 \times 10^{-6}}$$

$$R_{coil\ 1turn} = 43\mu\Omega\ per\ turn\ per\ coil$$

For this 12 pole winding, there are 6 coils per phase, and hence the resistance per phase per turn

$$R_{ph\ 1turn} = N^o of\ Coils\ per\ phase \times R_{coil\ 1turn} \tag{6.5}$$

$$R_{ph\ 1turn} = 6 \times 43 \times 10^{-6}$$

$$R_{ph\ 1turn} = 258\ \mu\Omega\ per\ turn$$

The value for the resistivity used above is a published value for 20°C [71]. This can be modified to any winding temperature within an acceptable operating range (i.e. up to 220-250°C) using a single-valued temperature coefficient of resistance for copper [97]

$$\rho = \rho_0\big(1 + \alpha(T - T_0)\big) \tag{6.6}$$

where

$$\alpha = 0.00386$$

$$T_0 = 20°C$$

The temperature coefficient of resistance for copper results in an increase of ~40% per 100°C temperature rise and hence, as an example to illustrate the significance of temperature, for an operating temperature of 200°C, the phase resistance per turn increases from 258μΩ per turn to 438μΩ per turn.

6.3.3. Implementation of the Resistance Calculation in Simulink

Figure 6.3a shows the principal operation of the calculation for resistance per phase in series, being dependant on the temperature of the winding and the number of turns. Figure 6.3b shows the series of Simulink blocks implementing the operation shown in figure 6.3a within the model which perform the scaling of the resistance per turn by the number of turns set for the particular simulation and scales the resistivity to reflect the operating temperature. The mean turn length and slot area calculated previously are included in the model and are scaled by assumed coil packing factor (0.5 in this study). There is one final scaling to account for the number of coils per phase.

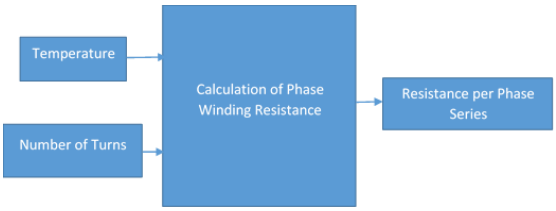

(a)

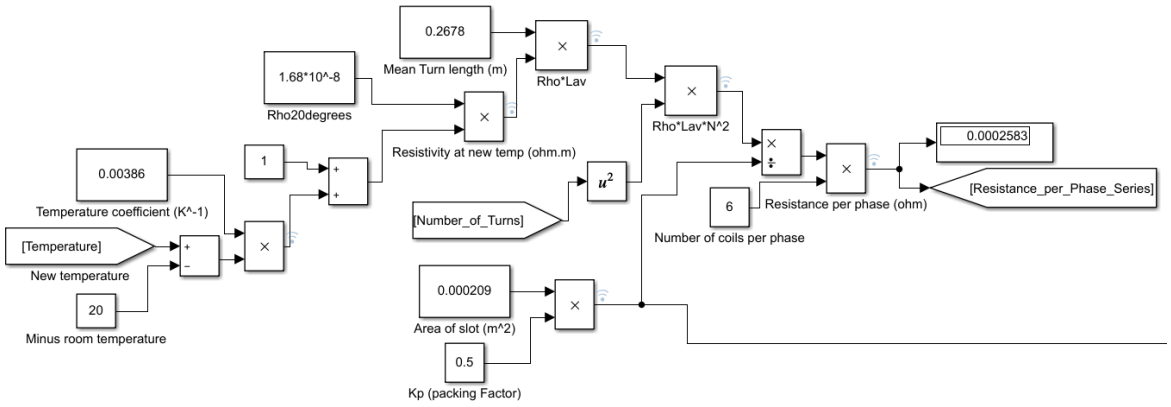

(b)

Figure 6.3 (a) Block Diagram, (b) Simulink implementation the calculation of the per-phase winding resistance (specific resistance per phase shown is for 1 turn coil).

6.3.4. Angular Position Signal

A key input to the model is an angular position signal which in turn is determined by the angular velocity as visualised in figure 6.4a. The process of translating a specified mechanical rotational speed in rpm to a re-setting 0° to 360° angular positional signal in electrical degrees is achieved with the arrangement of blocks shown in figure 6.4b along with the calculation of electrical frequency [98]. This includes a series of scaling factors to convert rpm into an electrical frequency, which then generates the instantaneous angular position variation. The resulting output, in this case for a 12 pole machine at 3,000rpm is shown in figure 6.5.

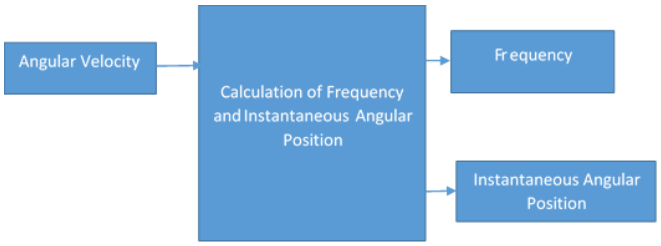

(a)

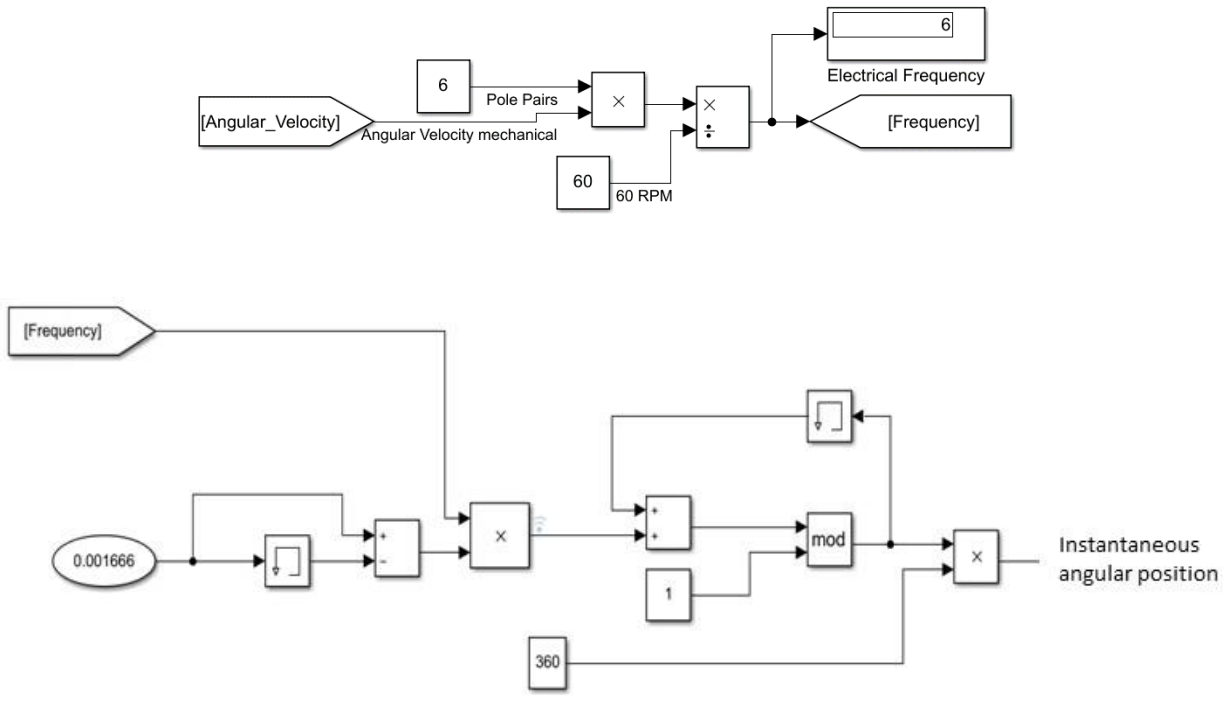

(b)

Figure 6.4 (a) Block Diagram, (b) Block diagrams of model elements which generate the re-setting angular position input for the model.

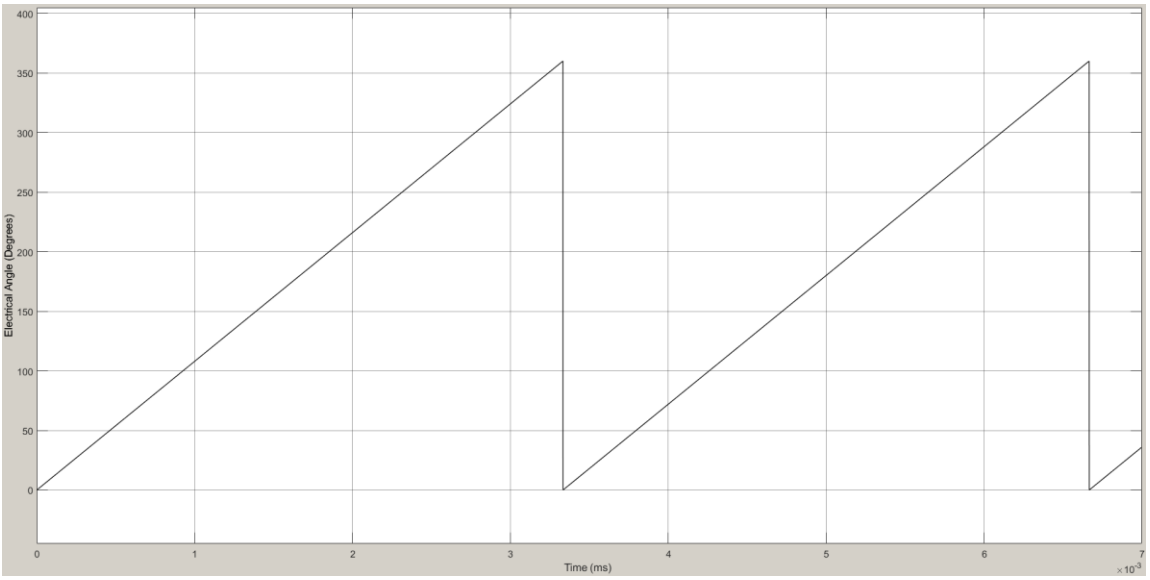

Figure 6.5 Electrical angular position produced by the sub-system in figure 6.4 for a 12 pole machine at 3,000rpm

6.3.5. Current Source Models

As noted previously, this is a current driven model and it is necessary to produce 3 phase displaced mmf waveforms to act as inputs to the flux-linkage calculations, which are synchronised to rotor angular position and allow for specification of a particular phase advance in the d-q axis frame. The parameters set for a particular simulation are the pole number, rotational speed, number of turns and the magnitude of the peak current. The principal diagram explaining this is shown in figure 6.6a and is repeated for all 3 phase currents. The arrangement of SIMULINK blocks used to generate the mmf waveforms is shown in figure 6.6b in this particular case for phase C which is 240° displaced from phase A which acts as the reference phase (defined as being at 0° at t=0 in the simulation). The input to this sequence of blocks is the re-setting 0-360° ramping electrical angle. Figure 6.7 shows a typical output from this set of blocks, in this case at a rotational speed of 8,000rpm for this 12 pole rotor under the maximum torque condition (see explanation in the next section of angular displacement convention that results in this current versus angular position variation producing maximum torque).

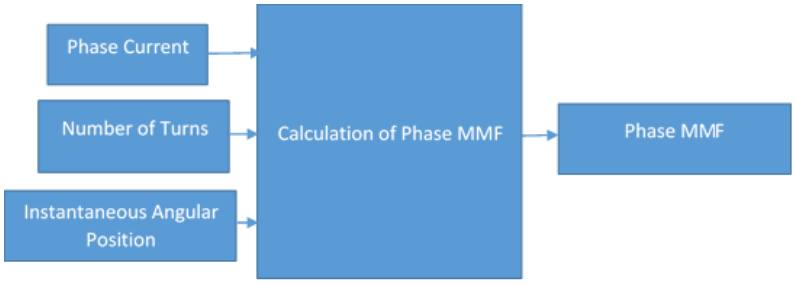

(a)

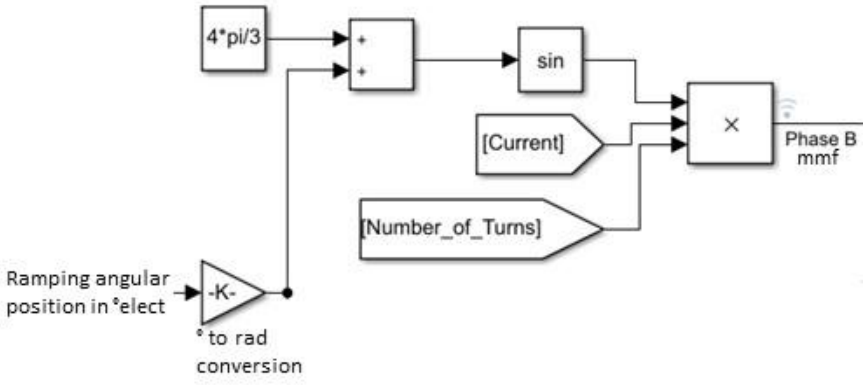

(b)

Figure 6.6 (a) Block Diagram, (b) SIMULINK blocks to generate 3 phase sinusoidal mmf waveforms

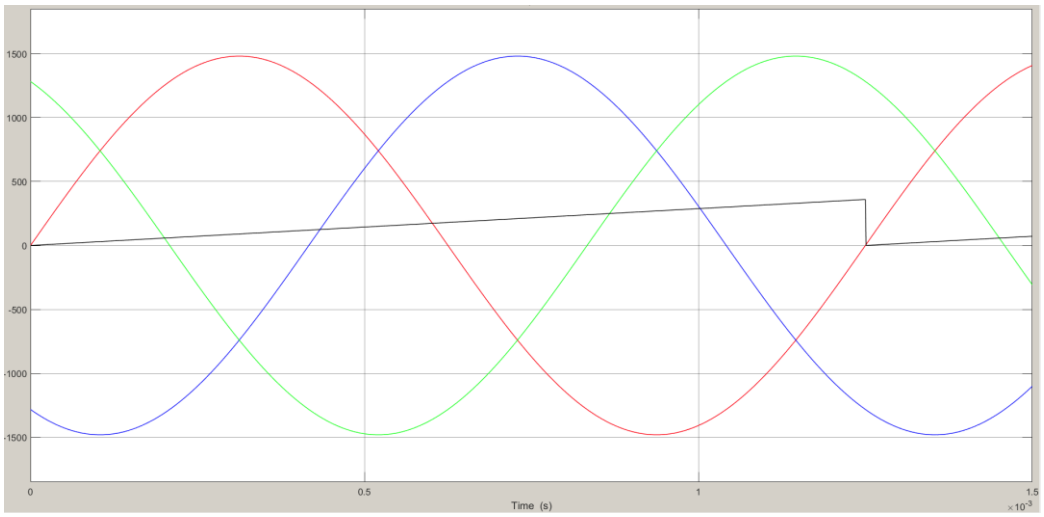

Figure 6.7 Three Phase mmf waveforms (y-axis in A.turns) and electrical angle waveform (y-axis in electrical degrees) for a rotational speed of 8,000rpm with a 12 pole rotor (phase A red; phase B blue; phase C green)

6.3.6. Flux-Linkage Look-up Tables.

The heart of the SIMULINK model is a series of four look up tables which capture the full non-linear and harmonic nature of the electromagnetic behaviour of the machine. The first three of these look-up tables contain information on the value of flux-linkage in each phase of this rotor, at different combinations of currents in all three phases and rotor angle. I.e. the flux-linkage characteristic captures the mutual coupling between phases and the fine detail of the variation with rotor angular position. The fourth look-up table maps the instantaneous torque to a given combination of phase currents and rotor angular position. Although in principle the torque could be calculated from the flux-linkage variations, given that a value of finite element predicted torque is a readily obtained as a by-product of the finite element calculations performed to establish the flux-linkage, then a separate torque look-up table offers a convenient method within the model of calculating torque for any combination of phase currents and rotor angular position.

This series of flux-linkage tables map any combination of input currents in all 3 phases (within an upper limit) and rotor angular position to a phase flux-linkage, all of which are scaled to a single-turn winding for subsequent scaling as appropriate by the number of turns under investigation in a particular simulation. Although there are four input variables which are mapped to a single value of flux-linkage for a phase, for a star-connected machine, the relationship between the phase currents at the stator point is enforced by Kirchhoff's Law, i.e. $i_a + i_b + i_c = 0$. This results in a single unique value for i_c for any combination of i_a and i_b. Therefore, this allows a reduction in the number of input variables and hence degrees of freedom in the look-up table. Despite the significant computational saving from exploiting this relationship between currents, populating the tables at a reasonable resolution does requires a very large number of finite element field solutions and a large multi-degree-of-freedom look-up table. Although the machine has a rated rms current density of 10A/mm^2, its flux-linkage was characterised up to 12A/mm^2 to both ensure that all values around the rated rms current density were interpolated between known values and allowed consideration of short-term overload within the SIMULINK model.

There is complete freedom to adopt any convention for the reference angular displacement in the look-up table, specifically the physical rotor / stator orientation that corresponds to 0° in the data set, providing this convention is then adopted consistently through the model. Figure 6.8 shows the selected rotor and stator orientation which corresponds to 0° in the data set. For this convention, then starting the rotor as 0° at the start of the simulation (i.e. at *t=0*s) means that the current in phase A has zero phase offset relative to *t=0*s for the maximum torque condition, as shown previously in figure 6.7. If a simulation is required for a particular combination of i_d and i_q within a rotating d-axis frame,

then some conversion would be required to ensure the correct phase offset for the 3 phase currents relative to *t=0*.

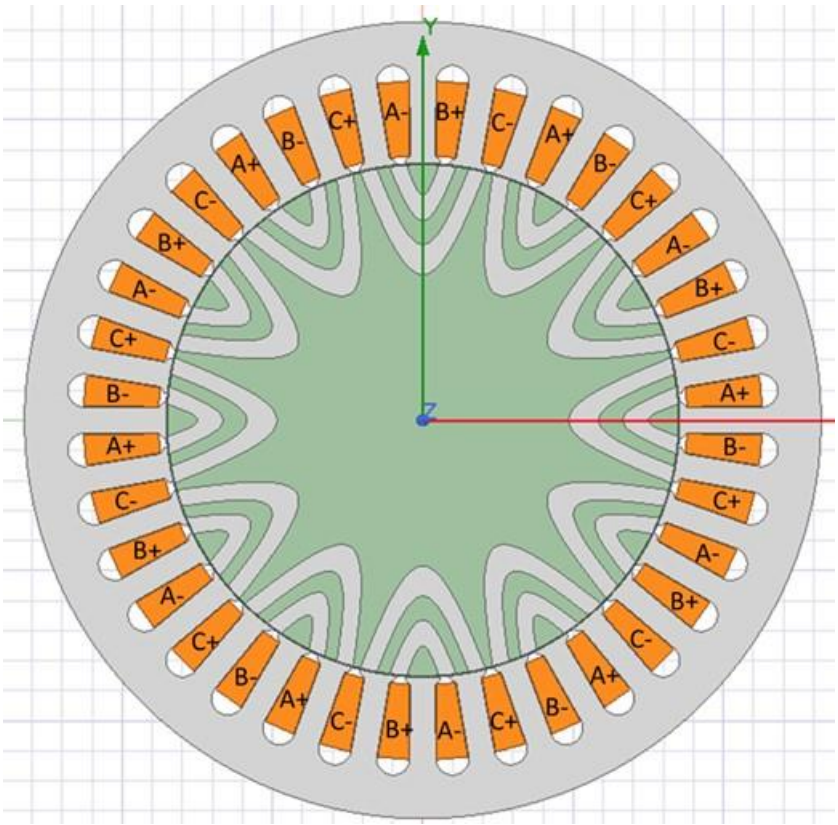

Figure 6.8 Stator/rotor orientation for 0° angular displacement with the adopted convention

The process by which the table is built up from finite element analysis can be best appreciated by working through an example. Taking the point on a sinusoidal waveform at which the currents in phases A and B are set to +1777A (which is 50% of the peak current in single turn, in one slot at the rated rms current density of 12A/mm^2) then from the constraint imposed on the current in phase C by the star connection, this current can only take a value of -3554A (corresponds to the peak current in a single turn in one slot). If this combination of currents is then imposed in the machine slots as a fixed 'DC' current at the required value, and the rotor is then rotated through one electrical cycle allowing it to interact with the static magnetic field produced by the fixed currents, then the flux-linkage waveforms in the 3 phases can be calculated from a series of finite element calculations at discrete intervals over the cycle. An example of these waveforms is shown in figure 6.9. These variations of flux-linkage with angular position are specific to this combination of currents alone, recalling that it is strictly specific to a combination of i_a and i_b since i_c is uniquely defined.

This process was repeated for combinations of phase currents to generate a comprehensive look-up table. The increments of current used to generate the look-up table involves a trade-off between

capturing the full intricacies of non-linear magnetic behaviour and the time taken to perform the simulations and the resulting size of the look-up table. It is worth noting that SIMULINK employs high-order interpolation to extract intermediate values between calculated points in look-up tables. For the purposes of this study, inclusive combinations of 11 values of i_a and i_b were considered spanning the DC currents from +1777A to -1777A in 355 A increments in each case (20% of maximum). This resulted in 120 finite element simulations for the combinations, each spanning one electrical cycle. The double zero combination for i_a and i_b (which would be the 121st case) is trivial in this singly excited machine. For each combination of i_a and i_b, a unique value of i_c comes out of Kirchoff's law at the star point. This allows a full range of flux-linkage plots to be built up for the rotor. It is worth noting that data for the variation in flux-linkages of phases A, B and C and torque across an electrical cycle can be extracted from one finite element simulation. For example, figure 6.9 shows the variation of flux-linkage in all 3 phases across one cycle (in 3° electrical angular increments using the convention of angular displacement is 0° at the rotor/stator alignment shown previously in figure 6.8) for one particular combination of i_a and i_b and, by implication, i_c. This is one of a set of flux-linkage characteristics for all 3 phases which are derived from 121 such finite element simulations (i.e. all-inclusive combinations of 11 values of both i_a and i_b).

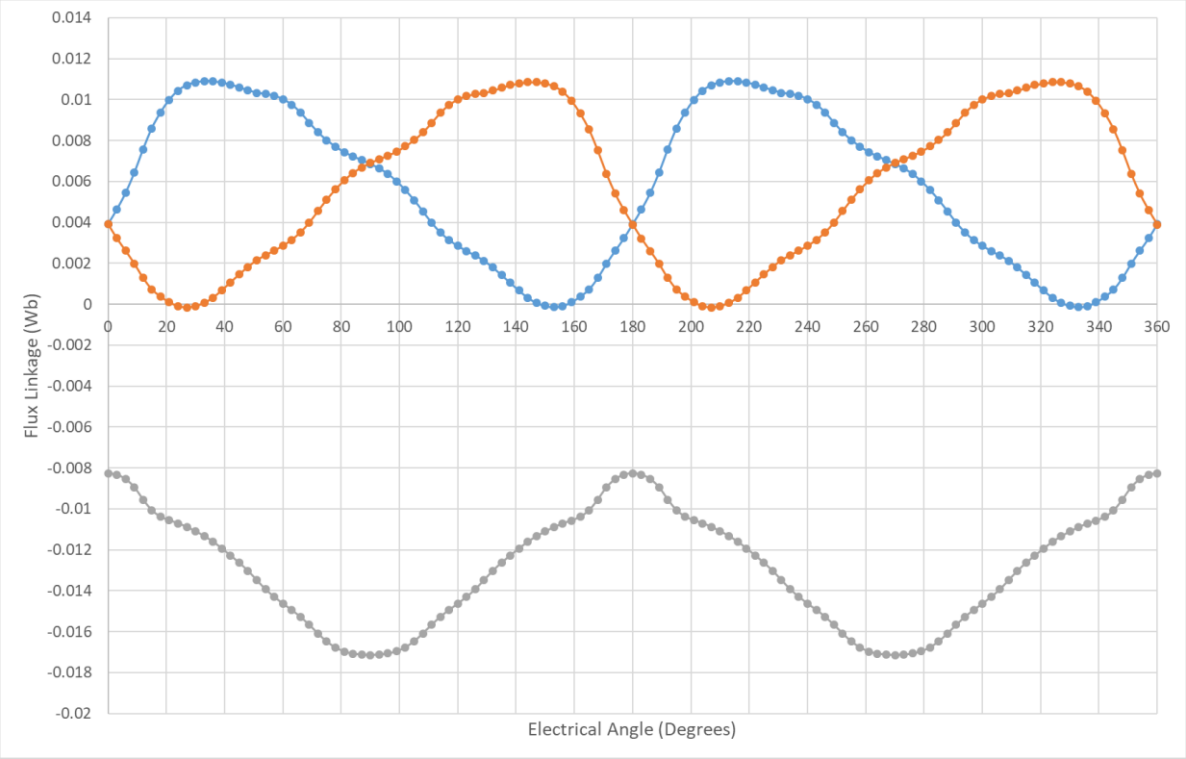

Figure 6.9 Typical variation in flux-linkage over one electrical cycle for phases A, B and C (fixed DC currents of +711A, +711A and -1422A in phases A, B and C respectively)

Some conversion was required from the ANSYS Maxwell output which is in a CSV (comma separated value) format and specific to that simulation, and the rows and columns format required for the look-up table. The resulting SIMULINK 3D look up table for phase A flux-linkage is an 11x11x120 table in which inputs of i_a, i_b and rotor angular position generate a unique value of flux-linkage or torque. A visualisation of this process is shown in figure 6.10a. Each of the three phase flux-linkage tables is used to generate the overall flux-linkage, including a contribution for the end-winding inductance using the arrangement of SIMULINK blocks shown in figure 6.10b.

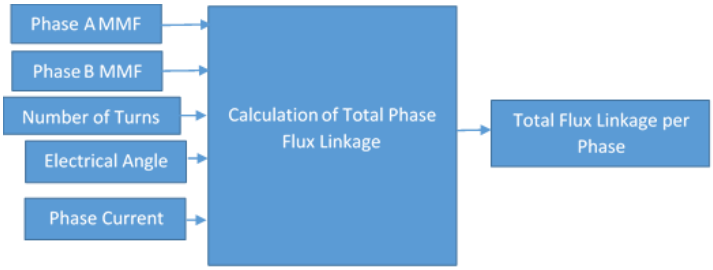

(a)

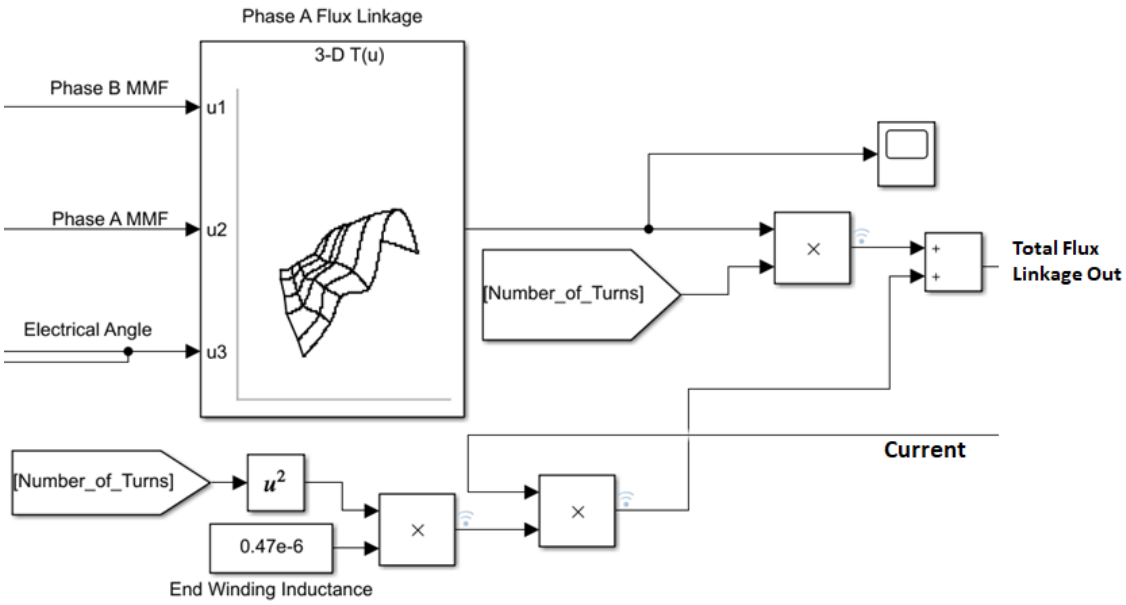

(b)

Figure 6.10 (a) Block Diagram, (b) Block arrangement for calculation of total phase flux-linkage

The setting up of this multi-dimensional table with a large data set (14,520 entries) required significant testing to ensure correct data alignment, correct offsetting of rotor angle to table elements etc. As an example, figure 6.11 shows a comparison between the variation of flux-linkage with time, generated within Maxwell for a peak current of 1481A at 1 turn corresponding to a rms current density of 10A/mm^2 and a mechanical speed of 60rpm, which is an electrical frequency of 6Hz, and the

representative flux-linkage waveform from the look-up table at the same conditions that were input to Ansys.

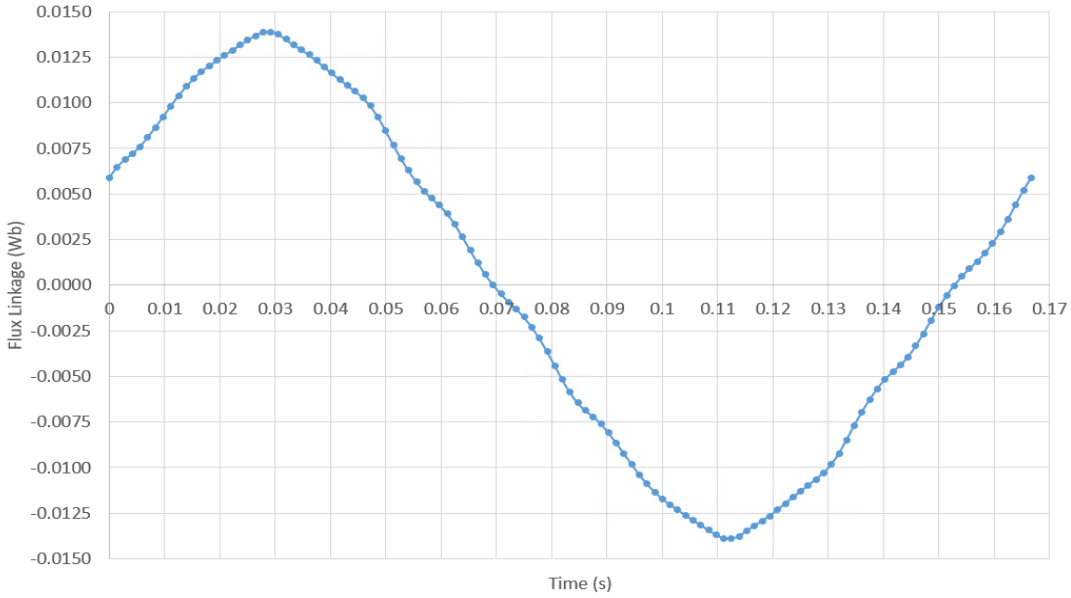

(a) Flux-linkage from Maxwell

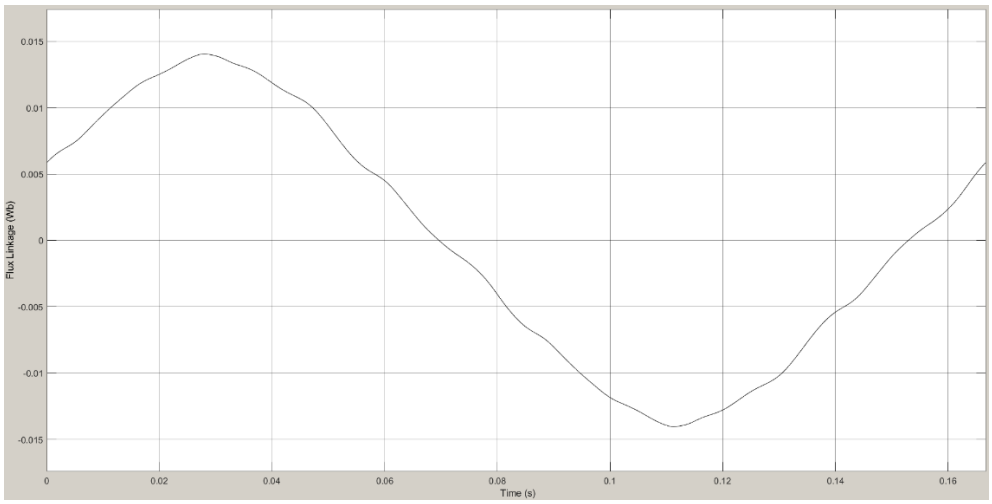

(b) Flux-linkage from look-up-table

Figure 6.11 Comparison of flux-linkage waveforms for phase A using a peak current of 1481A at 1 turn corresponding to a rms current density of 10A/mm^2 at a mechanical speed of 60rpm

6.3.7. Calculation of Back EMF

Having mapped the full variation of flux-linkage with current and rotor angular position, the resulting values of induced emf can be calculated by application of Faraday's law, $e = -N\frac{\partial \varphi}{\partial t}$ [99]. This is shown visually in figure 6.12a and using the arrangement of SIMULINK blocks shown in figure 6.12b, again

with scaling for the number of turns. It is recognised that the use of a derivative block requires careful consideration within a time-stepped SIMULINK simulation, especially around start-up where initial conditions must be managed to avoid a very large and entirely mathematical based transient at start up.

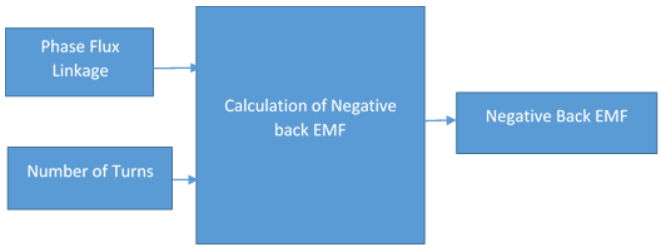

(a)

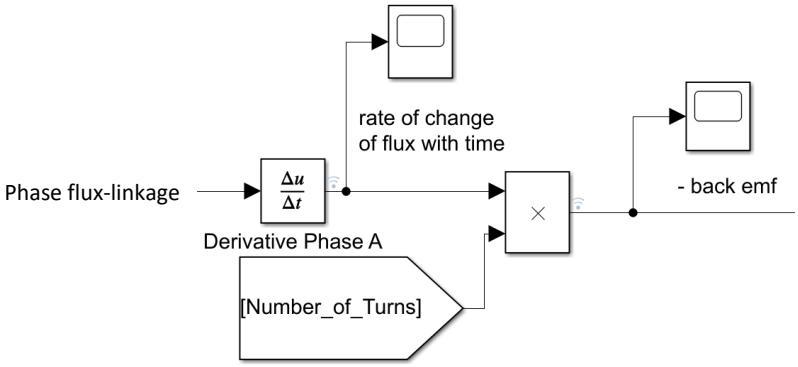

(b)

Figure 6.12 (a) Block Diagram, (b) Arrangement of SIMULINK blocks for calculation of induced voltage from phase flux-linkage.

6.3.8. Calculation of Terminal Phase Voltage

In this singly-exited machine, the back-emf, or induced emf, includes all inductive effects within the active region and a simplified representation of the end-winding. The only additional component which must be added to the induced emf to establish the instantaneous terminal voltage is the resistive volts drop contribution which can be calculated straightforwardly from the resistance and the instantaneous current (both scaled appropriately for the number of turns). The calculation of the terminal voltage is shown visually in figure 6.13a and achieved with the arrangement of SIMULINK blocks shown in figure 6.13b which also includes the calculation of the line to line-voltages.

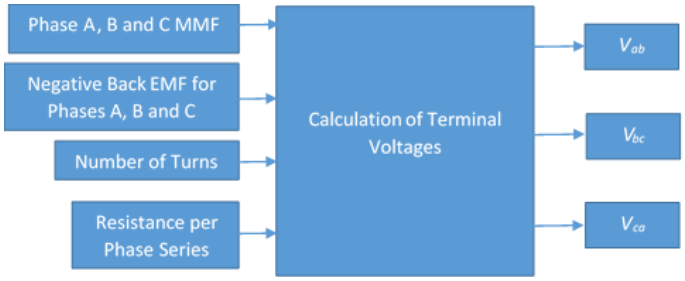

(a)

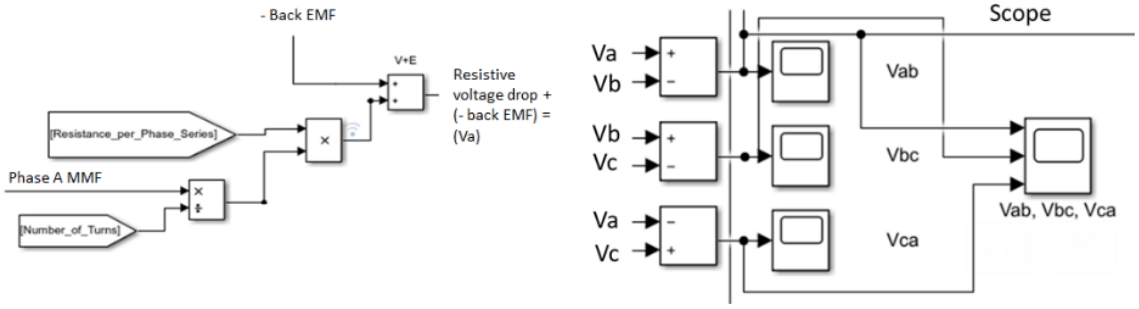

(b)

Figure 6.13 (a) Block Diagram, (b) Arrangement of SIMULINK blocks for calculation of terminal voltage.

6.4. Winding Analysis and Design

The various models described in the previous section can in combination allow the line voltage to be calculated for a given imposed current waveform, with full account of spatial and time harmonics and magnetic saturation. From a design perspective, this approach of establishing the maximum voltage required to deliver the desired current waveform (and hence torque) provides an efficient means of establishing the number of turns required on each coil to make best use of the available converter voltage limit. Following from the mechanical analysis in chapter 5, the winding was designed for a maximum rotational speed of 9,500rpm.

Figure 6.14 shows the calculated line-to-line terminal voltage waveforms for the machine rotating at 9,500rpm with a peak phase current of 494A in 3 turns per coil (18 turns per phase), which corresponds to the rated peak mmf of 1482A at a rms current density of 10A/mm^2. The current phase angle in the d-q axis frame is 42°, this value being the optimal current angle for this design established from finite element analysis. For a winding temperature of 200°C, the phase resistance for this 3 turn winding is 3.94mΩ. As will be apparent, the resulting voltage waveforms involve a significant deviation from a

sinusoidal voltage with a peak value of 578V. An FFT of the terminal voltage waveform of phase A is shown in figure 6.15, from which it is apparent that the fundamental only has a magnitude of 440V.

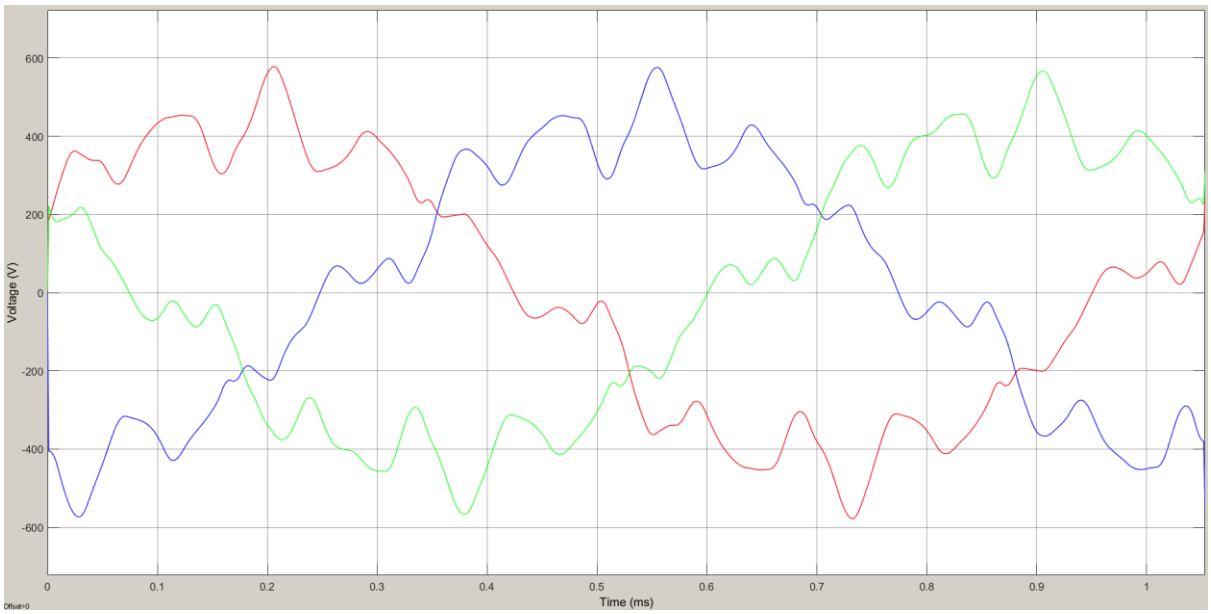

Figure 6.14 Predicted terminal voltage at 9,500rpm for a sinusoidal phase current with a peak of 494A in a winding with 3 turns per coil (V_{ab} – red; V_{bc} – blue; V_{ca} – green)

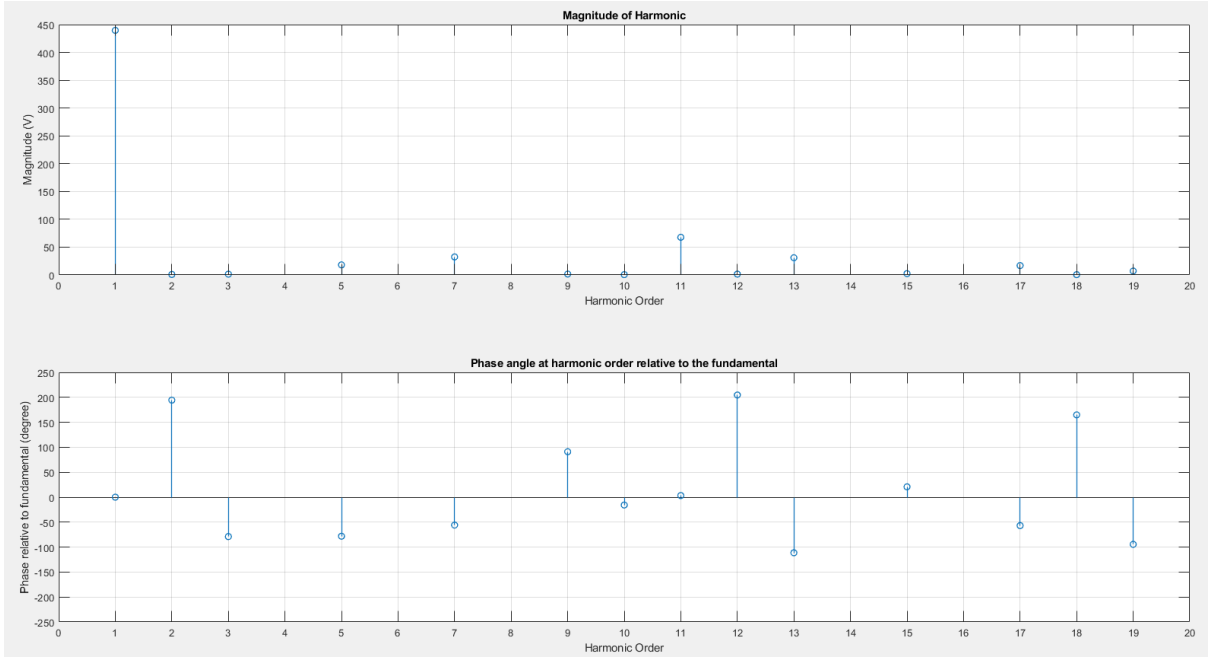

Figure 6.15 FFT spectrum for the V_{ab} line-to-line voltage waveform of figure 6.14 at 9,500rpm for 3 turn coils

It is interesting to compare the magnitude of the fundamental from the FTT with an analytically derived value based on a standard d-q axis model described in chapter 2. For a current of peak

magnitude 484A in 3 turns at an advanced angle of 42° then the peak d-axis and q-axis currents are 440A and 397A respectively. The d-axis and q-axis inductances for 3 turns are 0.0984mH and 0.0486mH respectively. Neglecting the small influence of the voltage drop due to phase resistance and with the reference to the phasor diagram and accompanying analysis in chapter 2, the calculated terminal voltage is 497V peak. This demonstrates a fair agreement with the fundamental from the FFT of 439V, but is significantly lower than the peak value of 578V in figure 6.14.

Given that the peak voltage with 3 turns as shown figure 6.14 still has some margin to the 800V supply specified in chapter 1, the number of turns was increased to 4 per coils which corresponds to 24 turns per phase for the 6 series connected coils. Figure 6.16 shows the terminal line-to-line voltage waveforms for 4 turns per coil at 9,500rpm and rated torque (corresponds to a peak phase current of 370.5A) while figure 6.17 shows the corresponding FFT spectrum for V_{ab}. In this case the resulting peak line-to-line voltage is increased to 771V with a 586V fundamental. Given that the peak voltage is right on the limit of the supply voltage, there would appear to be no scope for moving beyond 4 turns per coil while remaining within the available supply voltage.

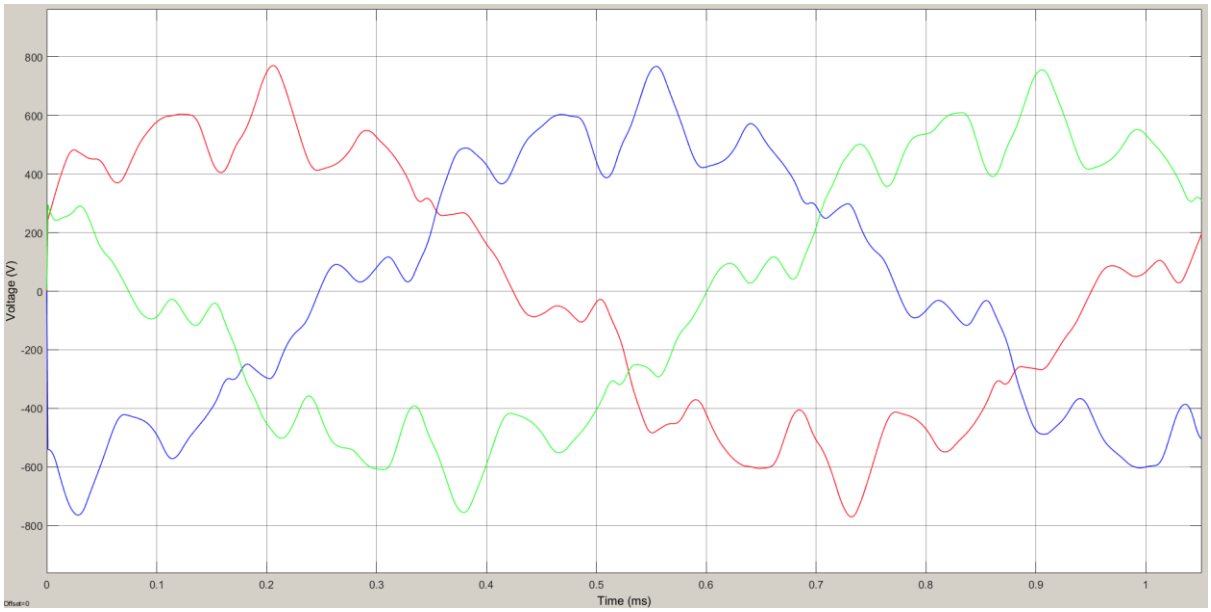

Figure 6.16 Predicted terminal voltage at 9,500rpm for a sinusoidal phase current with a peak of 370.5A in a winding and with 4 turns per coil

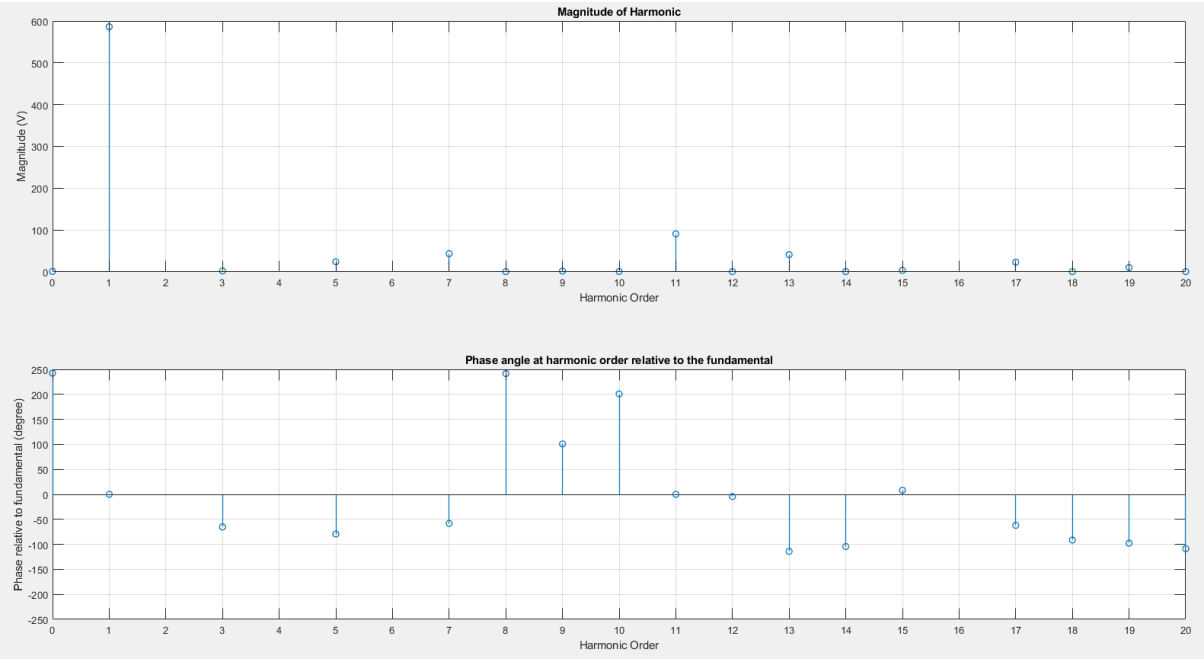

Figure 6.17 FFT spectrum for the V_{ab} line-to-line voltage waveform of figure 6.16 at 9,500rpm for 4 turn coils

Adopting 4 turns per coil results in a converter with a rating of 800V pk line-to-line voltage and a peak phase current of 370.5A, correspond to a converter VA rating of 296kVA. At 9,500rpm, the mechanical output power for 85Nm torque is only 71.2kW. Hence the utilisation of the converter VA rating, which determines its size, cost and losses, is a very poor at 24%. This measure of mechanical output power as a percentage of converter VA rating is in many ways analogous to a power factor in a purely sinusoidal context, and dramatically illustrates a well-recognised shortcoming of the SYNCRELs, i.e. the poor utilisation converter rating and poor power factor at 0.24. Despite the potential low cost of the SYNCREL machine itself, the knock-on effect on converter cost can consume or indeed exceed the cost benefits of the machine compared to say a permanent machine and converter combination. This is a well-recognised trade-off in switched reluctance machines where the converter cost is often prohibitive.

It is worth noting that to some degree the problem in this machine has been exacerbated by requiring significant voltage overhead to maintain a purely sinusoidal current in the face of significant harmonic flux-linkage effects. If 5 turns were to be adopted then at some instances during the cycle, e.g at 0.2ms for V_{ab} in figure 6.16 (which is for 4 turns), the closed loop controller which is maintaining the sinusoidal current would saturate and the current would fail to track the demanded sine-wave until the voltage demand again dropped below the available supply.

This chapter has explored the winding design and electrical simulation for the machine, and following on from this, the construction of the prototype is explained in the next chapter.

7. Prototype Manufacture

7.1. Introduction

The planned culmination of the research project was the manufacture of a demonstrator machine based on the 12 pole design established at the end of chapter 5 with the winding design of chapter 6. The design was fixed and drawings prepared for the manufacture of the various elements by a combination of external companies and internal workshop facilities. This work was initiated prior to the COVID19 lock-down, but was severely affected by a combination of external delivery and more particularly in-house workshop shut-down and subsequent capacity. These difficulties were compounded by a re-design of the proposed casing being required to accommodate the larger end-windings and technical issues related to the in-house machining of the FR4 composite sheet. At the time of submission of this thesis, although several of the component parts have eventually been completed, some key elements remain outstanding and prevented assembly or any useful testing of the machine. Nevertheless, the following section described the progress that was made, almost all of which was achieved during lock-down.

7.2. Stator Core Manufacture

The stator core was externally manufactured by LCD LaserCut AG. This was achieved by bonding together a series of 0.2mm thick laser cut Cogent NO20 Silicon iron sheets which were pre-coated with Suralac 9000 adhesive. The bonded stator core, which is 66.2mm thick is shown in figure 7.1.

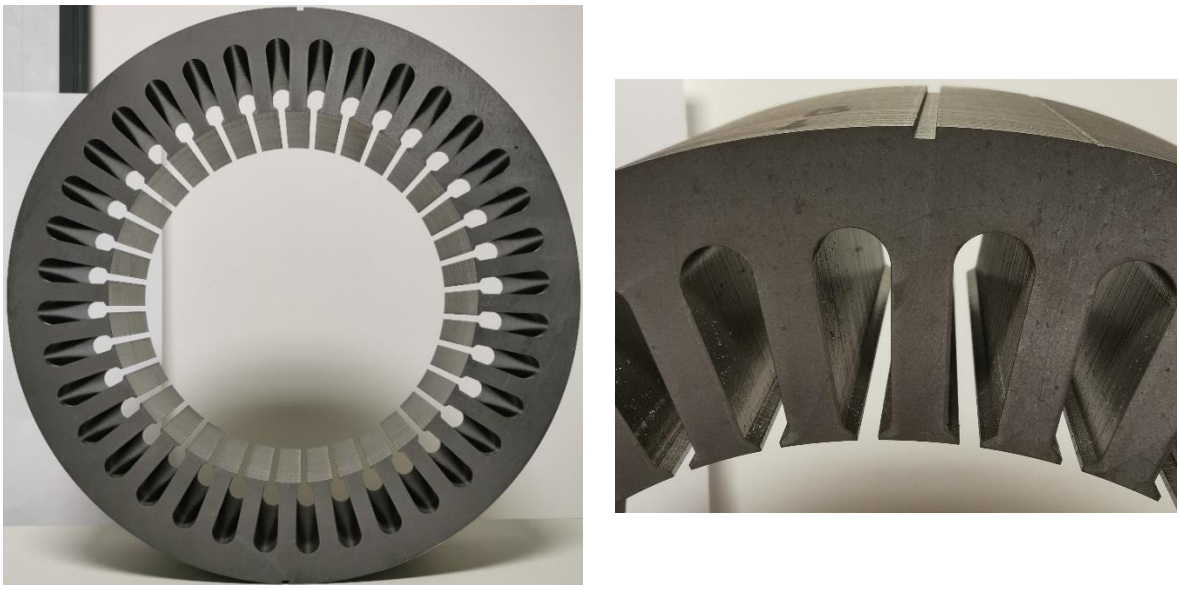

(a) Complete stator core **(b) Close up of stator slot and keyway slot**

Figure 7.1 Manufacture silicon iron stator core

7.3. Stator Winding

At the end of chapter 6 it was established that a winding with 4 turns per slot and a series connection of the six coils in a phase would provide a match with some overhead to an 800V supply voltage when delivering rated sinusoidal peak phase current of 370Apk at 9500rpm. As noted in chapter 6, the low power factor of this machine (approximately 0.31 at a rms current density of 10A/mm^2) results in a poor utilisation of the supply VA requiring a converter VA rating of 275kVA for a mechanical power of 84.6kW. A commercial converter was to be made available from another project to support testing of the 12 pole prototype. This is a Semikron SKAI 45 A2 GD12-WCI with a voltage rating of 800V and 300A [100]. The current rating of this drive is not sufficient to test the machine at full torque even at low speed with the original 4 turn per coil winding. In setting out a plan for testing of this machine and given the absence of a suitably rated converter, it was decided to arrange the winding such that it operates with two distinct connections to allow the torque to be verified at low speed and the high-speed operation to also be verified in a separate test, albeit with a reconfigured winding, although this would necessarily not be at full torque. It is important to stress that re-configuring the winding into different series / parallel arrangements was intended for testing purposed only given the constraints of the proposed converter, and is not a viable operational mode for the machine in service. In operation it would be necessary to rate the power electronic converter appropriately to cover the full torque and speed range.

The starting basis for reconfiguring the actual winding design for normal operation consists of 6 series connected coils each of which has 4 turns (located in 12 slots as 6 pairs of ‘go’ and ‘return’ conductors in a single layer winding) as shown in figure 7.2a. Several options were reviewed. The final configuration adopted was to increase the number of turns per coil to 12 and then arrange the winding in the two arrangements shown in figures 7.2b and c. The parallel connection shown in figure 7.2c replicates the behaviour of the original winding design of figure 7.2a from a terminal voltage and slot mmf perspective while the series arrangement in figure 7.2b allows rated torque operation up to ~3000rpm before reaching the voltage limit. The series arrangement in figure 7b section also allows the current density in the coils to be increased well beyond 10A/mm^2 if required for a brief interval to measure the short-term overload capability while remaining within the power converter rating.

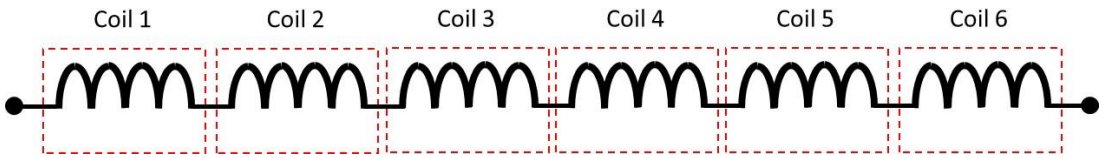

(a) As –designed phase winding from chapter 6 (6 series connected coil each of 4 turns)

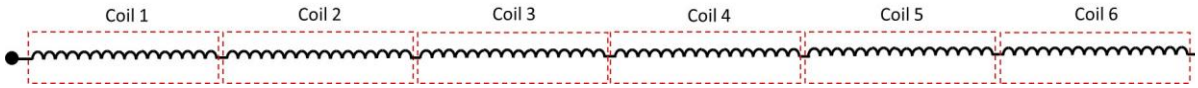

(b) Low speed series connection for rated torque and above (6 series connected coils each o 12 turns)

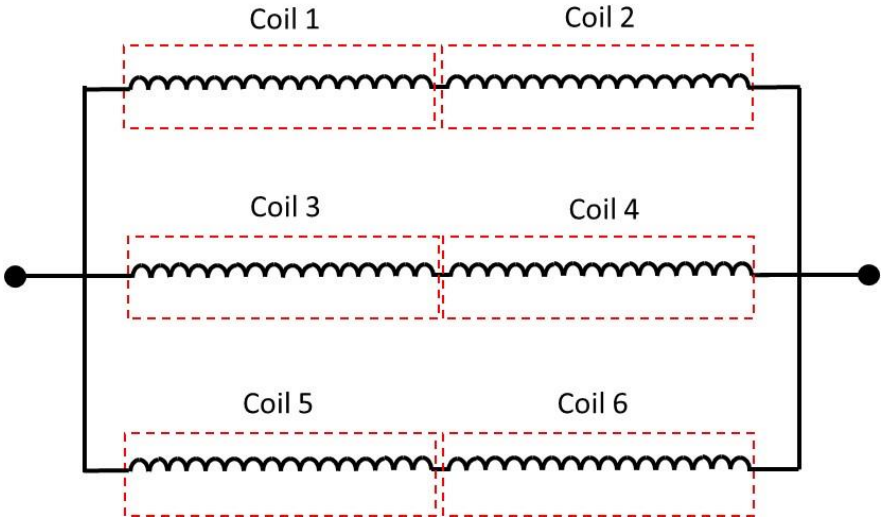

(c) High-speed connection (3 parallel paths each with 2 series connected coils of 12 turns)

Figure 7.2 Alternative winding configurations to manage converter limitations

The increase in the number of turns per coil and hence per slot results in a proportional decrease in the conductor-sectional area per turn. However, the three-fold reduction in the cross-section of the bundles of parallel strands being wound with the 12 turn per coil variant is useful in terms of coil manipulation and forming of the end-windings.

The manufactured stator core was sent out for winding by an external winding company (Portland Electrical Ltd) in line with the winding design set out above. Figure 7.3 shows the wound stator part-way during manufacture while figure 7.4 shows the completed stator winding (dip varnished) from which it will be evident that the end-windings achieved are not as compact as those expected at the design stage or would be acceptable in volume production. As can be seen, the section of end-winding which runs circumferentially from one slot to the other follows an arc shape while the linear extension

beyond the core is 35mm rather than the 10mm assumed in the model of figure 6.2. This vastly greater axial extension was deemed necessary by the winding company to allow the manual preforming of looped coils with sufficient spare length to allow manipulation into the slot. It would be expected that this could be reduced dramatically for a machine-wound stator.

The overall axial length of the wound stator including the end-winding is 201mm, with the slightly greater overhang at the coil termination end (maximum of 73mm) compared to the non-termination end (maximum of 62mm). Approximate measurements were taken of the end-winding lengths with ~163mm at the termination and ~150mm at the non-termination end. This gives an approximate measured mean length per turn of 445mm which is considerably greater than the 267.8mm assumed in the design phase. The final winding consisted of 12 turns in each slot, with each individual turn made up from 11 parallel strands of 1.00mm wire. This gives an overall cross-sectional area for 1 turn of 8.64mm^2 and a slot packing factor of 0.496 which is very close to the 0.50 values used throughout the design in this thesis (well within the resolution of discrete wire diameters available).

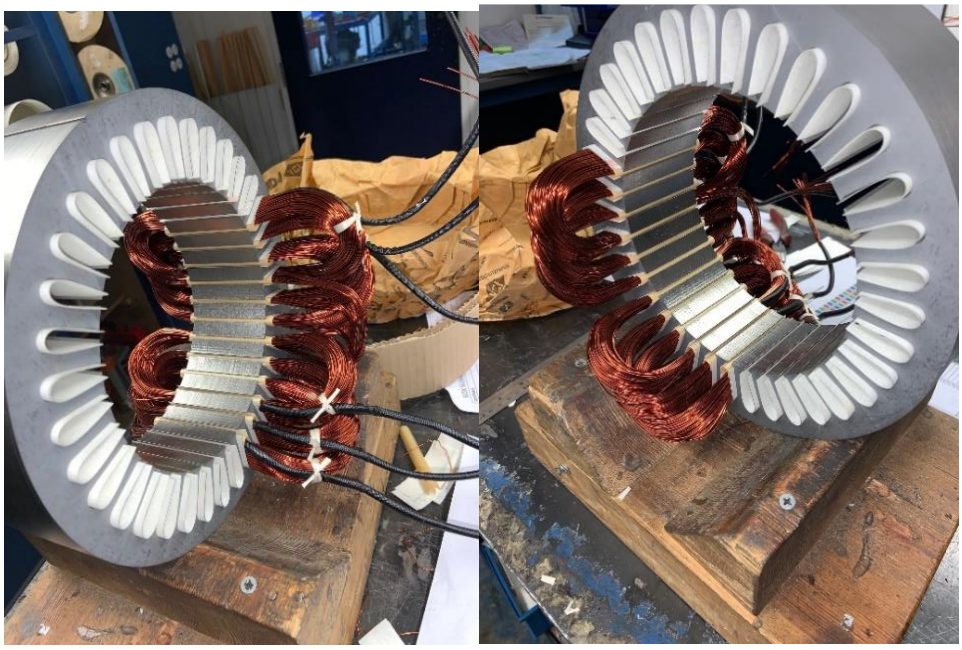

Figure 7.3 Stator part-way through coil winding

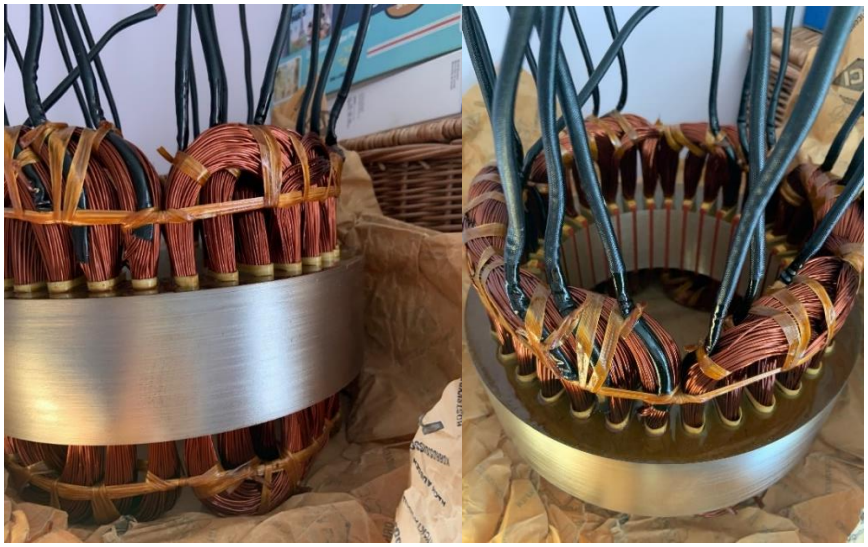

Figure 7.4 Completed stator winding

7.4. Rotor Flux Guides

The rotor flux guides were manufacture by CNC wire-erosion of a pre-bonded stack of the same 0.2mm thick lamination sheets with Suralac 9000 coating by an external supplier. The 24 flux guides manufactured are shown in figure 7.5

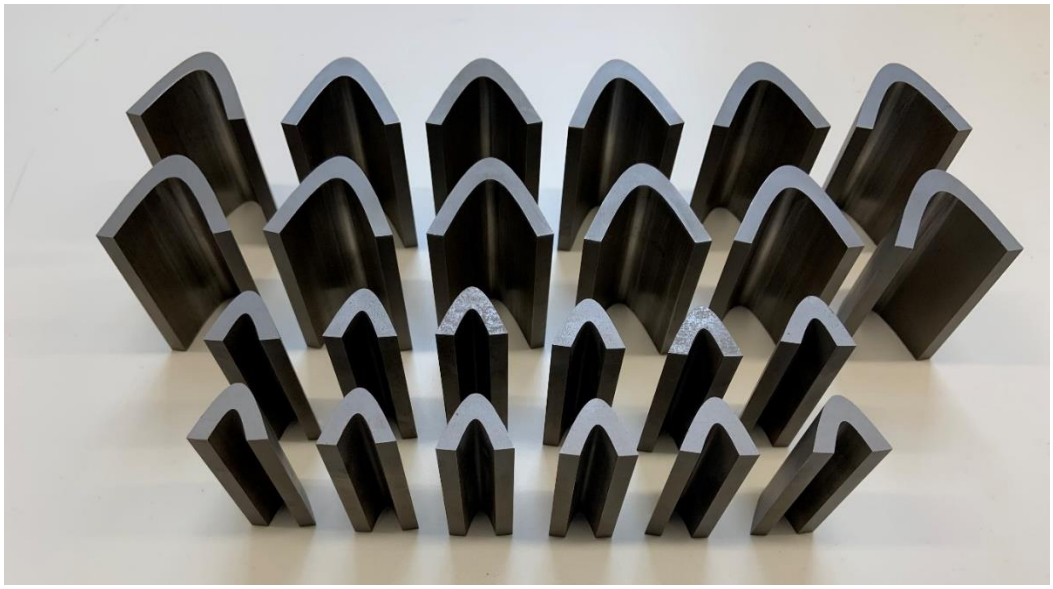

Figure 7.5 Manufactured flux guides

7.5. Composite Rotor Hub

As discussed in chapter 1, although the ultimate concept for this rotor was to employ form of moulding of a fibre reinforced material such as a bulk-moulding compound, in practice it proved necessary to employ 20mm thick commercially produced FR4 sheets. A large 1.2m x 0.6m sheet of 20mm thick FR4

was sourced but this required external water-jet cutting to produce square pieces for a CNC milling process. The parts to be milled are shown in the CAD renders of figure 7.6, the two slightly different parts being for mid-sections and end-sections. The complex profiles which locate the flux guides are blind channels to a depth of 13.1mm in each of the end-plates plate. As will be apparent, these parts have additional material on what would be the outer surface of the rotor. The manufacturing method selected was to bond the flux guides and tie-rods into the FR4 disks and join them to each other, following which the rotor would be machined and then ground back such that the front face of the flux guide just became visible. This allowed the location of the flux guides to be set by the precision of the CNC machined hub rather than the fitting together of multiple section of the hub.

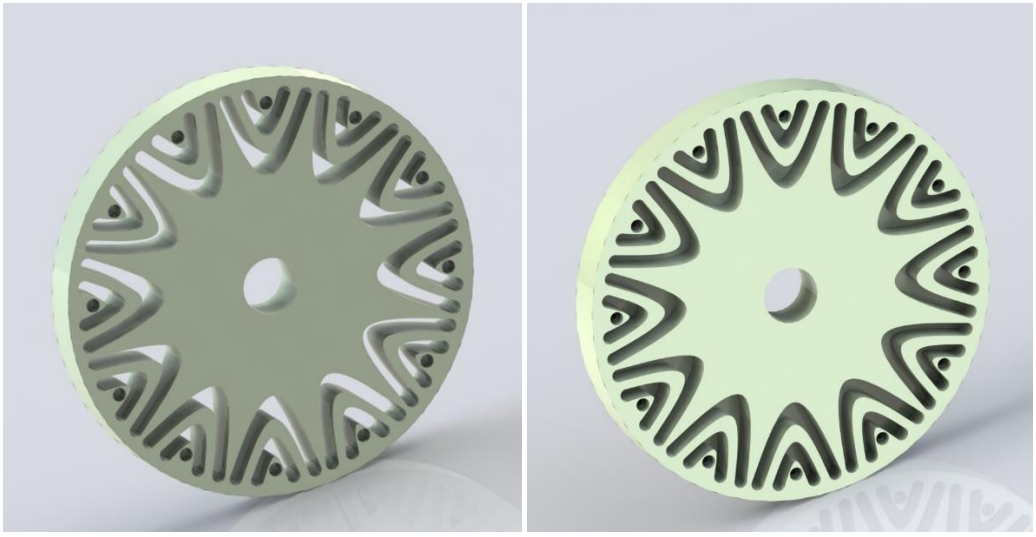

Figure 7.6 CAD drawings of the two FR4 component (2 of each required to achieve the desired overall length)

Although the blank sheets have been cut up in preparation for CNC milling by water-jet cutting as shown in figure 7.7, the CNC cutting of the rotor pieces for figure 7.6 have been held up by reduced workshop availability and some of de-laminating issues on some plates from the water jet cutting.

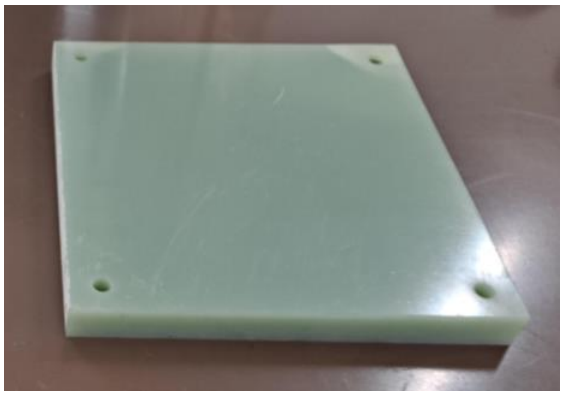

Figure 7.7 FR4 board blank ready for CNC machining of the profile of figure 7.6

7.6. Summary of Prototyping Status

Although the build and test activity was intended to be the culmination of the research project, extended delays due to lock-down have resulted in the prototype remaining unfinished at the point of thesis submission. However, significant progress was made in bringing this challenging prototype to fruition and, as identified in chapter 8, completion of the prototype and its testing is the core recommendation of immediate future work on this topic.

8. Conclusions and Future Work

8.1. Conclusions

This thesis has reported on an extensive investigation into a novel concept for a high-speed synchronous reluctance machine in which an array of flux guides is embedded in a glass-fibre reinforced hub. Ultimately, it has been shown through detailed electromagnetic and mechanical modelling that this concept does not in practice offer the combination of high power density and high speed capability envisaged by the original industry sponsor. This shortfall in performance was mainly due to the difficulty in mechanically retaining the flux guides and the very severe penalty in torque density which is incurred when the effective magnetic airgap is opened up to accommodate retaining features around the outside of the rotor. This is by no means a failure of the machine concept, but when referring to the original question proposed at the start of chapter 1 the answer should be considered as a possible no. This style of machine, designed using this pole number and with this diameter constraint was not a machine that could operate at high speeds. It would be much more suited for maybe lower speed, smaller diameter designs. Or perhaps the desired speed could be achieved with a smaller diameter, longer axial length machine.

It is recognised that many of the mechanical challenges resulted from the specification of a 170mm diameter rotor at the outset of the project and that scope to fix on a smaller rotor would have allowed a higher rotational speed. However, it is important to note that the mechanical stresses on the rotor are determined by the peripheral speed and not the rotational speed, and since torque density tends to increase with rotor diameter (due to the scaling effect of electric loading) then a smaller initial diameter specification would not necessarily have led to a more effective design in terms of power density.

Although the final design is not a very competitive in the context of the magnet-free EV machine with a speed range that offers little or no improvement over a conventional SYNCREL single-piece flux guide/flux barrier rotor, the research has generated several novel and interesting studies and contributions to knowledge:

Study of high pole number synchronous reluctance machines – As noted in the introduction to chapter 4, published studies on SYNCREL machines are dominated by the consideration of 4 pole machines with only occasional publications concerned with higher pole number SYNCREL machines. It is arguable that on the basis of published literature there is very little guidance to designers on the implications of higher pole number machines. The systematic study of pole numbers to a common performance specification has demonstrated quantitatively some of the trade-offs and design

implications of increasing the pole number. In machines prone to magnetic saturation such as SYNCRELs, the benefits of having a very high mmf per pole (which is usually regarded as an advantage of low pole number machines) is not of such value. Hence, in SYNCREL machines operating at 10A/mm^2 rms, saturation of the core is a limiting factor on performance even at the higher pole number. Other contributions to knowledge from this systematic study include the tendency to generate large ripple torque associated with slotting effects and the absence of a very clear pole number that is the most effective. Although iron loss was not a major feature of this research, some interesting behaviour in connection with rotor loss was observed, but not followed through to a more fundamental understanding.

In-depth study of mechanical behaviour of complex rotor geometries – Although there are numerous papers on mechanical analysis of electrical machine rotors, including some on SYNCREL machines, many of these are superficial and deal with ideal bonded components or single-piece rotors. It has been demonstrated in chapter 5 via numerous geometry variants that contact interfaces and their careful representation is key to representing the type of multi-component rotor structure which feature in many high performance machines. The very optimistic performance of an ideal bonded rotor provides a valuable cautionary tale over the limitations of some standard default settings in analysis and that a full appreciation of contact behaviour is important before embarking on detailed design. It has been demonstrated that relative movement of components and deformation of the rotor structure is a problem of as much, if not a greater, importance as localised stress levels. A notable aspect of chapter 5 is the detailed appraisal of adhesive bonding of parts, an aspect of manufacturing and operation that has received little attention in electrical machines published literature. Chapter 5 also addressed rotor-dynamic performance, and as is common in electrical machine rotors, issues of stress and deformation were far more restrictive in terms of operating speed than rotor dynamic considerations, such as the need to retain a margin below the first critical speed.

The formulation and deployment of a dynamic SIMULINK model – The model developed in chapter 6 was able to capture the full non-linear and intricate behaviour of a SYNCREL machine. This included an interesting approach to establishing the maximum number of turns required to avoid saturation of the close-loop current controller. Although only used for winding design in this study, the modelling approach developed lends itself to system level studies of many aspects of drive and vehicle performance.

Influence of rotor geometry on machine performance – Although many papers have been published on the very arcane and specific details of individual rotor types, including intricate formal optimisation, there are relatively few systematic and quantitative assessments of the merits of different rotor

topologies. Chapter 3 included a consistent and detailed comparison between flux guide, flux barrier and more conventional salient pole or cruciform SYNCREL topologies. The results included consideration of torque capability and highlighted the influence of harmonics concerned with multiple flux guides.

Overall, the reported programme of research has considered many aspects of SYNCREL behaviour which have read across to more conventional topologies as well as the specific concept which initiated this project.

8.2. Recommendations for Future Work

The proposed concept for a lightweight fibre reinforced hub with an array of individual flux guides would appear to offer a limited prospect for further developments as a competitive concept in high speed machine designs. There may be some scope to enhance the speed range with some higher strength adhesive, or a stiffer rotor hub material into which could provide more effective captive features for the flux guides, and some pre-stressing of the sleeve material could yield some dividend providing the underlying composite hub can manage the compressive forces. This work does show that the overall concept of this type of design is viable at lower speed ranges. Perhaps in future work it would be interesting to investigate a smaller diameter, lower pole number and lower speed machine for use in commercial applications such as fan motors. Or if higher speed designs are still interesting for investigation then maybe splitting the rotor flux guides into 2 in the middle, and placing a reinforcement hub into the centre of the rotor, sort of like the over-mould at the end caps of the rotor. This may prevent the excessive bending of the central nonmagnetic material that was witnessed in chapter 5.

The element of this project which is the most obvious aspect to take forward in future work is the completion of the build and test which was interrupted severely in this project. This could ultimately include some mechanical validation in a spin-test rig, possibly to destruction in a dedicated rotor burst facility once other testing had been completed. This would provide some validation of the predicted mechanical behaviour in terms of the speed at which failure occurs and the deformation of the outer surface and would be by far the most compelling experimental validation of electrical machine rotor mechanical performance in the public-domain.

In terms of the electromagnetic aspects of the research, the systematic study of pole number could be enhanced to establish some more fundamental principles which lie behind the observations made in chapter 4. For example, the rate at which the inductance ratio and the absolute inductance difference change with pole number. It is recognised that SYNCREL machines in which the stator tooth

width approach the flux guide width overlay some doubly-salient behaviour at slotting frequency onto the fundamental torque component predicted by d-q axis theory. Some elucidation of slot and flux guide numbers to enhance the overall torque or reduce ripple torque would be a good area for future work and make useful design guidelines. It could also be interesting to investigate the short term overload capability of this style of machine, as if it was to be researched further for the automotive traction machine market then that would be a subject field that the market would be interested in.

In common with much, but not all, research in the field of SYNCRELs, the power factor was considered as an output of the design rather than a key performance driver of the design. Given the very significant effect this has on converter rating and hence system cost / economic viability, then a parametric investigation into power factor, which might include some level of permanent magnet assistance, would be a useful contribution. It has been demonstrated in chapter 4 that designs can be achieved with respectable levels of power density and efficiency. Allied to their low cost nature, SYNCRELs should be a contender in some of the less demanding vehicle applications. However, the need for a large converter VA with this machine type remains in many respects its Achilles heel when compared at a system level to competing machine types.

9. References

[1] Department for Business, Energy & Industrial Strategy (2019a), “The Climate Change Act 2008 (2050 Target Amendment) Order 2019,” The National Archives, 2019.

[2] Department for Transport, (2019a),, “Transport Statistics Great Britain 2019,” 2019. [Online]. Available: https://assets.publishing.service.gov.uk/government/uploads/system/uploads/attachment_data/file/870647/tsgb-2019.pdf. [Accessed 22 October 2020].

[3] Department for Enviroment, Food and Rural Affairs, and Department for Transport (2017), “UK plan for tackling roadside nitrogen dioxide concentrations,” 2017. [Online]. Available: https://assets.publishing.service.gov.uk/government/uploads/system/uploads/attachment_data/file/633269/air-quality-plan-overview.pdf. [Accessed 12 July 2020].

[4] Department for transport; Office for Low Emission Vehicles; Department for Business, Energy & Industrial Strategy; The Rt Hon Alok Sharma MP; The Rt Hon Grant Shapps MP, “Government takes historic step towards net-zero with end of sale of new petrol and diesel cars by 2030,” Gov.uk, 18 November 2020. [Online]. Available: https://www.gov.uk/government/news/government-takes-historic-step-towards-net-zero-with-end-of-sale-of-new-petrol-and-diesel-cars-by-2030. [Accessed 07 July 2021].

[5] T. Denton, Electric and Hybrid Vehicles, Routledge, 2020.

[6] Z. Shahan, “1 Million Pure EVs Worldwide: EV Revolution Begins!,” Clean Technica, 22 November 2016. [Online]. Available: https://cleantechnica.com/2016/11/22/1-million-ev-revolution-begins/. [Accessed 5 January 2021].

[7] C. E. Thomas, “Fuel cell and battery electric vehicles compared,” *International Journal of Hydrogen Energy,* vol. 34, no. 15, pp. 6005-6020, 2009.

[8] Ricardo, “Ricardo develops next-generation electric vehicle motor,” Ricardo, 2015. [Online]. Available: https://ricardo.com/news-and-media/news-and-press/ricardo-develops-next-generation-electric-vehicle. [Accessed 5 Jan 2019].

[9] Automotive Council UK; Advanced Propulsion Centre UK, “Electric Machines Roadmap 2020,” February 2021. [Online]. Available: https://www.apcuk.co.uk/app/uploads/2021/02/Exec-summary-Technology-Roadmap-Electric-Machines-final.pdf. [Accessed 8 July 2021].

[10] Aerospace Technology Institute, “Insight 07 - Electrical Power Systems,” July 2018. [Online]. Available: https://www.ati.org.uk/media/ntlocbb4/insight_07-electrical-power-systems.pdf. [Accessed 8 July 2021].

[11] SAE, “Power From Within,” *SAE Vehicle Electrification Special Issue,* 2011.

[12] A. Mahmoudi, W. L. Soong, G. Pellegrino and E. Armando, “Efficiency maps of electrical machines,” *2015 IEEE Energy Conversion Congress and Exposition (ECCE),* pp. 2791-2799, 2015.

[13] Y. Yang, A. Walton and R. Sheridan, “REE Recovery from End-of-Life NdFeB Permanent Magnet Scrap: A Critical Review,” *J. Sustain, Metall. 3,* pp. 122-149, 2017.

[14] Z. Wang, T. W. Ching, S. Huang and T. X. Hongtao Wang, “Challenges Faced by Electric Vehicle Motors and their Solutions,” *IEEE Access,* vol. 9, pp. 5228-5249, 2021.

[15] A. Walker, M. Galea, C. Gerada, A. Mebarki and D. Gerada, “A topology selection consideration of electrical machines for traction applications: towards the FreedomCar 2020 targets,” *2015 Tenth International Conference on Ecological Vehicles and Renewable Energies (EVER),* pp. 1-10, 2015.

[16] T. Jahns, “Getting Rare-Earth Magnets Out of EV Traction Machines,” *IEEE Electrification Magazine,* no. March, pp. 6-18, 2017.

[17] G. Bailey, N. Mancheri and K. V. Acker, “Sustainability of Permanent Rare Earth Magnet Motors in (H)EV Industry,” *Journal of Sustainable Metallurgy,* vol. 1, no. 1, 2015.

[18] C. Hurst, “China's Rare Earth Elements Industry: What Can the West Learn?,” Institute for the Analysis of Global Security [IAGS], 2010.

[19] C. C. Pavel, R. Lacal-Arantegui, A. Marmier, D. Schuler, E. Tzimas, M. Buchert, W. Jenseit and D. Blagoeva., “Substitution Strategies for Reducing the use of Rare Earths in Wind Turbines.,” *Resources Policy,* vol. 52, pp. 349-357, 2017.

[20] A. Leader, G. Gaustad and C. Babbitt, “The Effect of Critical Material Prices on the Competitiveness of Clean Energy Technologies.,” *Materials for Renewable and Sustainable Energy,* vol. 8, no. 8, pp. 1-17, 2019.

[21] N. Sekine, I. Daigo and Y. Goto, “Dynamic Substance Flow Analysis of Neodymium and Dysprosium Associated with Neodymium Magnets in Japan.,” *Journal of Industrial Ecology,* vol. 21, no. 2, pp. 356-367, 2016.

[22] J. W. Lyman and G. R. Palmer, Recycling of Neodymium Iron Boron Magnet Scrap, United States Department of the Interior, Bureau of Mines, 1993.

[23] A. Trench and J. Sykes, “Rare Earth Permenant Magnets and their place in the Future Economy,” *Engineering,* vol. 6, 2020.

[24] E. Osmanbasic, “The Many Types of EV Motors,” Engineering.com, 25 May 2020. [Online]. Available: https://www.engineering.com/ElectronicsDesign/ElectronicsDesignArticles/ArticleID/20293/The-Many-Types-of-EV-Motors.aspx. [Accessed 11 Jan 2021].

[25] K. Atallah and D. Howe, “Modular permanent magnet brushless machines for aerospace and automotive applications,” *Proc. 20th int. Workshop Rare-Earth Magnets and Their Applications,* pp. 1543-1552, 10-14 sept 2000.

[26] I. R. Harris and G. W. Jewell, “Rare-earth magnets: properties, processing and applications,” *Functional Materials for Sustainable Energy Applications, Elsevier,* pp. Chapter 19, 600-639, Jan 2012.

[27] Q. Gao, C. Lv, N. Zhao, H. Zang, H. Jiang, Z. Zhang and F. Zhang, “Regenerative braking systems of PM synchronous motor,” in *AIP Conference Proceedings 1955, 040111*, 2018.

[28] Q. Wang, S. Wang and C. Chen, “Review of sensorless control techniques for PMSM drives,” *IEEJ Transactions of Electrical and Electronic Engineering,* vol. 14, no. 10, pp. 1543-1552, 2019.

[29] M. Biček, T. Pepelnjak and F. Pušavec, “Production aspect of direct drive in-wheel motors,” *Procedia CIRP,* vol. 81, pp. 1278-1283, 2019.

[30] A. Walker, M. Galea, D. Gerada, C. Gerada, A. Mebarki and N. Brown, “Development and design of a high performance traction machine for the FreedomCar 2020 traction machine targets,” *2016 XXIII International Conference on Electrical Machines (ICEM),* pp. 1611-1617, 2016.

[31] Equipmake Ltd, “APM 200 Datasheet,” Equipmake Ltd, Hethel, 2021.

[32] C. Woodford, “Induction Motors,” ExplainThatStuff, 21 April 2020. [Online]. Available: https://www.explainthatstuff.com/induction-motors.html. [Accessed 28 January 2021].

[33] Z. Q. Zhu and D. Howe, “Electrical Machines and Drives for Electric, Hybrid, and Fuel Cell Vehicles,” *Proceedings of the IEEE,* vol. 95, no. 4, pp. 746-765, 2007.

[34] A. Harson, P. H. Mellor and D. Howe, “Design considerations for induction machines for electric vehicle drives,” *Proceedings IEEE International Conference Electrical Machines and Drives,* pp. 16-20, September 1995.

[35] S. Jurkovic, K. M. Rahman, J. C. Morgate and P. J. Savagian, “Induction Machine Design and Analysis for General Motors e-Assist Electrification Technology,” IEEE Transactions on Industry Applications, Pontiac, 2015.

[36] K.T.Chau and W. Li., “Overview of electric machines for electric and hybrid vehicles.,” The University of Hong Kong, Pokfulam, 2010.

[37] G. Pellegrino, A. Vagati, B. Boazzo and P. Guglielmi, “Comparison of Induction and PM Synchronous Motor Drives for EV Application Including Design Examples,” *IEEE Transactions on Industry Applications,* vol. 48, no. 6, pp. 2322-2332, 2012.

[38] S. Jurkovic, K. M. Rahman, J. C. Morgante and P. J. Savagian, “Induction Machine Design and Analysis for General Motors e-Assist Electrification Technology,” *IEEE Transactions on Industry Applications,* vol. 51, no. 1, pp. 631-639, 2015.

[39] C. H. T. Lee, K. T. Chau, C. Liu, D. Wu and S. Gao, “Quantitative Comparison and Analysis of Magnetless Machines with Reluctance Topologies,” *IEEE Transactions on Magnetics,* vol. 49, no. 7, pp. 3969-3972, 2013.

[40] S. D. Caverley, G. W. Jewell and R. J. Saunders, “Calculation of centrifugal Stress in four-pole switched- reluctance rotors,” in *IEE Proceedings: Electric Power Applications 150(1):97-105*, 2003.

[41] S. A. Long, Z. Q. Zhu and D. Howe, “Vibration behaviour of stators of switched reluctance motors,” *IEE Proceedings: Electric Power Applications,* vol. 148, no. 3, pp. 257-264, 2001.

[42] W. Cai, P. Pillay, Z. Tang and A. M. Omekanda, “Low-vibration design of switched reluctance motors for automotive applications using modal analysis,” *IEEE Transactions on Industry Applications,* vol. 39, no. 4, pp. 971-977, 2003.

[43] J. Li, X. Song and Y. Cho, “Comparison of 12/8 and 6/4 Switched Reluctance Motor: Noise and Vibration Aspects,” *IEEE Transations on Magnetics,* vol. 44, no. 11, pp. 4131-4138, 2008.

[44] J. Barta and C. Ondrusek, “Computer Aided Rotor Design and Simulation of Synchronous Reluctance Machine,” Core.ac.uk.

[45] D. A. Staton, W. L. Soong, C. Cossar and T. J. E. Miller, “Unified Theory of Torque Production in Switched and Synchronous Reluctance Motors,” in *Conference Record of the 1993 IEEE Industry Applications Conference Twenty-Eighth IAS Annual Meeting*, Toronto, 1993.

[46] B. Ban, S. Stipetic and M. Klanac, “Synchronous Reluctance Machines: Theory, Design and the Potential Use in Traction Applications,” in *2019 International Conference on ElectricalDrives & Power Electronics (EDPE)*, The High Tetras, Slovakia, 2019.

[47] Y. Guan, Z. Q. Zhu, I. A. A. Afinowi, J. C. Mipo and P. Farah, “Design of Synchronous Reluctance and Permanent Magnet Synchronous Reluctance Machines for Electric Vehicle Application,”

in *17th International Conference on Electrical Machines and Systems (ICEMS)*, Hangzhou, 2014.

[48] X. Y. Ma, G. J. Li, Z. Q. Zhu, G. W. Jewell and J. E. Green, "Investigation on Synchronous Reluctance Machines with Different Rotor Topologies and Winding Configurations," IEEE, Sheffield, 2017.

[49] E. Agamloh, A. v. Jouanne and A. Yokochi, "An Overview of Electric Machine Trends in Modern Electric Vehicles," *MDPI Machines,* vol. 8, no. 2, pp. 1-16, 2020.

[50] C. Oprea, A. Dziechciarz and C. Martis, "Comparative analysis of different synchronous reluctance motor topologies," *2015 IEEE 15th International Conference on Enviroment and Electrical Engineering (EEEIC),* pp. 1904-1909, 2015.

[51] T. Mohanarajah, J. Rizk, M. Nagrial and A. Hellany, "Design of synchronous reluctance motors with improved power factor," *2017 11th IEEE International Conference on Compatibility, Power Electronics and Power Engineering (CPE-POWERENG),* pp. 340-345, 2017.

[52] G. Pellegrino, F. Cupertino and C. Gerada, "Barriers shapes minimum set of rotor parameters in the automated design of Synchronous Reluctance machines," *2013 International Electric Machines & Drives Conference,* pp. 1204-1210, 2013.

[53] S. Tahi, R. Ibtiouen and M. Bounekhla, "Design Optimization of Two Synchronous Reluctance Machine Structures with Maximized Torque and Power Factor," *Progress in Electromagnetics Research B,* vol. 25, pp. 369-387, 2011.

[54] M. Hofer and M. Schroedl, "Comparison of a flux barrier and a salient pole synchronous reluctance machine for high rotational speeds in electric traction applications," *2017 20th International Conference on Electrical Machines and Systems (ICEMS),* pp. 1-6, 2017.

[55] A. Dziechciarz, C. Oprea and C. Martis, "Multi-physics design of synchronous reluctance machine for high speed applications," *IECON 2016 - 42nd Annual Conference of the IEEE Industrial Electronics Society,* pp. 1704-1709, 2016.

[56] A. Credo, M. Villani, M. Popescu and N. Riviere, “Synchronous Reluctance Motors with Asymmetric Rotor Shapes and Epoxy Resin for Electric Vehicles,” Research Gate, L'Aquila, Wrexham, 2019.

[57] Y. Bao, M. Degano, S. Wang, L. Chuan, H. Zhang, Z. X and C. Gerada, “A Novel Concept of Ribless Synchronous Reluctance Motor for Enhanced Torque Capability,” IEEE, Nottingham, 2020.

[58] S. Tahi and R. Ibtiouen, “Finite Element Calculation of the dq-Axes Inductances and Torque of Synchronous Reluctance Motor,” ResearchGate, Alglers, 2014.

[59] T. Hamiti, T. Lubin, L. Baghli and A. Rezzoug, “Modeling of a synchronous reluctance machine accounting for space harmonics in view of torque ripple minimization,” *Mathematics and Computers in Simulation,* vol. 81, no. 0.1016/j.matcom.2010.07.024 . hal-00558540, pp. pp.354-366, 2010.

[60] I. Nasui-Zah, A. Nicorici and C. Martis, “Saturation and cross-saturation in synchronous reluctance machines,” *2018 International Conference and Exposition on Electrical and Power Engineering (EPE),* pp. 0347-0351, 2018.

[61] N. Bianchi, E. Fornasiero and W. Soong, “Selection of PM Flux Linkage for Maximum Low-Speed Torque Rating in a PM-Assisted Synchronous Reluctance Mschine,” *IEEE Transactions on Industry Applications,* vol. 51, no. 5, pp. 3600-3608, 2015.

[62] J. D. Widmer, R. Martin and B. C. Mecrow, “Optimization of an 80-kW Segmental Rotor Switched Reluctance Machine for Automotive Traction,” *IEEE Transactions on Industry Applications,* vol. 51, no. 4, pp. 2990-2999, 2015.

[63] G. J. Li, K. Zhang, Z. Q. Zhu and G. W. Jewell, “Comparative Studies of Torque Performance Impovement for Different Doubly Salient Synchronous Reluctance Machines by Current Harmonic Injection,” *IEEE Transactions on Energy Conversion,* vol. 34, no. 2, pp. 1094-1104, 2019.

[64] X. Y. Ma, G. J. Li, G. W. Jewell and Z. Q. Zhu, “Quantitative Analysis of Contribution of Air-Gap Field Harmonics to Torque Production in Three-Phase 12-Slot/8-Pole Doubly Salient

Synchronous Reluctance Machines," *IEEE Transactions on Magnetics,* vol. 54, no. 9, pp. 1-11, 2018.

[65] J. D. Widmer, R. Martin and B. C. Mecrow, "Precompressed and Stranded Aluminum Motor Windings for Traction Motors," *IEEE Transactions on Industry Applications,* vol. 52, no. 3, pp. 2215-2223, 2016.

[66] ABB, "Synchronous Reluctance Motors (SynRM)," 2021. [Online]. Available: https://new.abb.com/motors-generators/iec-low-voltage-motors/process-performance-motors/synchronous-reluctance-motors. [Accessed 8 July 2021].

[67] Ricardo, "Ricardo develops next-generation electric vehicle motor," Ricardo, 2015.

[68] Tata Steel , "Typical data for SURA® M250-35A," June 2008. [Online]. Available: https://www.tatasteeleurope.com/ts/sites/default/files/m250-35a.pdf. [Accessed 11 July 2021].

[69] Emetor AB, "Electric motor winding calculator," Emetor, 2021. [Online]. Available: https://www.emetor.com/windings/. [Accessed 2021].

[70] A. Torreggiani, C. Bianchini, M. Davoli and A. Bellini, "Design for Reliability: The Case of Fractional-Slot Surface Permanent-Magnet Machines," *Energies,* vol. 12, no. 9, 2019.

[71] HyperPhysics, "Resistivity and Temperature Coefficient at 20 C," HyperPhysics, 2020. [Online]. Available: http://hyperphysics.phy-astr.gsu.edu/hbase/Tables/rstiv.html. [Accessed 14 12 2020].

[72] B. V. Lingesh, B. M. Rudresh and B. N. Radikumar, "Effect of short glass fibers on mechanical properties of Polyamide66 and Polypropylene (PA66/PP themoplastic blend composites," *Procedia Materials Science,* vol. 5, pp. 1231-1240, 2014.

[73] Ai Engineering Plastics & Laminates, "Epoxy 4W/EP Sheet," 2017. [Online]. Available: https://www.aiplastics.com/media/amari/datasheets/4WEP%20Datasheet.pdf. [Accessed 09 11 2020].

[74] Tata Steel Europe, “NO20-1200H Data sheet,” 03 2019. [Online]. Available: https://www.tatasteeleurope.com/ts/sites/default/files/tata-steel-hi-lite-electrical-steel-no20-1200h-datasheet-en.pdf. [Accessed 5 01 2021].

[75] Menzolit, “Product information: menzolit BMC 0200,” 2006. [Online]. Available: https://menzolit.com/wp-content/uploads/2020/11/Menzolit-S-PI-BMC-0200-en.pdf. [Accessed 12 July 2021].

[76] The European Alliance for SMC/BMC, “Design for Success: A Design & Technology Manual for SMC BMC.,” 2020. [Online]. Available: https://smcbmc-europe.org/design_for_success/rapport_design_for_success.pdf. [Accessed 26th October 2020].

[77] S. D. Calverley, G. W. Jewell and R. J. Saunders, “Calculation of centrifugal stress in four-pole switched-reluctance rotors,” *IEE Proceedings - Electric Power Applications,* vol. 150, no. 1, pp. 97-105, 2003.

[78] Chegg Inc. , “Chegg Study: Principal Stresses,” Chegg Inc., 2020. [Online]. Available: https://www.chegg.com/homework-help/definitions/principal-stresses-5. [Accessed 23 10 2020].

[79] Kelly, “Engineering Auckland: Solid Mechanics Part II pages 203 to 221,” [Online]. Available: http://homepages.engineering.auckland.ac.nz/~pkel015/SolidMechanicsBooks/Part_II/07_3DElasticity/07_3DElasticity_02_3D_StressStrain.pdf. [Accessed 28 10 2020].

[80] K. Gramoll, “Mechanics - Theory: Maximum and Minimum Normal Stress,” eCourses, 2020. [Online]. Available: https://www.ecourses.ou.edu/cgi-bin/eBook.cgi?doc=&topic=me&chap_sec=07.2&page=theory. [Accessed 28 10 2020].

[81] Value Design Consulting , “Stress Theories,” Value Design Consulting , 2019. [Online]. Available: http://www.value-design-consulting.co.uk/stress-theories.html#. [Accessed 28 10 2020].

[82] S. A. Long, Z. Q. Zhu and D. Howe, “Vibration behaviour of stators of switched reluctance motors,” *IEE Proceedings - Electric Power Applications,* vol. 148, no. 3, pp. 257-264, 2001.

[83] S. D. Garvey, “The vibrational behaviour of laminated components in electrical machines,” *1989 Fourth International Conference on Electrical Machines and Drives,* pp. 226-231, 1989.

[84] Ozgun, “Mechead,” Mechead, 28 July 2018. [Online]. Available: http://www.mechead.com/contact-types-and-behaviours-in-ansys/. [Accessed 16 April 2020].

[85] Hyper Flight, “6mm Carbon Rod,” Hyper Flight, - - -. [Online]. Available: https://www.hyperflight.co.uk/products.asp?code=CARBON-ROD-6MM&name=6mm-carbon-rod. [Accessed 12 May 2020].

[86] M. Elices, G. V. Guinea, J. Gomez and J. Planas, “The cohesive zone model: advantages, limitations and challenges.,” *Engineering Fracture Mechanics,* no. 69, pp. 137-163, 2002.

[87] Permabond Engineering Adhesives, “Permabond TA439 Toughened Acrylic Adhesive Technical Datasheet,” Permabond, -, 2018.

[88] E. J. Gunter, “Dyrobes,” October 2001. [Online]. Available: https://dyrobes.com/wp-content/uploads/2016/04/Introduction-to-Rotor-Dynamics-Critical-Speed-and-Unbalance-Response-Analysis-E.-J.-Gunter_linked.pdf. [Accessed 05 11 2020].

[89] F. Luise, A. Tessarolo, F. Agnolet, S. Pieri, M. Scalabrin and P. Faffin., “A High-Performance 640-kW 10.000-rpm Halbach-Array PM Slotless Motor with Active Magnetic Bearings. Part I: Preliminary and Detailed Design.,” International Symposium on Power Electronics, Electrical Drives, Automation and Motion., Italy, 2014.

[90] NPTEL, “Simple Rotor Systems,” IIT GUWAHATI, 23 4 2014. [Online]. Available: https://nptel.ac.in/courses/112103024/4. [Accessed 6 6 2019].

[91] R. Beardmore, “Useful Tables,” 20 01 2013. [Online]. Available: https://roymech.org/Useful_Tables/Drive/Shaft_Critical_Speed.html. [Accessed 25 01 2019].

[92] E. Toolbox, “Area Moment of Inertia - Typical Cross Sections I,” 2008. [Online]. Available: https://www.engineeringtoolbox.com/area-moment-inertia-d_1328.html. [Accessed 1 1 2019].

[93] Substances & Technologies, “Carbon Steel SAE 1045,” 2 6 2012. [Online]. Available: http://www.substech.com/dokuwiki/doku.php?id=carbon_steel_sae_1045. [Accessed 3 6 2019].

[94] SKF, “Angular Contact Ball Bearings, Super-Precision,” 2019. [Online]. Available: https://www.skf.com/uk/products/bearings-units-housings/super-precision-bearings/angular-contact-ball-bearings/acbb-skf-high-and-super-precision/index.html. [Accessed 6 6 2019].

[95] SKF Technical Support, *SKF 61905,* 2011.

[96] E. B. Rosa and F. W. Grover, Formulas and Tables for the Calculation of Mutual and Self-Inductance, Leopold Classic Library, 2017.

[97] B. -. Thomson, “LECT11_212216,” 2006. [Online]. Available: https://courses.physics.ucsd.edu/2010/Fall/physics1b/documents/LECT11_212216.pdf. [Accessed 14 12 2020].

[98] ixymotor, “How to Calculate the Mechanical and Elctrical Angle of the Motor.,” 11 01 2020. [Online]. Available: https://www.ixymotor.com/news/how-to-calculate-the-mechanical-and-electrical-angle-of-the-motor.html. [Accessed 15 12 2020].

[99] Electrical4U, “Faraday's Laws of Electromagnetic Induction: First & Second Law,” Electrical4U, 28 10 2020. [Online]. Available: https://www.electrical4u.com/faraday-law-of-electromagnetic-induction/. [Accessed 21 12 2020].

[100] Semikron, “SKAI 45 A2 GD12-WCI,” Semikron Innovation + Service, 2021. [Online]. Available: https://www.semikron.com/products/product-classes/systems/detail/skai-45-a2-gd12-wci-14282031.html. [Accessed 5 06 2021].

Appendix A – M250-35A material magnetisation curve

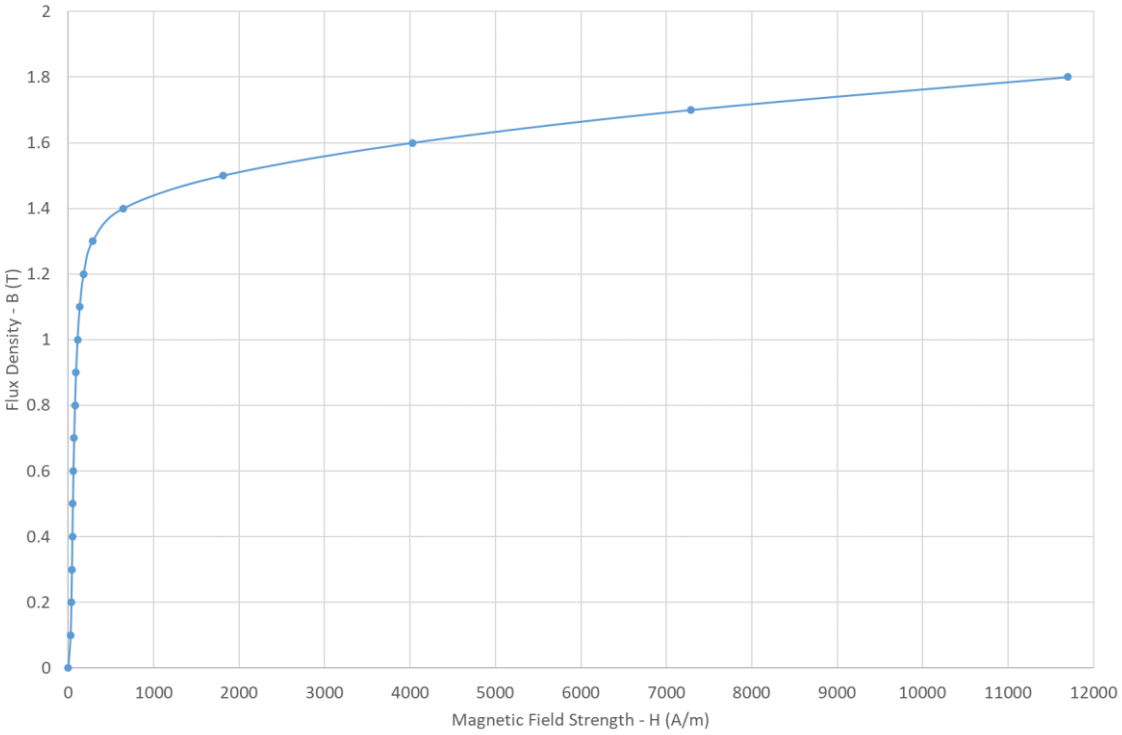

Appendix A: Magnetisation curve for the material M250-35A, as used in Ansys Maxwell